CORA Cork Open Research Archive
Cartlann Taighde Oscailte Chorcaí

Title	Modelling of thin film oxide growth and etching
Authors	Mullins, Rita
Publication date	2023
Original Citation	Mullins, R. H. 2023. Modelling of thin film oxide growth and etching. PhD Thesis, University College Cork.
Type of publication	Doctoral thesis
Rights	© 2023, Rita Helena Mullins. - https://creativecommons.org/licenses/by/4.0/
Download date	2026-10-29 07:46:38
Item downloaded from	https://hdl.handle.net/10468/16417

UCC
University College Cork, Ireland
Coláiste na hOllscoile Corcaigh

Ollscoil na hÉireann, Corcaigh

National University of Ireland, Cork



Modelling of Thin Film Oxide Growth and Etching

Thesis presented by

Rita Helena Mullins

https://orcid.org/0000-0002-3898-7328

for the degree of

Doctor of Philosophy

University College Cork

Tyndall National Institute

Head of Department: Dr. Fatima Gunning

Supervisor: Dr. Michael Nolan

2023

Table of Contents

Declaration.....vi

Acknowledgements.....vii

List of Publications.....viii

Conferences Attended.....ix

Awards.....x

Abstract.....xi

1 Introduction 1

1.1 Thin Film Deposition techniques……1

1.1.1 Physical Vapor Deposition……..... 1

1.1.2 Chemical Vapor Deposition……..2

1.2 Atomic Layer Deposition (ALD) ……2

1.2.1 ALD process…… 3

1.2.2 Thermal and Plasma-Enhanced ALD…….. 5

1.2.3 Precursor requirements……... 5

1.3 Atomic Layer Etching (ALE)…… 6

1.3.1 Thermal ALE Process…….....6

1.4 High-k Metal Oxides……7

1.5 Barrier + liner material for advanced interconnects…… 8

1.6 Modelling atomic scale processes……8

1.7 Thesis Outline…… 9

2 Thermal ALE & Metal ALD: Bridging Theory and Experiment for Mechanistic Clarity 15

2.1 Atomic Layer Etching……. 15

2.1.1 Introduction……... 15

2.1.2 Thermal ALE of metal oxides……...15

2.1.3 Identification of etch species…….…… 24

2.1.4 First principles simulations of thermal ALE processes…… 26

2.2 Atomic Layer Deposition……29

2.2.1 Introduction……..……... 29

2.2.2 Barrier and Liner materials in interconnect……30

2.2.3 Experimental work on ALD of Ru & Co…….…… 33
2.2.3.1 Experimental Ru ALD……...……... 33
2.2.3.2 Experimental Co ALD……...……... 37
2.2.3.3 TaN deposition with ALD……38
2.2.4 ALD Modelling of Ru and Co to explore the reaction mechanism……....38
2.3 Research Gaps and Questions Identified for my Thesis……...43
2.3.1 Thermal ALE of metal oxides……... 43
2.3.2 ALD to incorporate Ru/Co into TaN for combined diffusion barrier-liner films ……..,,,,……... 44

3 Density Functional Theory, Methods and Computational Models 60

3.1 Introduction…… 60
3.2 Schrodinger Equation……...60
3.3 Born-Oppenheimer Approximation……61
3.4 Hartree-Fock Method……...62
3.5 Hohenberg-Kohn Theorems…….64
3.6 Kohn-Sham Equations…… 65
3.7 Practical Implementation of DFT…… 66
3.7.1 Basis Set…….…… 66
3.7.2 Pseudopotentials……...……... 68
3.7.3 Projector Augmented Waves (PAW)…….…… 67
3.7.4 Exchange-Correlation Functional…….…… 70
3.7.5 Local Density Approximation……... 70
3.7.6 Generalized Gradient Approximation…….……... 70
3.7.7 Hybrid DFT…….…….……... 71
3.8 Methods and Computational Models……... 71
3.8.1 Crystalline HfO_2……...73
3.8.2 Crystalline ZrO_2……... 75
3.8.3 Amorphous HfO_2…… 76
3.8.4 ZnO…….……... 78
3.8.5 Ru…….…… 79
3.8.6 TaN…….……... 80
3.9 Natarajan−Elliott Analysis for ALE Thermodynamics……... 81

4 Modelling Atomic Layer Etching of Thin Film Crystalline Metal Oxides 89

4.1 Self-limiting Product State Models…….…… .89

4.2 Thermodynamics of Self-limiting vs Spontaneous Etch…….……..90

4.2.1 Reaction Free Energy Profiles (FEPs)…….92

4.3 Adsorption of One HF Molecule at HfO_2 and ZrO_2……..……...95

4.4 Stability of Different HF Coverages…… 97

4.5 Water Formation…….. 102

4.6 Effect of surface facets on crystalline HfO_2 etching……... 104

4.7 HCl as an alternative to HF……..106

4.7.1 Chlorination of HfO_2 and ZrO_2 using HCl…….……..…….. 106

4.7.2 Chlorination and Fluorination of ZnO…….…….. 107

4.8 Discussion……110

4.9 Conclusions……..115

5 Modelling Atomic Layer Etching of Amorphous HfO_2 118

5.1 Self-limiting vs Spontaneous Etch……...…118

5.2 Adsorption of one HF to the bare amorphous HfO_2 surface……... 122

5.3 Stability of higher HF coverages……. 123

5.4 Spontaneous formation of H_2O and H_2O_2……..……..126

5.5 Discussion……128

5.6 Conclusions……..130

6 Mechanism of the ligand exchange chemistry between fluorinated HfO_2 and $SiCl_4$ in the second half cycle of self-limiting thermal ALE of HfO_2 131

6.1 Interaction of $SiCl_4$ at fluorinated HfO_2 surfaces…….……..132

6.2 Role of surface Hf site on ligand exchange of $SiCl_4$ on 8O/16F HfO_2 surface..135

6.3 Mechanism involving the formation of $SiFCl_3$…….....139

6.4 Thermodynamic analysis of the energetics of formation of etch species……...143

6.5 Discussion…….. 144

6.6 Conclusions……146

7 Stability of NH_x-Surface Terminations of TaN Diffusion Barrier 148

7.1 Charge analysis of bare ε-TaN (110) surface….....148

7.2 Surface Terminations of ε-TaN (110) to be studied.....149

7.3 Single N-H_x and Ta-NH_x adsorbates.....150

7.4 Mixed NH/NH_2 terminations of ε-TaN (110)..... 153

7.5 One Monolayer Coverage of NH/NH_2 terminations of ε-TaN (110).....156

7.6 Coverage of N-H_x terminated ε-TaN (110).....157

7.7 Coverage of Ta-NH_x terminated ε-TaN (110)..... 158

7.8 Conclusions.....162

8 Incorporation of ruthenium or cobalt into TaN for a combined barrier and liner material 164

8.1 Chemistry of Bis(cyclopentadienyl)ruthenium(II), $RuCp_2$, precursor at TaN surfaces.....165

8.1.1 $RuCp_2$ interaction at 1 ML N-H-terminated ε-TaN surface.....165

8.1.2 $RuCp_2$ interaction at other ε-TaN (110) surface terminations.....167

8.1.3 Single $RuCp_2$ Reaction Pathway on 1 ML N-H ε-TaN.....167

8.1.4 Effect of $RuCp_2$ coverage on 1 ML N-H ε-TaN (110).....169

8.1.5 H_2 plasma radical chemistry on $RuCp_2$ treated 1 ML N-H ε-TaN (110) surface.....174

8.2 ALD Chemistry with Bis(ethylcyclopentadienyl)ruthenium(II), $Ru(EtCp)_2$ Precursor..... 176

8.2.1 $Ru(EtCp)_2$ interaction at NH_x-terminated ε-TaN (110) surfaces.....176

8.2.2 Single $Ru(EtCp)_2$ Reaction Pathway on NH_x-terminated ε-TaN..... 179

8.2.3 Effect of $Ru(EtCp)_2$ coverage on 1 ML N-H ε-TaN and 0.5 ML N-H/0.5 ML N-H_2 ε-TaN..... 181

8.2.4 H_2 plasma radical chemistry on $Ru(EtCp)_2$ treated 1 ML N-H and 0.5 ML N-H/0.5 ML N-H_2 ε-TaN surfaces..... 186

8.3 Chemistry of ToRuS, RuO_4, precursor on ε-TaN surfaces..... 188

8.3.1 RuO_4 adsorption at NH_x-terminated ε-TaN surfaces.....188

8.3.2 Single RuO_4 Reaction Pathways.....189

8.3.2.1 1 ML N-H ε-TaN (110) surface..... 189

8.3.2.2 RuO_4 chemistry on 0.5 ML N-H/0.5 ML N-H_2 ε-TaN (110) surface191

8.3.3 H_2 plasma radical chemistry on RuO_4 treated 0.5 ML N-H/0.5 ML N-H_2 ε-TaN surface 193
8.4 ALD chemistry of Bis(cyclopentadienyl)cobalt(II), $CoCp_2$, at ε-TaN surfaces .. 197
8.4.1 $CoCp_2$ interaction at NH_x-terminated ε-TaN surfaces 197
8.4.2 Single $CoCp_2$ Reaction Pathway on NH_x-terminated ε-TaN 199
8.4.3 Chemistry of $CoCp_2$ 1 ML N-H ε-TaN at higher $CoCp_2$ coverage 202
8.4.4 H_2 plasma radical chemistry $CoCp_2$ precursor fragments on the 1 ML N-H ε-TaN surface 207
8.5 ALD Chemistry with the Bis(ethylcyclopentadienyl)cobalt(II), $Co(EtCp)_2$ precursor 209
8.5.1 7.4.1 $Co(EtCp)_2$ interaction at NH_x-terminated ε-TaN surfaces 209
8.5.2 Single $Co(EtCp)_2$ Reaction Pathway on NH_x-terminated ε-TaN 212
8.5.3 Effect of $Co(EtCp)_2$ coverage on the 1 ML N-H and 0.5 ML N-H/0.5 ML N-H_2 ε-TaN surfaces 215
8.5.4 H_2 plasma radical chemistry on $Co(EtCp)_2$ treated 1 ML N-H ε-TaN surface 220
8.6 Discussion 222
8.7 Conclusions 224

9 Modelling Atomic Layer Deposition of Ru using RuO_4 and H_2 228
9.1 Coverage of RuO_4 Precursors 228
9.2 Reaction of H_2 with Surface Bound RuO_4 Precursors 238
9.3 Conclusions 244

10 Conclusions and Outlook 247
10.1 Conclusions 247
10.1.1 Modelling thermal ALE of metal oxides 247
10.1.2 Incorporation of Ru or Co into TaN and ALD of Ru using RuO_4 252
10.2 Outlook and Future Work 255

Appendix 260

Declaration

This is to certify that the work I am submitting is my own and has not been submitted for another degree, either at University College Cork or elsewhere. All external references and sources are clearly acknowledged and identified within the contents. I have read and understood the regulations of University College Cork concerning plagiarism and intellectual property.

Acknowledgements

First, I would like to thank my supervisor, Dr. Michael Nolan, for offering me this opportunity. I really appreciate his guidance, expertise and mentorship throughout my PhD journey. I am grateful for his support in facilitating my attendance at international conferences and workshops which gave me great opportunities to present my research to the global scientific community.

I would like to thank my thesis committee, Dr. Davide Tiana and Dr. James Rohan for their valuable feedback and encouragement at my progress reviews. Thank you to my co-authors, Dr. Suresh Kondati Natarajan, Dr. Simon D. Elliott, Dr. Ji Liu and Dr. José Julio Gutiérrez Moreno.

I acknowledge support from LAM Research and Science Foundation Ireland (SFI) through the SFI-NSF China Partnership Program, NITRALD Grant No. 17/NSFC/5279. I also acknowledge access to Tyndall computing facilities supported by SFI and the Irish Centre for High-End Computing.

Thank you to the members of the Materials Modelling for Devices group for their kindness and support. Special thanks to Cara and Arbresha for their encouragement during our coffee breaks.

Thank you to my parents Pauline and Paschal for their love and unwavering encouragement. Their belief in me has remained an everlasting source of motivation. Thank you to my Aunt Marion and Uncle Kevin for looking after me and always being there for me throughout the years I stayed with them for school, university and my PhD. Thank you to my brother Paschal for always offering words of motivation during challenging times. Your presence and encouragement have made an immeasurable difference. Thank you to Maura for always keeping me in her thoughts and sending heartfelt wishes my way throughout my PhD. Thank you also to all my other friends and family for their support.

Finally, thank you to Odhran for your unconditional love and encouragement throughout my academic journey. Your belief in me has been a constant source of strength, pushing me to achieve beyond what I thought possible.

List of Publications

1. Rita Mullins, Suresh Kondati Natarajan, Simon D. Elliott, and Michael Nolan. "Self-Limiting Temperature Window for Thermal Atomic Layer Etching of HfO_2 and ZrO_2 Based on the Atomic-Scale Mechanism." *Chemistry of Materials* **2020** 32 (8), 3414-3426. https://doi.org/10.1021/acs.chemmater.9b05021

2. Rita Mullins, José Julio Gutiérrez Moreno, Michael Nolan. "Origin of enhanced thermal atomic layer etching of amorphous HfO_2." *Journal of Vacuum Science and Technology A* **2022** 40 (2), 022604. https://doi.org/10.1116/6.0001614

3. Ji Liu, Rita Mullins, Hongliang Lu, David Wei Zhang, and Michael Nolan. "Nucleation of Co and Ru Precursors on Silicon with Different Surface Terminations: Impact on Nucleation Delay." *The Journal of Physical Chemistry C* **2023** 127 (28), 13651-13658. https://doi.org/10.1021/acs.jpcc.3c02933

In this thesis, my responsibility involved collaborating with my co-authors to develop the studies. I performed different types of DFT calculations (geometry relaxation and nudged elastic band calculations), carried out thermodynamic calculations and computed Bader charges. I analysed the results and presented them at conferences and workshops. I prepared manuscripts for publication and responded to reviewer comments. For publication 1 in the list, authors Rita Mullins and Dr. Suresh Kondati Natarajan contributed equally to the manuscript in terms of analysis and preparation. I developed the models and performed all the DFT calculations related to the thermodynamic and mechanistic investigation.

Conferences Attended

Poster presentations:

- Rita Mullins, Suresh Kondati Natarajan and Michael Nolan.
  ALD/ALE 2019, July 21 – 24, Bellevue, WA, USA.
  A Mechanistic Study of the HF Pulse in the Thermal Atomic Layer Etch of HfO_2 and ZrO_2.
- Rita Mullins, Suresh Kondati Natarajan and Michael Nolan.
  15th International conference on materials chemistry (MC15), 12 - 15 July 2021, online.
  Modelling Atomic Layer Etching of Thin Film Metal Oxides.
- Rita Mullins, Suresh Kondati Natarajan and Michael Nolan.
  240th ECS Virtual Meeting, October 10 – 14, 2021, Digital Meeting.
  A Mechanistic Study of the HF Pulse in Thermal Atomic Layer Etch of Crystalline and Amorphous HfO_2.

Oral presentations:

- Rita Mullins, Suresh Kondati Natarajan, Simon D. Elliott and Michael Nolan.
  ALD/ALE 2020 Virtual Meeting, June 29 – July 1, online.
  Mechanism of the HF Pulse in the Thermal Atomic Layer Etch of HfO_2 and ZrO_2: A First Principles Study.
- Rita Mullins, Suresh Kondati Natarajan and Michael Nolan
  239th ECS Meeting, May 30-June 3, 2021, Digital Meeting.
  Modelling the Growth and Etch of Thin Film Metal Oxides.
- Rita Mullins, Suresh Kondati Natarajan and Michael Nolan.
  ALE/ALE 2021 Virtual Meeting, June 27 – 30, Online.
  Modelling Atomic Layer Etching of Thin Film Metal Oxides.
- Rita Mullins and Michael Nolan.
  ALD/ALE 2022, June 26 – 29, Ghent, Belgium.
  Modelling Ruthenium Deposition in Atomic Layer Deposition of Ru-doped TaN.

Awards

- Best ALE Poster Award at the International ALD/ALE 2019 Bellevue, Washington, USA.
- Rising Talent Award Tyndall Postgraduate Publication of the Year 2020.
- ALE 2021 Student Award Finalist at the International ALD/ALE 2021 virtual meeting.
- Editor's Pick for the publication "Origin of enhanced thermal atomic layer etching of amorphous HfO_2" (publication 2 in the list of publications).

Abstract

As integrated circuit technology follows Moore's Law and continues to shrink, conventional methods for depositing and etching thin films encounter numerous challenges. Moreover, the challenges intensify due to the expected widespread adoption of 'more-than-Moore' devices designed for non-conventional computing applications. Traditional deposition methods will struggle to deliver continuous films at increasingly thinner levels and on complex 3D structures. Moreover, traditional continuous-wave plasma etching faces problems in achieving precise critical dimension control, enhanced selectivity, and with minimal plasma damage, especially below the 10 nm scale. In response to these limitations, atomic-scale processing techniques have emerged; producing thin films tailored to meet the demands of smaller and more intricate structures crucial for future semiconductor devices.

Atomic layer deposition (ALD) and atomic layer etching (ALE) offer uniform and conformal processing with precise thickness control and can be achieved using sequential, self-limiting thermal surface reactions. These are used in various applications, such as employing ALE for etching high dielectric metal oxides necessary for gate dielectrics in complex transistor structures such as Gate-All-Around or Complementary FET, and utilizing ALD to deposit barrier/liner thin films within interconnects. Presently, ALD is widely used in the semiconductor industry whereas thermal ALE is in the early stage of development and is an emerging and promising frontier in thin film processing.

It is difficult to investigate ALD and ALE reactions directly using experimental techniques. First principles density functional theory (DFT) can give deep insights into precursor chemistry and reaction mechanisms of ALD and ALE processes.

In my thesis I studied the hydrogen fluoride (HF) pulse as the first step in thermal ALE of high dielectric metal oxides. A thermodynamic analysis is used to predict the temperature at which the targeted self-limiting (SL) reactions are favoured over continuous spontaneous etching (SE) in an ALE cycle. Furthermore, calculations of HF adsorption are performed on the oxide surfaces to understand the mechanistic details of the HF pulse and calculate theoretical etch rates. The results are compared between the metal oxides studied: monoclinic HfO_2 and ZrO_2, orthorhombic HfO_2, amorphous HfO_2 and ZnO. HCl is examined as an alternative to HF for crystalline HfO_2, ZrO_2 and ZnO. The second step in thermal ALE, the ligand exchange reaction is examined for crystalline HfO_2 using HF and $SiCl_4$ allowing us to determine how the target Hf species can be chlorinated before being eliminated as volatile Cl-containing species.

A combined barrier and liner material incorporating Ru or Co into TaN has been proposed to replace the tri-layer stack of TaN/Ta/Cu for advanced interconnect technology. This will accommodate high aspect ratio trench structures with the continued miniaturization of devices and extend the use of Cu in interconnects for the next generation of electronic devices. Ruthenium and cobalt are also potential replacements for Cu in next-generation interconnects. In this thesis, DFT calculations are also used to explore the nature of N_2/H_2 terminated TaN surfaces that are produced after a plasma pulse (with H_2 or N_2/H_2 plasma) in Plasma Enhanced ALD to incorporate Ru or Co into TaN. The reactivity of Ru and Co precursors is studied on stable NH_x-terminated TaN surfaces. This work will help guide experimental PEALD for the incorporation of ruthenium or cobalt into TaN as a combined barrier and liner material. Finally the mechanism of Ru ALD using the novel precursor RuO_4 and molecular H_2 was investigated to elucidate the role of both reactants.

1 Introduction

Traditional methods to deposit and etch thin films face many challenges as the integrated circuit device follows Moore's Law and shrinks every year. In addition, so-called more-than-Moore devices for unconventional computing will become widespread.[1] It is difficult to obtain continuous films at such thin thicknesses and on complex 3D structure using physical vapor deposition (PVD) and chemical vapor deposition (CVD). It is also difficult to satisfy higher selectively, compact critical dimension control and reduced plasma damage below the 10 nm mode using traditional continuous-wave plasma etching.[2] Atomic-scale processing techniques have emerged as important methods for developing thin films for the smaller and more spatially demanding structures needed in future semiconductor devices. Atomic layer deposition (ALD) and atomic layer etching (ALE) offer uniform and conformal processing with precise thickness control and can be achieved using sequential, self-limiting thermal reactions. These atomic-scale processing techniques can be used to develop thin films for various applications such as ALE to etch high dielectric metal oxides for gate dielectrics in transistors[3] and ALD to deposit barrier/liner thin films in interconnects.[4] ALD is widely used in the semiconductor industry today whereas there are only a few thermal ALE processes and none are in volume production, so that this remains an emerging but exciting research area.[3] For both ALD and ALE first principles simulations are invaluable in understanding and developing new processes and the aim of my thesis is to explore new ALD and ALE processes using atomistic simulations.

1.1 Thin Film Deposition techniques

1.1.1 Physical Vapor Deposition

The PVD process entails extracting atoms from a solid or a liquid (condensed phase) by thermal heating of the source or energetic particle bombardment by electrons, atoms, ions, molecules or photons and depositing these vapour phase atoms on a surface resulting in a condensed thin film.[5] These are atoms that are not normally found in the gas phase. The main PVD processes are thermal evaporation and physical sputtering. Thermal evaporation PVD involves heating the source of the atoms to remove them, making it a thermodynamically driven process. Energetic particle bombardment to remove atoms from the source using electrons, ions or photons as part of a sequence of energetic collisions near the surface is termed physical sputtering PVD.[5] The atoms removed from the initial surface will then diffuse inside an

evacuation chamber until the vapour condenses on the substrate to form a thin film.[6] The thickness of thin films deposited using PVD processes are within a few nm to microns. PVD is used to deposit materials used for multilayer coatings such as TiN on orthopedic implants to prevent metallic ions leaking into the human body.[7] PVD can also be used to deposit diffusion barriers e.g. amorphous ruthenium doped with phosphorous[8], Cu seed layers[9] and etch stops such as AlN as an interconnect etch stop[10]. PLD (pulsed laser deposition) is another thin film processing technique used in the fabrication of various materials, including thin films and coatings. In PLD a laser is used to vaporize the target material and then deposit the resulting vaporized material onto a substrate to create a thin film.[11] However PLD has limited applications in high volume commercial settings due to its low throughput capability.[12]

1.1.2 Chemical Vapor Deposition

CVD is different from PVD as in PVD the main source of the depositing species is a solid or liquid, whereas in CVD processes thin solid films are formed on a substrate by a chemical reaction between vapour phase precursors.[13] These chemical reactions between the precursors can also take place on the substrate. Well known CVD processes are thermal CVD, photo-assisted CVD and plasma-enhanced CVD (PECVD). PECVD can occur at low temperatures allowing temperature sensitive substrates to be used giving it an advantage over thermal CVD.[13] The development of CVD processes arose when other thin film deposition techniques were inadequate, for example, the production of multiple thin films in modern semiconductor devices which appeared during the rapid development of the microelectronic industry since the 1970s.[13] High purity films with precise control of uniformity, composition and doping are required. The thickness of thin films deposited by CVD can vary from single atomic layers to hundreds of nanometers and microns. The layer of thickness grown depends on the CVD process used. Processes such as thermal CVD and PECVD with high temperatures, pressures and growth rates produce thicker films.

1.2 Atomic Layer Deposition (ALD)

ALD was first introduced in the early 1970s by T. Suntola and co-workers who referred to the this growth method as “atomic layer epitaxy” and it was originally developed for electroluminescent (EL) flat panel displays in Finland.[14] The term epitaxy actually means single crystal growth on a substrate, which is widely used in the semiconductor industry and therefore “atomic layer deposition” was agreed to be a more suitable name for the process.[15]

ALD is a variant of CVD that produces thin films one atomic layer at a time (at least in principle) and is based on *sequential self-limiting surface reactions* at lower temperatures than thermal CVD.[14,16] Self-limiting saturation of a precursor on the substrate is reached when all available reactive sites are used up.[17] No other thin film deposition technique can come close to the conformality obtained by ALD on high aspect structures.

1.2.1 ALD process

The ideal ALD growth cycle results in a perfect monolayer of deposited material formed after each half-cycle. A single ALD cycle consists of the following steps as shown in Figure 1.1.[18]

1. First precursor pulse exposure to the substrate.
2. Purge the reaction chamber using an inert gas to remove reaction products and any excess precursor.
3. Pulse of the second precursor
4. Purge reaction products and excess reactants.

Steps 1 & 2 are the 1st half-cycle and steps 3 & 4 are the 2nd half cycle. The purge step removes residual precursor and reactant species to ensure that ALD surface reactions take place and not CVD.[19] The alternating self-limiting surface reactions enable controlled growth of the material with excellent conformality and thickness uniformity.[18] In principle, one ALD cycle deposits one monolayer of material and the ALD cycle is repeated until the desired film thickness is achieved. ALD processes generally result in sub-monolayer growth after each cycle which can be due to e.g. steric effects of the precursors' ligands obstructing active sites or competing reactions.[20] The growth per cycle for (GPC) Al_2O_3 ALD using TMA and H_2O had rates of 1.1 – 1.2 Å/cycle which is clearly much lower than the monolayer thickness of 3.8 Å.[16] Similarly for TiO_2, HfO_2 or ZnO growth rates of 0.73, 1.00, 1.01 Å/cycle are observed[21–23], again smaller than the GPC expected for true monolayer growth.

A defining feature of ALD processes is the self-limiting saturation of precursors which is influenced by either the steric effect of the adsorbed precursor fragments or the concentration of active sites on the surface.[20] If the active sites are scattered the saturation will be more dependent on the coverage of active sites. The saturation could be restricted on a surface with a high density of active sites due to precursor fragments blocking nearby available active sites.

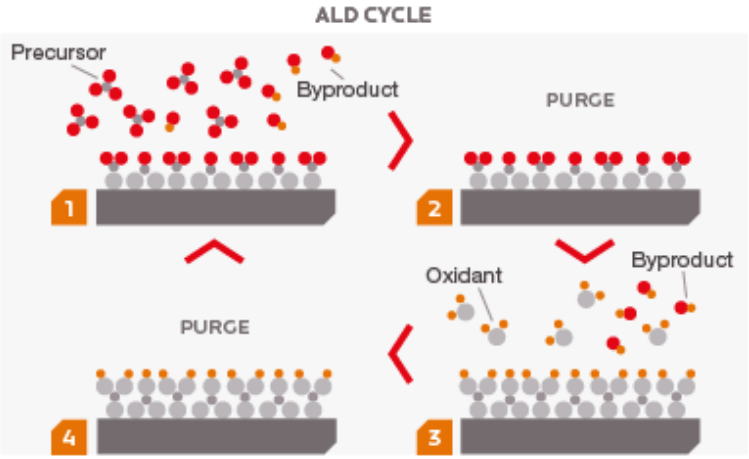


Figure 1.1: Schematic representation of ALD cycle. Source ASM[51].

Precursors can adsorb on a surface through chemisorption or physisorption. Physisorption is when there are intermolecular forces such as van der Waals or hydrogen bonding between the precursor and the substrate, typically with interaction energies of less than 0.2 eV. Physisorption is not considered to be the main step for growth in ALD processes.[20] This is because intermolecular forces are weak between the precursors and substrate which will likely lead to desorption during the purge step. However, in theoretical ALD studies, physisorption is found to play a contributing role in ALD. A precursor can interact with the surface through physisorption as the first step, which may help in contributing to the following chemisorption step.[24]

Chemisorption takes place when a new chemical bond is formed between the precursor and the substrate, typically with interaction energies of larger than 1 eV. Precursor chemisorption mechanisms onto a substrate include intact adsorption, ligand exchange with the surface and precursor dissociation into surface adsorbed fragements.[20] Ligand exchange is the exchange of ligands between two species, e.g. surface OH group can undergo ligand exchange with Cl ligand of $HfCl_4$ to release HCl.[25] Dissociative adsorption occurs when the precursor dissociates and all fragments chemisorb with the surface. At ALD process temperatures precursors should only react with the surface and not with themselves to ensure the self-limiting nature of ALD. Volatile byproducts formed by chemisorption desorb from the surface and are purged away in the following step.

1.2.2 Thermal and Plasma-Enhanced ALD

In thermal ALD, the activation energy for the chemical reaction of the precursor onto the substrate is driven by substrate heating. At low substrate temperatures the ALD GPC decreases when the thermal energy becomes insufficient to drive the chemical reaction. The "ALD window" is limited by low/high substrate temperatures, incomplete surface reactions, thermal decomposition of precursors and thermal desorption.[16] In plasma-enhanced ALD (PEALD), plasma-generated radicals are used to enable/accelerate chemical reactions with the deposited precursor layer that are too slow or limited by thermal energy and standard reactants.[26] Typical plasmas used in in PEALD are those produced in O_2, N_2 and H_2 reactant gases or mixtures comprising the plasmas and they replace the ligand-exchange reactions characteristic of H_2O and NH_3 in thermal ALD.[19] Additionally, plasmas produced in gases or vapors, such as NH_3 and H_2O, have been reported, wherein a simultaneous occurrence of both plasma and thermal atomic layer deposition (ALD) surface reactions is possible.[19] PEALD offers greater processing flexibility compared to thermal ALD as well as increasing the number of precursors used. Lower substrate temperatures are possible in PEALD compared to thermal ALD while the GPC can be maintained. In thermal ALD of HfO_2 using TDMAH and H_2O the process window was between 200 – 250 ºC whereas in PEALD where H_2O was replaced with oxygen plasma, ALD can be performed down to 150 ºC.[27] Consequently, PEALD expands the range of materials that can be deposited.

1.2.3 Precursor requirements

Precursors used in ALD processes must meet the following requirements:[28]

- Precursors must be available or synthesized.
- Precursors are thermally stable, volatile and highly reactive.
- Volatile enough to be in the gas phase at room temperature or when moderately heated.
- Should not decompose until they have reached and reacted with the surface.
- Precursors should not damage the substrate, the film being grown or the ALD reaction chamber.

1.3 Atomic Layer Etching (ALE)

ALE is a self-limiting process that allows highly controlled layer-by-layer removal of material.[29] ALE removes material with atomic-scale precision using sequential self-limiting surface reactions .[30] In the semiconductor industry ALE is an alternative to plasma etching known as continuous etching where multiple surface reactions are occurring continuously and simultaneously.[31] Disadvantages of plasma etching are damage from plasma, etching accuracy and unlimited reactivity.[32] There are two ALE processes, plasma ALE and thermal ALE.[33,34] Plasma ALE removes surface species using energetic ions that yield anisotropic etching.[33] The self-limiting nature of thermal ALE reactions allows isotropic and conformal etching.[35] The ALE reactions modelled in this thesis are based on the thermal ALE mechanism which will be explained in the following section.

1.3.1 Thermal ALE Process

Thermal ALE relies on temperature and thermochemically favourable reactions to remove surface species.[34] There are two main steps in thermal ALE, the surface modification step and secondly the volatilization step.[36] The surface modification step produces an altered reactive non-volatile surface layer which does not penetrate into the remainder of the substrate and is removed in the volatilization reaction. For metal oxides, the thermal ALE mechanism is based on fluorination and ligand exchange reactions as shown in Figure 1.2.[3]

1. The metal-containing film is converted to its corresponding nonvolatile metal fluoride using a suitable reactant. Thermal ALE processes of metal oxides generally use HF for the fluorination reaction however other reactants such as SF_4 and NbF_5 have also been explored and other modification processes are of significant interest, avoiding using of fluorinated chemicals.
2. Purge the reaction chamber using an inert gas to remove reaction products and any excess precursor.
3. Typically a metal-containing precursor is exposed to the fluorinated surface where it exchanges one of its ligands with a fluoride species from the modified surface and the ligand from the precursor binds to the etch target. This produces stable and volatile metal products that can desorb from the surface.
4. Purge reaction products and excess reactant leaving a film where up to one layer of material has been removed.

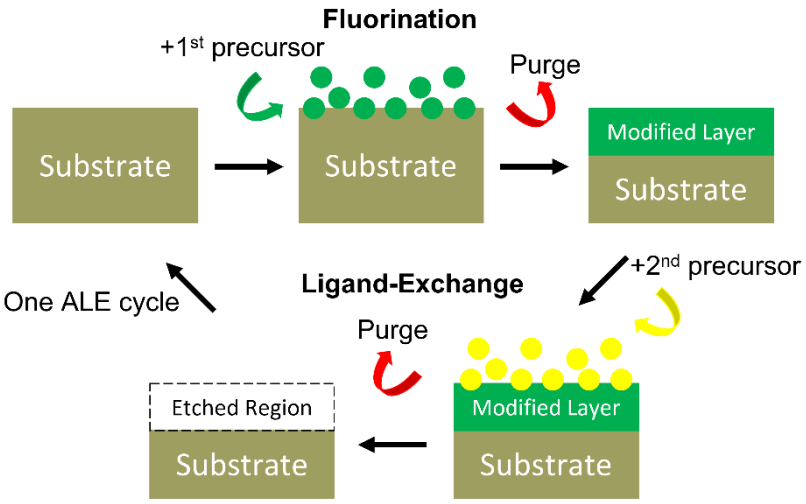


Figure 1.2: Schematic model of the thermal ALE process.[50]

Other mechanisms for thermal ALE include conversion, oxidation, oxidation/chlorination, halogenation and chlorine-fluorine ligand exchange.[36] Thermal ALE has many advantages such as atomic-scale precision, conformal etching, selective etching and ultra smooth etched surfaces.[32] Applications of thermal ALE include surface cleaning for the removal of metal impurities in semiconductor fabrication, conformal etching in high-aspect-ratio structures, and smoothing of surfaces to obtain flat and damage-free layers, which are also important in the semiconductor industry.[3,32]

1.4 High-*k* Metal Oxides

Due to Moore's law scaling, semiconductor devices have features at the nanometer scale. With the shrinking of device feature sizes, SiO_2 films for gate dielectrics are so thin (under 1.4 nm) that electron tunnelling through the dielectric layer which leads to high leakage currents (exceeding 1 A/cm^2 at 1 V) is impossible to avoid.[37] The solution is to replace SiO_2 (dielectric constant of 3.9) with a high dielectric oxide. The replacement oxide must have a dielectric constant that is high enough for a practical number of years of scaling and be thermodynamically stable when interfaced with the Si channel.[37] Materials with a high dielectric constant allow a high drive current to be maintained, while minimized leakage currents and a low equivalent oxide thickness can be achieved.[38] HfO_2 and ZrO_2 are high dielectric metal oxides with dielectric constants of 22 and 23, respectively, that have replaced SiO_2.[38] While SiO_2 can be grown by thermal oxidation of Si, high dielectric oxides must be deposited using a thin film deposition process such as CVD or ALD processes.[39] High dielectric metal oxides can also be etched using thermal ALE to produce thin films with conformal

nanometer scale feature sizes in high aspect ratio structures. This can be done to exploit the deposition of thick films with ALD and then employ ALE to reduce their thickness to the desired value.

1.5 Barrier + liner material for advanced interconnects

Copper is used as an interconnect metal in semiconductor technology and has a reduced propagation delays and lower power consumption compared to aluminum.[40] TaN is used as a barrier material to prevent copper migration into the dielectric layer in CMOS transistors.[41] Copper however requires a liner material to allow for the electroplating of conducting films, since at dimensions of a few nm, copper prefers to form isolated non-conducting islands. However since advanced interconnect technology will require high aspect ratio and smaller volume trench structures, the liner and barrier stack should therefore only take up a small volume of the trench to preserve the low copper resistivity at the 14 nm node and smaller. One solution pursued in our group is a single phase combined barrier + liner material that will allow space for copper electroplating. DFT studies have shown 100% ruthenium doped TaN surface and 1 ML ruthenium passivated surface are contenders for the combined barrier + liner material.[42] Ruthenium is studied as an interconnect material or as a seed layer for copper interconnects and cobalt is a potential candidate for replacing copper for interconnects.[43] ALD can be used to grow these combined barrier + liner materials, with DFT analyzing the reactivity of these reactions to search for potential ruthenium and cobalt precursors.

1.6 Modelling atomic scale processes

Reaction mechanisms of atomic scale processing methods cannot be fully understood through experiments alone. First principles density functional theory (DFT) simulations are crucial for the development of atomic-scale processing techniques that can guide or complement experimental studies.[44–48] It can give deep insights into the precursor chemistry and the reactions that drive ALD and ALE processes. Databases typically only contain information on bulk materials and therefore only bulk deposition or etching reactions can be studied. First principles DFT can therefore be used to model and study surface reactions for ALD and ALE processes. Further discussion of DFT and the methods used in this thesis can be found in Chapter 3.

1.7 Thesis Outline

Chapter 2 reviews the literature for ALD and ALE processes for the materials of interest in this thesis. Experimental thermal ALE processes are discussed mainly for the fluorination and ligand exchange mechanism as well as for other thermal ALE mechanisms. We also look at experimental work that identified volatile etch species formed during thermal ALE. First principles DFT modelling of thermal ALE processes are also discussed. We then move onto the ALD portion of the chapter and first discuss barrier and liner materials in interconnects with a focus on the DFT work for the proposed combined barrier and liner material. Experimental ALD processes are explored for Ru and Co along with how previous modelling work can be used to examine ALD mechanisms of these materials.

Chapter 3 discusses the theoretical background starting with the approaches to solving the Schrodinger equation, and finishing with DFT and its implementations as this is the computational method used for the work described in this thesis. The rest of the chapter includes the computational methods and models used in this thesis.

Chapter 4 discusses the HF pulse as the first step of thermal ALE of crystalline HfO_2, ZrO_2 and ZnO. A thermodynamic analysis predicts the conditions at which a self-limiting (SL) or continuous spontaneous etch (SE) reaction becomes thermodynamically favourable. This is first examined for the monoclinic (111) surfaces of HfO_2 and ZrO_2. This thermodynamic analysis is extended to examine other surface facets and oxide phases of HfO_2 to represent polycrystalline HfO_2. HF adsorption studies are carried out to understand better the mechanism of surface fluorination and predict etch rates of the oxides. HCl is studied as an alternative surface modification reagent to HF in thermal ALE of HfO_2, ZrO_2 and ZnO using the same analysis as for HF. The results of the HF pulse on the monoclinic (111) surfaces of HfO_2 and ZrO_2 has been published in Chemistry of Materials under the title "Self-Limiting Temperature Window for Thermal Atomic Layer Etching of HfO_2 and ZrO_2 Based on the Atomic-Scale Mechanism".[49]

Chapter 5 moves on to explore the HF pulse on amorphous HfO_2 using the same strategy applied to crystalline HfO_2. The results in this chapter are compared to crystalline HfO_2 to examine why amorphous HfO_2 has a higher etch rate than crystalline HfO_2. The thermodynamic analysis along with HF adsorption studies reveals the factors contributing to enhanced etching in amorphous HfO_2. The results in this chapter have been published in the Journal of Vacuum Science and Technology A under the title "Origin of enhanced thermal atomic layer etching of amorphous HfO_2".[50]

Chapter 6 studies the mechanism of the ligand exchange chemistry between fluorinated HfO_2 and $SiCl_4$ in the second half cycle in thermal ALE of HfO_2. The interaction of $SiCl_4$ is first examined at the partially and fully fluorinated HfO_2 surfaces described in Chapter 4. Reaction energies are used to predict the possible routes for F/Cl ligand exchange as well as possible mechanisms. A thermodynamic analysis is also used to examine possible spontaneous etch reactions. The results in this chapter are compared to experimental data to gain an overall understating of the ligand exchange mechanism. This chapter concludes the ALE modelling work studied in this thesis.

Chapter 7 uses DFT calculations to explore the nature of the N_2/H_2 terminated TaN surfaces that are produced post plasma pulse in PEALD for the incorporation of Ru or Co into TaN. We begin with single terminations of possible N_2/H_2 post plasma terminations on the ε-TaN (110) surface. This is then followed by higher coverages to find stable NH_x-terminations on TaN. Their reactivity towards different ruthenium and cobalt precursors are explored in the following chapter.

Chapter 8 studies the incorporation of ruthenium or cobalt into TaN for NH_x-terminated ε-TaN (110) surfaces that were discussed in chapter 7 using DFT. Ruthenium precursors, $RuCp_2$, $Ru(EtCp)_2$ and RuO_4, and cobalt precursors $CoCp_2$ and $Co(EtCp)_2$, are examined on the stable NH_x-terminated ε-TaN (110) surfaces. We begin by studying the interaction of a single Ru/Co precursor on each NH_x-terminated ε-TaN (110) surface. This is followed by calculating the reaction energy after the first ligand is removed via hydrogen transfer from the NH_x-terminated ε-TaN (110) surface. Surfaces that favorably promote ligand elimination are further investigated by examining the reaction pathway which includes any energetic barriers. The reactions for higher precursor coverages are also studied to determine the nature of the surface post the metal precursor pulse. Finally, the interaction of hydrogen plasma with the -Cp, -EtCp or oxygen ligands bound to the metal fragments on the surface is examined to determine if the subsequent plasma pulse can remove these ligands to deposition Ru or Co on the surface.

Chapter 9 explores the reaction mechanism of Ru metal ALD using novel precursor RuO_4 and molecular H_2 using DFT calculations. Coverages of RuO_4 on the Ru surface are first examined to determine the coverage at which the precursor saturates. The charges of the Ru atoms in the surface as well as in the subsurface layer for different RuO_4 coverages are analyzed to test at which coverage all Ru atoms are oxidized. The H_2 reduction step is studied by introducing one H_2 molecule at a time to the surface with the highest RuO_4 coverage and allowing it to relax. We also examine the reaction pathway to remove oxygen from the surface that did not form H_2O spontaneously including hydrogen transfer energy barriers.

Chapter 10 gives an overall review of the conclusions drawn from the ALE and ALD modelling work in this thesis. Potential future research based on the work in this thesis is also discussed.

Chapter References

(1) Chen, R.; Li, Y. C.; Cai, J. M.; Cao, K.; Lee, H. B. R. Atomic Level Deposition to Extend Moore's Law and beyond. *Int. J. Extrem. Manuf.* **2020**, *2* (2), 022002. https://doi.org/10.1088/2631-7990/AB83E0.

(2) Yuan, G.; Wang, N.; Huang, S.; Liu, J. A Brief Overview of Atomic Layer Deposition and Etching in the Semiconductor Processing. In *2016 17th International Conference on Electronic Packaging Technology (ICEPT)*; 2016; pp 1365–1368. https://doi.org/10.1109/ICEPT.2016.7583377.

(3) George, S. M.; Lee, Y. Prospects for Thermal Atomic Layer Etching Using Sequential, Self-Limiting Fluorination and Ligand-Exchange Reactions. *ACS Nano* **2016**, *10* (5), 4889–4894. https://doi.org/10.1021/acsnano.6b02991.

(4) Li, Z.; Tian, Y.; Teng, C.; Cao, H. Recent Advances in Barrier Layer of Cu Interconnects. *Materials* **2020**, *13* (21), 1–22. https://doi.org/10.3390/MA13215049.

(5) Rossnagel, S. M. Thin Film Deposition with Physical Vapor Deposition and Related Technologies. *Journal of Vacuum Science & Technology A: Vacuum, Surfaces, and Films* **2003**, *21* (5), S74. https://doi.org/10.1116/1.1600450.

(6) Faraji, G.; Kim, H. S.; Kashi, H. T. Introduction. In *Severe Plastic Deformation*; Elsevier, 2018; pp 1–17. https://doi.org/10.1016/b978-0-12-813518-1.00020-5.

(7) Kumar, M.; Kumar, R.; Kumar, S. Coatings on Orthopedic Implants to Overcome Present Problems and Challenges: A Focused Review. *Mater Today Proc* **2021**, *45*, 5269–5276. https://doi.org/10.1016/J.MATPR.2021.01.831.

(8) Perng, D. C.; Hsu, K. C.; Tsai, S. W.; Yeh, J. Bin. Thermal and Electrical Properties of PVD Ru(P) Film as Cu Diffusion Barrier. *Microelectron Eng* **2010**, *87* (3), 365–369. https://doi.org/10.1016/J.MEE.2009.06.007.

(9) Kelly, J.; Lin, X.; Nogami, T.; van der Straten, O.; Demarest, J.; Li, J.; Murphy, R.; Zhang, X.; Penny, C.; Parks, C.; Edelstein, D. Electrodeposited Cu Film Morphology on Thin PVD Cu Seed Layers. *J. Electrochem. Soc.* **2013**, *160* (12), D3171–D3178. https://doi.org/10.1149/2.031312JES/XML.

(10) Ren, H.; Cheng, Y.; Cao, Y.; Guggilla, S.; Kesapragada, S.; Ye, W.; Naik, M. Physical Vapor Deposited AlN as Scalable and Reliable Interconnect Etch-Stop ≤ 10nm Node. In *2016 IEEE International Interconnect Technology Conference / Advanced Metallization Conference, IITC/AMC 2016*; Institute of Electrical and Electronics Engineers Inc., 2016; pp 24–26. https://doi.org/10.1109/IITC-AMC.2016.7507646.

(11) Haider, A. J.; Alawsi, T.; Haider, M. J.; Taha, B. A.; Marhoon, H. A. A Comprehensive Review on Pulsed Laser Deposition Technique to Effective Nanostructure Production: Trends and

Challenges. *Optical and Quantum Electronics 2022 54:8* **2022**, *54* (8), 1–25. https://doi.org/10.1007/S11082-022-03786-6.

(12) Shepelin, N. A.; Tehrani, Z. P.; Ohannessian, N.; Schneider, C. W.; Pergolesi, D.; Lippert, T. A Practical Guide to Pulsed Laser Deposition. *Chem. Soc. Rev.* **2023**, *52* (7), 2294–2321. https://doi.org/10.1039/D2CS00938B.

(13) Jones, A. C.; Hitchman, M. L. Chapter 1. Overview of Chemical Vapour Deposition. In *Chemical Vapour Deposition*; Royal Society of Chemistry, 2008; pp 1–36. https://doi.org/10.1039/9781847558794-00001.

(14) Suntola, T. Atomic Layer Epitaxy. *Materials Science Reports*. Elsevier January 1, 1989, pp 261–312. https://doi.org/10.1016/S0920-2307(89)80006-4.

(15) Puurunen, R. L. A Short History of Atomic Layer Deposition: Tuomo Suntola's Atomic Layer Epitaxy. *Chemical Vapor Deposition* **2014**, *20* (10-11–12), 332–344. https://doi.org/10.1002/CVDE.201402012.

(16) George, S. M. Atomic Layer Deposition: An Overview. *Chem Rev* **2010**, *110* (1), 111–131. https://doi.org/10.1021/cr900056b.

(17) Lu, J.; Elam, J. W.; Stair, P. C. Atomic Layer Deposition—Sequential Self-Limiting Surface Reactions for Advanced Catalyst "Bottom-up" Synthesis. *Surf Sci Rep* **2016**, *71* (2), 410–472. https://doi.org/10.1016/J.SURFREP.2016.03.003.

(18) Leskelä, M.; Niinistö, J.; Ritala, M. Atomic Layer Deposition. In *Comprehensive Materials Processing*; Elsevier, 2014; Vol. 4, pp 101–123. https://doi.org/10.1016/B978-0-08-096532-1.00401-5.

(19) Profijt, H. B.; Potts, S. E.; Sanden, M. C. M. van de; Kessels, W. M. M. Plasma-Assisted Atomic Layer Deposition: Basics, Opportunities, and Challenges. *J. Vac. Sci. Technol. A* **2011**, *29* (5), 050801. https://doi.org/10.1116/1.3609974.

(20) Richey, N. E.; de Paula, C.; Bent, S. F. Understanding Chemical and Physical Mechanisms in Atomic Layer Deposition. *Journal of Chemical Physics*. AIP Publishing LLCAIP Publishing January 22, 2020, p 040902. https://doi.org/10.1063/1.5133390.

(21) Aarik, L.; Arroval, T.; Rammula, R.; Mändar, H.; Sammelselg, V.; Aarik, J. Atomic Layer Deposition of TiO2 from TiCl4 and O3. *Thin Solid Films* **2013**, *542*, 100–107. https://doi.org/10.1016/J.TSF.2013.06.074.

(22) Kolanek, K.; Tallarida, M.; Michling, M.; Schmeisser, D. In Situ Study of the Atomic Layer Deposition of HfO2 on Si. *J. Vac. Sci. Technol. A* **2012**, *30* (1), 01A143. https://doi.org/10.1116/1.3668080/100139.

(23) Muneshwar, T.; Shoute, G.; Barlage, D.; Cadien, K. Plasma Enhanced Atomic Layer Deposition of ZnO with Diethyl Zinc and Oxygen Plasma: Effect of Precursor Decomposition. *J. Vac. Sci. Technol. A* **2016**, *34* (5), 050605. https://doi.org/10.1116/1.4961885/245502.

(24) Duan, Y.; Lin, J. M.; Teplyakov, A. v. Computational Investigation of Electronic and Steric Effects in Surface Reactions of Metalorganic Precursors on Functionalized Silicon Surfaces. *Journal of Physical Chemistry C* **2015**, *119* (24), 13670–13681. https://doi.org/10.1021/acs.jpcc.5b02722.

(25) Puurunen, R. L. Analysis of Hydroxyl Group Controlled Atomic Layer Deposition of Hafnium Dioxide from Hafnium Tetrachloride and Water. *J. Appl. Phys* **2004**, *95* (9), 4777–4786. https://doi.org/10.1063/1.1689732.

(26) Oehrlein, G. S.; Metzler, D.; Li, C. Atomic Layer Etching at the Tipping Point: An Overview. *ECS Journal of Solid State Science and Technology* **2015**, *4* (6), N5041–N5053. https://doi.org/10.1149/2.0061506jss.

(27) Kim, H. Characteristics and Applications of Plasma Enhanced-Atomic Layer Deposition. *Thin Solid Films* **2011**, *519* (20), 6639–6644. https://doi.org/10.1016/J.TSF.2011.01.404.

(28) Johnson, R. W.; Hultqvist, A.; Bent, S. F. A Brief Review of Atomic Layer Deposition: From Fundamentals to Applications. *Mater. Today* **2014**, *17* (5), 236–246. https://doi.org/10.1016/J.MATTOD.2014.04.026.

(29) T. Carver, C.; J. Plombon, J.; E. Romero, P.; Suri, S.; A. Tronic, T.; B. Turkot, R. Atomic Layer Etching: An Industry Perspective. *ECS Journal of Solid State Science and Technology* **2015**, *4* (6), N5005–N5009. https://doi.org/10.1149/2.0021506jss.

(30) Faraz, T.; Roozeboom, F.; Knoops, H. C. M.; Kessels, W. M. M. Atomic Layer Etching: What Can We Learn from Atomic Layer Deposition? *ECS Journal of Solid State Science and Technology* **2015**, *4* (6), N5023–N5032. https://doi.org/10.1149/2.0051506JSS/XML.

(31) Kanarik, K. J.; Tan, S.; Gottscho, R. A. Atomic Layer Etching: Rethinking the Art of Etch. *J. Phys. Chem. Lett* **2018**, *9*, 4814–4821. https://doi.org/10.1021/acs.jpclett.8b00997.

(32) Fang, C.; Cao, Y.; Wu, D.; Li, A. Thermal Atomic Layer Etching: Mechanism, Materials and Prospects. *Prog. Nat. Sci-Mater.* **2018**, *28* (6), 667–675. https://doi.org/https://doi.org/10.1016/j.pnsc.2018.11.003.

(33) Kanarik, K. J.; Lill, T.; Hudson, E. A.; Sriraman, S.; Tan, S.; Marks, J.; Vahedi, V.; Gottscho, R. A. Overview of Atomic Layer Etching in the Semiconductor Industry. *J. Vac. Sci. Technol. A* **2015**, *33* (2), 020802. https://doi.org/10.1116/1.4913379.

(34) Lee, Y.; George, S. M. Atomic Layer Etching of Al2O3 Using Sequential, Self-Limiting Thermal Reactions with Sn(Acac)2 and Hydrogen Fluoride. *ACS Nano* **2015**, *9* (2), 2061–2070. https://doi.org/10.1021/nn507277f.

(35) Lee, Y.; George, S. M. Thermal Atomic Layer Etching of Al2O3, HfO2, and ZrO2 Using Sequential Hydrogen Fluoride and Dimethylaluminum Chloride Exposures. *J. Phys. Chem. C* **2019**, *123*, 18455–18466. https://doi.org/10.1021/acs.jpcc.9b04767.

(36) George, S. M. Mechanisms of Thermal Atomic Layer Etching. *Accounts Chem. Res.* **2020**, *53* (6), 1151–1160. https://doi.org/10.1021/acs.accounts.0c00084.

(37) Robertson, J. High Dielectric Constant Gate Oxides for Metal Oxide Si Transistors. *Reports on Progress in Physics* **2006**, *69* (2), 327–396. https://doi.org/10.1088/0034-4885/69/2/R02.

(38) Raghu, P.; Yim, C.; Shadman, F.; Shero, E. Susceptibility of SiO2, ZrO2, and HfO2 Dielectrics to Moisture Contamination. *AIChE J.* **2004**, *50*, 1881–1888. https://doi.org/10.1002/aic.10148.

(39) Robertson, J. High Dielectric Constant Oxides. *The European Physical Journal - Applied Physics* **2004**, *28* (3), 265–291. https://doi.org/10.1051/EPJAP:2004206.

(40) Li, B.; Sullivan, T. D.; Lee, T. C.; Badami, D. Reliability Challenges for Copper Interconnects. *Microelectronics Reliability* **2004**, *44* (3), 365–380. https://doi.org/10.1016/J.MICROREL.2003.11.004.

(41) Lane, M.; Dauskardt, R. H.; Krishna, N.; Hashim, I. Adhesion and Reliability of Copper Interconnects with Ta and TaN Barrier Layers. *J Mater Res* **2000**, *15* (1), 203–211. https://doi.org/10.1557/JMR.2000.0033.

(42) Kondati Natarajan, S.; Nies, C. L.; Nolan, M. The Role of Ru Passivation and Doping on the Barrier and Seed Layer Properties of Ru-Modified TaN for Copper Interconnects. *J. Chem. Phys.* **2020**, *152* (14), 144701. https://doi.org/10.1063/5.0003852.

(43) Liu, J.; Lu, H.; Zhang, D. W.; Nolan, M. Self-Limiting Nitrogen/Hydrogen Plasma Radical Chemistry in Plasma-Enhanced Atomic Layer Deposition of Cobalt. *Nanoscale* **2022**, *14* (12), 4712–4725. https://doi.org/10.1039/D1NR05568B.

(44) Kondati Natarajan, S.; Elliott, S. D. Modeling the Chemical Mechanism of the Thermal Atomic Layer Etch of Aluminum Oxide: A Density Functional Theory Study of Reactions during HF Exposure. *Chem. Mater.* **2018**, *30* (17), 5912–5922. https://doi.org/10.1021/acs.chemmater.8b01930.

(45) Kondati Natarajan, S.; Cano, A. M.; Partridge, J. L.; George, S. M.; Elliott, S. D. Prediction and Validation of the Process Window for Atomic Layer Etching: HF Exposure on TiO2. *J. Phys. Chem. C* **2021**, *125* (46), 25589–25599. https://doi.org/10.1021/ACS.JPCC.1C08110/SUPPL_FILE/JP1C08110_SI_001.PDF.

(46) Sharma, V.; Elliott, S. D.; Blomberg, T.; Haukka, S.; Givens, M. E.; Tuominen, M.; Ritala, M. Thermal Atomic Layer Etching of Aluminum Oxide (Al2O3) Using Sequential Exposures of Niobium Pentafluoride (NbF5) and Carbon Tetrachloride (CCl4): A Combined Experimental and Density Functional Theory Study of the Etch Mechanism. *Chem. Mater.* **2021**, *33* (8), 2883–2893. https://doi.org/10.1021/acs.chemmater.1c00142.

(47) Afshar, A.; Cadien, K. C. Growth Mechanism of Atomic Layer Deposition of Zinc Oxide: A Density Functional Theory Approach. *Appl Phys Lett* **2013**, *103* (25), 251906. https://doi.org/10.1063/1.4852655.

(48) Liu, J.; Lu, H.; Zhang, D. W.; Nolan, M. Reactions of Ruthenium Cyclopentadienyl Precursor in the Metal Precursor Pulse of Ru Atomic Layer Deposition. *J. Mater. Chem. C* **2021**, *9* (8), 2919–2932. https://doi.org/10.1039/d0tc03910a.

(49) Mullins, R.; Kondati Natarajan, S.; Elliott, S. D.; Nolan, M. Self-Limiting Temperature Window for Thermal Atomic Layer Etching of HfO2 and ZrO2 Based on the Atomic-Scale Mechanism. *Chem. Mater.* **2020**, *32* (8), 3414–3426. https://doi.org/10.1021/acs.chemmater.9b05021.

(50) Mullins, R.; Gutiérrez Moreno, J. J.; Nolan, M. Origin of Enhanced Thermal Atomic Layer Etching of Amorphous HfO2. *Journal of Vacuum Science & Technology A* **2022**, *40* (2), 022604. https://doi.org/10.1116/6.0001614.

(51) *Atomic Layer Deposition*. https://www.asm.com/technology/key-technologies/atomic-layer-deposition (accessed 2022-12-29).

2 Thermal ALE & Metal ALD: Bridging Theory and Experiment for Mechanistic Clarity

2.1 Atomic Layer Etching

2.1.1 Introduction

Atomic Layer Etching was first reported in 1988 in Yoder's patent titled "Atomic Layer Etching" of crystalline diamond.[1] Its first wave of research took place during the 1990s and reemerged in the mid-2010s in response to then rising demand for etching technologies with the ability to remove a controlled amount of material as part of downscaling of semiconductor devices.[2] Conventional ALE processes are anisotropic as they use directional high-energy ion bombardment to remove a modified surface layer.[3] An example of this is etching of GaN with Cl_2 plasma modification and Ar ion removal.[4] In recent years we have seen an increased interest in thermal and self-limiting ALE, which permits the removal of thin films with atomic-scale precision and delivers anisotropic etch using sequential and self-limiting (SL) surface reactions,[3,5–8] similar in principle and thought of as opposite to Atomic Layer Deposition.

Thermal self-limiting ALE is a relatively new atomic scale processing technique and was first reported in 2015 for thermal ALE of Al_2O_3.[9] The mechanisms for thermal ALE include fluorination & ligand exchange, conversion & chlorination and ligand addition which are used to etch metal oxides[10–21], metal nitrides[4,22–29] and metals[30–32]. Applications of thermal ALE may include surface cleaning for the removal of metal impurities in semiconductor fabrication[7,33], conformal etching in high-aspect-ratio structures[6,34,35], and smoothing of surfaces to obtain flat and damage-free layers, which are also important in the semiconductor industry. In this section we first describe thermal ALE processes that are relevant to the high-k metal oxides studied in my thesis. We also report on the modelling work done that investigated thermal ALE processes.

2.1.2 Thermal ALE of metal oxides

The scaling of semiconductor devices means that features are required at the nanometer scale. As a result of the shrinking of device feature sizes, SiO_2 gate dielectrics would become so thin that electron tunneling through the dielectric layer, which leads to high leakage currents,[36] is impossible to avoid. Materials with high dielectric constant, *k*, allow a high drive current to be maintained, while minimized leakage current and a low equivalent oxide thickness can be

achieved.[36] HfO_2 and ZrO_2 are high-k dielectric materials with dielectric constants of 22−23,[36,37] which are used in semiconductor devices. Other materials such as Al_2O_3, SiO_2, Si_3N_4 and TiN are all important in semiconductor device processing.[5] HfO_2 and ZrO_2 are thermodynamically stable when interfaced with silicon in semiconductor applications.[38]

Conformal nanometer-scale feature sizes in high-aspect-ratio structures are difficult to achieve with traditional wet and dry chemical etching methods, which do not permit the level of control required. ALE has gained significant interest for the controlled etching of thin films, in particular, for nanoelectronic devices and will be particularly important where complex three-dimensional device structures will be present such as Gate-All-Around and Complementary FET (GAA and CFET) devices; see Figure 2.1.



Figure 2.1. Used from https://www.imec-int.com/en/articles/smaller-better-faster-imec-presents-chip-scaling-roadmap (Accessed 16/11/2023).

.

Many technologically important materials have been etched using ALE including HfO_2,[5,10,11,21,39] ZrO_2,[5,10,12,21] SiO_2,[13,14,24,40] Si_3N_4,[41] SiGe,[42] Al_2O_3,[9,10,15–18,43–50] AlF_3,[47,51] $HfZrO_4$,[21] TiO_2,[24,52–54] VO_2,[55] Si,[56–58] Ge,[59] Co,[60,61] Cu,[30] W,[31,32,62] Ni,[63] WO_3,[62] ZnO,[12,19,64] CoO,[12] Ga_2O_3,[20] B_2O_3,[65] Fe,[66] Fe_2O_3,[12] NiO,[12] InGaAs,[67] InAlAs,[67] MoS_2,[68] AlN,[23] TiN,[24–27] and GaN[4,29,69]. Plasma ALE of Si_3N_4,[70] SiO_2[71] and SiN[72] can be achieved using a fluorocarbon polymer. Metal thermal ALE can be achieved by ligand-addition for example $NiCl_2$ was

spontaneously etched by ligand-addition with $P(Me)_3$ which formed stable volatile complexes.[73]

We now discuss some relevant thermal ALE mechanisms found in the literature.

Fluorination and Ligand-Exchange

Figure 2.2 shows a schematic of a fluorination-ligand exchange process that has been widely used in metal oxide etch. In brief the mechanism involves the formation of a reactive but nonvolatile layer on the initial film, which is followed by a material removal step to take off only the modified layer as indicated schematically in Figure 2.2. The second reaction produces stable etch products, which are now volatile and can be easily removed, leaving behind a film from which one layer or a fraction of a layer has been removed.

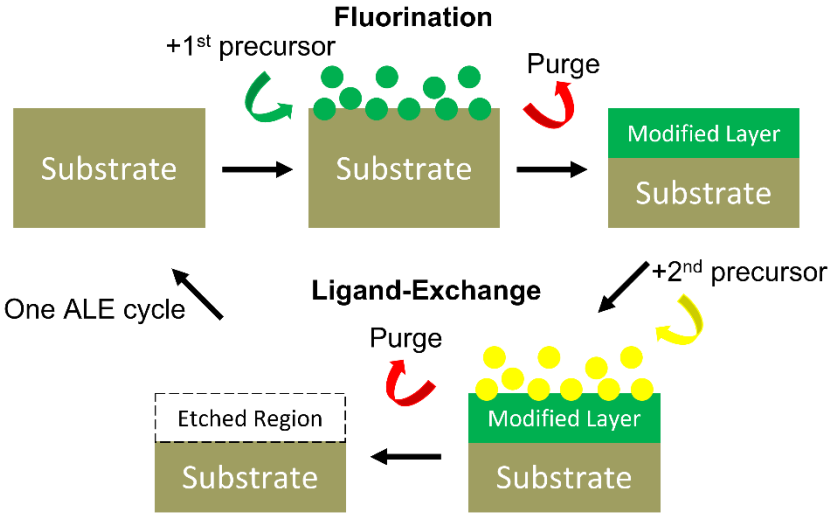


Figure 2.2. Schematic model of the thermal ALE process.

Thermal ALE of HfO_2 was performed using sequential, self-limiting thermal reactions using HF for fluorination and $Sn(acac)_2$ for ligand exchange to form the volatile etch products, $Hf(acac)_2$, SnF(acac) and H_2O.[39] The proposed role of HF is to fluorinate the HfO_2 surface layer (eliminating water) yielding HfF_x, but without fully converting to HfF_4. Quartz crystal microbalance (QCM) measurements were used to examine the products of thermal ALE of HfO_2 and allowed mass changes after the individual exposures of the precursors used to be obtained. Etch rates were also obtained. The mechanism for thermal HfO_2 ALE was developed from the measured mass change per cycle (MCPC) and individual mass changes during the precursors' exposures. Fourier transform infrared (FTIR) analysis identified the reaction products on the surface. The HfO_2 film showed a linear etch behaviour at 200 ºC after 100 ALE

cycles of sequential $Sn(acac)_2$ and HF exposures with an etch rate of 0.116 Å/cycle.[39] The MCPC was measured with different reactant exposure times (0 – 2 s) to study the self-limiting nature of the precursors' surface reactions.

The reaction sequence for $Sn(acac)_2$ is denoted as x-30-1-30 where x represents possible exposure times of $Sn(acac)_2$, the N_2 purge is constant at 30 s and HF was exposed for 1 s.[39] The ALE reactions with $Sn(acac)_2$ were self-limiting, in which the MCPC *versus* $Sn(acac)_2$ exposure times dropped quickly and plateaued at an MCPC of -11 ng/(cm^2 cycle).[39] For HF the reaction sequence was 1-30-x-30 where $Sn(acac)_2$ was exposed for 1 s.[39] Unlike $Sn(acac)_2$ the MCPC versus HF exposure time does not plateau and keeps decreasing indicating that the HF reaction was not self-limiting.[39] It was suggested that HF had not reached saturation and longer exposure times would be needed to achieve truly self-limiting behaviour.[39] Another possibility was that higher HF exposures lead to chemical vapour etching (CVE) due to $Sn(acac)_2$ and HF both being present in the reactor at the same time.[39] HF exposures on HfO_2 alone showed that HF had reached saturation and HF does not spontaneously etch HfO_2.[39] The etch rates varied with temperature. For example at 150 ºC the etch rate was 0.070 Å/cycle whereas at 250 ºC the etch rate was 0.117 Å/cycle.[39] Thermal ALE of Al_2O_3 was also performed using HF and $Sn(acac)_2$ where the HF exposure converted Al_2O_3 to the key intermediate AlF_3 which was then removed during the $Sn(acac)_2$ exposure, following a similar mechanism to thermal ALE of HfO_2.[9,74]

Selectivity in thermal ALE was explored for Al_2O_3, HfO_2, ZrO_2, SiO_2, Si_3N_4 and TiN thin films on silicon wafers using fluorination reagent HF and ligand exchange metal precursors $Sn(acac)_2$, TMA ($Al(CH_3)_3$), DMAC ($AlCl(CH_3)_2$) and $SiCl_4$.[5] The film thicknesses of the different materials were measured using SE (spectroscopic ellipsometer) measurements. Film thicknesses were measured after 50, 100, 200 and 400 ALE cycles using sequential HF and $Sn(acac)_2$ exposures at 200 ºC.[5] The high-k oxides Al_2O_3, HfO_2 and ZrO_2 were etched linearly with etch rates of 0.23 Å/cycle, 0.06 Å/cycle and 0.14 Å/cycle respectively.[5] The film thickness did not change for SiO_2, Si_3N_4 and TiN using HF and $Sn(acac)_2$ at 200 ºC.[5] This suggests that the fluorination of SiO_2 or Si_3N_4 does not proceed fully to form SiF_4 as SiF_4 is very volatile and neither SiO_2 or Si_3N_4 were spontaneously etched by HF.[5] The strong Si-F bond (7.24 eV)[75] could also prevent the ligand exchange step as the activation energy to break the bond would be too high. There may also be a TiN_xO_y or TiO_2 layer on the TiN surface in which the fluorination reaction using HF on these possible surfaces would be thermochemically neutral.[5] Film thicknesses were measured after 25, 50, 100 and 200 ALE cycles using HF and TMA as reactants at 300 ºC.[5] Only Al_2O_3 and HfO_2 were etched linearly with the number of ALE cycles

with etch rates of 0.45 Å/cycle and 0.10 Å/cycle respectively.[5] Sequential HF and DMAC exposures at 250 ºC etched Al_2O_3, HfO_2 and ZrO_2 linearly with etch rates of 0.32 Å/cycle, 0.77 Å/cycle and 0.96 Å/cycle respectively.[5] Finally using HF and $SiCl_4$ as reactants the film thickness was measured after 50, 100, 200 and 400 ALE cycles at 350 ºC.[5] HfO_2 and ZrO_2 were etched linearly with etch rates 0.05 Å/cycle and 0.14 Å/cycle.[5]

The etch rates for thermal HfO_2 and ZrO_2 ALE using HF and $SiCl_4$ were measured at increasing exposure times (0.0 – 2.5 s) for $SiCl_4$ with a constant HF exposure time of 1.0 s to confirm self-limiting behavior.[5] The etch rates remained constant for both materials as the exposure time of $SiCl_4$ increased.[5] The test was repeated for increasing exposure times of HF with a constant exposure time of 2.0 s for $SiCl_4$.[5] Self-limiting behaviour was observed for HfO_2 through constant etch rates versus HF exposures, whereas for ZrO_2 the etch rate began to plateau only at higher HF exposures.[5] The longer HF exposures lead to CVE during $SiCl_4$ exposure with residual HF in the reactor.[5]

These etch rates are based on the fluorination and ligand-exchange mechanism where the extent of etch in one ALE cycle is determined by how much of the starting material is fluorinated in the first step and then to what extent the metal fluoride can be removed during ligand exchange.[5] These etch rates are also clearly less than a monolayer per cycle, typical of self-limiting atomic level processing.[5]

Thin films of Al_2O_3, HfO_2 and ZrO_2 were etched by most of the different ligand exchange metal precursors. Reaction products AlF_3, HfF_4 and ZrF_4 formed after the initial fluorination step are non volatile and sublime only at temperatures of 1276, 970 and 912 ºC respectively, which prevents continuous removal of the target species. The subsequent ligand exchange reactions produced stable and volatile products produced from these metal fluorides for most of the metal precursors.[5] For sequential $SiCl_4$ and HF exposures, Hf and Zr form volatile metal chlorides and SiF_4 is released.[5]

Thermochemistry calculations using HSC Chemistry[76] software were performed for ligand exchange between $SiCl_4$ and AlF_3, HfF_4 and ZrF_4 producing SiF_4 and $AlCl_3$, $HfCl_4$ and $ZrCl_4$.[5] The results showed that ligand exchange between $SiCl_4$ and HfF_4 or ZrF_4 is thermochemically favourable at temperatures above 200 ºC whereas with AlF_3 this reaction was not favourable at any temperature.[5] Spectroscopic ellipsometry measurements showed that HfO_2 and ZrO_2 were not etched at 250 ºC using HF and $SiCl_4$ but become measurable at temperatures above 300 ºC and the etch rate for ZrO_2 (0.14 Å/cycle) is greater than HfO_2 (0.05 Å/cycle) at 350 ºC.[5]

Thermal ALE of Al_2O_3, HfO_2 and ZrO_2 using HF and DMAC were measured in a temperature range of 200 – 300 ºC.[10] DMAC is a useful ligand exchange precursor as it provides both CH_3

and Cl ligands, which can produce stable and volatile metal chlorides for groups 4-6 and groups 13-15.[10] Metal alkyls in groups 12-15 such as TMA and diethylzinc are also stable and volatile.[10] The etch rates of Al_2O_3, HfO_2 and ZrO_2 using HF and DMAC increased with temperature to between 0.36 Å/cycle and 1.24 Å/cycle for HfO_2 and between 0.91 Å/cycle and 1.59 Å/cycle for ZrO_2.[10]

The metal precursors TMA and DMAC were compared due to their similarities in reactivity and boiling points. At 250 ºC sequential exposures of HF and TMA on HfO_2 lead to negligible etching.[10] Replacing TMA with DMAC at the same temperature resulted in HfO_2 etching with an etch rate of 0.98 Å/cycle.[10] This is due to the Cl ligand of DMAC forming volatile $HfCl_4$; $Hf(CH_3)_4$ is unstable at higher temperatures .[10]

The same etch chemistry is seen for etching of ZrO_2 whereby HF and DMAC exposures at 250 ºC gave an etch rate at 1.33 Å/cycle, whereas HF and TMA did not etch ZrO_2 at 250ºC. Thin films of ZrO_2 were successfully demonstrated as an etch stop during thermal ALE of Al_2O_3 using HF and TMA at 285 ºC.[77] ZrO_2 was deposited on Al_2O_3 using TEMAZ (tetrakis(ethylmethylamido)zirconium) and H_2O.[77] One monolayer of ZrO_2 was grown between Al_2O_3 layers, Al_2O_3 was etched using HF and TMA until the ZrO_2 monolayer brought the etching to a stop. The mechanism here is that ZrF_4 was not removed by the introduction of TMA.[77] Exposures of HF and DMAC were successfully used to remove the ZrO_2 from Al_2O_3.[77]

$TiCl_4$ is another metal chloride reactant that can be used for ligand exchange. Thermal ALE of HfO_2 using HF and $TiCl_4$ was studied at 200 – 300 ºC.[11] The etch rate changed from 0.11 Å/cycle at 200 ºC to 0.59 Å/cycle at 300 ºC and the HfO_2 films were etched linearly versus the number of HF and $TiCl_4$ ALE reaction cycles.[11] $TiCl_4$ interacts with the HfF_4 surface layer to form volatile etch products TiF_4 and $HfCl_4$.[11] Other likely etch products of mixed hafnium fluoride/chloride species such as $HfFCl_3$, HfF_2Cl_2 and HfF_3Cl are possible if their vapour pressure is sufficiently high at the ALE temperature of 250 ºC.[11] The same can also occur for mixed titanium fluoride/chloride etch products if they are volatile at the operating temperature.[11] ZrO_2 was also etched linearly using HF and $TiCl_4$ at 250 ºC with an etch rate of 0.38 Å/cycle.[11] When tested on Al_2O_3, SiO_2, Si_3N_4, and TiN films there was no measurable thickness change showing HF and $TiCl_4$ did not etch these materials, presumably since products that are volatile at the ALE temperature are not formed.[11]

Thermal ALE of amorphous and crystalline HfO_2, ZrO_2 and $HfZrO_4$ were studied using HF, XeF_2 and SF_4 as the fluorination reactants and $TiCl_4$ and DMAC as the metal precursors for ligand exchange.[21] A very interesting result is that the etch rates of the amorphous and crystalline materials were significantly different when using HF and $TiCl_4$ at 250 ºC; the etch

rates were measured using up to 300 ALE cycles.[21] Crystalline HfO_2 had an etch rate of 0.02 Å/cycle whereas amorphous HfO_2 had an etch rate 18 times higher at 0.36 Å/cycle.[21] For ZrO_2, similar results are obtained: the crystalline film had an etch rate of 0.26 Å/cycle and the amorphous film had a higher etch rate of 0.61 Å/cycle. After 150 ALE cycles using HF and $TiCl_4$ the amorphous ZrO_2 film was completely removed.[21] Amorphous $HfZrO_4$ also had a higher etch rate than crystalline $HfZrO_4$ and was completely etched after 150 cycles.[21]

Changing the metal precursor to DMAC, the experiments were repeated using HF and DMAC at 250 ºC obtaining the etch rates from measurements up to 300 ALE cycles.[21] Amorphous HfO_2 had an etch rate of 0.68 Å/cycle and was completely removed after 150 cycles.[21] Crystalline HfO_2 had a much smaller etch rate of 0.08 Å/cycle.[21] For ZrO_2, both the amorphous and crystalline films had high etch rates of 1.11 Å/cycle and 0.82 Å/cycle respectively, but the amorphous film still has the larger etch rate.[21] Amorphous ZrO_2 was completely removed after 75 cycles and crystalline ZrO_2 after 100 cycles.[21] .[21] Replacing $TiCl_4$ with DMAC resulted in higher etch rates for the amorphous and crystalline films of HfO_2, ZrO_2 and $HfZrO_4$.[21] However, for every material studied the amorphous film had a higher etch rate than the crystalline which may be due to amorphous materials having a lower density than crystalline materials which may facilitate fluorination, but this was not definitively established.[21] Crystalline materials also have more uniform bond lengths and configurations compared to amorphous materials.

SF_4 and XeF_2 have been used as fluorination reactants and both are stronger than HF.[21] HF and SF_4 are both nucleophilic fluorination reactants where the fluoride anion serves as the active reaction species.[55] SF_4 has a lone pair of electrons making it more nucleophilic than HF and therefore a stronger fluorinating reagent. XeF_2 is an electrophilic fluorination reagent where F acts an electron acceptor.[21] The thermal decomposition of XeF_2 can also be controlled where XeF_2 decomposes into gaseous xenon and atomic fluorine on the target surface.[78,79] Thermal ALE using SF_4 and $TiCl_4$ was performed on crystalline and amorphous HfO_2, ZrO_2 and $HfZrO_4$ films at 250 ºC.[21] Amorphous HfO_2 had an etch rate of 0.70 Å/cycle which was greater than the crystalline HfO_2 etch rate which was measured to be 0.08 Å/cycle.[21] The same was also observed for ZrO_2 where the amorphous etch rate was greater than the crystalline etch rate for which values of 1.08 Å/cycle and 0.36 Å/cycle are obtained, respectively.[21] The ALE process was tested using SF_4 and DMAC at 250 ºC.[21] The etch rates of amorphous HfO_2, ZrO_2 and $HfZrO_4$ were 0.50, 0.46 and 0.49 Å/cycle respectively which are all comparable in value.[21] Crystalline HfO_2 and $HfZrO_4$ were not etched using SF_4 and DMAC with the reason for the lack of etching not being understood at the time.[21] However crystalline ZrO_2 was etched at 0.34

Å/cycle.[21] Using SF_4 with DMAC decreased the etch rates when compared to using SF_4 with $TiCl_4$.[21]

XeF_2 is a stronger fluorination reactant compared to HF and SF_4. Amorphous and crystalline HfO_2, ZrO_2 and $HfZrO_4$ films were etched using XeF_2 and $TiCl_4$ at 250 ºC.[21] The etch rates for amorphous HfO_2, ZrO_2 and $HfZrO_4$ films were 1.96, 2.69 and 2.07 Å/cycle respectively.[21] The crystalline films had etch rates of 1.26, 1.75 and 1.71 Å/cycle for HfO_2, ZrO_2 and $HfZrO_4$ respectively.[21] When using XeF_2 and $TiCl_4$ the amorphous films continue to have higher etch rates than the crystalline films. These etch rates are also significantly larger than the etch rates when fluorination reactants HF and SF_4 were used with metal precursor $TiCl_4$.[21] A similar study on Al_2O_3 showed that amorphous Al_2O_3 could be etched in the presence of crystalline Al_2O_3 to remove it while keeping crystalline Al_2O_3.[15]

Thermal ALE of VO_2 was studied using HF or SF_4 as the fluorination reactants and $Sn(acac)_2$ as the ligand exchange precursor.[55] The etch rate using SF_4 was 0.30 Å/cycle and using HF was 0.11 Å/cycle at 200 ºC.[55] QCM experiments were used to study the effect of SF_4 and HF exposure on the VO_2 ALD grown film.[55] The SF_4 exposure was conducted at 500 mTorr and compared to HF exposures at 60 mTorr and 500 mTorr.[55] The mass gain was greater for the SF_4 exposure at 500 mTorr compared to the HF exposures at 60 mTorr and 500 mTorr shown in Figure 2.3. The mass gain for the HF exposures was 20.5 ng/cm^2 at 60 mTorr and 500 mTorr showing that the mass change is independent of pressure.[55] The mass gain for the SF_4 exposure at 500 mTorr was 38.5 ng/cm^2.[55] This showed that SF_4 yields greater fluorination of VO_2 compared to HF and this leads to a higher etch rate using SF_4. The same study was done on Al_2O_3 with comparable etch rates of 0.20 and 0.28 Å/cycle for SF_4 and HF respectively.[55] Fischer and coworkers found through their models that the fluorination step in thermal ALE is responsible for the amount of material that is subsequently etched in the ligand exchange step so that the fluorination step determines the etch rate.[80] They also determined that the ligand exchange dosing predominantly controlled the etch profile.[80]

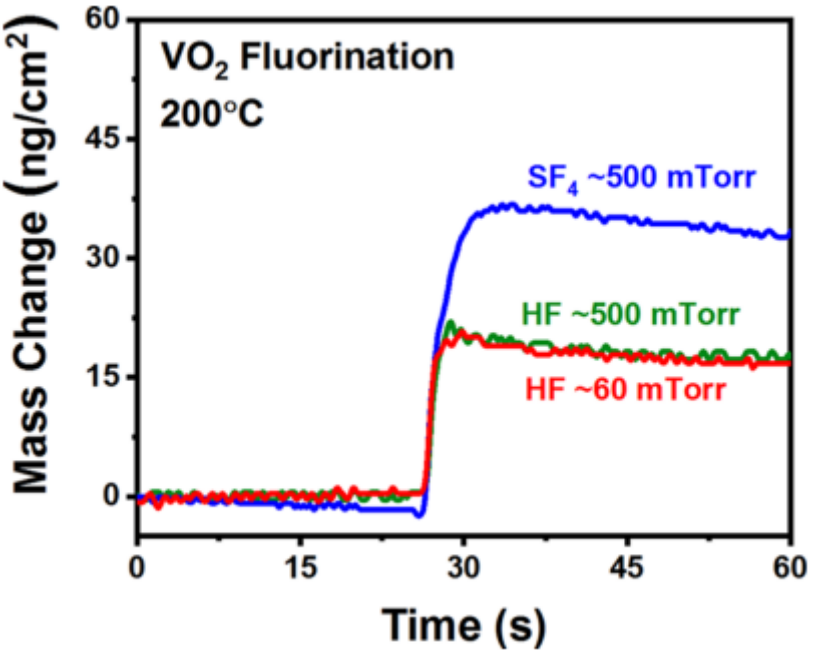


Figure 2.3 Mass changes during SF_4 and HF exposure on VO_2. Taken from ref.[55].

Conversion-etch mechanism

Thermal ALE of ZnO using HF and TMA was performed by a conversion-etch mechanism where after the initial ZnO fluorination, the TMA reactant converts the polycrystalline ZnO surface to an Al_2O_3 surface layer.[19] Sequential exposures of HF and TMA were performed for 100 ALE cycles at 265 ºC which etched ZnO linearly with an etch rate of 2.11 Å/cycle.[19] The large mass loss during the first TMA reaction suggested that an additional reaction took place.[19] This additional reaction was believed to be the conversion of underlying ZnO film to Al_2O_3 using TMA.[19] The subsequent HF exposure fluorinated the Al_2O_3 surface to AlF_3 and the process follows the mechanism of thermal ALE of Al_2O_3. The fluorination reaction was found to be self-limiting with a HF exposure of 1 s sufficient to reach HF saturation.[19] The TMA exposure was found to be almost self-limiting with additional mass losses associated with the conversion of additional ZnO to Al_2O_3 at higher exposures of TMA.[19] The polycrystalline ZnO RMS roughness was reduced from 11 Å to 5.8 Å after 200 ALE cycles.[19] Adjusting the temperature also influenced the etch rates for thermal ZnO ALE with 0.01 Å/cycle at 205 ºC to 2.19 Å/cycle at 295 ºC where the etch rate plateaus at higher temperatures.[19] This was due to the TMA induced conversion to Al_2O_3 for which ALE using HF and TMA is independent

of temperature.[17] Thermal ALE of WO_3 was also achieved by first the conversion to B_2O_3 using BCl_3 followed by spontaneous etching using HF.

Chlorination and Ligand-Addition

Thermal ALE of ZnO was also achieved using chlorination and ligand-addition reactions at 250 ºC with reactants SO_2Cl_2 and TMEDA (tetramethylethylenediamine).[12] This thermal ALE mechanism was also explored on CoO, Fe_2O and NiO.[12] The chlorination and ligand-addition mechanism is useful for metal oxides that have associated metal fluorides that resist volatilization through ligand-exchange reactions. Sequential exposures of SO_2Cl_2 and TMEDA on ZnO powder found that the $ZnCl(TMEDA)^+$ ion intensity signal was the main ion signal during TMEDA exposures on chlorinated ZnO.[12] The ligand-addition of TMEDA to the chlorinated ZnO was self-limiting as there was a limited amount of chlorine present on the ZnO surface.[12] The mass change of the ZnO powder was measured using QMS which was found to decrease linearly with an etch rate of 0.12 Å/cycle.

2.1.3 Identification of etch species

Clancy and coworkers first identified the volatile etch species formed during thermal ALE of Al_2O_3 at 300 ºC using QMS.[46] The fluorination reactant used was HF with ligand exchange precursors TMA and DMAC.[46] Mass spectrum results confirmed that H_2O was the main reaction product observed during the fluorination of Al_2O_3 powder with HF and the F^+ signal was linked to excess HF.[46] The prominent molecular ions observed when using TMA and DMAC were $Al_2F(CH_3)_4^+$ and $Al_2F_2(CH_3)_3^+$ which both resulted from dimers of $AlF(CH_3)_2$ with itself or with TMA after a methyl group was lost.[46] Trimer $Al_3F_3(CH_3)_5^+$ was also detected.[46] Mixed halogen products were also observed at lower signal intensities when using DMAC such as $Al_2FCl(CH_3)_3^+$, $Al_2F_2Cl(CH_3)_2^+$ and $Al_3F_3Cl(CH_3)_4^+$.[46] During ligand exchange for both TMA and DMAC, CH_3 was the dominant species due to the similarly for both precursors.[46] A computational analysis also showed that the dimer products were more stable than monomer products, supporting the experimental results.[46]

I*n situ* QMS was used to determine the volatile etch products produced during ligand exchange reactions on metal fluoride powders by Lii-Rosales and coworkers.[81] The metal fluoride powders studied were AlF_3, HfF_4, GaF_3, InF_3 and SnF_4 and the ligand exchange precursors used were TMA, $SiCl_4$ and $TiCl_4$.[81] Combinations of TMA + AlF_3, $SiCl_4$ + HfF_4, $SiCl_4$ + InF_3, $TiCl_4$ + SnF_4, TMA + GaF_3 and $SiCl_4$ + AlF_3 represented thermal ALE reactions.[81]

Regarding thermal ALE chemistry of fluorinated HfF_4 using $SiCl_4$, a variety of $HfF_xCl_y^+$ ion species (x = 0-2, y = 2-4) were identified from in situ QMS studies based on their characteristic Hf and Cl isotopes during spontaneous etching of HfF_4 powders by $SiCl_4$.[81] The ion $HfCl_4^+$ was detected in the mass spectrum with the highest peak intensity at m/z = 320 amu indicating complete ligand-exchange that replaces all fluorine ligands on $HfCl_4$ with Cl atoms. Other ion species detected were $HfFCl_2^+$ and $HfFCl_3^+$ with the highest peak intensities m/z = 269 amu and m/z = 304 amu respectively.[81] It was suggested that the $HfFCl_2^+$ ion may be a fragment of the parent $HfFCl_3^+$ molecular ion[81] indicating that partial chlorination of HfF_x is also possible. A temperature dependence of the ligand exchange reaction between HfF_4 powder and $SiCl_4$ was also observed shown in Figure 2.4. There were no ligand-exchange products detected that correlate with the decreasing $SiCl_3^+$ signal until a temperature of 200 °C (473 K) where the SiF_3^+ signal starts to rise.[81] At temperatures above 200 °C, SiF_4 can be fully formed from $SiCl_4$ observed in the complementary behaviour of the change in intensity of the $SiCl_4$ reactant and SiF_4 product signals.[81] In addition, volatile Hf-containing etch products were not detected until 450 °C suggesting that chlorine must be building up in the HfF_4 film until there is enough present to form $HfCl_4$ species.[81]

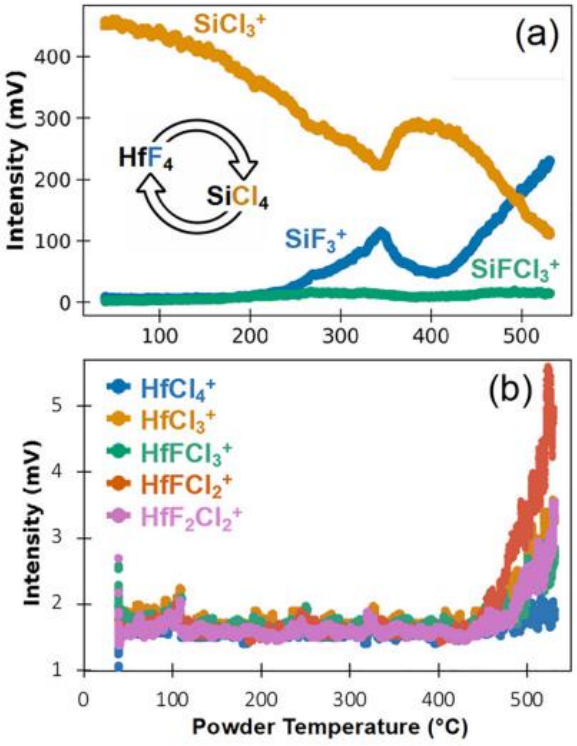


Figure 2.4 Temperature dependence of the ligand exchange reaction between $SiCl_4$ and HfF_4 powder. Taken from ref. [81].

The effect of different ligands on silane precursors $SiCl_4$, $SiCl_2(CH_3)_2$, $SiCl(CH_3)_2H$ and $Si(CH_3)_4$ were studied for spontaneous etching of metal fluorides GaF_3, ZnF_2, and ZrF_4 in powder form.[82] The strong Si – F covalent bonds make silanes important precursors for ligand exchange with metal fluorides.[75] Different exchange reactions of F/Cl, F/CH_3 and F/H were investigated by measuring the intensity of the ligand exchange and metal etch products.[82] When $SiCl_4$ was exposed to ZrF_4 powder at 450 ºC, the highest ion signal was observed for $ZrFCl_3^+$ which resulted from three F/Cl ligand exchanges between $SiCl_4$ and HfF_4.[82] Other smaller ion signals for $ZrCl_4^+$ and $ZrF_2Cl_2^+$ were observed.[82] These ion species were not observed until 425 ºC indicating that Cl was building up on the ZrF_4 powder before becoming volatile.[82] Similar for silane precursor $SiCl_2(CH_3)_2$, $ZrFCl_3^+$ was observed showing only F/Cl ligand exchange only took place.[82] The ion signal intensities of the Zr-containing etch products were not detected until 375 ºC suggesting again that Cl needs to build up in the ZrF_4 powder.[82] No CH_3 containing etch products were observed due to the small Zr-CH_3 bond energy.[83] When $SiCl(CH_3)_2H$ was exposed to ZrF_4 powder only F/Cl ligand exchange took place with $ZrFCl_3^+$ and $ZrCl_4^+$ ion signals observed.[82] There was no ligand exchange observed for $Si(CH_3)_4$ exposure on ZrF_4 powder.

2.1.4 First principles simulations of thermal ALE processes

In thermal ALE studies, thermochemical calculations can be used to model the reactions of interest.[5,9,11,21] Data from thermochemical tables is employed to model these reactions using the HSC Chemistry software.[76] The information in the databases are commonly based on bulk materials, therefore the thermochemical calculations provide insight for bulk etching but not for surface ALE reactions.[53] Modelling thermal ALE using atomistic first principles density functional theory allows use to examine any specific phase or surface of a solid material as well as any gas phase molecule that may be used in thermal ALE.

The chemical mechanism during HF exposure for Al_2O_3 thermal ALE was modelled using DFT by Natarajan and Elliott.[84] The postulated reactions during HF exposure on Al_2O_3 were modelled including bulk to gas (continuous etch) and surface to surface (self-limiting) shown schematically in Figure 2.5.[84]

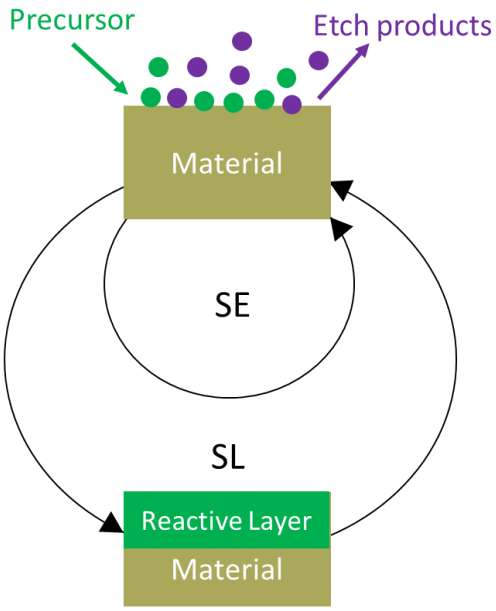


Figure 2.5: Schematic representation of the bulk to gas continuous spontaneous etch (SE) and surface to surface self-limiting (SL).

Bulk θ-Al_2O_3 and gaseous HF were the reactants considered for the bulk to gas reactions that produced gaseous AlF_3, Al_2F_6, AlOF and H_2O byproducts.[84] Reactants are modelled with a clean Al_2O_3 ($\bar{2}$ 0 1) slab with gaseous HF. Products are modelled with a F-covered Al_2O_3 surface and H_2O in a model of the surface to surface reaction.[84] The reaction energy at 0 K for the self-limiting surface to surface reaction (-3.60 eV/Al_2O_3) was more favourable than the continuous etch reactions (0.40, -1.53 and 9.88 eV/Al_2O_3 for Al-containing products AlF_3, Al_2F_6 and AlOF respectively) suggesting the HF pulse is self-limiting in nature.[84] The adsorption of HF was also studied on the bare Al_2O_3 surface. A single HF molecule does not start to dissociate until O-H and Al-F bonds were formed between HF and the surface.[84] The gain in energy upon adsorption is -0.44 eV, showing favourable interaction of HF at Al_2O_3. HF coverages up to 15.5 HF/nm^2 shown in Figure 2.6, were examined and a theoretical etch rate of -0.57 ± Å/cycle was calculated as well as a maximum etch rate of -1.14 ± Å/cycle to remove a monolayer of material.[84]

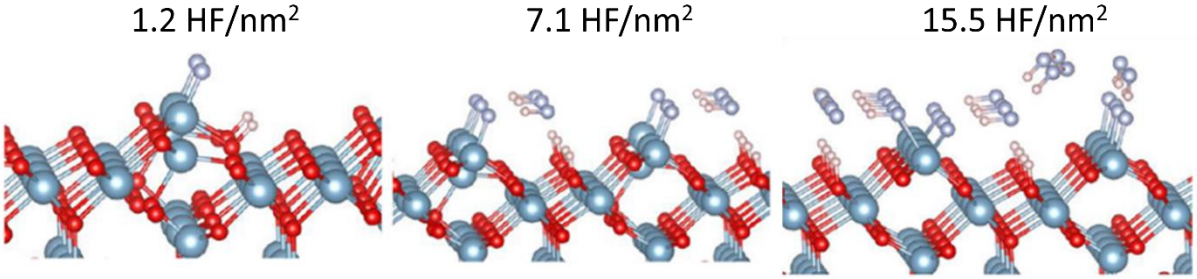


Figure 2.6: HF coverage on ($\bar{2}$ 0 1) Al_2O_3 surface. Adapted from ref [84].

The HF exposure on TiO_2 in thermal ALE was investigated by a combined computational and experimental study.[53] The HF exposure was predicted to continuously etch TiO_2 within the 87 – 497 ºC temperature range Figure 2.7 (a), which agreed well with FTIR measurements that showed spontaneous etching of TiO_2 was favourable from an onset temperature of 80 – 90 ºC Figure 2.7 (b).[53] Adjusting the pressure of reactant HF for 0.01 to 4 Torr with a constant product pressure of 0.01 did not change the onset temperature for the continuous etch pathway.[53] Model reactions for continuous etch of TiO_2 with HF exposure predicted that the reaction product TiF_4 is favourable and that $TiOF_2$ is unfavorable and this agrees with mass spectrometry measurements that identified TiF_4 and H_2O as the etch products.[53]

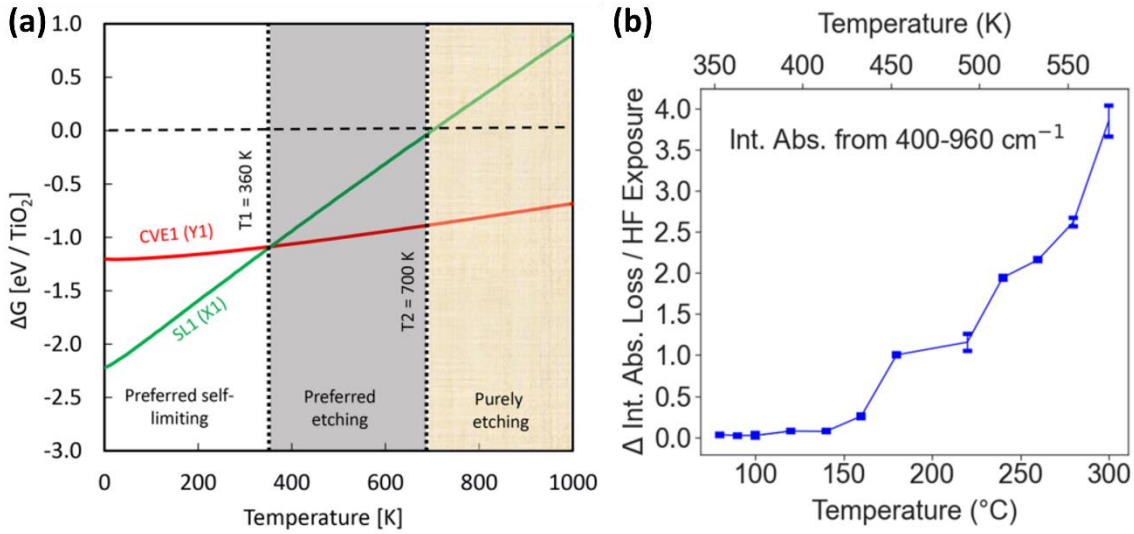


Figure 2.7: Combined computational and experimental TiO_2 thermal ALE study. (a) FEPs of continuous etch (CVE1 – red line) and self-limiting (SL1 – green line). (b) Etch rate measured by change in integrated FTIR absorbance of the Ti−O vibrational modes from 80 to 300 ºC. Adapted from ref [53].

Another study of thermal ALE of Al_2O_3 using NbF_5 and CCl_4 consisted of a combination of DFT modelling and experimental work to study the etch mechanism.[85] NbF_5 was selected as the fluorinating reactant since it is safer to handle and store compared to HF. The first step in the proposed etch mechanism was the conversion of the Al_2O_3 surface to $AlF_x[O]$.[85] The experimental results proposed that the fluorination reaction was not self-limiting and as a result a thicker $AlF_x[O]$ layer formed.[85] DFT calculations found $AlCl_3$ and $CFCl_3$ were the most favourable etch products from the full ALE cycle. Both the experimental and DFT results also found that the etch per cycle was not self-limiting and it depended on the fluorination step.[85]

Other investigations of thermal ALE using DFT include the following:

Hu and Schuster investigated the $AlMe_3$ exposure on AlF_3 using DFT with α-AlF_3 (012) surface representing the HF fluorinated Al_2O_3.[86] Selective etching of SiO_2 against Si by HF was investigated using DFT which showed that spontaneous etching of SiO_2 by HF was at near room temperature whereas etching of Si by HF was negligible due to high activation energies.[87] A thermal ALE process for cobalt was investigated.[88] An overall ALE cycle for combinations of different reactants was established.[88] Reaction mechanisms for thermal ALE of W were investigated using first principles simulation for the oxidation/chlorination of W.[89] DFT calculations showed that plasma-driven reactions were more favourable for GaN ALE over thermal etch process.[28] Simulations predicted that NbF_5 could enhance the etch rate of TiN which was experimentally verified in thermal ALE of TiN.[27] DFT was also used to predict and help understand the continuous etch reaction of HF on B_2O_3 which formed after the conversion of WO_3 to B_2O_3 using BCl_3.[62,65]

2.2 Atomic Layer Deposition

2.2.1 Introduction

Thin film applications were widely used for optical applications in the beginning of the 20th century for example telescopes and mirrors.[90] Physical properties of thin films for hardness and wear resistance were used in the middle of the century. The development of microelectronics industry in the late 1900s contributed to many applications of thin films mainly involving the deposition and manipulation of thin metal, nitride and dielectric films.[90] Miniaturization in the semiconductor industry requires atomic level control of thin film deposition.[91] ALD can deposit metal thin films on high aspect ratio structures and allows control of growth at the atomic scale.[91] Plasma enhanced ALD (PEALD) uses plasma-generated radicals to enable/accelerate chemical reactions with the deposited precursor layer. Advantages of PEALD over thermal ALD include lower deposition temperatures, higher reactivity, a wide range of possible chemistries, denser films and lower impurites.[92]

Applications of ALD include microelectronics such as transistors and capacitors, energy storage and conversion, desalination, catalysts and medical devices.[92] Modelling can examine the materials, mechanisms and deposition characteristics of ALD processes.[93] In this section we discuss relevant ALD chemistries that can help address challenges in downscaled interconnects, including choice of interconnect metal and novel single phase barrier/liner

materials. We discuss briefly previous DFT modelling work in our group that designed new combined barrier/liner films for interconnects as background. In my thesis, I build on this to firstly discuss previously reported Ru ALD and Co ALD processes from the literature as well as available modelling studies. Then I discuss how we can apply what we have learned from the literature to explore ALD processes for Ru and Co which can be used either as the interconnect metals to replace copper or can be incorporated into TaN (giving Ru-doped TaN or Co-doped TaN), which have been predicted as single phase combined barrier/liner materials.

2.2.2 Barrier and Liner materials in interconnect.

Interconnects play a crucial role in every microelectronic circuit, serving as an essential component. They perform vital functions, including the distribution of electrical signals and facilitating the provision of power and grounding for different circuit components. According to the International Technology Roadmap for Semiconductors (ITRS) and in line with Moore's law, both the scaling of transistor gate pitch and interconnect pitch play equal roles in the miniaturization of microelectronic circuits.[94] The current materials used in interconnects are putting limits on interconnect scaling, which has also caused the rate of increase in the number of transistors on a chip to slow down potentially limiting future device miniaturization.

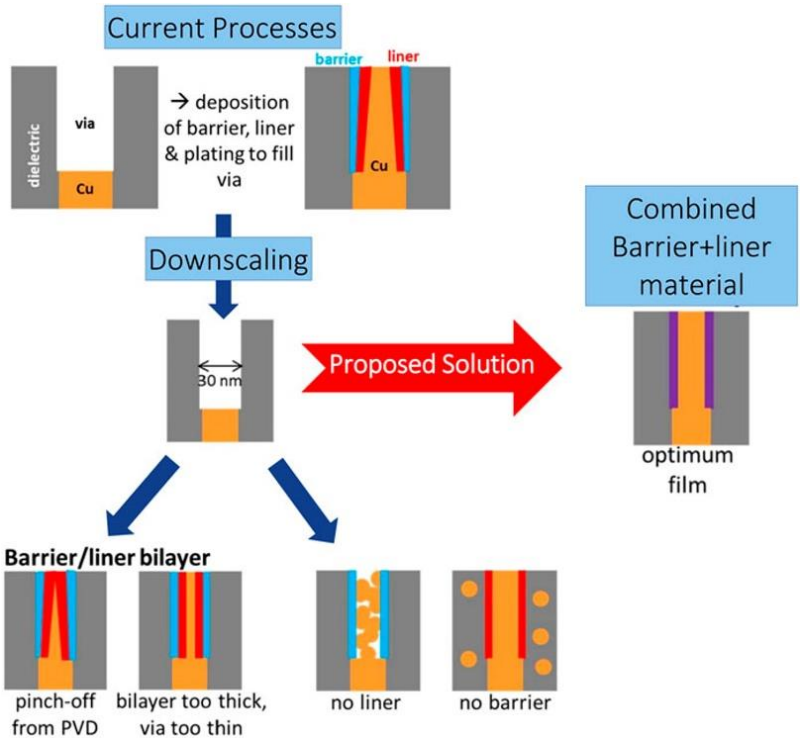


Figure 2.8: Challenges involved with the interconnect bottleneck and proposed solutions. Taken from ref [96].

In Figure 2.8 the downscaling of the current process leads to issues including: a pinch-off effect at the top of the via or the bilayer being too thick. Deposition of Cu will be difficult without a liner layer the promotes Cu deposition and without a barrier Cu migration into the dielectric occurs as shown in Figure 2.8. Therefore the proposed solution is a single combined barrier and liner material which will be discussed in more detail in this section. TaN is used as a diffusion barrier layer to prevent migration of copper, the currently used interconnect, into the dielectric layer in CMOS transistors at typical local temperatures.[95] The consequence of copper migration is a short circuit. There are unfortunately some disadvantages with copper as device dimensions continue their aggressive shrinking. At the length scales typical of high-performance transistor nodes copper would prefer to aggregate into islands or clusters which will not form smooth conducting films. In addition, dimensional reduction also increases the resistivity of copper films. With the first challenge, copper requires a liner or seed layer to promote the electroplating of conducting copper films, while its replacement with another metal can overcome the resistivity problem.

Currently, the semiconductor industry uses a tri-layer stack of TaN/Ta/Cu with TaN as the barrier and Ta as the liner. However advanced interconnect technology will require high aspect ratio trench structures, and therefore the copper, liner and barrier stack should only take up a small volume of the trench to preserve the low copper resistivity at the 14 nm node and smaller.[96] The tri-layer stack of TaN/Ta/Cu is also difficult to grow in high aspect ratio vias.[97] The solution is a combined barrier and liner material[96] that only takes up a small volume of the interconnect and can be grown using ALD. Ruthenium and Cobalt liners can be used as liner layers between the TaN barrier and Cu. Ru-liners allow direct plating and Co-liners allow thinner seeds. Ru metal is also known to show high potential in semiconductor devices due to its low bulk resistivity (7 μΩ), high work function (4.7 eV), high chemical and thermal stability and catalytic activity; its position as a precious metal does count as a negative point.[98]

Ru passivated and Ru doped ε-TaN surfaces (in which Ru is incorporated into the TaN surface layer, which could be achieved through ALD) as a combined single phase barrier and liner material were studied using DFT by Nies and Natarajan in a series of papers.[96,99–101] The 1 ML Ru passivated TaN surface was found to be better at preventing Cu association then on the 2 ML Ru passivated TaN surface as association of Cu atoms could lead to Cu islands.[99] Ru sites in the Ru doped TaN surface promoted Cu nucleation.[99] The adsorption energies for a single Cu atom on 1 ML Ru passivated TaN surface and 100 % Ru doped surface were greater than on the bare TaN surface showing Cu bonds well to the surfaces with Ru incorporation.[96]

The morphology of Cu was also investigated using DFT on bare TaN, 1 ML Ru passivated TaN and Ru incorporated into TaN surface layer at Ru concentrations of 25%, 50% and 100%.[101] The bare TaN surface did not promote the 2D wetting of Cu and led to the formation of 3D Cu islands as shown in Figure 2.9 (a). By contrast, a smooth Cu film formed on the 1 ML Ru passivated TaN surface shown in Figure 2.9 (b), showing that as little as one monolayer of Ru acts as a good Cu liner and this can help reduce the volume used by the barrier/liner stack. A two-layer structure of Cu formed on 50% Ru doped TaN shown in Figure 2.9 (c). The formation of 3D copper islands formed on 25% Ru doped TaN showing higher Ru content is required to promote 2D growth.[101] To ensure thermal stability and prevent Cu, Ru and N migration Ta atoms are required in the Ru doped TaN surface layer and a Ru doping concentration of 50% is suitable.

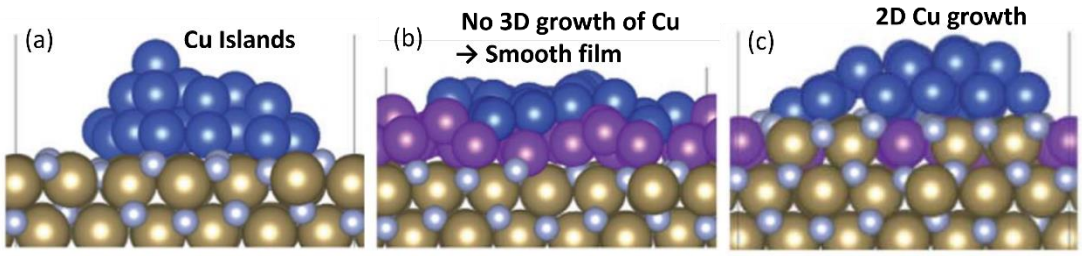


Figure 2.9 Cu morphology on (a) Bare TaN, (b) 1 ML Ru passivated TaN and (c) 50% Ru doped TaN. Colour coding: Ta = brown, N = light blue, Cu = dark and Ru = purple. Adapted from ref.[101].

The same DFT analysis was carried out for Cu on 25% and 50% Co doped TaN surface layers.[100] On both Co doped TaN surfaces the Cu atoms formed a two-layered structure similar to Ru doped TaN as shown in Figure 2.10. Co doped TaN surfaces were shown to prevent 3D island growth of Cu making it a suitable candidate for a combined barrier and liner material.[100] This study also found a 100% W doped TaN surface layer or in other words WN passivation of TaN presents a suitable combined barrier and liner material.[100] These proposed single layer combined barrier/liner materials can be prepared using atomic layer deposition (ALD), using a supercycle at the end of the process to incorporate the other metal.[102–105] Alternatively ALD can also be used to deposit these metals to nm-scale precision if they are to be used as seed layers or deposited onto TaN.

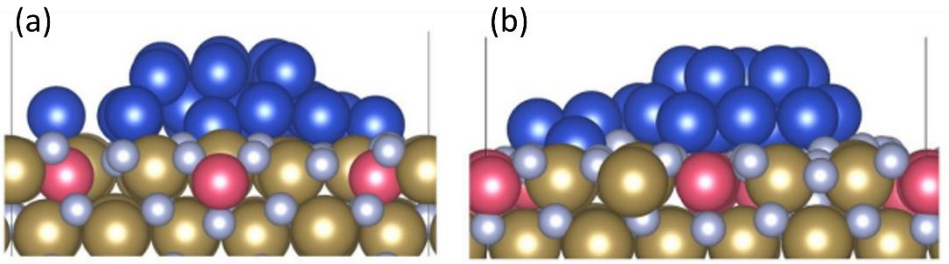


Figure 2.10 Cu morphology on (a) 25% Co doped TaN and (b) 50% Co doped TaN. Colour coding: Ta = brown, N = light blue, Cu = dark blue and Co = pink. Adapted from ref

Interconnect wire widths are expected to reach dimensions of 10 nm and smaller in the next decade and as a result, Cu intrinsic properties will limit the interconnect performance.[106] Half-pitch dimensions of interconnects will reach 8 nm after 2025 according to the International Roadmap for Device and Systems (IRDS).[107] Sub-10 nm dimensions lead to a decrease in the relative wire volume used by Cu which leads to an increase in the resistance of the wire per unit length.[106,108] Replacing Cu with another metal can overcome the scalable issues of interconnects. The alternative metals must have a resistance to electromigration and a low resistance in small dimensions which is preferably lower than the combination of Cu with the barrier/liner layers.[106] Ruthenium is a promising material to replace Cu as the metal for interconnects but it does not adhere well to the Si oxide dielectric material and is not an effective diffusion barrier. Cobalt is also a promising candidate for replacing Cu in small-dimension interconnects, with lower resistivity than Cu at sub-10 nm although there is high demand for this metal in battery technologies.[109]

2.2.3 Experimental work on ALD of Ru & Co

2.2.3.1 Experimental Ru ALD

Ru ALD processes have used metal-organic precursors such as $RuCp_2$,[110–113] $Ru(EtCp)_2$,[103,114–117] (EtCp)Ru(MeCp),[118] $Ru(DMPD)_2$,[119,120] and $Ru(Cp)(CO)_2Et$[121,122] and O_2 is generally the co-reactant. The molecular properties of Cp-based metal precursors can be tuned by functionalizing the Cp ring with various substituents to increase their thermal stability and volatility as well decreasing melting points; methyl and ethyl substituted Cp ligands have been studied.[123] Ru ALD processes that use oxygen to decompose metal-organic precursors can lead to problems with film integrity and substrate sensitivity.[124]

Bis(ethylcyclopentadienyl)ruthenium(II), (or Diethylruthenocene) $Ru(EtCp)_2$ is an inexpensive commercially available liquid precursor and can be used in thermal and plasma-enhanced ALD processes with a variety of co-reactants. PEALD of Ru using $Ru(EtCp)_2$ and O_2 plasma at 400 °C on Ta_2O_5, TiN and TaN substrates showed that complete nucleation is achieved on TaN whereas for Ta_2O_5 poor adhesion to the substrate caused blistering of the film.[125] High quality and low resistivity (10 – 14 μΩcm) Ru thin films were deposited on ALD grown TiN(2nm)/Si and ALD TaN(5nm)/Si substrates by PEALD at growth temperature 270 °C.[126,127] PEALD of Ru using $Ru(EtCp)_2$ and O_2 plasma on bare silicon and silicon oxide surfaces led to 3D growth due to poor nucleation.[128] Thermal ALD of Ru using $Ru(EtCp)_2$ and O_2 produces smooth film surfaces at 250 °C.[129] Modifying the silicon and silicon oxide surfaces with a TaN sublayer of 0.3 nm allows for more efficient nucleation of ruthenium films.[125,128] Annealing at 400 °C, the polycrystalline tetragonal RuO_2 structure changes to polycrystalline hexagonal Ru film.[128] This shows that RuO_2 decomposes during annealing and the disproportionation reaction with the creation of volatile RuO_4 is also likely with competitive oxygen plasma etching of ruthenium.[128]

Using O_2 as a reactant in Ru ALD can create a metal oxide film interfaced with the barrier material resulting in interconnection failures.[130,131] Oxygen was present in ALD grown Ru that used $RuCp_2$ and O_2 at a deposition temperature of 245 °C.[132] PEALD using NH_3 instead of O_2 can prevent the formation of interfacial metal oxide.[133] At deposition temperature 270 °C on a 40 nm thick TiN/100 nm thick SiO_2/Si wafer, the NH_3 plasma reduces $Ru(EtCp)_2$ and the film growth saturates at 0.38 Å/cycle with a consistent Ru film resistivity of 12 μΩ cm.[133] The impurity levels of oxygen, carbon and nitrogen were below the detection limit, therefore showing the excited species in NH_3 plasma formed volatile compounds with the $Ru(EtCp)_2$ ligands.[133] However the exact species formed were not described. It was also postulated that the lone pair electron in the NH_3 plasma interacts with $Ru(EtCp)_2$ and weakens the Ru-(EtCp) bond.[133,134] The surface roughness of Ru films is improved by applying PEALD using NH_3 instead of conventional ALD using O_2 gas.[115,133,135] Ru growth does not occur using molecular H_2 and NH_3 as reducing co-reactants whereas H_2 and NH_3 plasma work well with NH_3 being most effective.[136]

SiO_2 surfaces treated with NH_3 plasma and SiN_x surfaces grown by CVD enhance the nucleation of ruthenium on them compared to bare SiO_2.[117] An NH_3 plasma-treated SiO_2 surface showed no incubation period whereas bare SiO_2 and SiN_x had considerable incubation periods of 200 and 100 ALD cycles respectively.[117] The delay in nucleation on the SiN_x surface is due to the surface still retaining some oxide despite being treated with HF.[117] The nitrogen

containing surface groups provide reactive adsorption sites for the $Ru(EtCp)_2$ precursor as well as the formation of defect sites and the incorporation of atomic hydrogen on the surface.[117] However the exact details of the adsorption mechanism and chemical nature of the adsorption sites required more investigation.

Ru-incorporated TaN (Ru-TaN) films were prepared by intermixing Ru and TaN using PEALD at 230 °C which interrupted the polycrystalline growth of both materials forming an amorphous structure with a minimum carbon impurity and low resistivity.[137] TaN exposed to O_2 or NH_3 plasma resulted in Ta_2O_5 or Ta_3N_5 respectively with high resistivity.[137] Replacing the plasma with N_2/H_2 resulted in a TaN and Ta_3N_5 mixing phase with a much lower resistivity compared to using O_2 or NH_3 plasma.[137] PEALD TaN was deposited using Tertiaryamylimidotris-(dimethlyamido)tantalum and H_2 and Ru was deposited using $Ru(EtCp)_2$ and N_2/H_2 plasma. A high H_2 exposure time on the TaN films reduces the carbon impurities with hydrogen radicals breaking the Ta-C bonds to form metallic Ta.[137]

When using N_2/H_2 plasma, the hydrogen radicals can break the Ta-C bonds and the nitrogen radicals react with metallic Ta making TaN during the Ru subcycle.[137] The same can also be done for Ru-TiN by intermixing TiN and Ru using PEALD at 200 °C forming an amorphous film.[138] Ru deposited on TaN using (carbonyl) - (alkylcyclohexadienyl)Ru/H_2 CVD at 250 °C grew linearly.[139] PEALD at 300 ºC using $RuCp_2$ and $Ru(EtCp)_2$ with NH_3 plasma showed no nucleation delay on various substrates TaN_x, Ta_2O_5, Si and SiO_2 whereas nucleation delay was observed for thermal ALD using O_2.[140] It was suggested that N containing radicals were responsible for the removal of ligands during PEALD.[140] No nitrogen or carbon peaks were detected from XPS spectra for Ru PEALD.[140]

The pretreatment of TaN substrates used for Ru ALD at 330 ºC using $RuCp_2$ and O_2 was studied.[141] Two different pretreatment options were explored (i) low energy Ar ion bombardment and (ii) PVD pre-deposited Ru were performed on TaN before Ru ALD. The Ru ALD film grown on the Ar^+-pretreated TaN surface was smooth and uniform.[141] Ru nucleation occurred on Ru islands on the PVD pre-deposited Ru TaN surface resulting in a rougher surface.[141] It was suggested that a few nitrogen atoms were selectivity removed by Ar ion bombardment, leaving a more metallic surface so that $RuCp_2$ can easily adsorb.[141]

Polycrystalline ruthenium is an unsuitable Cu diffusion barrier because its columnar grain structure allows a fast diffusion path for Cu atoms at 450 °C.[142] Amorphous ruthenium has a higher adhesion strength to Cu and a better diffusion barrier compared to polycrystalline ruthenium.[143] Ruthenium films that contain a significant concentration of nitrogen atoms exhibit a nanocrystalline structure with a very short-range ordering[144] or potentially an

amorphous morphology.[145] Nitrided Ru barriers created through PVD had suitable barrier qualities.[143,144] However, direct Cu electrodeposition is challenging on RuN_x surfaces due to RuN_x having a high electrical resistance. Bilayer barriers Ru/RuN_x were deposited on mesoporous SiO_2 dielectric layers by an in-situ two-step PEALD process. The PEALD RuN_x films were deposited at 200 °C using $Ru(EtCp)_2$ and N_2/H_2 plasma and metallic Ru was deposited on the RuN_x layer using the same Ru precursor and just H_2 plasma.[145] The deposited Ru on RuN_x reduces the sheet resistance and allows direct electroplating of Cu.[145] RuN_x is thermally unstable above 275 °C where it decomposes into metallic Ru and nitrogen.[143] Cu electrodeposition on the 400 °C annealed Ru/RuN_x bilayer was unsuccessful due to the partial thermal decomposition of the underlying RuN_x layer where nitrogen atoms migrated up into the metallic ruthenium layer.[145] Cu can be electroplated on the as deposited Ru/RuN_x bilayer and the Cu layer functions as a protective passivation layer, effectively inhibiting the thermal degradation of the Ru/RuN_x barrier at 500 °C and below.[145,146]

A carbon free precursor ToRuS (*Total Ruthenium Solution,* RuO_4 in a solvent) was used to overcome the problems with impurity incorporation when depositing Ru thin films.[147] ToRuS is non-toxic, non-corrosive, non-flammable, a liquid over a wide range of temperatures and compatible with most materials.[147] RuO_4 has a high oxidation state of +8 and can be used as a reactant for ALD; it can be an oxidizing agent and a Ru source.[148–150] For growing Ru metal a suitable co-reactant with ToRuS is H_2, which is a reducing agent.[147,150–153] Metal-organic Ru precursors typically require deposition temperatures greater than 200 °C and long incubation times which can lead to films with high roughness.[153] Ru thin films were also deposited using a beta-diketonate Ru precursor, dicarbonyl-bis(5-methyl-2,4-hexanediketonato) Ru(II) ($C_{16}H_{22}O_6Ru$, known as Carish) and molecular H_2 at a substrate temperature of 250 °C which showed self-limited growth with negligible oxygen impurities.[151] The lowest temperature for thermal ALD of Ru using RuO_4 and molecular H_2 was reported by Minjauw et al. to be 100 °C[153], at which temperature the growth on a sputtered Ru substrate was entirely driven by surface reactions from alternate exposures of the precursor RuO_4 and reactant molecular H_2, with oxygen the only detectable impurity (2% atom).[153] Replacing molecular H_2 with H_2 plasma, plasma enhanced ALD of Ru can be achieved at temperatures as low as 50 °C using RuO_4 as the Ru precursor.[152]

The downscaling of interconnects results in an increase in Joule heating (current flow in interconnects can cause a temperature increase due to self-heating) which exacerbates the performance and causes problems with the reliability of electromigration.[154] The thermal boundary resistance (TBR) at the barrierless Ru/SiO_2 interface is high due to poor adhesion

between Ru and SiO_2.[155] Therefore Ru requires an adhesion layer such as TaN or TiN between it and the dielectric layer which reduces the TBR.[154] It was also found that the TBR decreases when the nitrogen content in the TaN layer increased due to enhanced bonding at the interface.[154]

2.2.3.2 Experimental Co ALD

The reducing agent used in the ALD processes of cobalt metal can influence the quality of the films obtained. Thermal ALD of Co using $CoCp_2$ and H_2 resulted in a C-contaminated amorphous phase when deposited on SiO_2 substrate due to the low reducing powder of H_2.[156] NH_3 plasma reactant is used with $CoCp_2$ to remove Cp ligands and reduce carbon incorporation in PE-ALD on Si and SiO_2 substrates at 250 – 400 °C producing metallic, low resistivity films.[156] The nitrogen incorporation in these films was found to be minimal despite using the NH_3 reactant.[156] Plasma mixture of N_2/H_2 can also be used as a reducing agent instead of NH_3.[157] Using just H_2 or N_2 plasma, the sheet resistance of the PEALD Co thin films is unmeasurably high, whereas using both plasmas results in low resistivity Co thin films.[157] The growth rate increases with temperature from 0.26 Å/cycle at 150 °C to 0.65 Å/cycle at 450 °C and the resistivity decreases with increasing temperatures (18 μΩcm at 450 °C).[157] At low growth temperatures significant amounts of nitrogen are present whereas at temperatures higher than 300 °C nitrogen incorporation is minimum, similar when using NH_3.[157,158]

It was also found that radical species formed from NH_3 are important for PEALD of Co films compared to N or H radicals when using N_2/H_2 plasma.[157] ALD of Co using $CoCp_2$ and H_2 on H-terminated Silicon substrates showed that no Co was deposited due to difficulty in nucleation.[156] Whereas when using NH_3 plasma the formation of Si-N_x or Si-NH_x terminated surface provides reaction sites for nucleation.[156,159] The reaction by-product using $CoCp_2$ and NH_3 or H_2/N_2 plasmas in PEALD of Co was CpH.[158,160] The remaining Cp ligands are removed by NH_x species (x = 1, 2) formed by the plasma in the co-reactant subcycle which also produce CpH.[158] Surface bound NH_x can react with the precursor molecule $CoCp_2$ in the next cycle.[158] Separating the exposures of H_2 and N_2 plasma leads to significant amounts of O, C and N impurities in the bulk of the film which may be due to the absence of NH_x species in the plasma.[158] NH_2 plasma species promoted the dissociation of the metal-carbon bond in $CoCp_2$ in hot-wire-assisted ALD of Co.[161] PEALD of Co using $Co(EtCp)_2$ on metallic Ta showed that the exposure of N_2/H_2 plasma formed a Ta nitride interlayer TaN_x with an amorphous microstructure on which Co was deposited.[162] Continuous and uniform films of Co was

deposited on TaN for PEALD of Co using $Co(EtCp)_2$ and NH_3 plasma after 1200 cycles at 125 ºC.

There have also been reported ALD processes of cobalt nitride films using cobalt precursors $Co(^{ipr2}AMD)_2$[163] and $CoCp_2$[164] It was shown that both cobalt and cobalt nitride films can be grown using $CoCp_2$ and NH_3 plasma by adjusting the temperature.[164] At temperatures 230 ºC and 260 ºC cobalt nitride was grown with crystal structure Co_2N.[164] A mixed phase material of Co_3N and Co was observed at 300 ºC and pure Co was obtained at 350 ºC.[164] High concentrations of carbon impurities were found in cobalt nitride films deposited on silicon samples at 300 ºC and below showing NH_3 plasma did not remove the $CoCp_2$ precursor.[165] The choice of plasma reactant used in PEALD of cobalt thin films using $CpCo(CO)_2$ influences the material deposited. High quality CoN_x films were obtained when using H_2/N_2 plasma.[166] NH_3 plasma resulted in Co films with high carbon and nitrogen incorporation as well as having high film resistances.[166] Very high carbon content CoC_x films were formed when using H_2/Ar plasma as a coreactant.[166] Metallic cobalt was deposited using dicobalt hexacarbonyl-1-heptyne [$Co_2(CO)_6HC{\equiv}CC_5H_{11}$] and hydrogen plasma for a temperature window of 50 and 110 ºC.[167]

2.2.3.3 TaN deposition with ALD

Hydrogen and nitrogen plasma have been reported as co-reactants for TaN ALD processes.[168] Polycrystalline Ta-N thin films were deposited for PEALD using TBTDET and hydrogen radicals at 260 ºC where the hydrogen radicals reduced TBTDET fully.[169] Plasma assisted CVD of TaN using $TaBr_5$ with N_2 and H_2 co-reactants grew TaN_x with low carbon and oxygen impurities.[170] ALD of TaN was achieved by first using TaF_5 with hydrogen plasma to deposit Ta followed by thermal nitridation with NH_3 to form cubic TaN at 350 ºC.[171] The T/N ratio was reported to be 1:1 regardless of the NH_3 dosage time.[171] In plasma assisted nitridation using a NH_3/H_2/Ar gas mixture, the highly reactive plasma species formed Ta_3N_5.[172] Hydrogen plasma post-treatment can be used to reduce the nitrogen-rich TaN phase on the film surface to the stoichiometric TaN phase. [173] PEALD using $TiCl_4$ with H_2/N_2 plasma mixture deposited cubic-TaN thin films whereas Ta_3N_5 is formed when using NH_3.[174]

2.2.4 ALD Modelling of Ru and Co to explore the reaction mechanism

NH_x (x = 1 or 2) species cannot be directly detected using quadrupole mass spectrometry[158] therefore DFT can examine the formation, stability and coverage of these proposed post-plasma species on the substrate. A DFT study from our group examined the coverage and stability of

NH_x-terminated ruthenium and cobalt surfaces which are difficult to examine using experimental techniques.[175] The ruthenium surfaces were terminated with amine (NH_2) or imine (NH) species and mixed termination with NH_2 and NH and stable coverages were determined.[175] These surfaces are then used in subsequent calculations to explore hydrogen transfer steps for possible Cp ligand elimination from $RuCp_2$ and $CoCp_2$ precursors in the metal step in the ALD process and this can be influenced by the nature and stability of the NH_x-terminated metal surface.[175–177] The ruthenium and cobalt surfaces examined were the (001) and (100) facets with single NH and NH_2 to analyse the preferred binding site.[175] NH prefers to bind on the hcp site and NH_2 prefers the bridge site on the (001) surface.[175] Both NH and NH_2 prefer to bind to a bridge site on the (100) surface.[175] NH and NH_2 are in an upright position after relaxation on both surfaces.[175] On the Ru(001) surface the saturation coverage of NH species is 1 ML and on the Co(001) surface the saturation coverage of NH species is 0.67 ML shown in Figure 2.11 (a) and (b).[175] The saturation coverage of NH on both the Ru(100) and Co(100) surfaces is 2 ML due to their zigzag structure as shown in (c) and (d) in Figure 2.11.[175] For NH_2 species, both Ru(001) and Co(001) have saturation coverages of 0.67 ML and for Ru(100) 1.33 ML and Co(100) 1 ML shown in Figure 2.12.[175] Mixed NH and NH_2 termination on the Ru(001) surface is not stable whereas Co(001) have stable coverages of $5NH + 3NH_2$ or $6NH + 2NH_2$.[175] A coverage of 2 ML mixed NH and NH_2 can be achieved on the (100) surfaces for both metals.[175]

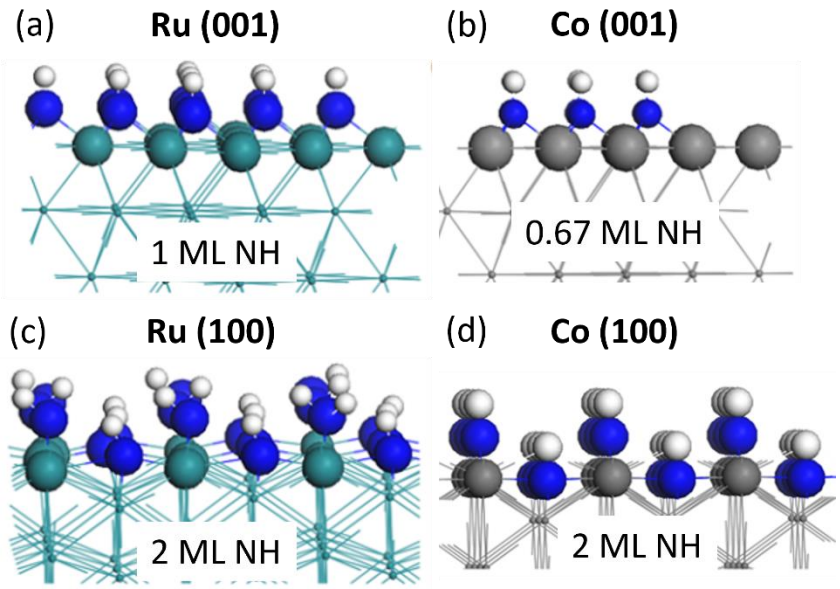


Figure 2.11: NH coverage on (a) Ru(001), (b) Co(001), (c) Ru(100) and (d) Co(100) surface facets. Adapted from ref [175].

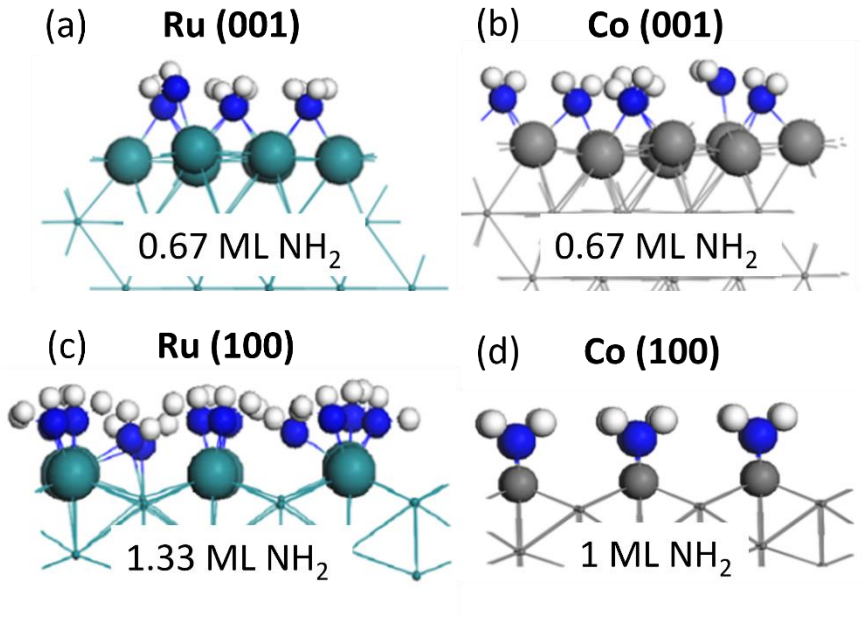


Figure 2.12: NH_2 coverage on (a) Ru(001), (b) Co(001), (c) Ru(100) and (d) Co(100) surface facets. Taken from ref [175].

There have been other DFT studies for Ru ALD that explored surface reactions of precursors such as dicarbonyl-bis(5-methyl-2,4-hexanediketonato) Ru(II) or "Carish" for simplicity,[178] $Ru(EtCp)_2$[179] and $Ru(DMBD)(CO)_3$[180]. The dissociative adsorption of Carish on a clean Ru(0001) surface into its individual components has a large exothermicity of -11.39 eV.[178] $Ru(EtCp)_2$ can act as a homometallic precursor inhibitor for area selective deposition of Ru.[179] $Ru(EtCp)_2$ adsorbs on the Ru surface through the dissociative chemisorption of EtCp ligands favourably at -6.32 eV as shown in Figure 2.13.[179] The adsorption of Carish on the EtCp-terminated surface is unfavourable at 2.10 eV shown in Figure 2.13.[179] Carish also did adsorb favourably on the EtCp-terminated (3.29 eV) surface that had undergone hydrolysis.[179] $Ru(DMBD)(CO)_3$ physisorbs on the fully hydroxylated α-SiO_2 surface with adsorption energies ranging from -0.27 eV to -0.56 eV.[180] The changes in the Gibbs free energies for the first and second hydrogenation of the -CH_2 group of DMBD are 0.03 eV and 0.20 eV where dimethyl butene then desorbs.[180] DFT modelling of $Ru(EtCp)_2$ on Ru surfaces found that replacing O_2 with atomic H as a nonoxidizing co-reactant gas volatized the EtCp ligands through surface-catalyzed hydrogenation.[181] Two kinetic barriers of 0.8 eV and 0.9 eV were calculated for the interaction between adsorbed EtCp and adsorbed atomic hydrogen.[181]

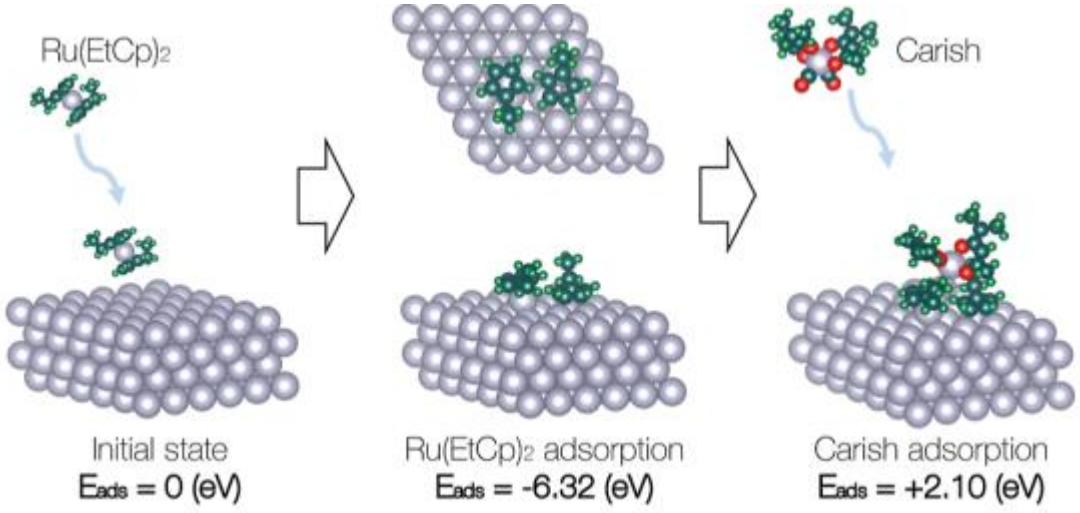


Figure 2.13: $Ru(EtCp)_2$ on Ru substrate and Carish on EtCp-terminated surface. Adapted from ref[179].

A study showed that Cp ligand elimination from $CoCp_2$ via hydrogen transfer from NH_x-terminated cobalt surfaces is favourable for both Cp ligands on the Co(100) surface and for the first Cp ligand on the Co(001) surface at ALD operating conditions.[177] The first and second hydrogen transfer energy barriers are moderate for Cp ligand removal on the NH_x-terminated Co(100) surface with values of 0.52 and 0.85 eV respectively.[177] Increasing the metal precursor coverage to two $CoCp_2$ promotes the reactivity with the first hydrogen transfer being barrierless and the second transfer barrier being lowered to 0.79 eV.[177] On the NH_x-terminated Co(001) surface the activation barrier for the hydrogen transfer to the Cp ligand is 0.56 eV.[177] An increase in the $CoCp_2$ coverage raises the barrier to 0.74 eV which is still moderate enough that the process does not require high temperatures.[177]

On NH_x-terminated ruthenium surfaces, Cp ligand elimination from $RuCp_2$ by hydrogen transfer is endothermic at ALD operating temperatures.[176] Increasing the $RuCp_2$ coverage promotes the first Cp ligand elimination which is exothermic on both surfaces.[176] The first hydrogen transfer on the Ru(001) surface is endothermic with high barriers of 1.33 eV and 1.51 eV for 1 ML NH Ru(001) and 0.89 ML NH Ru(001) respectively.[176] Decreasing the NH coverage to as low as 0.06 ML NH Ru(001) does not affect the endothermic reaction energy difference and high activation barrier.[176] Two Cp ligands can be removed on the NH_x-terminated Ru(100) surface but only for higher coverage of $RuCp_2$ with barriers 2.02 eV and 1.01 eV for the first and second hydrogen transfer steps.[176] H_2 formation was also observed. The computed hydrogen transfer barriers are high on the ruthenium surface compared to those on the cobalt surfaces. The $Ru(Cp)_2$ precursor appears to be much less reaction on the NH_x-terminated Ru surfaces when compared to $Co(Cp)_2$.

RuCp and CoCp fragments on the ruthenium and cobalt surfaces respectively could react with the N_2/H_2 plasma species in subsequent plasma steps and be removed. Plasma-generated radicals $^{\bullet}H$, $^{\bullet}N$, $^{\bullet}NH$ and $^{\bullet}NH_2$ in the subsequent plasma step can react with $CoCp_2$ treated Co(001) and Co(100) surfaces.[182] The NH_x-terminated Co(001) surface contains CoCp fragments after the metal precursor pulse.[182] The plasma radicals identified from experimental work[158] that could promote Cp ligand removal were $^{\bullet}H$, $^{\bullet}N$ and $^{\bullet}NH$. The formation and desorption of CpH with hydrogen radicals was overall endothermic at 1.32 eV.[182] The formation and desorption of pyridine and pyridinium formed by insertion of $^{\bullet}N$ and $^{\bullet}NH$ radicals into the Cp ring is exothermic at -1.06 eV and -0.37 eV respectively shown in Figure 2.14.[182] From this the primary product of eliminating the Cp ligand is pyridine. It was also found that surface NH species that were present on the Co surface can be removed by the formation and desorption of NH_3 through reaction with $H^{\cdot}$ radicals is exothermic at -0.14 eV on the CoCp/NHx-terminated Co(001) surface.[182] When the Cp ligands are removed first by pyridine formation followed by complete removal of the NH surface species by NH_3 formation, the overall process is highly exothermic at -4.85 eV.[182] This shows that Cp ligands are eliminated before the NH species on the Co(001) surface.

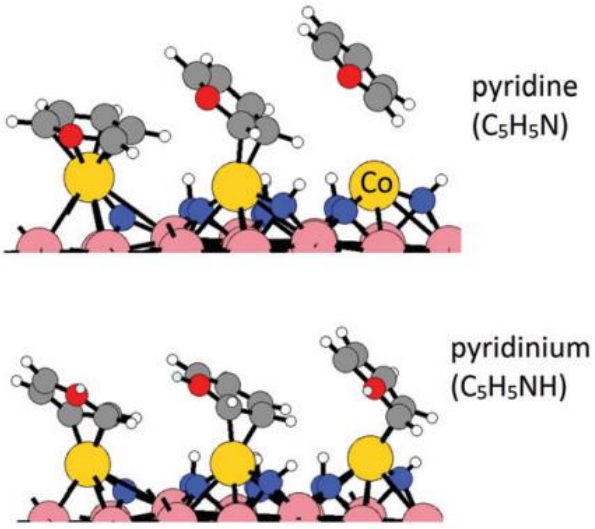


Figure 2.14: Formation of pyridine and pyridinium with N and NH radicals. Adapted from ref[182].

The NH_x-terminated Co(100) surface is terminated with Co atoms after the $CoCp_2$ pulse.[182] The NH_x-terminated Co(100) surface contains surface NH_2 and trench N atoms post Cp ligand elimination after the metal precursor pulse.[182] It was found that the surface NH_2 species cannot be removed as NH_3 with $^{\bullet}H$ radicals due to the overall reaction energy being endothermic at

5.80 eV.[182] The trench N species on the Co(100) surface can react favourably with the •H radicals to form NH with one •H radical forming a Co-H bond.[182] No NH_2 surface species or NH_3 byproducts were formed between the trench N atoms and •H radicals showing difficulty in removing N species from the Co(100) surface.[182] The formation of hydrazine (N_2H_4) and diazene (N_2H_2) was also found to be unfavourable.[182] The surface NH species formed between the trench N and •H radicals provide reactive sites for the next metal precursor pulse. Ab initio molecular dynamics were performed on the NH_x-terminated Co(001) surface with CoCp fragments that had formed pyridine with •N radicals.[182] The •H radicals formed NH_3 with the NH_x surface species and surface bound pyridine can either desorb or form pyridinium which then desorbs from the surface.[182] The dynamics were also explored on the Co(100) surface which showed no desorption of surface NH_x species and at a higher temperature the Co atoms formed small Co nanoclusters due to trench N migrating to surface sites forming Co_xN.[182]

2.3 Research Gaps and Questions Identified for my Thesis

2.3.1 Thermal ALE of metal oxides

Experimental studies of self-limiting thermal ALE developed the reaction mechanisms based on the MCPC and the individual mass changes during precursor exposure. However it is difficult to investigate the ALE reactions directly using experimental techniques. First principles based atomic-level simulations using DFT can give deep insights into the precursor chemistry and the reactions that drive the etch of metal oxides. Modelling of thermal ALE allows us to examine any material of intertest as well as its various oxide phases and surface facets. Experimental studies have shown that the fluorination step (surface modification) is responsible for the extent of material etched in the ligand exchange step which also determines the etch rate. Therefore, studying the fluorination reaction using DFT modelling could deliver a detailed atomistic understanding of the etch mechanism based on surface fluorination.

In the subsequent ligand exchange step using HfF_4 and $SiCl_4$, for example, a suggested reaction is:

$$HfF_{4(s)} + SiCl_{4(g)} \rightarrow HfCl_{4(g)} + SiF_{4(g)}$$

However various ion species were detected through mass spectrometry and therefore the ligand exchange reaction may not necessarily go to complete chlorination and instead eliminate mixed Cl/F species. DFT can examine what reactions drive the ligand exchange step. In this thesis

first principles based DFT will be used to model the following etch chemistries and deliver the hitherto lacking atomic level information required to understand the reaction chemistries:

- The fluorination step in crystalline high-k metal oxides HfO_2 and ZrO_2.
- Surface modification in ALE chemistry of crystalline ZnO.
- The origin of enhanced etching of amorphous HfO_2.
- Ligand exchange interaction between fluorinated HfO_2 and $SiCl_4$.

This information will deliver a significant advance in our understanding of the mechanisms of thermal ALE on metal oxides.

2.3.2 ALD to incorporate Ru/Co into TaN for combined diffusion barrier-liner films

DFT studies have shown that combined barrier/liner materials with the incorporation of ruthenium or cobalt into the TaN surface layer are interesting solutions for extending the use of Cu in interconnects in for the next generation of electronic devices. ALD can be used to incorporate Ru or Co into TaN. Ruthenium and cobalt are also being considered to replace Cu in next generation interconnects. Therefore, the ALD of Ru/Co on TaN and other surfaces is of high interest.

TaN layers have been shown to promote the nucleation of ruthenium.[96,99,125,128,140,154] Unwanted interfacial metal oxide films can form when using oxygen plasma therefore N_2/H_2 plasma is a suitable choice to prevent this. Although numerous investigations have been conducted on Ru and Co PEALD, there is a lack in the understanding of the mechanism of plasma promoted ALD on of TaN and the role of the metal precursors. DFT can be used to explore the reaction mechanism and precursor reactivity for PEALD of Ru or Co on TaN. In this thesis first principles based DFT will be used to address the following outstanding research questions:

- Stability of NH_x-surface terminations of TaN, which are required for reasonable surface models of TaN for the metal precursor chemistry.
- The interaction of Ru and Co precursors with Cp and EtCp ligands on the various NH_x-surface terminations of TaN.
- The interaction of H radicals with the metal precursor treated NH_x-terminated TaN surfaces.

This can predict Ru and Co ALD chemistries which can be examined experimentally.

In addition, I also explore the chemistry of the $RuO_4 + H_2$ process for Ru deposition.

Chapter References

(1) Yoder, M. N. Atomic Layer Etching. US4756794A, 1988.

(2) Fischer, A.; Routzahn, A.; George, S. M.; Lill, T. Thermal Atomic Layer Etching: A Review. *J. Vac. Sci. Technol. A* **2021**, *39* (3), 030801. https://doi.org/10.1116/6.0000894.

(3) Kanarik, K. J.; Lill, T.; Hudson, E. A.; Sriraman, S.; Tan, S.; Marks, J.; Vahedi, V.; Gottscho, R. A. Overview of Atomic Layer Etching in the Semiconductor Industry. *J. Vac. Sci. Technol. A* **2015**, *33* (2), 020802. https://doi.org/10.1116/1.4913379.

(4) Ohba, T.; Yang, W.; Tan, S.; Kanarik, K. J.; Nojiri, K. Atomic Layer Etching of GaN and AlGaN Using Directional Plasma-Enhanced Approach. *Jpn. J. Appl. Phys.* **2017**, *56* (6), 06HB06. https://doi.org/10.7567/JJAP.56.06HB06.

(5) Lee, Y.; Huffman, C.; George, S. M. Selectivity in Thermal Atomic Layer Etching Using Sequential, Self-Limiting Fluorination and Ligand-Exchange Reactions. *Chem. Mater.* **2016**, *28* (21), 7657–7665. https://doi.org/10.1021/acs.chemmater.6b02543.

(6) Oehrlein, G. S.; Metzler, D.; Li, C. Atomic Layer Etching at the Tipping Point: An Overview. *ECS Journal of Solid State Science and Technology* **2015**, *4* (6), N5041–N5053. https://doi.org/10.1149/2.0061506jss.

(7) George, S. M.; Lee, Y. Prospects for Thermal Atomic Layer Etching Using Sequential, Self-Limiting Fluorination and Ligand-Exchange Reactions. *ACS Nano* **2016**, *10* (5), 4889–4894. https://doi.org/10.1021/acsnano.6b02991.

(8) Johnson, R. W.; Hultqvist, A.; Bent, S. F. A Brief Review of Atomic Layer Deposition: From Fundamentals to Applications. *Mater. Today* **2014**, *17* (5), 236–246. https://doi.org/10.1016/J.MATTOD.2014.04.026.

(9) Lee, Y.; George, S. M. Atomic Layer Etching of Al2O3 Using Sequential, Self-Limiting Thermal Reactions with Sn(Acac)2 and Hydrogen Fluoride. *ACS Nano* **2015**, *9* (2), 2061–2070. https://doi.org/10.1021/nn507277f.

(10) Lee, Y.; George, S. M. Thermal Atomic Layer Etching of Al2O3, HfO2, and ZrO2 Using Sequential Hydrogen Fluoride and Dimethylaluminum Chloride Exposures. *J. Phys. Chem. C* **2019**, *123*, 18455–18466. https://doi.org/10.1021/acs.jpcc.9b04767.

(11) Lee, Y.; George, S. M. Thermal Atomic Layer Etching of HfO2 Using HF for Fluorination and TiCl4 for Ligand-Exchange. *J. Vac. Sci. Technol. A* **2018**, *36* (6), 061504. https://doi.org/10.1116/1.5045130.

(12) Partridge, J. L.; Murdzek, J. A.; Johnson, V. L.; Cavanagh, A. S.; Fischer, A.; Lill, T.; Sharma, S.; George, S. M. Thermal Atomic Layer Etching of CoO, ZnO, Fe2O3, and NiO by Chlorination and Ligand Addition Using SO2Cl2 and Tetramethylethylenediamine. *Chem. Mater.* **2023**, *35* (5), 2058–2068. https://doi.org/10.1021/ACS.CHEMMATER.2C03616/ASSET/IMAGES/MEDIUM/CM2C03616_0015.GIF.

(13) Miyoshi, N.; Kobayashi, H.; Shinoda, K.; Kurihara, M.; Kawamura, K.; Kouzuma, Y.; Izawa, M. Atomic Layer Etching of SiO2 with Self-Limiting Behavior on the Surface Modification Step Using Sequential Exposure of HF and NH3. *J. Vac. Sci. Technol. A* **2021**, *40* (1), 012601. https://doi.org/10.1116/6.0001517.

(14) DuMont, J. W.; Marquardt, A. E.; Cano, A. M.; George, S. M. Thermal Atomic Layer Etching of SiO2 by a “Conversion-Etch” Mechanism Using Sequential Reactions of Trimethylaluminum and Hydrogen Fluoride. *ACS Appl. Mater. Interfaces* **2017**, *9* (11), 10296–10307. https://doi.org/10.1021/acsami.7b01259.

(15) Murdzek, J. A.; Rajashekhar, A.; Makala, R. S.; George, S. M. Thermal Atomic Layer Etching of Amorphous and Crystalline Al 2 O 3 Films. *J. Vac. Sci. Technol. A* **2021**, *39* (4), 042602. https://doi.org/10.1116/6.0000995.

(16) Cano, A. M.; Marquardt, A. E.; Dumont, J. W.; George, S. M. Effect of HF Pressure on Thermal Al2O3 Atomic Layer Etch Rates and Al2O3 Fluorination. *J. Phys. Chem. C* **2019**, *123* (16), 10346–10355. https://doi.org/10.1021/ACS.JPCC.9B00124/ASSET/IMAGES/MEDIUM/JP-2019-00124U_0015.GIF.

(17) Lee, Y.; Dumont, J. W.; George, S. M. Trimethylaluminum as the Metal Precursor for the Atomic Layer Etching of Al2O3 Using Sequential, Self-Limiting Thermal Reactions. *Chem. Mater.* **2016**, *28* (9), 2994–3003. https://doi.org/10.1021/acs.chemmater.6b00111.

(18) Cano, A. M.; Partridge, J. L.; George, S. M. Thermal Atomic Layer Etching of Al2O3 Using Sequential HF and BCl3 Exposures: Evidence for Combined Ligand-Exchange and Conversion Mechanisms. *Chem. Mater.* **2022**, *34* (14), 6440–6449. https://doi.org/10.1021/ACS.CHEMMATER.2C01120/ASSET/IMAGES/MEDIUM/CM2C01120_0016.GIF.

(19) Zywotko, D. R.; George, S. M. Thermal Atomic Layer Etching of ZnO by a “Conversion-Etch” Mechanism Using Sequential Exposures of Hydrogen Fluoride and Trimethylaluminum. *Chem. Mater.* **2017**, *29* (3), 1183–1191. https://doi.org/10.1021/acs.chemmater.6b04529.

(20) Lee, Y.; Johnson, N. R.; George, S. M. Thermal Atomic Layer Etching of Gallium Oxide Using Sequential Exposures of HF and Various Metal Precursors. *Chem. Mater.* **2020**, *32* (14), 5937–5948. https://doi.org/10.1021/acs.chemmater.0c00131.

(21) Murdzek, J. A.; George, S. M. Effect of Crystallinity on Thermal Atomic Layer Etching of Hafnium Oxide, Zirconium Oxide, and Hafnium Zirconium Oxide. *J. Vac. Sci. Technol. A* **2020**, *38* (2), 022608. https://doi.org/10.1116/1.5135317.

(22) Kim, W.-H.; Sung, D.; Oh, S.; Woo, J.; Lim, S.; Lee, H.; Bent, S. F. Thermal Adsorption-Enhanced Atomic Layer Etching of Si3N4. *J. Vac. Sci. Technol. A* **2017**, *36* (1), 01B104. https://doi.org/10.1116/1.5003271.

(23) Johnson, N. R.; Sun, H.; Sharma, K.; George, S. M. Thermal Atomic Layer Etching of Crystalline Aluminum Nitride Using Sequential, Self-Limiting Hydrogen Fluoride and Sn(Acac) 2 Reactions and Enhancement by H 2 and Ar Plasmas. *J. Vac. Sci. Technol. A* **2016**, *34* (5), 050603. https://doi.org/10.1116/1.4959779.

(24) Jung, J. H.; Oh, H.; Shong, B. Fluorination of TiN, TiO2, and SiO2 Surfaces by HF toward Selective Atomic Layer Etching (ALE). *Coatings 2023, Vol. 13, Page 387* **2023**, *13* (2), 387. https://doi.org/10.3390/COATINGS13020387.

(25) Shinoda, K.; Miyoshi, N.; Kobayashi, H.; Izawa, M.; Ishikawa, K.; Hori, M. Rapid Thermal-Cyclic Atomic-Layer Etching of Titanium Nitride in CHF3/O2 Downstream Plasma. *J. Phys. D Appl. Phys.* **2019**, *52* (47), 475106. https://doi.org/10.1088/1361-6463/ab3cf3.

(26) Lee, Y.; George, S. M. Thermal Atomic Layer Etching of Titanium Nitride Using Sequential, Self-Limiting Reactions: Oxidation to TiO2 and Fluorination to Volatile TiF4. *Chem. Mater.* **2017**, *29* (19), 8202–8210. https://doi.org/10.1021/acs.chemmater.7b02286.

(27) Sharma, V.; Kondati Natarajan, S.; Elliott, S. D.; Blomberg, T.; Haukka, S.; Givens, M. E.; Tuominen, M.; Ritala, M. Combining Experimental and DFT Investigation of the Mechanism Involved in Thermal Etching of Titanium Nitride Using Alternate Exposures of NbF5 and CCl4, or CCl4 Only. *Adv. Mater. Interfaces* **2021**, *8*, 2101085. https://doi.org/10.1002/admi.202101085.

(28) Chittock, N. J.; Shu, Y.; Elliott, S. D.; M Knoops, H. C.; M Kessels, W. M.; M Mackus, A. J.; Phys Lett, A. Isotropic Atomic Layer Etching of GaN Using SF6 Plasma and Al(CH3)3. *J. Appl. Phys.* **2023**, *134* (7), 075302. https://doi.org/10.1063/5.0158129.

(29) Johnson, N. R.; Hite, J. K.; Mastro, M. A.; Eddy, C. R.; George, S. M. Thermal Atomic Layer Etching of Crystalline GaN Using Sequential Exposures of XeF2 and BCl3. *Appl. Phys. Lett.* **2019**, *114* (24), 243103. https://doi.org/10.1063/1.5095938/594370.

(30) Mohimi, E.; Chu, X. I.; Trinh, B. B.; Babar, S.; Girolami, G. S.; Abelson, J. R. Thermal Atomic Layer Etching of Copper by Sequential Steps Involving Oxidation and Exposure to Hexafluoroacetylacetone. *ECS J. Solid State Sci. Technol.* **2018**, *7* (9), P491–P495. https://doi.org/10.1149/2.0211809JSS/XML.

(31) Xie, W.; Lemaire, P. C.; Parsons, G. N. Thermally Driven Self-Limiting Atomic Layer Etching of Metallic Tungsten Using WF6 and O2. *ACS Appl. Mater. Interfaces* **2018**, *10* (10), 9147–9154. https://doi.org/10.1021/acsami.7b19024.

(32) Xie, W.; Parsons, G. N. Thermal Atomic Layer Etching of Metallic Tungsten via Oxidation and Etch Reaction Mechanism Using O2 or O3 for Oxidation and WCl6 as the Chlorinating Etchant. *J. Vac. Sci. Technol. A* **2020**, *38* (2), 22605. https://doi.org/10.1116/1.5134430/15855650/022605_1_ACCEPTED_MANUSCRIPT.PDF.

(33) Fang, C.; Cao, Y.; Wu, D.; Li, A. Thermal Atomic Layer Etching: Mechanism, Materials and Prospects. *Prog. Nat. Sci-Mater.* **2018**, *28* (6), 667–675. https://doi.org/https://doi.org/10.1016/j.pnsc.2018.11.003.

(34) T. Carver, C.; J. Plombon, J.; E. Romero, P.; Suri, S.; A. Tronic, T.; B. Turkot, R. Atomic Layer Etching: An Industry Perspective. *ECS Journal of Solid State Science and Technology* **2015**, *4* (6), N5005–N5009. https://doi.org/10.1149/2.0021506jss.

(35) George, S. M. Mechanisms of Thermal Atomic Layer Etching. *Accounts Chem. Res.* **2020**, *53* (6), 1151–1160. https://doi.org/10.1021/acs.accounts.0c00084.

(36) Raghu, P.; Yim, C.; Shadman, F.; Shero, E. Susceptibility of SiO2, ZrO2, and HfO2 Dielectrics to Moisture Contamination. *AIChE J.* **2004**, *50*, 1881–1888. https://doi.org/10.1002/aic.10148.

(37) Raghu, P.; Rana, N.; Yim, C.; Shero, E.; Shadman, F. Adsorption of Moisture and Organic Contaminants on Hafnium Oxide, Zirconium Oxide, and Silicon Oxide Gate Dielectrics. *J Electrochem Soc* **2003**, *150* (10), F186. https://doi.org/10.1149/1.1605747/XML.

(38) Hausmann, D. M.; Kim, E.; Becker, J.; Gordon, R. G. Atomic Layer Deposition of Hafnium and Zirconium Oxides Using Metal Amide Precursors. *Chem. Mater.* **2002**, *14* (10), 4350–4358. https://doi.org/10.1021/cm020357x.

(39) Lee, Y.; DuMont, J. W.; George, S. M. Atomic Layer Etching of HfO 2 Using Sequential, Self-Limiting Thermal Reactions with Sn(Acac) 2 and HF. *ECS J. Solid State Sci. Technol.* **2015**, *4* (6), N5013–N5022. https://doi.org/10.1149/2.0041506jss.

(40) Gasvoda, R. J.; Zhang, Z.; Hudson, E. A.; Agarwal, S. Gas-Phase Surface Functionalization of SiN x with Benzaldehyde to Increase SiO 2 to SiN x Etch Selectivity in Atomic Layer Etching. *J. Vac. Sci. Technol. A* **2021**, *39*, 40401. https://doi.org/10.1116/6.0001046.

(41) Abdulagatov, A. I.; George, S. M. Thermal Atomic Layer Etching of Silicon Nitride Using an Oxidation and "Conversion Etch" Mechanism. *J. Vac. Sci. Technol. A* **2020**, *38* (2), 022607. https://doi.org/10.1116/1.5140481.

(42) Abdulagatov, A. I.; Sharma, V.; Murdzek, J. A.; Cavanagh, A. S.; George, S. M. Thermal Atomic Layer Etching of Germanium-Rich SiGe Using an Oxidation and "Conversion-Etch" Mechanism. *J. Vac. Sci. Technol. A* **2021**, *39* (2), 22602. https://doi.org/10.1116/6.0000834/13671496/022602_1_ACCEPTED_MANUSCRIPT.PDF.

(43) Hennessy, J.; Moore, C. S.; Balasubramanian, K.; Jewell, A. D.; France, K.; Nikzad, S. Enhanced Atomic Layer Etching of Native Aluminum Oxide for Ultraviolet Optical Applications. *J. Vac. Sci. Technol. A* **2017**, *35* (4), 041512. https://doi.org/10.1116/1.4986945.

(44) Hennessy, J.; Jewell, A. D.; Jones, J. P.; Crouch, G. M.; Nikzad, S. Aluminum Precursor Interactions with Alkali Compounds in Thermal Atomic Layer Etching and Deposition Processes. *ACS Appl. Mater. Interfaces* **2021**, *13* (3), 4723–4730. https://doi.org/10.1021/acsami.0c19399.

(45) Fischer, A.; Routzahn, A.; Lee, Y.; Lill, T.; George, S. M. Thermal Etching of AlF 3 and Thermal Atomic Layer Etching of Al 2 O 3. *J. Vac. Sci. Technol. A* **2020**, *38* (2), 022603. https://doi.org/10.1116/1.5135911.

(46) Clancey, J. W.; Cavanagh, A. S.; Smith, J. E. T.; Sharma, S.; George, S. M. Volatile Etch Species Produced during Thermal Al2O3Atomic Layer Etching. *J. Phys. Chem. C* **2020**, *124* (1), 287–299. https://doi.org/10.1021/ACS.JPCC.9B06104/ASSET/IMAGES/MEDIUM/JP9B06104_0017.GIF.

(47) DuMont, J. W.; George, S. M. Competition between Al2O3 Atomic Layer Etching and AlF3 Atomic Layer Deposition Using Sequential Exposures of Trimethylaluminum and Hydrogen Fluoride. *J. Chem. Phys.* **2017**, *146* (5), 052819. https://doi.org/10.1063/1.4973310.

(48) Fischer, A.; Routzahn, A.; Wen, S.; Lill, T. Causes of Anisotropy in Thermal Atomic Layer Etching of Nanostructures. *J. Vac. Sci. Technol. A* **2020**, *38* (4), 042601. https://doi.org/10.1116/6.0000261/246949.

(49) Rahman, R.; Mattson, E. C.; Klesko, J. P.; Dangerfield, A.; Rivillon-Amy, S.; Smith, D. C.; Hausmann, D.; Chabal, Y. J. Thermal Atomic Layer Etching of Silica and Alumina Thin Films Using Trimethylaluminum with Hydrogen Fluoride or Fluoroform. *ACS Appl. Mater. Interfaces* **2018**, *10* (37), 31784–31794. https://doi.org/10.1021/acsami.8b10899.

(50) Zywotko, D. R.; Faguet, J.; George, S. M. Rapid Atomic Layer Etching of Al2O3 Using Sequential Exposures of Hydrogen Fluoride and Trimethylaluminum with No Purging. *J. Vac. Sci. Technol. A* **2018**, *36* (6), 061508. https://doi.org/10.1116/1.5043488/15849044/061508_1_ACCEPTED_MANUSCRIPT.PDF.

(51) Lee, Y.; Dumont, J. W.; George, S. M. Atomic Layer Etching of AlF3 Using Sequential, Self-Limiting Thermal Reactions with Sn(Acac)2 and Hydrogen Fluoride. *J. Phys. Chem. C* **2015**, *119* (45), 25385–25393. https://doi.org/10.1021/ACS.JPCC.5B07236/ASSET/IMAGES/MEDIUM/JP-2015-07236K_0014.GIF.

(52) Lemaire, P. C.; Parsons, G. N. Thermal Selective Vapor Etching of TiO2: Chemical Vapor Etching via WF6 and Self-Limiting Atomic Layer Etching Using WF6 and BCl3. *Chem. Mater.* **2017**, *29* (16), 6653–6665. https://doi.org/10.1021/acs.chemmater.7b00985.

(53) Kondati Natarajan, S.; Cano, A. M.; Partridge, J. L.; George, S. M.; Elliott, S. D. Prediction and Validation of the Process Window for Atomic Layer Etching: HF Exposure on TiO2. *J. Phys. Chem. C* **2021**, *125* (46), 25589–25599. https://doi.org/10.1021/ACS.JPCC.1C08110/SUPPL_FILE/JP1C08110_SI_001.PDF.

(54) Song, S. K.; Saare, H.; Parsons, G. N. Integrated Isothermal Atomic Layer Deposition/Atomic Layer Etching Supercycles for Area-Selective Deposition of TiO2. *Chem. Mater.* **2019**, *31* (13), 4793–4804. https://doi.org/10.1021/ACS.CHEMMATER.9B01143/SUPPL_FILE/CM9B01143_SI_001.PDF.

(55) Gertsch, J. C.; Cano, A. M.; Bright, V. M.; George, S. M. SF4 as the Fluorination Reactant for Al2O3 and VO2 Thermal Atomic Layer Etching. *Chem. Mater.* **2019**, *31* (10), 3624–3635. https://doi.org/10.1021/acs.chemmater.8b05294.

(56) Abdulagatov, A. I.; George, S. M. Thermal Atomic Layer Etching of Silicon Using O2, HF, and Al(CH3)3 as the Reactants. *Chem. Mater.* **2018**, *30* (23), 8465–8475. https://doi.org/10.1021/ACS.CHEMMATER.8B02745/ASSET/IMAGES/MEDIUM/CM-2018-02745G_0016.GIF.

(57) Ibbotson, D. E.; Mucha, J. A.; Flamm, D. L.; Cook, J. M. Plasmaless Dry Etching of Silicon with Fluorine-containing Compounds. *J. Appl. Phys.* **1984**, *56* (10), 2939–2942. https://doi.org/10.1063/1.333834.

(58) Imái, S.; Haga1, T.; Matsuzaki, O.; Hattori, T.; Matsumura, M. Atomic Layer Etching of Silicon by Thermal Desorption Method. *Jpn. J. Appl. Phys.* **1995**, *34* (9R), 5049–5053. https://doi.org/10.1143/JJAP.34.5049/XML.

(59) Ikeda, K.; Imai, S.; Matsumura, M. Atomic Layer Etching of Germanium. *Appl. Surf. Sci.* **1997**, *112*, 87–91. https://doi.org/10.1016/S0169-4332(96)00995-6.

(60) Konh, M.; He, C.; Lin, X.; Guo, X.; Pallem, V.; Opila, R. L.; Teplyakov, A. V.; Wang, Z.; Yuan, B. Molecular Mechanisms of Atomic Layer Etching of Cobalt with Sequential Exposure to Molecular Chlorine and Diketones. *J. Vac. Sci. Technol. A* **2019**, *37* (2), 21004. https://doi.org/10.1116/1.5082187/247181.

(61) Zhao, J.; Konh, M.; Teplyakov, A. Surface Chemistry of Thermal Dry Etching of Cobalt Thin Films Using Hexafluoroacetylacetone (HfacH). *Appl. Surf. Sci.* **2018**, *455*, 438–445. https://doi.org/10.1016/J.APSUSC.2018.05.182.

(62) Johnson, N. R.; George, S. M. WO3 and W Thermal Atomic Layer Etching Using "Conversion-Fluorination" and "Oxidation-Conversion-Fluorination" Mechanisms. *ACS Appl. Mater. Interfaces* **2017**, *9* (39), 34435–34447. https://doi.org/10.1021/acsami.7b09161.

(63) Basher, A. H.; Krstić, M.; Fink, K.; Ito, T.; Karahashi, K.; Wenzel, W.; Hamaguchi, S. Formation and Desorption of Nickel Hexafluoroacetylacetonate Ni(Hfac)2 on a Nickel Oxide Surface in Atomic Layer Etching Processes. *J. Vac. Sci. Technol. A* **2020**, *38* (5), 52602. https://doi.org/10.1116/6.0000293/246825.

(64) Mameli, A.; Verheijen, M. A.; Mackus, A. J. M.; Kessels, W. M. M.; Roozeboom, F. Isotropic Atomic Layer Etching of ZnO Using Acetylacetone and O 2 Plasma. *ACS Appl. Mater. Interfaces* **2018**, *10* (44), 38588–38595. https://doi.org/10.1021/acsami.8b12767.

(65) Cano, A. M.; Kondati Natarajan, S.; Partridge, J. L.; Elliott, S. D.; George, S. M. Spontaneous Etching of B2O3 by HF Gas Studied Using Infrared Spectroscopy, Mass Spectrometry, and Density Functional Theory. *J. Vac. Sci. Technol. A* **2022**, *40* (2), 022601. https://doi.org/10.1116/6.0001542/2843646.

(66) Lin, X.; Chen, M.; Janotti, A.; Opila, R. In Situ XPS Study on Atomic Layer Etching of Fe Thin Film Using Cl2 and Acetylacetone. *J. Vac. Sci. Technol. A* **2018**, *36* (5), 51401. https://doi.org/10.1116/1.5039517/16686186/051401_1_ACCEPTED_MANUSCRIPT.PDF.

(67) Lu, W.; Lee, Y.; Gertsch, J. C.; Murdzek, J. A.; Cavanagh, A. S.; Kong, L.; Del Alamo, J. A.; George, S. M. In Situ Thermal Atomic Layer Etching for Sub-5 Nm InGaAs Multigate MOSFETs. *Nano Lett.* **2019**, *19* (8), 5159–5166. https://doi.org/10.1021/ACS.NANOLETT.9B01525/SUPPL_FILE/NL9B01525_SI_001.PDF.

(68) Kim, K. S.; Kim, K. H.; Nam, Y.; Jeon, J.; Yim, S.; Singh, E.; Lee, J. Y.; Lee, S. J.; Jung, Y. S.; Yeom, G. Y.; Kim, D. W. Atomic Layer Etching Mechanism of MoS2 for Nanodevices. *ACS Appl Mater Interfaces* **2017**, *9* (13), 11967–11976. https://doi.org/10.1021/acsami.6b15886.

(69) Kauppinen, C.; Khan, S. A.; Sundqvist, J.; Suyatin, D. B.; Suihkonen, S.; Kauppinen, E. I.; Sopanen, M. Atomic Layer Etching of Gallium Nitride (0001). *J. Vac. Sci. Technol. A* **2017**, *35* (6), 060603. https://doi.org/10.1116/1.4993996.

(70) Lin, K.-Y.; Li, C.; Engelmann, S.; Bruce, R. L.; Joseph, E. A.; Metzler, D.; Oehrlein, G. S. Achieving Ultrahigh Etching Selectivity of SiO2 over Si3N4 and Si in Atomic Layer Etching by Exploiting Chemistry of Complex Hydrofluorocarbon Precursors. *J. Vac. Sci. Technol. A* **2018**, *36* (4), 040601. https://doi.org/10.1116/1.5035291.

(71) Wang, X.; Wang, M.; Biolsi, P.; Kushner, M. J. Scaling of Atomic Layer Etching of SiO2 in Fluorocarbon Plasmas: Transient Etching and Surface Roughness. *J. Vac. Sci. Technol. A* **2021**, *39* (3), 033003. https://doi.org/10.1116/6.0000941.

(72) Hirata, A.; Fukasawa, M.; Kugimiya, K.; Nagaoka, K.; Karahashi, K.; Hamaguchi, S.; Iwamoto, H. Mechanism of SiN Etching Rate Fluctuation in Atomic Layer Etching. *J. Vac. Sci. Technol. A* **2020**, *38* (6), 062601. https://doi.org/10.1116/6.0000257.

(73) Lii-Rosales, A.; Johnson, V. L.; Sharma, S.; Fischer, A.; Lill, T.; George, S. M. Volatile Products from Ligand Addition of P(CH3)3to NiCl2, PdCl2, and PtCl2: Pathway for Metal Thermal Atomic Layer Etching. *J. Phys. Chem. C* **2022**, *126* (19), 8287–8295. https://doi.org/10.1021/acs.jpcc.1c10690.

(74) Lee, Y.; DuMont, J. W.; George, S. M. Mechanism of Thermal Al2O3 Atomic Layer Etching Using Sequential Reactions with Sn(Acac)2 and HF. *Chem. Mater.* **2015**, *27* (10), 3648–3657. https://doi.org/10.1021/ACS.CHEMMATER.5B00300.

(75) Walsh, R. Bond Dissociation Energy Values in Silicon-Containing Compounds and Some of Their Implications. *Acc. Chem. Res.* **1981**, *14* (8), 246–252. https://doi.org/10.1021/AR00068A004/ASSET/AR00068A004.FP.PNG_V03.

(76) A; Roine. Outokumpu HSC Chemistry for Windows, Version 5.1. 2002.

(77) Zywotko, D. R.; Zandi, O.; Faguet, J.; Abel, P. R.; George, S. M. ZrO2 Monolayer as a Removable Etch Stop Layer for Thermal Al2O3Atomic Layer Etching Using Hydrogen Fluoride and Trimethylaluminum. *Chem. Mater.* **2020**, *32* (23), 10055–10065. https://doi.org/10.1021/ACS.CHEMMATER.0C03335/ASSET/IMAGES/LARGE/CM0C03335_0015.JPEG.

(78) Batisse, N.; Guérin, K.; Dubois, M.; Hamwi, A.; Spinelle, L.; Tomasella, E. Fluorination of Silicon Carbide Thin Films Using Pure F2 Gas or XeF2. *Thin Solid Films* **2010**, *518* (23), 6746–6751. https://doi.org/10.1016/J.TSF.2010.05.120.

(79) Tramšek, M.; Žemva, B. Synthesis, Properties and Chemistry of Xenon (II) Fluoride. *Acta Chim Slov* **2006**, *53* (2), 105–116. https://doi.org/10.1002/chin.200721209.

(80) Fischer, A.; Mui, D.; Routzahn, A.; Gasvoda, R.; Sims, J.; Lill, T. Surface Reaction Modelling of Thermal Atomic Layer Etching on Blanket Hafnium Oxide and Its Application on High Aspect Ratio Structures. *J. Vac. Sci. Technol. A* **2023**, *41* (1), 12601. https://doi.org/10.1116/6.0002244/2871799.

(81) Lii-Rosales, A.; Cavanagh, A. S.; Fischer, A.; Lill, T.; George, S. M. Spontaneous Etching of Metal Fluorides Using Ligand-Exchange Reactions: Landscape Revealed by Mass Spectrometry. *Chem. Mater.* **2021**, *33* (19), 7719–7730. https://doi.org/10.1021/acs.chemmater.1c01950.

(82) Lii-Rosales, A.; Johnson, V. L.; Cavanagh, A. S.; Fischer, A.; Lill, T.; Sharma, S.; George, S. M. Effectiveness of Different Ligands on Silane Precursors for Ligand Exchange to Etch Metal Fluorides. *Chem. Mater.* **2022**, *34* (19), 8641–8653. https://doi.org/10.1021/ACS.CHEMMATER.2C01603/SUPPL_FILE/CM2C01603_SI_001.PDF.

(83) Berthold, H. J.; Groh, G. Preparation of Tetramethylzirconium, Zr(CH3)4. *Angew. Chem., Int. Ed. Engl.* **1966**, *5* (5), 516–516. https://doi.org/10.1002/ANIE.196605162.

(84) Kondati Natarajan, S.; Elliott, S. D. Modeling the Chemical Mechanism of the Thermal Atomic Layer Etch of Aluminum Oxide: A Density Functional Theory Study of Reactions during HF Exposure. *Chem. Mater.* **2018**, *30* (17), 5912–5922. https://doi.org/10.1021/acs.chemmater.8b01930.

(85) Sharma, V.; Elliott, S. D.; Blomberg, T.; Haukka, S.; Givens, M. E.; Tuominen, M.; Ritala, M. Thermal Atomic Layer Etching of Aluminum Oxide (Al2O3) Using Sequential Exposures of Niobium Pentafluoride (NbF5) and Carbon Tetrachloride (CCl4): A Combined Experimental and Density Functional Theory Study of the Etch Mechanism. *Chem. Mater.* **2021**, *33* (8), 2883–2893. https://doi.org/10.1021/acs.chemmater.1c00142.

(86) Hu, X.; Schuster, J. Chemical Mechanism of AlF3 Etching during AlMe3 Exposure: A Thermodynamic and DFT Study. *J. Phys. Chem. C* **2022**, *126* (17), 7410–7420. https://doi.org/10.1021/acs.jpcc.2c00158.

(87) Hidayat, R.; Kim, H. L.; Khumaini, K.; Chowdhury, T.; Mayangsari, T. R.; Cho, B.; Park, S.; Lee, W. J. Selective Etching Mechanism of Silicon Oxide against Silicon by Hydrogen Fluoride: A Density Functional Theory Study. *Phys. Chem. Chem. Phys.* **2023**, *25* (5), 3890–3899. https://doi.org/10.1039/d2cp05456f.

(88) Natarajan, S. K.; Nolan, M.; Theofanis, P.; Mokhtarzadeh, C.; Clendenning, S. B. In Silico Design of a Thermal Atomic Layer Etch Process of Cobalt. *J. Vac. Sci. Technol. A* **2021**, *39* (2), 022603. https://doi.org/10.1116/6.0000804.

(89) Natarajan, S. K.; Nolan, M.; Theofanis, P.; Mokhtarzadeh, C.; Clendenning, S. B. Mechanism of Thermal Atomic Layer Etch of W Metal Using Sequential Oxidation and Chlorination: A First-Principles Study. *ACS Appl. Mater. Interfaces* **2020**, *12*, 36680. https://doi.org/10.1021/acsami.0c06628.

(90) Rossnagel, S. M. Thin Film Deposition with Physical Vapor Deposition and Related Technologies. *Journal of Vacuum Science & Technology A: Vacuum, Surfaces, and Films* **2003**, *21* (5), S74. https://doi.org/10.1116/1.1600450.

(91) George, S. M. Atomic Layer Deposition: An Overview. *Chem Rev* **2010**, *110* (1), 111–131. https://doi.org/10.1021/cr900056b.

(92) Oviroh, P. O.; Akbarzadeh, R.; Pan, D.; Coetzee, R. A. M.; Jen, T. C. New Development of Atomic Layer Deposition: Processes, Methods and Applications. *Science and Technology of Advanced Materials*. Taylor & Francis December 31, 2019, pp 465–496. https://doi.org/10.1080/14686996.2019.1599694.

(93) Shahmohammadi, M.; Mukherjee, R.; Sukotjo, C.; Diwekar, U. M.; Takoudis, C. G. Recent Advances in Theoretical Development of Thermal Atomic Layer Deposition: A Review. *Nanomaterials* **2022**, *12* (5), 831. https://doi.org/10.3390/nano12050831.

(94) Graef, E.; Huizing, B.; Mahnkopf, R. 2015 International Technology Roadmap for Semiconductors (ITRS) - Semiconductor Industry Association. *International Technology Roadmap forSemiconductors 2.0* **2015**.

(95) Lane, M.; Dauskardt, R. H.; Krishna, N.; Hashim, I. Adhesion and Reliability of Copper Interconnects with Ta and TaN Barrier Layers. *J Mater Res* **2000**, *15* (1), 203–211. https://doi.org/10.1557/JMR.2000.0033.

(96) Kondati Natarajan, S.; Nies, C. L.; Nolan, M. The Role of Ru Passivation and Doping on the Barrier and Seed Layer Properties of Ru-Modified TaN for Copper Interconnects. *J. Chem. Phys.* **2020**, *152* (14), 144701. https://doi.org/10.1063/5.0003852.

(97) Wu, Z.; Li, R.; Xie, X.; Suen, W.; Tseng, J.; Bekiaris, N.; Vinnakota, R.; Kashefizadeh, K.; Naik, M. PVD- Treated ALD TaN for Cu Interconnect Extension to 5nm Node and Beyond. *2018 IEEE International Interconnect Technology Conference, IITC 2018* **2018**, 149–151. https://doi.org/10.1109/IITC.2018.8430433.

(98) Kotsugi, Y.; Han, S. M.; Kim, Y. H.; Cheon, T.; Nandi, D. K.; Ramesh, R.; Yu, N. K.; Son, K.; Tsugawa, T.; Ohtake, S.; Harada, R.; Park, Y. B.; Shong, B.; Kim, S. H. Atomic Layer Deposition of Ru for Replacing Cu-Interconnects. *Chem. Mater.* **2021**, *33* (14), 5639–5651. https://doi.org/10.1021/acs.chemmater.1c01054.

(99) Kondati Natarajan, S.; Nies, C. L.; Nolan, M. Ru Passivated and Ru Doped ϵ-TaN Surfaces as a Combined Barrier and Liner Material for Copper Interconnects: A First Principles Study. *J. Mater. Chem. C* **2019**, *7* (26), 7959–7973. https://doi.org/10.1039/c8tc06118a.

(100) Nies, C. L.; Nolan, M. Incorporation of Tungsten or Cobalt into TaN Barrier Layers Controls Morphology of Deposited Copper. *J. Phys. Mater.* **2023**, *6* (3), 035008. https://doi.org/10.1088/2515-7639/acdeaa.

(101) Nies, C. L.; Natarajan, S. K.; Nolan, M. Control of the Cu Morphology on Ru-Passivated and Ru-Doped TaN Surfaces – Promoting Growth of 2D Conducting Copper for CMOS Interconnects. *Chem. Sci.* **2022**, *13* (3), 713–725. https://doi.org/10.1039/D1SC04708F.

(102) Bonvalot, M.; Vallée, C.; Mannequin, C.; Jaffal, M.; Gassilloud, R.; Possémé, N.; Chevolleau, T. Area Selective Deposition Using Alternate Deposition and Etch Super-Cycle Strategies. *Dalton Trans* **2022**, *51* (2), 442–450. https://doi.org/10.1039/D1DT03456A.

(103) Mackus, A. J. M.; Schneider, J. R.; Macisaac, C.; Baker, J. G.; Bent, S. F. Synthesis of Doped, Ternary, and Quaternary Materials by Atomic Layer Deposition: A Review. *Chem. Mater.* **2019**, *31* (4), 1142–1183. https://doi.org/10.1021/ACS.CHEMMATER.8B02878/ASSET/IMAGES/MEDIUM/CM-2018-02878X_0012.GIF.

(104) Vos, M. F. J.; Chopra, S. N.; Ekerdt, J. G.; Agarwal, S.; Kessels, W. M. M. (Erwin); Mackus, A. J. M. Atomic Layer Deposition and Selective Etching of Ruthenium for Area-Selective Deposition: Temperature Dependence and Supercycle Design. *J. Vac. Sci. Technol. A* **2021**, *39* (3), 032412. https://doi.org/10.1116/6.0000912.

(105) Nam, T.; Lee, C. W.; Cheon, T.; Lee, W. J.; Kim, S. H.; Kwon, S. H.; Lee, H. B. R.; Kim, H. Cobalt Titanium Nitride Amorphous Metal Alloys by Atomic Layer Deposition. *J. Alloy. Comd.* **2018**, *737*, 684–692. https://doi.org/10.1016/J.JALLCOM.2017.12.023.

(106) Wen, L. G.; Roussel, P.; Pedreira, O. V.; Briggs, B.; Groven, B.; Dutta, S.; Popovici, M. I.; Heylen, N.; Ciofi, I.; Vanstreels, K.; Østerberg, F. W.; Hansen, O.; Petersen, D. H.; Opsomer, K.; Detavernie, C.; Wilson, C. J.; Elshocht, S. Van; Croes, K.; Bömmels, J.; Tökei, Z.; Adelmann, C. Atomic Layer Deposition of Ruthenium with TiN Interface for Sub-10 Nm Advanced Interconnects beyond Copper. *ACS Appl Mater Interfaces* **2016**, *8* (39), 26119–26125. https://doi.org/10.1021/acsami.6b07181.

(107) International Roadmap for Devices and Systems (IRDS™). 2020. https://irds.ieee.org/editions/2020 (accessed 2023-06-26).

(108) Plombon, J. J.; Andideh, E.; Dubin, V. M.; Maiz, J. Influence of Phonon, Geometry, Impurity, and Grain Size on Copper Line Resistivity. *Appl Phys Lett* **2006**, *89* (11), 113124. https://doi.org/10.1063/1.2355435.

(109) Mont, F. W.; Zhang, X.; Wang, W.; Kelly, J. J.; Standaert, T. E.; Quon, R.; Ryan, E. T. Cobalt Interconnect on Same Copper Barrier Process Integration at the 7nm Node. In *IITC 2017 - 2017 IEEE International Interconnect Technology Conference*; Institute of Electrical and Electronics Engineers Inc., 2017. https://doi.org/10.1109/IITC-AMC.2017.7968971.

(110) Aaltonen, T.; Ritala, M.; Tung, Y. L.; Chi, Y.; Arstila, K.; Meinander, K.; Leskelä, M. Atomic Layer Deposition of Noble Metals: Exploration of the Low Limit of the Deposition Temperature. *J. Mater. Res.* **2004**, *19* (11), 3353–3358. https://doi.org/10.1557/JMR.2004.0426.

(111) Färm, E.; Lindroos, S.; Ritala, M.; Leskelä, M. Microcontact Printed RuOx Film as an Activation Layer for Selective-Area Atomic Layer Deposition of Ruthenium. *Chem. Mater.* **2012**, *24* (2), 275–278. https://doi.org/10.1021/CM202468S.

(112) Montague, J. R.; Dalberth, M.; Gray, J. M.; Seghete, D.; Bertness, K. A.; George, S. M.; Bright, V. M.; Rogers, C. T.; Sanford, N. A. Analysis of High-Q, Gallium Nitride Nanowire Resonators in Response to Deposited Thin Films. *Sensor. Actuat. A-Phys.* **2011**, *165* (1), 59–65. https://doi.org/10.1016/J.SNA.2010.03.014.

(113) Park, K. J.; Terry, D. B.; Stewart, S. M.; Parsons, G. N. In Situ Auger Electron Spectroscopy Study of Atomic Layer Deposition: Growth Initiation and Interface Formation Reactions during Ruthenium ALD on Si-H, SiO2, and HfO2 Surfaces. *Langmuir* **2007**, *23* (11), 6106–6112. https://doi.org/10.1021/la061898u.

(114) Lee, D. J.; Yim, S. S.; Kim, K. S.; Kim, S. H.; Kim, K. B. Formation of Ru Nanotubes by Atomic Layer Deposition onto an Anodized Aluminum Oxide Template. *Electrochem. Solid-State Lett.* **2008**, *11* (6), K61. https://doi.org/10.1149/1.2901542/XML.

(115) Kwon, O.-K.; Kwon, S.-H.; Park, H.-S.; Kang, S.-W. PEALD of a Ruthenium Adhesion Layer for Copper Interconnects. *J. Electrochem. Soc.* **2004**, *151* (12), C753. https://doi.org/10.1149/1.1809576/XML.

(116) Kwon, S.-H.; Kwon, O.-K.; Kim, J.-H.; Jeong, S.-J.; Kim, S.-W.; Kang, S.-W. Improvement of the Morphological Stability by Stacking RuO2 on Ru Thin Films with Atomic Layer Deposition. *J. Electrochem. Soc.* **2007**, *154* (9), H773. https://doi.org/10.1149/1.2750448/XML.

(117) Yim, S. S.; Lee, D. J.; Kim, K. S.; Kim, S. H.; Yoon, T. S.; Kim, K. B. Nucleation Kinetics of Ru on Silicon Oxide and Silicon Nitride Surfaces Deposited by Atomic Layer Deposition. *J. Appl. Phys.* **2008**, *103* (11), 113509. https://doi.org/10.1063/1.2938052.

(118) Kukli, K.; Aarik, J.; Aidla, A.; Uustare, T.; Jgi, I.; Lu, J.; Tallarida, M.; Kemell, M.; Kiisler, A. A.; Ritala, M.; Leskel, M. Structure and Morphology of Ru Films Grown by Atomic Layer Deposition from 1-Ethyl-1'-Methyl-Ruthenocene. *J. Cryst. Growth* **2010**, *312* (12–13), 2025–2032. https://doi.org/10.1016/J.JCRYSGRO.2010.03.033.

(119) Methaapanon, R.; Geyer, S. M.; Lee, H. B. R.; Bent, S. F. The Low Temperature Atomic Layer Deposition of Ruthenium and the Effect of Oxygen Exposure. *J. Mater. Chem.* **2012**, *22* (48), 25154–25160. https://doi.org/10.1039/C2JM35332F.

(120) van der Straten, O.; Rossnagel, S. M.; Doyle, J. P.; Rodbell, K. P. Metal-Organic Atomic Layer Deposition of Metals for Applications in Interconnect Technology. *ECS Trans.* **2006**, *1* (10), 51–56. https://doi.org/10.1149/1.2209329/XML.

(121) Choi, S.-H.; Cheon, T.; Kim, S.-H.; Kang, D.-H.; Park, G.-S.; Kim, S. Thermal Atomic Layer Deposition (ALD) of Ru Films for Cu Direct Plating. *J. Electrochem. Soc.* **2011**, *158* (6), D351. https://doi.org/10.1149/1.3575163/XML.

(122) Leick, N.; Agarwal, S.; MacKus, A. J. M.; Kessels, W. M. M. Dehydrogenation Reactions during Atomic Layer Deposition of Ru Using O2. *Chem. Mater.* **2012**, *24* (19), 3696–3700. https://doi.org/10.1021/CM301115S.

(123) Bernal Ramos, K.; Saly, M. J.; Chabal, Y. J. Precursor Design and Reaction Mechanisms for the Atomic Layer Deposition of Metal Films. *Coord Chem Rev* **2013**, *257* (23–24), 3271–3281. https://doi.org/10.1016/j.ccr.2013.03.028.

(124) Schaekers, M.; Capon, B.; Detavernier, C.; Blasco, N. The Deposition of Ru and RuO2 Films for DRAM Electrode. *ECS Trans* **2010**, *33* (2), 135–144. https://doi.org/10.1149/1.3485250/XML.

(125) Smirnova, E. A.; Miakonkikh, A. V.; Rogozhin, A. E.; Rudenko, K. V. Atomic Layer Deposition of Ruthenium on Different Interfaces for an Advanced Metallization System of ICs. *J. Phys.: Conf. Ser.* **2020**, *1695* (1), 012045. https://doi.org/10.1088/1742-6596/1695/1/012045.

(126) Xie, Q.; Musschoot, J.; Detavernier, C.; Deduytsche, D.; Van Meirhaeghe, R. L.; Jiang, Y. L.; Ru, G. P.; Li, B. Z.; Qu, X. P. Comparison of the Ru Thin Films Grown on Si, TiN/Si and TaN/Si Substrates by Plasma Enhanced Atomic Layer Deposition. *International Conference on Solid-State and Integrated Circuits Technology Proceedings, ICSICT* **2008**, 1231–1234. https://doi.org/10.1109/ICSICT.2008.4734770.

(127) Kwon, O. K.; Kim, J. H.; Park, H. S.; Kang, S. W. Atomic Layer Deposition of Ruthenium Thin Films for Copper Glue Layer. *J. Electrochem. Soc.* **2004**, *151* (2), G109. https://doi.org/10.1149/1.1640633/XML.

(128) Rogozhin, A.; Miakonkikh, A.; Smirnova, E.; Lomov, A.; Simakin, S.; Rudenko, K. Plasma Enhanced Atomic Layer Deposition of Ruthenium Films Using Ru(Etcp)2 Precursor. *Coatings* **2021**, *11* (2), 1–11. https://doi.org/10.3390/coatings11020117.

(129) Müller, R.; Ghazaryan, L.; Schenk, P.; Wolleb, S.; Beladiya, V.; Otto, F.; Kaiser, N.; Tünnermann, A.; Fritz, T.; Szeghalmi, A. Growth of Atomic Layer Deposited Ruthenium and Its Optical Properties at Short Wavelengths Using Ru(EtCp)2 and Oxygen. *Coatings 2018, Vol. 8, Page 413* **2018**, *8* (11), 413. https://doi.org/10.3390/COATINGS8110413.

(130) Wang, Z.; Sakaue, H.; Shingubara, S.; Takahagi, T. Influence of Surface Oxide of Sputtered TaN on Displacement Plating of Cu. *Jpn J Appl Phys* **2003**, *42* (4 B), 1843–1846. https://doi.org/10.1143/jjap.42.1843.

(131) Lee, S. J.; Kim, S. H. Effects of Annealing on the Properties of Atomic Layer Deposited Ru Thin Films Deposited by NH3 and H2 as Reactants. *Thin Solid Films* **2016**, *612*, 122–127. https://doi.org/10.1016/J.TSF.2016.05.048.

(132) Jiang, X.; Gür, T. M.; Prinz, F. B.; Bent, S. F. Atomic Layer Deposition (ALD) Co-Deposited Pt-Ru Binary and Pt Skin Catalysts for Concentrated Methanol Oxidation. *Chem. Mater.* **2010**, *22* (10), 3024–3032. https://doi.org/10.1021/CM902904U/SUPPL_FILE/CM902904U_SI_001.PDF.

(133) Kwon, O. K.; Kwon, S. H.; Park, H. S.; Kang, S. W. Plasma-Enhanced Atomic Layer Deposition of Ruthenium Thin Films. *Electrochemical and Solid-State Letters* **2004**, *7* (4), C46. https://doi.org/10.1149/1.1648612.

(134) Jung, S. H.; Kang, S. W. Formation of TiO2 Thin Films Using NH3 as Catalyst by Metalorganic Chemical Vapor Deposition. *Jpn J Appl Phys* **2001**, *40* (5 R), 3147–3152. https://doi.org/10.1143/jjap.40.3147.

(135) Kwon, S.-H.; Kwon, O.-K.; Kim, J.-H.; Oh, H.-R.; Kim, K.-H.; Kang, S.-W. Initial Stages of Ruthenium Film Growth in Plasma-Enhanced Atomic Layer Deposition. *J Electrochem Soc* **2008**, *155* (5), H296. https://doi.org/10.1149/1.2868779/XML.

(136) Sari, W.; Eom, T.-K.; Kim, S.-H.; Kim, H. Plasma Enhanced Atomic Layer Deposition of Ruthenium Thin Films Using Isopropylmethylbenzene-Cyclohexadiene-Ruthenium and NH3 Plasma. *J Electrochem Soc* **2011**, *158* (1), D42. https://doi.org/10.1149/1.3515320/XML.

(137) Kim, S.-W.; Kwon, S.-H.; Jeong, S.-J.; Kang, S.-W. Improvement of Copper Diffusion Barrier Properties of Tantalum Nitride Films by Incorporating Ruthenium Using PEALD. *J. Electrochem. Soc.* **2008**, *155* (11), H885. https://doi.org/10.1149/1.2975341/XML.

(138) Kwon, S.-H.; Kwon, O.-K.; Min, J.-S.; Kang, S.-W. Plasma-Enhanced Atomic Layer Deposition of Ru–TiN Thin Films for Copper Diffusion Barrier Metals. *J. Electrochem. Soc.* **2006**, *153* (6), G578. https://doi.org/10.1149/1.2193335/XML.

(139) Grillo, F.; Soethoudt, J.; Marques, E. A.; de Martín, L.; van Dongen, K.; van Ommen, J. R.; Delabie, A. Area-Selective Deposition of Ruthenium by Area-Dependent Surface Diffusion. *Chem. Mater.* **2020**, *32* (22), 9560–9572. https://doi.org/10.1021/ACS.CHEMMATER.0C02588/ASSET/IMAGES/MEDIUM/CM0C02588_M020.GIF.

(140) Park, S. J.; Kim, W. H.; Lee, H. B. R.; Maeng, W. J.; Kim, H. Thermal and Plasma Enhanced Atomic Layer Deposition Ruthenium and Electrical Characterization as a Metal Electrode. *Microelectron. Eng.* **2008**, *85* (1), 39–44. https://doi.org/10.1016/J.MEE.2007.01.239.

(141) Zhou, M.; Chen, T.; Tan, J. J.; Ru, G. P.; Jiang, Y. L.; Liu, R.; Qu, X. P. Effect of Pretreatment of TaN Substrates on Atomic Layer Deposition Growth of Ru Thin Films. *Chinese Physics Letters* **2007**, *24* (5), 1400–1402. https://doi.org/10.1088/0256-307X/24/5/076.

(142) Chan, R.; Arunagiri, T. N.; Zhang, Y.; Chyan, O.; Wallace, R. M.; Kim, M. J.; Hurd, T. Q. Diffusion Studies of Copper on Ruthenium Thin Film a Plateable Copper Diffusion Barrier. *Electrochemical and Solid-State Letters* **2004**, *7* (8), G154. https://doi.org/10.1149/1.1757113.

(143) Damayanti, M.; Sritharan, T.; Mhaisalkar, S. G.; Gan, Z. H. Effects of Dissolved Nitrogen in Improving Barrier Properties of Ruthenium. *Appl Phys Lett* **2006**, *88* (4), 1–3. https://doi.org/10.1063/1.2167610.

(144) Damayanti, M.; Sritharan, T.; Mhaisalkar, S. G.; Engelmann, H. J.; Zschech, E.; Vairagar, A. V.; Chan, L. Microstructural Evolution of Annealed Ruthenium-Nitrogen Films. *Electrochemical and Solid-State Letters* **2007**, *10* (6), 15–17. https://doi.org/10.1149/1.2719563.

(145) Chang, C.-C.; Pan, F.-M. In Situ Two-Step Plasma Enhanced Atomic Layer Deposition of Ru/RuNx Barriers for Seedless Copper Electroplating. *J. Electrochem. Soc.* **2011**, *158* (4), G97. https://doi.org/10.1149/1.3554734/XML.

(146) Damayanti, M.; Sritharan, T.; Mhaisalkar, S. G.; Phoon, E.; Chan, L. Study of Ru Barrier Failure in the Cu/Ru/Si System. *J Mater Res* **2007**, *22* (9), 2505–2511. https://doi.org/10.1557/JMR.2007.0310/FIGURES/12.

(147) Gatineau, J.; Yanagita, K.; Dussarrat, C. A New RuO4 Solvent Solution for Pure Ruthenium Film Depositions. *Microelectron. Eng.* **2006**, *83* (11–12), 2248–2252. https://doi.org/10.1016/j.mee.2006.10.013.

(148) Minjauw, M. M.; Feng, J.-Y.; Sajavaara, T.; Detavernier, C.; Dendooven, J. Atomic Layer Deposition of Ternary Ruthenates by Combining Metalorganic Precursors with RuO4 as the Co-Reactant. *Dalton Trans.* **2022**. https://doi.org/10.1039/d1dt03543f.

(149) Hämäläinen, J.; Ritala, M.; Leskelä, M. Atomic Layer Deposition of Noble Metals and Their Oxides. *Chem. Mater.* **2013**, *26* (1), 786–801. https://doi.org/10.1021/CM402221Y.

(150) Minjauw, M. M.; Rijckaert, H.; Driessche, I. Van; Detavernier, C.; Dendooven, J. Nucleation Enhancement and Area-Selective Atomic Layer Deposition of Ruthenium Using RuO4 and H2 Gas. *Chem. Mater.* **2019**, *31* (5), 1491–1499. https://doi.org/10.1021/acs.chemmater.8b03852.

(151) Lee, S.-J.; Kim, S.-H.; Saito, M.; Suzuki, K.; Nabeya, S.; Lee, J.; Kim, S.; Yeom, S.; Lee, D.-J. Plasma-Free Atomic Layer Deposition of Ru Thin Films Using H2 Molecules as a Nonoxidizing Reactant. *J. Vac. Sci. Technol. A* **2016**, *34* (3), 031509. https://doi.org/10.1116/1.4946755.

(152) Minjauw, M. M.; Dendooven, J.; Capon, B.; Schaekers, M.; Detavernier, C. Near Room Temperature Plasma Enhanced Atomic Layer Deposition of Ruthenium Using the RuO4-Precursor and H2-Plasma. *J. Mater. Chem. C* **2015**, *3* (19), 4848–4851. https://doi.org/10.1039/C5TC00751H.

(153) Minjauw, M. M.; Dendooven, J.; Capon, B.; Schaekers, M.; Detavernier, C. Atomic Layer Deposition of Ruthenium at 100 °C Using the RuO4-Precursor and H2. *J. Mater. Chem. C* **2015**, *3* (1), 132–137. https://doi.org/10.1039/C4TC01961J.

(154) Zhan, T.; Sahara, K.; Takeuchi, H.; Yokogawa, R.; Oda, K.; Jin, Z.; Deng, S.; Tomita, M.; Wu, Y. J.; Xu, Y.; Matsuki, T.; Wang, H.; Song, M.; Guan, S.; Ogura, A.; Watanabe, T. Modification and Characterization of Interfacial Bonding for Thermal Management of Ruthenium Interconnects in Next-Generation Very-Large-Scale Integration Circuits. *ACS Appl. Mater. Interfaces* **2022**, *14* (5), 7392–7404. https://doi.org/10.1021/acsami.1c20366.

(155) Zhan, T.; Oda, K.; Ma, S.; Tomita, M.; Jin, Z.; Takezawa, H.; Mesaki, K.; Wu, Y. J.; Xu, Y.; Matsukawa, T.; Matsuki, T.; Watanabe, T. Effect of Thermal Boundary Resistance between the Interconnect Metal and Dielectric Interlayer on Temperature Increase of Interconnects in Deeply Scaled VLSI. *ACS Appl. Mater. Interfaces* **2020**, *12* (19), 22347–22356. https://doi.org/10.1021/ACSAMI.0C03010/ASSET/IMAGES/MEDIUM/AM0C03010_0006.GIF.

(156) Lee, H. B. R.; Kim, H. High-Quality Cobalt Thin Films by Plasma-Enhanced Atomic Layer Deposition. *Electrochemical and Solid-State Letters* **2006**, *9* (11), G323. https://doi.org/10.1149/1.2338777.

(157) Yoon, J.; Lee, H.-B.-R.; Kim, D.; Cheon, T.; Kim, S.-H.; Kim, H. Atomic Layer Deposition of Co Using N2/H2 Plasma as a Reactant. *J Electrochem Soc* **2011**, *158* (11), H1179. https://doi.org/10.1149/2.077111JES/XML.

(158) Vos, M. F. J.; Van Straaten, G.; Kessels, W. M. M. E.; Mackus, A. J. M. Atomic Layer Deposition of Cobalt Using H2-, N2-, and NH3-Based Plasmas: On the Role of the Co-Reactant. *Journal of Physical Chemistry C* **2018**, *122* (39), 22519–22529. https://doi.org/10.1021/ACS.JPCC.8B06342/ASSET/IMAGES/LARGE/JP-2018-06342U_0007.JPEG.

(159) Lee, H. B. R.; Park, Y. J.; Baik, S.; Kim, H. Initial Stage Growth during Plasma-Enhanced Atomic Layer Deposition of Cobalt. *Chemical Vapor Deposition* **2012**, *18* (1–3), 41–45. https://doi.org/10.1002/CVDE.201106937.

(160) Oh, I. K.; Kim, H.; Lee, H. B. R. Growth Mechanism of Co Thin Films Formed by Plasma-Enhanced Atomic Layer Deposition Using NH3 as Plasma Reactant. *Current Applied Physics* **2017**, *17* (3), 333–338. https://doi.org/10.1016/J.CAP.2016.12.021.

(161) Shimizu, H.; Sakoda, K.; Momose, T.; Koshi, M.; Shimogaki, Y. Hot-Wire-Assisted Atomic Layer Deposition of a High Quality Cobalt Film Using Cobaltocene: Elementary Reaction Analysis on NH x Radical Formation. *J. Vac. Sci. Technol. A* **2012**, *30* (1), 1–144. https://doi.org/10.1116/1.3666034/100008.

(162) Yoon, J.; Song, J. G.; Kim, H.; Lee, H. B. R. Plasma-Enhanced Atomic Layer Deposition of Co on Metal Surfaces. *Surf Coat Technol* **2015**, *264*, 60–65. https://doi.org/10.1016/J.SURFCOAT.2015.01.019.

(163) Fan, Q.; Sang, L.; Jiang, D.; Yang, L.; Zhang, H.; Chen, Q.; Liu, Z. Plasma Enhanced Atomic Layer Deposition of Cobalt Nitride with Cobalt Amidinate. *J. Vac. Sci. Technol. A* **2019**, *37* (1). https://doi.org/10.1116/1.5062842/245209.

(164) Van Straaten, G.; Deckers, R.; Vos, M. F. J.; Kessels, W. M. M.; Creatore, M. Plasma-Enhanced Atomic Layer Deposition of Cobalt and Cobalt Nitride: What Controls the Incorporation of Nitrogen? *J. Phys. Chem. C* **2020**, *124* (40), 22046–22054. https://doi.org/10.1021/ACS.JPCC.0C04223/ASSET/IMAGES/MEDIUM/JP0C04223_M016.GIF.

(165) O'Donnell, S.; Snelgrove, M.; Shiel, K.; Weiland, C.; Hughes, G.; Woicik, J.; O'Neill, D.; Jose, F.; McFeely, C.; O'Connor, R. Growth Chemistry of Cobalt Nitride by Plasma Enhanced Atomic Layer Deposition. *Mater. Res. Express* **2022**, *9* (10), 106402. https://doi.org/10.1088/2053-1591/AC9959.

(166) Reif, J.; Knaut, M.; Killge, S.; Winkler, F.; Albert, M.; Bartha, J. W. In Vacuo Studies on Plasma-Enhanced Atomic Layer Deposition of Cobalt Thin Films. *J. Vac. Sci. Technol. A* **2020**, *38* (1), 12405. https://doi.org/10.1116/1.5132891/280048.

(167) Franz, M.; Safian Jouzdani, M.; Kaßner, L.; Daniel, M.; Stahr, F.; Schulz, S. E. Low Temperature Atomic Layer Deposition of Cobalt Using Dicobalt Hexacarbonyl-1-Heptyne as Precursor. *Beilstein journal of nanotechnology* **2023**, *14*, 951–963. https://doi.org/10.3762/BJNANO.14.78.

(168) Lee, H. J.; Park, J. S.; Kwon, S. H. Plasma-Enhanced Atomic Layer Deposition of Tantalum Nitride Thin Films Using Tertiary-Amylimido-Tris(Dimethylamido)Tantalum and Hydrogen Plasma. *J Electroceram* **2016**, *36* (1–4), 165–169. https://doi.org/10.1007/S10832-016-0015-4/FIGURES/4.

(169) Park, J. S.; Lee, M. J.; Lee, C. S.; Kang, S. W. Plasma-Enhanced Atomic Layer Deposition of Tantalum Nitrides Using Hydrogen Radicals as a Reducing Agent. *Electrochem. Solid-State Lett.* **2001**, *4* (4), C17. https://doi.org/10.1149/1.1353160/XML.

(170) Chen, X.; Frisch, H. L.; Kaloyeros, A. E.; Arkles, B.; Sullivan, J. Low Temperature Plasma-Assisted Chemical Vapor Deposition of Tantalum Nitride from Tantalum Pentabromide for Copper Metallization. *J. Vac. Sci. Technol. B* **1999**, *17* (1), 182–185. https://doi.org/10.1116/1.590533.

(171) Kwon, J. D.; Park, J. S.; Lee, H. C.; Kang, S. W. A Chemical Reaction Path Design for the Atomic Layer Deposition of Tantalum Nitride Thin Films. *Electrochem. Solid-State Lett.* **2006**, *9* (9), G282. https://doi.org/10.1149/1.2216593/XML.

(172) Kwon, J. D.; Yun, J.; Kang, S. W. Comparison of Tantalum Nitride Films for Different NH3/H 2/Ar Reactant States in Two-Step Atomic Layer Deposition. *Jpn. J. Appl. Phys.* **2009**, *48* (2), 025504. https://doi.org/10.1143/JJAP.48.025504/XML.

(173) Chung, H.-S.; Kwon, J.-D.; Kang, S.-W. Plasma-Enhanced Atomic Layer Deposition of TaN Thin Films Using Tantalum-Pentafluoride and N2⁄H2⁄Ar Plasma. *J Electrochem Soc* **2006**, *153* (11), C751. https://doi.org/10.1149/1.2344834/XML.

(174) Kim, H.; Kellock, A. J.; Rossnagel, S. M. Growth of Cubic-TaN Thin Films by Plasma-Enhanced Atomic Layer Deposition. *J Appl Phys* **2002**, *92* (12), 7080–7085. https://doi.org/10.1063/1.1519949.

(175) Liu, J.; Nolan, M. Coverage and Stability of NH X-Terminated Cobalt and Ruthenium Surfaces: A First-Principles Investigation. *Journal of Physical Chemistry C* **2019**, *123* (41), 25166–25175. https://doi.org/10.1021/acs.jpcc.9b06287.

(176) Liu, J.; Lu, H.; Zhang, D. W.; Nolan, M. Reactions of Ruthenium Cyclopentadienyl Precursor in the Metal Precursor Pulse of Ru Atomic Layer Deposition. *J. Mater. Chem. C* **2021**, *9* (8), 2919–2932. https://doi.org/10.1039/d0tc03910a.

(177) Liu, J.; Lu, H.; Zhang, D. W.; Nolan, M. Reaction Mechanism of the Metal Precursor Pulse in Plasma-Enhanced Atomic Layer Deposition of Cobalt and the Role of Surface Facets. *Journal of Physical Chemistry C* **2020**, *124* (22), 11990–12000. https://doi.org/10.1021/acs.jpcc.0c02976.

(178) Nguyen, C. T.; Yoon, J.; Khan, R.; Shong, B.; Lee, H. B. R. Thermal Atomic Layer Deposition of Metallic Ru Using H2O as a Reactant. *Appl. Surf. Sci.* **2019**, *488*, 896–902. https://doi.org/10.1016/J.APSUSC.2019.05.242.

(179) Nguyen, C. T.; Cho, E. H.; Trinh, N. Le; Gu, B.; Lee, M.; Lee, S.; Lee, J. Y.; Kang, Y.; Lee, H. B. R. Area-Selective Deposition of Ruthenium Using Homometallic Precursor Inhibitor. *Chemistry of Materials* **2023**. https://doi.org/10.1021/acs.chemmater.3c00525.

(180) Gao, Z.; Le, D.; Khaniya, A.; Dezelah, C. L.; Woodruff, J.; Kanjolia, R. K.; Kaden, W. E.; Rahman, T. S.; Banerjee, P. Self-Catalyzed, Low-Temperature Atomic Layer Deposition of Ruthenium Metal Using Zero-Valent Ru(DMBD)(CO)3 and Water. *Chem. Mater.* **2019**, *31* (4), 1304–1317. https://doi.org/10.1021/ACS.CHEMMATER.8B04456/SUPPL_FILE/CM8B04456_SI_001.PDF.

(181) Bergschneider, M.; Ashburn, N.; Lang, X.; Kummel, A. C.; Cho, K. DFT Modeling of Atomic Layer Deposition of Ru Interconnect Metal for EUV Scaling. *MRS Adv* **2023**, *8* (14), 768–772. https://doi.org/10.1557/S43580-022-00482-1/FIGURES/3.

(182) Liu, J.; Lu, H.; Zhang, D. W.; Nolan, M. Self-Limiting Nitrogen/Hydrogen Plasma Radical Chemistry in Plasma-Enhanced Atomic Layer Deposition of Cobalt. *Nanoscale* **2022**, *14* (12), 4712–4725. https://doi.org/10.1039/D1NR05568B.

3 Density Functional Theory, Methods and Computational Models

3.1 Introduction

The fundamental laws of quantum mechanics that rule the behaviour of electrons can be used to predict the performance of materials for a targeted application.[1] Density functional theory (DFT) calculations can be applied as a standard tool for various materials modelling problems in chemistry, physics, materials science and engineering as well as other disciplines.[2] DFT is a successful approach to solving the fundamental equation that describes the quantum behaviour of atoms and molecules which is the Schrodinger equation.

3.2 Schrodinger Equation

To describe the properties of some well-defined collection of atoms such as an isolated molecule or the atoms that make up crystals of particular materials, their energy and properties derived from it are required. To define where an atom is, the position of the nucleus and the electrons must be defined. Solving the non-relativistic, time-independent Schrodinger equation, which has the form:

$$\widehat{H}\Psi = E\Psi \tag{3.1}$$

$\widehat{H}$ is the Hamiltonian operator which contains information regarding the kinetic and potential energies for all particles of a system and Ψ, the wavefunction, is a set of eigenstates of the Hamiltonian. E is the total energy of the system. Each eigenstate Ψ_n has a corresponding eigenvalue E_n which is a real number and is the energy of eigenstate Ψ_n. The Hamiltonian has the form:

$$\widehat{H} = -\frac{1}{2}\sum_{i=1}^{N}\nabla_i^2 - \frac{1}{2}\sum_{A=1}^{M}\frac{1}{M_A}\nabla_A^2 - \sum_{i=1}^{N}\sum_{A=1}^{M}\frac{Z_A}{r_{iA}} + \sum_{i=1}^{N}\sum_{j>i}^{N}\frac{1}{r_{ij}} + \sum_{A=1}^{M}\sum_{B>A}^{M}\frac{Z_A Z_B}{R_{AB}} \tag{3.2}$$

Consisting of N electrons and M nuclei in the absence of external magnetic or electric fields. A and B run over the M nuclei while i and j indicate the N electrons in the system.[3] The first two terms in equation (3.2) describe the kinetic energy of the electrons and nuclei respectively. The Laplacian operator ∇_q^2 is defined as a sum of differential operators in cartesian coordinates

$$\nabla_q^2 = \frac{\partial^2}{\partial x_q^2} + \frac{\partial^2}{\partial y_q^2} + \frac{\partial^2}{\partial z_q^2} \tag{3.3}$$

M_A is the mass of nucleus A and Z is its charge. The remaining three terms in equation (3.2) represent the potential energy of the system. These are the attractive electrostatic interaction between the nuclei and the electrons and the repulsive potential due to the electron-electron and nucleus-nucleus interactions respectively.[3] The distance between an electron and another particle (which can be an electron or the nucleus) is represented by $r_{pq} = \left|\vec{r}_p - \vec{r}_q\right|$ and $R_{PQ} = \left|\vec{R}_P - \vec{R}_Q\right|$ is the distances between the nuclei. Also note equation (3.2) employs atomic units where the reduced Planck's constant, $\hbar$, the electron mass and charge, m_e and e, and $4\pi\epsilon_0$, where ϵ_0 is the vacuum permittivity, are all set to unity.

3.3 Born-Oppenheimer Approximation

Atomic nuclei are much heavier than individual electrons which means that electrons respond more rapidly to changes in their surroundings than nuclei can. From this it can be taken that electrons are moving in the field of fixed nuclei; this is the Born-Oppenheimer approximation.[4] The kinetic energy of the nuclei is now zero and the nuclei-nuclei potential energy is a constant which can be set to zero. The Hamiltonian equation reduces to the electronic Hamiltonian when the Born-Oppenheimer approximation is applied.

$$\hat{H}_{elec} = -\frac{1}{2}\sum_{i=1}^{N}\nabla_i^2 - \sum_{i=1}^{N}\sum_{A=1}^{M}\frac{Z_A}{r_{iA}} + \sum_{i=1}^{N}\sum_{j>1}^{N}\frac{1}{r_{ij}} = \hat{T} + \hat{V}_{Ne} + \hat{V}_{ee} \tag{3.4}$$

The solution of the Schrodinger equation with $\hat{H}_{\text{elec}}$ is the electronic wavefunction Ψ_{elec} and the electronic energy E_{elec}.

$$\hat{H}_{elec}\Psi_{elec}(\vec{r}_1, \ldots, \vec{r}_N) = E_{elec}\Psi_{elec}(\vec{r}_1, \ldots, \vec{r}_N) \tag{3.5}$$

The Ψ_{elec} that gives the lowest E_{elec} is called the ground state. However, it is not possible to determine the Ψ_{elec} and due to electron-electron interaction terms in $\hat{H}_{\text{elec}}$ equation (3.4) is a many-body problem where all electrons must be simultaneously considered. The wavefunction cannot be measured but instead the probability that there are N electrons at some particular set of coordinates $\vec{r}_1, \ldots, \vec{r}_N$ is relevant. This probability is given by:

$$|\Psi(\vec{r}_1, \dots, \vec{r}_N)|^2 = \Psi^*(\vec{r}_1, \dots, \vec{r}_N)\Psi(\vec{r}_1, \dots, \vec{r}_N) \quad (3.6)$$

$\Psi(\vec{r}_1, \dots, \vec{r}_N)$ can be approximated as a product of individual electron wavefunctions $\Psi(\vec{r}_1, \dots, \vec{r}_N) \cong \psi_1(\vec{r})\psi_2(\vec{r}) \dots \psi_N(\vec{r})$, this is known as the Hartree product.
The density of electrons at a particular position in space $n(\vec{r})$ which can be written in terms of the individual electron wavefunctions as

$$n(\vec{r}) = 2\sum_i \psi_i^*(\vec{r})\psi_i(\vec{r}) \quad (3.7)$$

The summation goes over all the individual electron wavefunctions that are occupied by electrons, the term inside the summation is the probability that an electron in individual wavefunction $\psi_i(\vec{r})$ is located at position $\vec{r}$. The Pauli exclusion principle states that each individual electron wavefunction can be occupied by two separate electrons provided they have opposite spins, the factor of 2 in equation (3.7) accounts for this.[2] The electron density is a function of only three coordinates and contains a large quantity of information that is physically observable from the full wavefunction solution to the Schrodinger equations which is a function of 3N coordinates.

3.4 Hartree-Fock Method

A wavefunction of N electrons can be approximated by assuming the electrons have no effect on one another.[2] The Hamiltonian can then be written as

$$H = \sum_i^N h_i \quad (3.8)$$

The term h_i in equation (3.8) defines the kinetic and potential energy of electron *i*, and equation (3.4) takes this form when electron-electron interactions are ignored. Based on this Hamiltonian, the solutions to the Schrodinger equation would satisfy

$$h\chi = E\chi \quad (3.9)$$

The eigenfunctions described by equation (3.9) as called spin-orbitals. There are many eigenfunctions for every single-electron equation and this outlines a set of spin-orbitals $\chi_j(\vec{x}_i)(j\ 1,2,\dots)$ where $\vec{x}_i$ is a vector of coordinates that defines the position of electron *i* and its spin state. The energy of spin-orbital $\chi_j(\vec{x}_i)$ is represented by E_j. The eigenfunctions of H in equation (3.8) are products of the one-electron spin-orbitals

$$\psi(\vec{x}_1,\dots,\vec{x}_N) = \chi_{j1}(\vec{x}_1)\chi_{j2}(\vec{x}_2)\dots\chi_{jN}(\vec{x}_N) \tag{3.10}$$

The energy of this wavefunction is the sum of the spin-orbital energies ($E = E_{j1} + \cdots + E_{jN}$). A brief glance at this approximation to the N electron wavefunction (the Hartree product) was already seen in the previous section.

However, the Hartree product does not meet all the criteria for wavefunctions such as the antisymmetry principle. The antisymmetry principle arises from electrons being Fermions and indistinguishable. Therefore the wavefunction must change sign if two electrons are exchanged. The Hartree product wavefunction does not change sign under exchange. An improved approximation of the wavefunction can be achieved by using a Slater determinant. The wavefunction is expressed as the determinant of a matrix of single electron wavefunctions. For the case of two electrons, the Slater determinant is

$$\begin{aligned}\psi(\vec{x}_1,\vec{x}_2) &= \frac{1}{\sqrt{2}} det\begin{bmatrix}\chi_j(\vec{x}_1) & \chi_j(\vec{x}_2)\\ \chi_k(\vec{x}_1) & \chi_k(\vec{x}_2)\end{bmatrix}\\ &= \frac{1}{\sqrt{2}}[\chi_j(\vec{x}_1)\chi_k(\vec{x}_1) \quad \chi_j(\vec{x}_2)\chi_k(\vec{x}_2)]\end{aligned} \tag{3.11}$$

This expression changes sign if two electrons interchange, it doesn't distinguish between electrons and disappears if, 1) two electrons have the same coordinates or 2) if two of the one-electron wavefunctions are the same. Therefore, conditions of the Pauli exclusion principle are fulfilled. For a system of N electrons, the Slater determinant is a determinant of an $N \times N$ matrix of single electron spin-orbitals.

In a Hartree-Fock calculation, the positions of the atomic nuclei are fixed and the aim is to determine the wavefunction of *N* interacting electrons. The Schrodinger equation for each electron is written as[2]

$$\left[\frac{1}{2}\nabla^2 + V(\vec{r}) + V_H(\vec{r})\right]\chi_j(\vec{x}) = E_j\chi_j(\vec{x}) \tag{3.12}$$

The Hartree potential is defined as:

$$V_H(\vec{r}) = e^2 \int \frac{n\left(\overrightarrow{r'}\right)}{\left|\vec{r} - \overrightarrow{r'}\right|} d^3r' \tag{3.13}$$

The Hartree-Fock method presumes that the full wavefunction can be approximated using a single Slater determinant. The lowest *N* energy spin-orbitals of the single-electron equation are found, $\chi_j(\vec{x})$ for j = 1,…, *N* and the whole wavefunction is created from the Slater determinant of these spin-orbitals.[2] The spin-orbitals have to be defined using a finite amount of information to solve the single-electron equation. A set of functions called the basis set, $\phi_1(\vec{x}), \phi_2(\vec{x}), \ldots, \phi_K(\vec{x})$, are used to approximate the spin-orbitals as shown in equation (3.14).

$$\chi_j(\vec{x}) = \sum_{i=1}^{K} \alpha_{j,i}\,\phi_i(\vec{x}) \tag{3.14}$$

The Hartree-Fock method calculation is an iterative process outlined as follows:

1) An initial estimate of the spin-orbitals is made from the basis set.
2) Define the electron density from the current estimate of the spin-orbitals.
3) Solve the single-electron equations for the spin-orbitals using the density from step 2.
4) If the spin-orbitals from steps 2 and 3 are consistent with each other, these are the solutions to the Hartree-Fock calculation. If they aren't consistent, a new estimate must be made for the spin-orbitals and the procedure is repeated from step 2.

. The Hartree-Fock method is not confined to atoms or ions but can also be applied to the electrons of a molecule and solid.[5] An extensive discussion of the Hartree-Fock method can be found in the book by Szabo and Ostlund, 1982.[6]

3.5 Hohenberg-Kohn Theorems

The two fundamental theorems on which density functional theory depends were proved by Hohenberg and Kohn. The first theorem[2,7] states "The ground state energy *E* from Schrodinger's equation is a unique functional of the electron density $n(\vec{r})$." The second

theorem[2,7] states "The electron density that minimizes the energy of the overall functional is the true electron density corresponding to the full solution of the Schrodinger equation."
A functional is similar to the more familiar idea of a function where a function takes a value of a variable/variables and defines a single number from those variables as in equation (3.15).[2] A functional maps a function to a number as shown in equation (3.16).[3]

$$x \xrightarrow{f(x)} y \tag{3.15}$$

$$f(x) \xrightarrow{F[f(x)]} y \tag{3.16}$$

The ground state energy E can now be expressed as $E[n(\vec{r})]$ where $[n(\vec{r})]$ is the electron density, in other words, the ground state energy of a system can be expressed as a functional of the electron density.
The functional described by the Hohenberg-Kohn theorems can be written in terms of the single electron wavefunctions $E[\{\psi_i\}]$ which is composed of two parts as shown in equation (3.17).

$$E[\{\psi_i\}] = E_{known}[\{\psi_i\}] + E_{XC}[\{\psi_i\}] \tag{3.17}$$

The term $E_{known}[\{\psi_i\}]$ has four contributions: the electron kinetic energies and the Coulomb interactions between the electrons and nuclei, between the pair of electrons and between the pairs of nuclei respectively:

$$E_{known}[\{\psi_i\}] = \sum_i \int \psi_i^* \nabla^2 \psi_i d^3r + \int V(\vec{r}) n(\vec{r}) d^3r + \frac{1}{2} \iint \frac{n(\vec{r}) n(\overrightarrow{r'})}{\left|\vec{r} - \overrightarrow{r'}\right|} d^3r \, d^3r' + E_{ion} \tag{3.18}$$

The $E_{XC}[\{\psi_i\}]$ term is the exchange-correlation functional and includes all the quantum mechanical effects that aren't included in $E_{known}[\{\psi_i\}]$.

3.6 Kohn-Sham Equations

The Hohenberg-Kohn theorems do not provide an instruction on how to get the energy functional $E[n(\vec{r})]$. However, Kohn and Sham showed that the task of finding the right electron density can be expressed in a way that involves solving a set of equations, in which each equation involves only a single electron wave function as shown in equation (3.19).[8]

$$\left[\frac{1}{2}\nabla^2 + V(\vec{r}) + V_H(\vec{r}) + V_{XC}(\vec{r})\right]\psi_i(\vec{r}) = \varepsilon_i\psi_i(\vec{r}) \quad (3.19)$$

The potential due to the interaction between the electrons and the collection of atomic nuclei is $V(\vec{r})$, $V_H(\vec{r})$ is the Hartree potential and $V_{XC}(\vec{r})$ is the potential that defines the exchange and correlation contributions to the single electron equations. A solution to the Kohn-Sham equations is found by performing a self-consistent iterative method similar to Hartree-Fock:[2]

1) The initial trial electron density $n(\vec{r})$ is defined.
2) Using the defined trial electron density, solve the Kohn-Sham equations to find the single-particle wavefunctions $\psi_i(\vec{r})$.
3) Calculate the electron density defined by the Kohn-Sham single-particle wavefunctions from step (2) $\rightarrow n_{KS}(\vec{r}) = 2\sum_i \psi_i^*(\vec{r})\psi_i(\vec{r})$.
4) Compare $n_{KS}(\vec{r})$ to $n(\vec{r})$, if they are the same this is the ground state electron density which can be used to calculate the total energy. If they are different, $n(\vec{r})$ is updated and the process starts again from step (2).

The DFT method is defined by the Hohenberg-Kohn theorem and the Kohn-Sham equations. Solving by using the Kohn-Sham equations allows for more larger and complex systems to be studied due to the computational efficiency. DFT simulations can obtain information on properties that are not possible to measure experimentally. DFT have many applications such as the prediction of geometries of species under investigation, energetics and reaction mechanism such as finding energy barriers and the simulation of reaction pathways as well as computed vibrational frequencies.[9]

3.7 Practical Implementation of DFT

The implementation of DFT is done by the Kohn-Sham (KS) equation, however, three factors must be addressed before starting a DFT calculation: the selection of a basis set to expand the Kohn-Sham eigenfunctions, how core and valence electrons are described concerning interactions with the nuclei and the choice of approximation for the correlation-exchange term.

3.7.1 Basis Set

Basis sets are a set of functions used to approximate the atomic orbitals of atoms in the material using linear combination of atomic orbitals. Since a solid consists of a crystal structure that repeats periodically, this recurring unit can serve as a representative model for the entire material. The electrons within a periodic crystal structure move under the influence of a

periodic potential; i.e., $V(\vec{r}) = V(\vec{r} + \vec{L})$ for some characteristic distance $\vec{L}$ of the crystal lattice. The wavefunction of an electron in a crystalline material can be written as the product of a plane wave and a periodic function, this is known as Bloch's Theorem.[10] This is also true for the Kohn-Sham orbitals and can be expressed as:

$$\phi_n(\vec{r}) = e^{i\vec{q}.\vec{r}} u(\vec{r}) \tag{3. 20}$$

Where $e^{i\vec{q}.\vec{r}}$ is a plane wave, $\vec{q}$ is a wave vector and $u(\vec{r}) = u(\vec{r} + \vec{L})$ is a function with the same periodicity as the crystal lattice. $u(\vec{r})$ can be expressed as a linear combination of plane waves with wave vectors belonging to the reciprocal lattice (denoted $\vec{K}$):

$$u(\vec{r}) = \sum_{\vec{k} \in \vec{K}} c_{\vec{k}} e^{i\vec{k}.\vec{r}} \tag{3. 21}$$

$c_{\vec{k}}$ is the set of expansion coefficients. The single particle wavefunction can be expressed in terms of a plane wave basis set by combining equations (3. 20) and (3. 21):

$$\phi_n(\vec{r}) = \sum_{\vec{k} \in \vec{K}} c_{\vec{k}}^{\vec{n}} e^{i(\vec{q}+\vec{k}).\vec{r}} \tag{3. 22}$$

The wave vector $\vec{q}$ in equation (3. 22) belongs to the first Brillouin zone and the reciprocal lattice vectors, $\vec{k} \epsilon \vec{K}$, are an infinite set. However the use of an infinite set of vectors is not possible and the expansion is limited to $\vec{k} > \vec{k}_{max}$, where the cut-off is selected in a manner that ensures the wavefunction is sufficiently accurate when described by the finite basis set. The solution of the Kohn-Sham equations now simplifies to a matrix equation of the following form:

$$\mathbf{HC} = \mathbf{SCE} \tag{3. 23}$$

where H represents the Hamiltonian matrix, which is constructed using single-particle Hamiltonian operators. C is a square matrix formed by the expansion coefficients arranged in columns. S denotes the overlap matrix of basis functions, while E corresponds to a diagonal matrix containing the energy eigenvalues along the diagonal.

Plane wave basis sets are used to describe solid materials and a local atomic orbital basis sets are used to describe isolated molecules. Slater-type orbitals and Gaussian orbitals can describe

atomic orbitals but Gaussian orbitals tend to be used as they are less computationally expensive. The minimum basis set is the smallest atomic orbital basis set. A single basis function is used for each atom in the molecule to describe each atomic orbital s, p, d,…etc. *Double-zeta* basis sets use two basis functions for each atomic orbital and *triple-zeta* use three functions.

Periodic boundary conditions use plane wave basis sets where the number of plane waves is described by the cut-off energy. Describing core electrons with plane wave basis sets is highly computationally demanding. This is because core electrons cluster near the nuclei, oscillations of the core electrons lead to significant wavefunction and density gradients that requires a substantially higher cut-off energy. Therefore, pseudopotentials are used in combination with plane wave basis sets. A larger basis set will increase the accuracy of the calculations however it becomes more computationally expensive. The size of the system, properties of interest and computational resources are some of the factors that need to be considered when choosing the size of the basis set.

3.7.2 Pseudopotentials

The primary method for alleviating the computational load arising from core electrons is through the utilization of pseudopotentials. Core electrons play a relatively minor role in defining the chemical bonding and other physical properties of materials, as these characteristics are primarily governed by the less tightly bound valence electrons. This technique is referred to as the frozen core approximation, which significantly reduces the degrees of freedom, thereby requiring the solution only for the valence electrons. A pseudopotential replaces the electron density from a selected set of core electrons with a smoothed density chosen to match several important physical and mathematical properties of the actual ion core. The valence wavefunctions exhibit rapid variations near the ions to preserve orthonormality with the core wavefunctions. Describing this behaviour requires a large number of basis set functions. The ion potential is replaced by a pseudopotential for distances shorter than some core radius, $\vec{r}_c$. When $\vec{r} > \vec{r}_c$, the potential and the wavefunction are described exactly and when $\vec{r} < \vec{r}_c$, a pseudopotential is used shown in Figure 3.1. Above the core radius, the real and the pseudo wavefunction and potentials match; this smoothening of the wavefunctions influenced by the pseudopotential near the ions reduces the need for a larger number of plane wave basis functions.

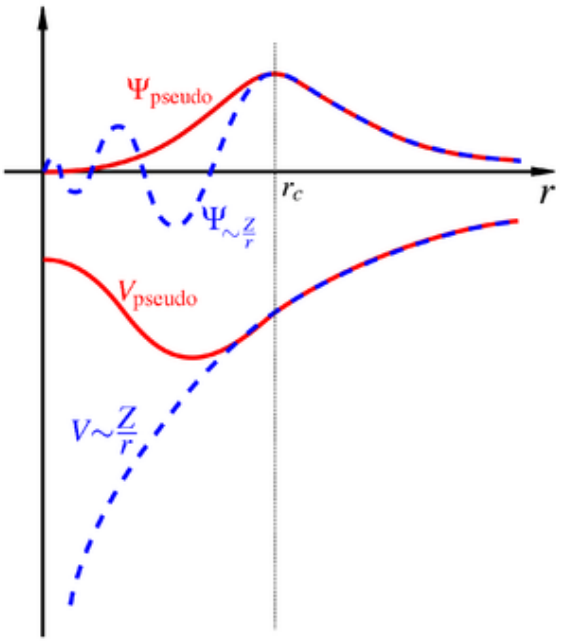


Figure 3.1: Graph illustrating the pseudopotential methodology where the pseudopotential replaces the real potential for $\vec{r} < \vec{r}_c$ to reduce the number of basis set functions needed to describe the wavefunction.

3.7.3 Projector Augmented Waves (PAW)

There are various types of pseudopotentials used such as ultra-soft pseudopotentials,[11] norm-conserving pseudopotentials[12] and all-electron projector augmented wave method (PAW)[13]. PAW is the pseudopotential used for the work in this thesis. In the PAW method, space is divided into two distinct regions: the core region ($\boldsymbol{r} < \boldsymbol{rc}$), which is close to the ions, and the interstitial region ($\boldsymbol{r} > \boldsymbol{rc}$), which is located further away from the ions. Using the PAW method, the Kohn-Sham orbital is written as a summation of three contributions:

$$\phi_n(\vec{r}) = \tilde{\phi}_n(\vec{r}) + \sum_a \phi_n^a(\vec{r}) - \sum_a \tilde{\phi}_n^a(\vec{r}) \qquad (3.\ 24)$$

The pseudo wavefunction is represented by $\tilde{\phi}_n(\vec{r})$ in equation (3. 24) and it exactly matches $\phi_n(\vec{r})$ in the interstitial region. Both the summation terms on the right side of equation (3. 24) run over the ions in the system and the functions within the summations are defined for the core regions. The terms within these summations, $\phi_n^a(\vec{r})$ and $\tilde{\phi}_n^a(\vec{r})$ correspond to all-electron and pseudo-one-centre wavefunctions respectively. Rapid oscillations in the core region are

accommodated by the all-electron functions $\phi_n^a(\vec{r})$ and in this region the pseudo functions $\widetilde{\phi}_n^a(\vec{r})$ are smooth. These functions can be written in terms of partial and pseudo partial wave basis sets, α_i and $\tilde{\alpha}_i$ and equation (3. 24) can be modified in Dirac notation to:

$$|\phi_n\rangle = |\tilde{\phi}_n\rangle + \sum_a \sum_i (|\alpha_i^a\rangle - |\tilde{\alpha}_i^a\rangle) \langle p_i^a | \tilde{\phi}_n \rangle \tag{3. 25}$$

The species-specific projector functions p_i^a are constructed to closely match the behaviour of the core electrons near the atomic cores. Solving equation (3. 25) enables the derivation of the wavefunctions $\phi_n(\vec{r})$.

3.7.4 Exchange-Correlation Functional

The $E_{XC}[\{\psi_i\}]$ term in equation (3.17) is unknown and this causes difficulties when trying to solve the Kohn-Sham equations as the exchange-correlation functional must be defined. Commonly used approximations for the exchange-correlation functional are the local density approximation (LDA), the generalised gradient approximation (GGA) and hybrid XC functional.

3.7.5 Local Density Approximation

In the LDA, the exchange-correlation functional can be derived for the case of uniform electron gas which yields a feasible way to use the Kohn-Sham equations.[2] At all points in space the electron density is constant, $n(\vec{r})$ = constant. The exchange-correlation potential at each point is set to be the known exchange-correlation potential for the uniform electron gas at the electron density observed at that point. It uses the local density to define the approximate exchange-correlation functional.

$$V_{XC}^{LDA}(\vec{r}) = V_{XC}^{electron\ gas}[n(\vec{r})] \tag{3.26}$$

3.7.6 Generalized Gradient Approximation

The generalized gradient approximation uses information regarding the local electron density and the spatial variation in the electron density to improve LDA for non-homogenous electron density.[14] The exchange-correlation is functional is expressed using the local electron density and the gradient in the electron density:

$$V_{XC}^{GGA}(\vec{r}) = V_{XC}[n(\vec{r}), \nabla n(\vec{r})] \quad (3.27)$$

There are numerous ways in which information from the gradient of the electron density can be included in the GGA functional and therefore there are a distinct number of GGA functionals. Two of the most frequently used functionals in calculations involving solids are the Perdew-Wang functional[15] (PW91) and the Perdew-Burke-Ernzerhof functional[16] (PBE).

3.7.7 Hybrid DFT

A hybrid functional is a functional that incorporates the exact Fock exchange term with contributions from GGA and LDA. For example the parameter free PBE0 functional where PBE exchange-correlation functional is chosen as the GGA part[17]:

$$E_{XC}^{hybrid} = E_{XC}^{GGA} + 0.25(E_X^{HF} - E_X^{GGA}) \quad (3.28)$$

This PBE0 functional is constructed with a mix of 25 % Fock exchange and 75 % of PBE exchange.[17] The electron correlation is represented by the by the correlation part of the PBE density functional.[16] Hybrid functionals improves upon the accuracy on properties related to energetics, such as reaction energies, band gaps, and molecular geometries. However, hybrid functionals can lead to longer computation times and greater memory requirements compared to simpler functionals.

3.8 Methods and Computational Models

In this section, the methods and computational models used to study the ALE and ALD processes in this thesis are discussed. All reported surface slab calculations in this thesis were performed within spin-polarized DFT with the Vienna ab initio Simulation Package (VASP)[18] version 5.4. The calculations are based on the generalized gradient approximation (GGA) using the Perdew−Burke−Ernzerhof (PBE) exchange−correlation (XC) functional.[16] The self-consistent energy for the electronic minimization is converged within 1×10^{-4} eV, and the forces for ionic relaxation are converged within -2×10^{-2} eV/Å (for calculations in Chapters 4-7). The default smearing method of Methfessel−Paxton first order is used with 0.1 eV broadening for electronic relaxation. The core electrons are described by projector-augmented wave (PAW) potentials,[19] and the valence electrons are treated using plane-wave basis sets with

a kinetic energy cutoff of 400 eV for surface calculations. For the surface slabs, enthalpy H and entropy S are computed using the Phonopy code by considering only the first layer of atoms.[20] The calculations for the reactant molecules and gas-phase byproducts are performed in VASP with a large periodic box of dimensions 15.0 Å × 16.0 Å × 15.5 Å and 400 eV plane-wave energy cutoff. The enthalpy and entropy for the gas phase molecules were calculated from the freeh program in the TURBOMOLE suite[21] at 1 atm pressure. These calculations for the reactant molecules and gas-phase byproducts are performed with the PBE exchange-correlation functional[16] and a polarized triple ζ basis set (def-TZVPP)[22,23] and default medium grid. Table 1 presents the valence electronic configuration for each atomic species.

Table 1: Valence electron configurations for each atomic species in this thesis.

Atomic species	Valence electron configuration
Hf	$6s^2\ 5d^2$
Zr	$5s^2\ 4d^2$
O	$2s^2\ 2p^4$
H	$1s^1$
F	$2s^2\ 2p^5$
Si	$3s^2\ 3p^2$
Cl	$3s^2\ 3p^5$
Ru	$4d^7\ 5s^1$
Ta	$6s^2\ 5d^3$
N	$2s^2\ 2p^3$
Co	$4s^2\ 3d^7$
C	$2s^2\ 2p^2$

Bader charge analysis was used to calculate the electronic charge on atoms in Chapters 7 and 8.[24–27] The Bader charges along with the valence electron charges (ZVAL in POTCAR) are used to calculate if an atom is oxidized or reduced as shown in equation (3.29).

$$q^{net} = N^{valence} - q^{Bader} \tag{3.29}$$

The van der Waals correction was applied using the DFT-D3 method to provide an accurate description of the dispersion interactions for the calculated adsorption energies in Chapters 6-8.[28] The activation energies in this thesis were computed using the nudged elastic band method with 4 or 6 images along with the initial and final geometries for those reported in Chapters 8

and 9 respectively and a force convergence of 0.05 eV/Å. The surface slab models were constructed from crystal structures available from the Materials Project database[29] and built using Biovia Materials Studio and the Atomic Simulation Environment (ASE)[30]. All figures of the geometries were generated using the Visualization for Electronic and Structural (VESTA) package.[31]

3.8.1 Crystalline HfO_2

The bulk unit cell monoclinic HfO_2[32] (space group: $P2_1/c$) was optimized by simultaneously relaxing the ionic positions, cell shape, and cell volume with an energy cutoff of 550 eV and a Monkhorst-Pack k-point sampling mesh of (6 × 6 × 6). The bulk monoclinic unit cell of HfO_2 has four Hf atoms and eight O atoms. The optimized lattice constants of HfO_2 from this setup are a = 5.142 Å, b = 5.195 Å, and c = 5.326 Å. Comparing our values to the experimental values for the baddeleyite[33] phase the deviations are, a = 0.43%, b = 0.48%, and c = 0.96%. A surface slab of monoclinic HfO_2 with a (111) orientation is used for the surface calculations as this is the most stable facet at low temperatures and has the lowest surface energy.[33,34] A surface supercell of HfO_2 with a (2 × 2) expansion of the hexagonal unit cell and 16 Å of vacuum separating the slabs is used for the surface models; this has a stoichiometry of $Hf_{80}O_{160}$ per supercell as shown in Figure 3.2. It consists of five layers of 16 HfO_2 units, and a k-point sampling mesh of (2 × 2 × 1) is used for geometry optimization. All Hf atoms are 6-fold coordinated by O atoms. O atoms are either 2-fold/3-fold coordinated by Hf atoms.

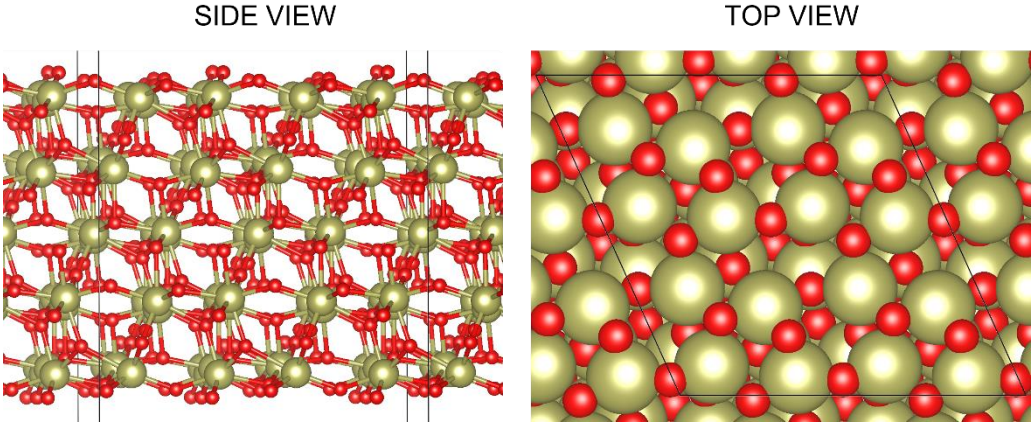


Figure 3.2: Side view and top view of monoclinic (111) surface supercell of HfO_2. Colour scheme: Hf = gold and O = red.

The surface slab of monoclinic HfO_2 with a (001) orientation shown in Figure 3.3 was also studied with the same stoichiometric details as described above. All Hf atoms are 5-fold coordinated by O atoms. All O atoms are 2-fold coordinated by Hf atoms.

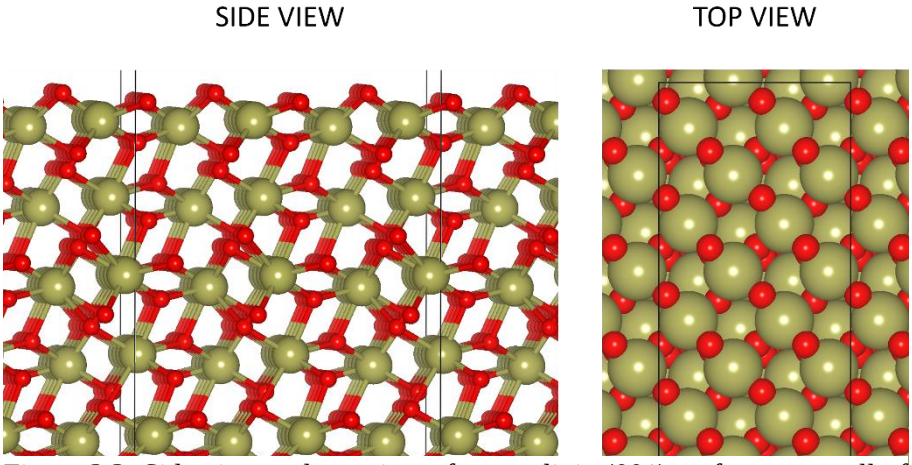


Figure 3.3: Side view and top view of monoclinic (001) surface supercell of HfO_2. Colour scheme is the same as in Figure 3.2.

The orthorhombic[35] phase was also examined for HfO_2 with the bulk unit cell (space group: $Pca2_1$) was optimized using the same strategy described above for the monoclinic phase. Comparing to experiment[36] the deviations in lattice constants are: a = 0.39%, b = 0.11%, and c = 0.18%. Surface slabs of orthorhombic HfO_2 with the (111) and (001) orientations were also studied. In oHfO_2(111) Figure 3.4 every Hf atom is 6-fold coordinated by O and O are either 2-fold/3-fold coordinated by Hf. For oHfO_2(001) Figure 3.5 Hf are either 5-fold/6-fold coordinated by O and every O is 2-fold coordinated by Hf.

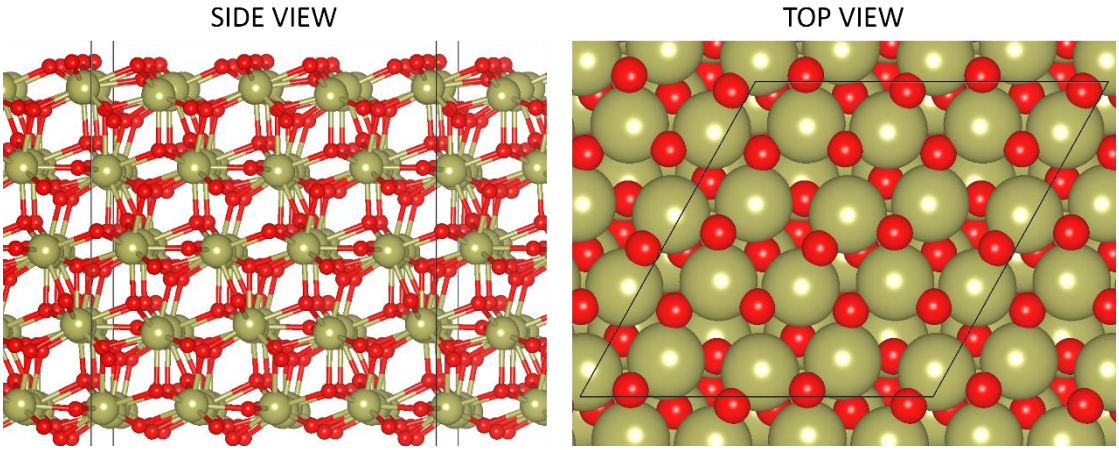


Figure 3.4: Side view and top view of orthorhombic (111) surface supercell of HfO2. Colour scheme is the same as in Figure 3.2.

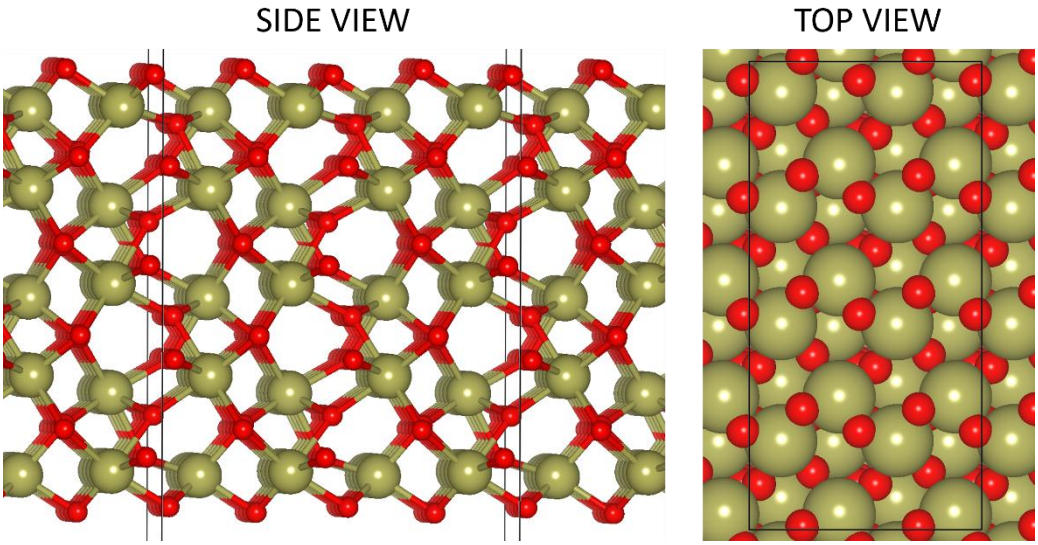


Figure 3.5: Side view and top view of orthorhombic (001) surface supercell of HfO_2. Colour scheme is the same as in Figure 3.2.

3.8.2 Crystalline ZrO_2

Similar to HfO_2, the bulk unit cell monoclinic ZrO_2 (space group: $P2_1/c$) was also optimized by simultaneously relaxing the ionic positions, cell shape, and cell volume with an energy cutoff of 550 eV and a Monkhorst-Pack k-point sampling mesh of (6 × 6 × 6). The bulk monoclinic unit cell of ZrO_2 has four Hf atoms and eight O atoms. From this, the optimized lattice constants of ZrO_2 are a = 5.140 Å, b = 5.189 Å, and c = 5.239 Å. Comparing to the baddeleyite phase[33] the deviations for ZrO_2 are a = 0.58%, b = 0.78%, and c = 1.89%. A surface slab of monoclinic ZrO_2 with a (111) orientation is used for the surface calculations as this is the most stable facet at low temperatures and has the lowest surface energy.[33] A surface supercell of ZrO_2 with a (2 × 2) expansion of the hexagonal unit cell and 16 Å of vacuum separating the slabs is used for the surface models; this has a stoichiometry of $Zr_{80}O_{160}$ per supercell as shown in Figure 3.6. Like HfO_2, it consists of five layers of 16 ZrO_2 units, and a k-point sampling mesh of (2 × 2 × 1) is used for geometry optimization.

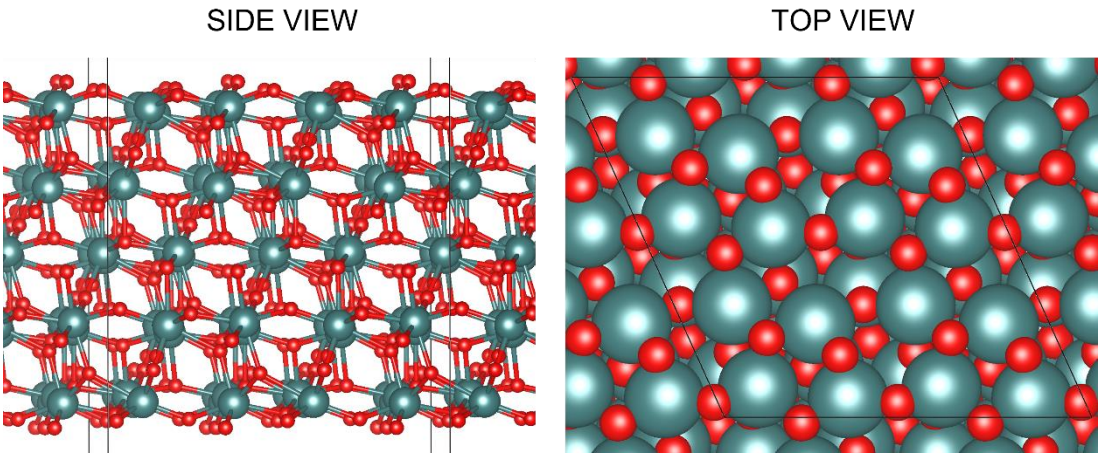


Figure 3.6: Side view and top view of monoclinic (111) surface supercell of ZrO_2. Colour scheme: Zr = green and O = red.

3.8.3 Amorphous HfO_2

The bulk amorphous HfO_2 ($aHfO_2$) used in this thesis was prepared using classical molecular dynamics (MD) simulations with the LAMMPS package[37] by Jose Julio Gutiérrez Moreno and the details below were published in ref.[38]. Atomic pair interactions were adopted from the Morse type potential developed by Broglia et al. which is accurate for the simulation of glasses at high temperatures and pressures, and has been previously used for the study of $aHfO_2$.[39] The Nosé-Hoover thermostat in its isothermal-isobaric form (NPT) was used to set the constant pressure at 1 atm and the temperatures during the simulation. The integration time step was set to 0.1 fs. The amorphous structure was produced using the melt-quenching method. Initially, a total of 216 atoms with a stoichiometric HfO_2 composition (72 Hf and 144 O atoms) are randomly placed in a periodic cubic box. After an initial equilibration, the system is warmed up to 4000 K at a rate of 10 K/ps. The temperature was set well above the experimental melting point and equilibrated for 2 ns to assure the initially random distribution of the atomic species in the model. The melted structure is then quenched to 300 K in consecutive steps of 10 K/ps (i.e., every 10^4 time steps) and finally equilibrated for 1 ns at room conditions. The quenching rate was chosen to be quick enough to produce an amorphous structure at equilibrium. The pair distribution function of $aHfO_2$ is shown in Figure 3.8 (a). The different pairs are colour-coded, with Hf-O pairs represented with a red line, Hf-Hf in black and O-O in green. The absence of long-range range order in our as-quenched hafnia model reflects the amorphous distribution of this solid. This procedure leads to an equilibrated cubic box with side dimensions of 13.72 Å. The density of the resulting simulation box is 9.62 g/cm^3, which is in good agreement with other $aHfO_2$ models generated by MD.[40–42]

The $aHfO_2$ bulk was relaxed with DFT by simultaneous relaxation of the ionic positions, cell volume, and cell with a higher plane wave kinetic energy cutoff of 550 eV to ensure an accurate description of the bulk. A Monkhorst–Pack k-point sampling mesh of (1 × 1 × 1) is used. The optimized lattice constants are a = 13.729 Å, b = 13.871 Å, and c = 13.796 Å, and angles alpha = 90.74°, beta = 89.14°, and gamma = 89.81°. The surface slab of $aHfO_2$ with 16 Å of vacuum separating the slabs is used for the surface models with a stoichiometry of $Hf_{72}O_{144}$ per supercell as shown in Figure 3.7. A k-point sampling mesh of (2 × 2 × 1) is used for geometry optimization.

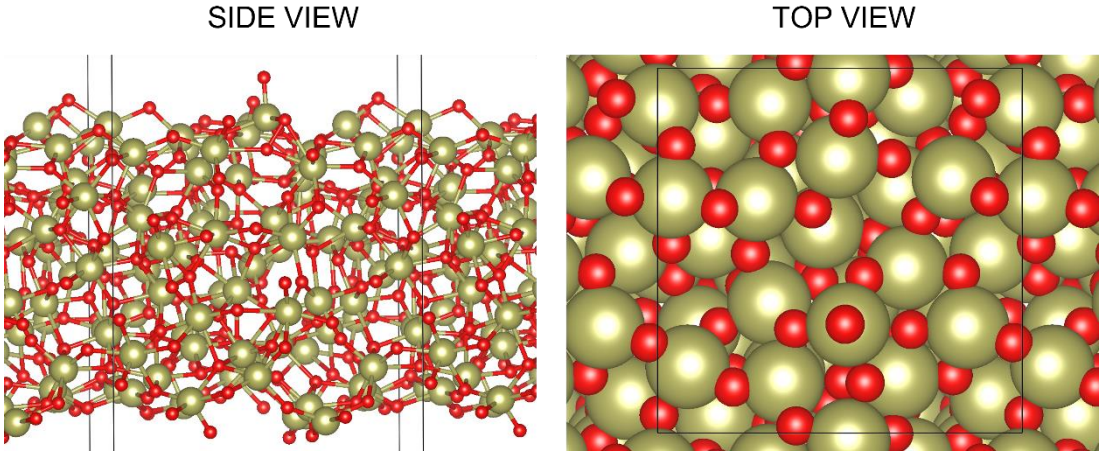


Figure 3.7: Side view and top view of $aHfO_2$ surface slab. Colour scheme is the same as in Figure 3.2.

Experimental studies have shown that the chemical composition of $aHfO_2$ is essentially stoichiometric.[43] Theoretical studies of $aHfO_2$ reported that the coordination numbers for the Hf atoms were five, six, seven, and eight with a preference for six and seven. For oxygen two, three, and four coordination are found, with a preference for three and four coordination.[40] The distribution of the coordination numbers for the Hf and O atoms of the bulk $aHfO_2$ model used in this thesis is shown in Figure 3.8 (b). To determine the coordination number, a cutoff radius of 2.50 Å derived from the behaviour of Hf–O bonds are used.[44] Three-coordinated O atoms and six-coordinated/seven-coordinated Hf atoms dominate the bulk $aHfO_2$ model, which agrees with previous classical[45] and *ab initio*[46,47] molecular dynamic studies.

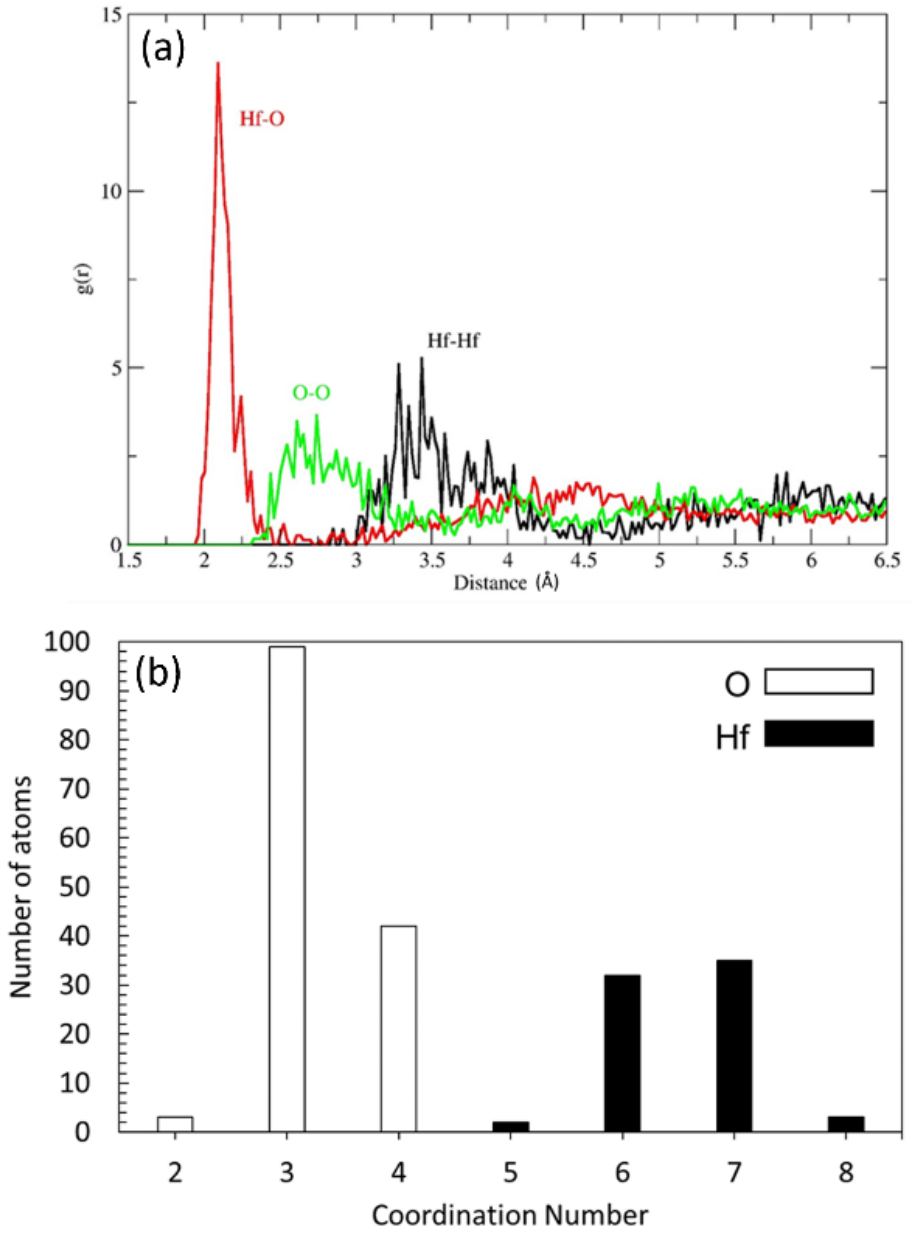


Figure 3.8: (a) Pair distribution function (PDF) of amorphous HfO_2 bulk model structure quenched at 10 K/ps rate and the plot uses 300 data points (b) distribution of coordination numbers for the bulk aHfO_2 model used in this thesis that was prepared using classical molecular dynamics.

3.8.4 ZnO

The bulk unit cell hexagonal ZnO[48] (space group: $P6_3mc$) was optimized by simultaneously relaxing the ionic positions, cell shape, and cell volume with an energy cutoff of 550 eV and a Γ- centered Monkhorst-Pack k-point sampling mesh of (6 × 6 × 6). The bulk hexagonal unit cell of ZnO has two Zn atoms and two O atoms. The optimized lattice constants of ZnO from this setup are a = b = 3.289 Å and c = 5.307 Å. Comparing to the experimental Wurtzite[49] phase

the deviations for ZnO are a = b = 1.21% and c = 1.98%. A surface slab of nonpolar $(10\bar{1}0)$ ZnO surface is studied as this is the most stable and abundant facet of Wurtzite ZnO.[50,51] A (3 × 4) supercell of ZnO with a stoichiometry of $Zn_{96}O_{96}$ per supercell and 14 Å of vacuum separating the slabs is shown in Figure 3.9. It consists of four layers of 24 ZnO units, and a gamma centered k-point sampling mesh of (2 × 2 × 1) is used for geometry optimization.

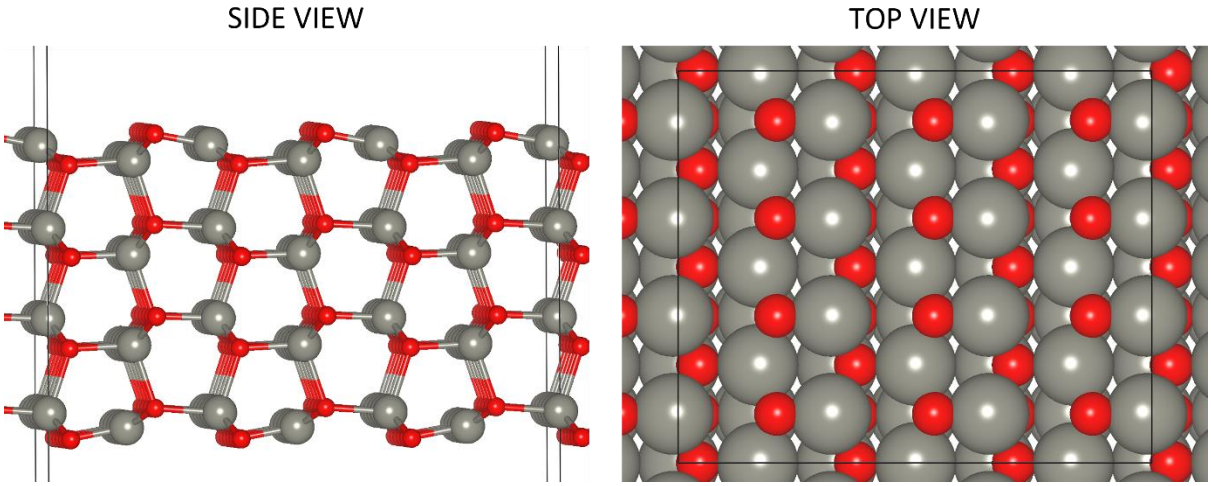


Figure 3.9: Side view and Top view of the ZnO $(10\bar{1}0)$ surface. Colour scheme is: Zn = grey and O = red.

3.8.5 Ru

The bulk Ru[52] crystal structure (space group: $P6_3/mmc$) is optimized by simultaneously relaxing the ionic positions, cell volume and cell shape at a higher plane wave energy cutoff of 550eV and a Monkhorst-Pack grid k-point mesh of 12×12× 6. The bulk Ru unit cell two Ru atoms. The resulting lattice constants are a = b = 2.71Å, and c = 4.28Å for Ru bulk which compares well with experimental results.[53] A (4 × 4) supercell of Ru (001) that contained 80 Ru atoms per supercell was studied in this thesis as shown in Figure 3.10. It consists of five layers of 16 Ru units, and a Monkhorst-Pack K-point mesh of (2 × 2 × 1) is used for geometry optimization.

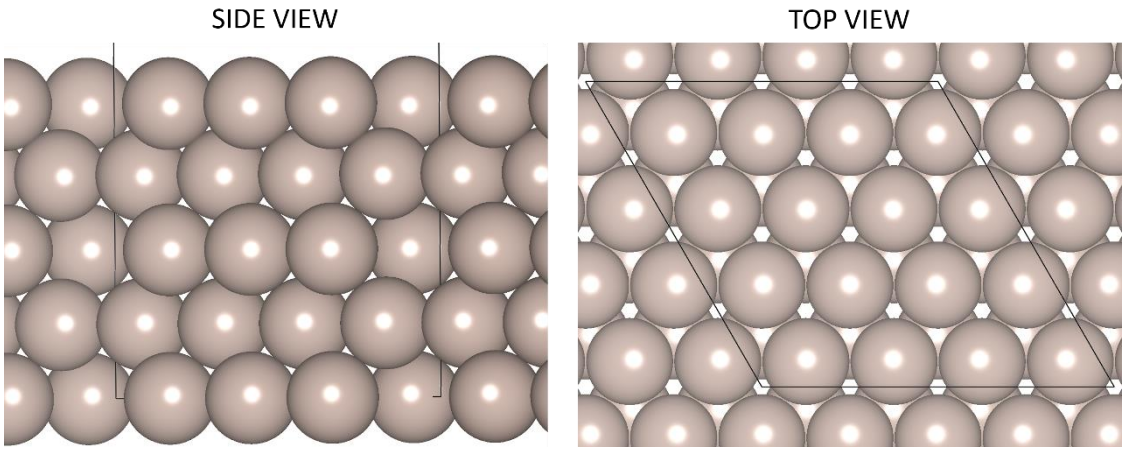


Figure 3.10: Side view and Top view of the Ru (001) surface. Colour scheme is Ru = grey.

3.8.6 TaN

The details of the ε-TaN model were previously published by Natarajan et al.[54] The bulk structure of ε-TaN[55] (space group: P62m) with Fe_2P crystal structure was optimised by simultaneously relaxing the ionic positions, cell volume and cell shape at a higher plane wave energy cutoff of 550 eV and a Monkhorst-Pack K-point mesh of 6×6×12. The equilibrium lattice parameters a = b = 5.23 Å, c = 2.92 Å, $\alpha = \beta = 90^o$ and $\gamma = 120^o$ agrees well the experimental results of a = b =5.20 Å and c = 2.91 Å.[56] A (2 × 4) supercell of TaN(110) with a stoichiometry of $Ta_{120}N_{120}$ per supercell as shown in Figure 3.11 was studied in this thesis. 12 Å of vacuum separating the slabs along the surface normal direction is included to avoid interactions between the two surfaces of the slab. It consists of five layers of 24 TaN units, and a k-point sampling mesh of (2 × 2 × 1) is used for geometry optimization.

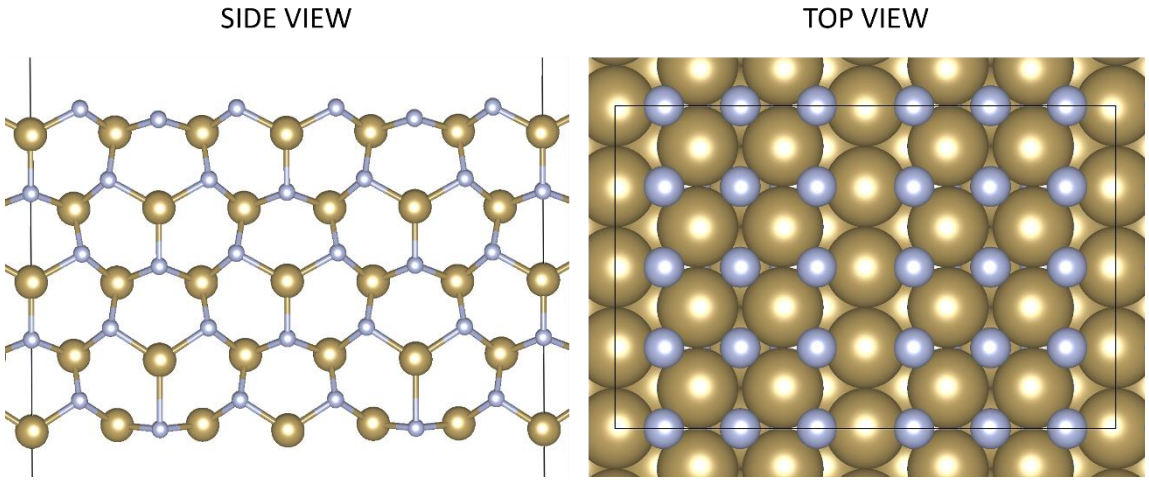


Figure 3.11: Side view and Top view of the TaN (110) surface. Colour scheme is: Ta = brown and N = blue.

3.9 Natarajan−Elliott Analysis for ALE Thermodynamics

The Natarajan-Elliott analysis[57] (N−E analysis, in short) was introduced to predict the conditions at which a self-limiting (SL) or continuous spontaneous etch (SE) reaction becomes thermodynamically favourable, subject to kinetic barriers. This information is important for directing experimental studies of thermal ALE. The relationship between the SE and SL processes of a substrate exposed to a single gaseous reactant is shown in Figure 3.12. In an SL reaction, represented by the solid green arrow in Figure 3.12 the reactant molecules passivate the material surface and form a nonvolatile layer that resists further reaction. Such a reaction is referred to as a "surface → surface" reaction.

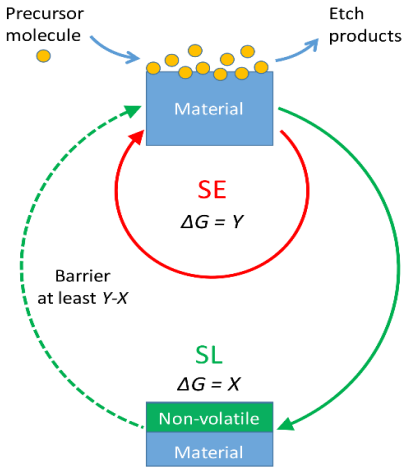


Figure 3.12: Schematic representation of the relationship between continuous spontaneous etch (SE, red) and self-limiting (SL, green) processes. ΔG represents the reaction free energy.[57]

$$\text{SL: } A_{surface} + B_{gas} \rightarrow C_{surface} \tag{3.30}$$

with the reaction free energy defined as ΔG = X. Here, the starting surface A is necessarily different from the final surface C. Byproducts may be released into the gas phase during this reaction.

$$\text{SL: } A_{surface} + B_{gas} \rightarrow C_{surface} + D_{gas} \tag{3.31}$$

Conversely, in a SE reaction, represented by the solid red arrow in Figure 3.12, the reactant molecules etch away units of bulk material continuously by forming stable and volatile etch

byproducts. This continues until the supply of the reactant gas molecules is stopped or the substrate material is exhausted (e.g., an etch stop is reached). Such a reaction is referred to as a "bulk → gas" reaction.

$$\text{SE: } A_{surface} + A_{bulk} + B_{gas} \rightarrow A_{surface} + E_{gas} \tag{3.32}$$

$$\text{SE: } A_{bulk} + B_{gas} \rightarrow E_{gas} \tag{3.33}$$

with the reaction free energy ΔG = Y. Clearly, Y is independent of $A_{surface}$. The reaction free energy ΔG at temperature T is computed as:

$$\Delta G = \Delta H - T\Delta S + RT\ ln(Q) \tag{3.34}$$

$$\Delta H = \Delta E + \Delta ZPE + \Delta W(T) \tag{3.35}$$

$$\Delta E = \sum_{p} \mu\, E_p - \sum_{r} \mu\, E_r \tag{3.36}$$

$$Q = \prod p_{products}^{\mu} / \prod p_{reactants}^{\mu} \tag{3.37}$$

In equation (3.34) ΔH and ΔS represent the changes in reaction enthalpy and reaction entropy, respectively. Since the partial pressures of the reactants and products are variable in the reaction chamber, the RT ln(Q) term is included. ΔH in equation (3.35) includes three contributions: electronic reaction energy ΔE, zero-point energy change ΔZPE, and a temperature-dependent enthalpic contribution ΔW(T). While the reaction energy (ΔE) in equation (3.36) includes only the bonding information at temperature T = 0 K, the reaction free energy (ΔG) provides finite temperature and pressure behaviour of a particular reaction. In equation (3.36), μ refers to the stoichiometric coefficient of the corresponding species and indices r and p indicate reactant and product species, respectively. The reaction quotient Q includes partial pressures of the gas-phase reactant and product molecules only. If the reactant and product pressures are the same, then ln Q becomes 0. A negative ΔS increases the free energy and tends to make the reaction more endergonic. Via the translational entropy, the value of ΔS is strongly dependent on the difference in molecularity between the products and the reactants. For example, if the number of gaseous molecules in the products is considerably smaller than in the reactants, then the ΔS value is likely to be negative and result in an increase in the reaction-free energy. A negative

value of ΔG means that the corresponding reaction is exergonic (favourable); otherwise, it is endergonic (unfavourable). The ΔG values are based on the SE and SL reactions as thermochemically isolated processes. However, it is useful to consider also the overall energetics of the reaction pathway that theoretically links SL to SE (depicted by the green dotted line in Figure 3.12). It may be possible to form SE reaction products from the SL reaction products by overcoming one or several energetic barriers. While it is possible to compute kinetic barriers at the first-principles level, this is omitted in favour of developing a computational approach that allows rapid screening of possible ALE chemistries. Balancing the energies in Figure 3.12 shows that these unknown barriers must be of magnitude at least Y − X (free energy difference of SL and SE reactions) in energy units. This term Y − X will be referred to as the "minimum barrier".

Based on the values of X and Y, four possible scenarios for the precursor pulse can be distinguished as shown in Figure 3.13. Each profile in Figure 3.13 depicts a set of SL and SE reaction-free energies separated by unknown energetic barriers, which in reality may consist of many barriers in the configurational space of the system. Computing all of the reaction pathways and barriers separating the SL and SE product states would be computationally demanding. This methodology aims to form useful conclusions without computing these pathways, thus accelerating process design. The minimum possible barrier to drive the etch reaction from the SL to SE product state is Y − X in energy units as mentioned earlier. In the energy profiles, the SL reaction appears on the left-hand side of the horizontal axis since the precursor molecules must first react with the surface before accessing the bulk. To cause etching from there onward, the precursor molecules may have to lift the surface atoms out of their lattice positions or diffuse into the subsurface region and finally form volatile products. Therefore, the SE reaction is shown to the right of the SL reaction in these energy profiles.

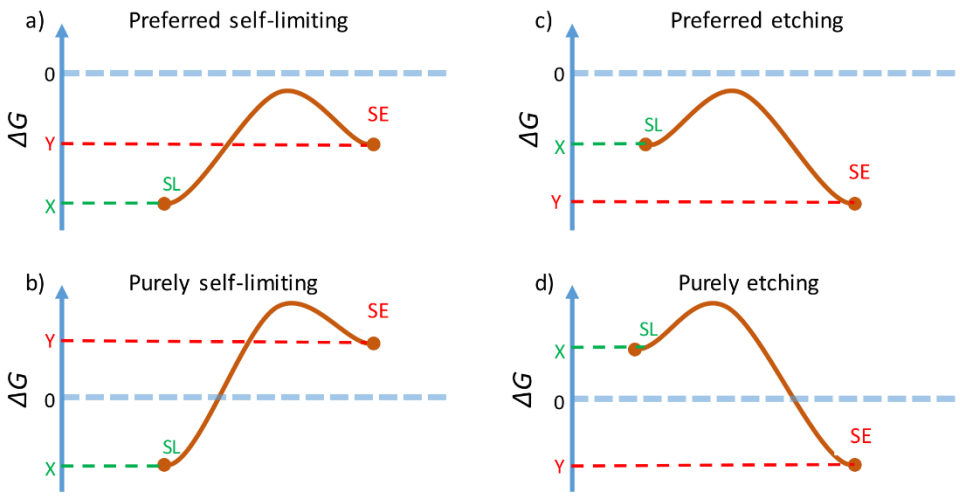


Figure 3.13: Schematic energy profiles representing (a) preferred self-limiting, (b) purely self-limiting, (c) preferred etching, and (d) purely etching.

Depending on whether the SL reaction or the SE reaction is the most favourable (based on their ΔG values), the energy profiles in Figure 3.13 are classified broadly as self-limiting or etching. The energy profile in Figure 3.13a is termed as "preferred self-limiting" since the SL reaction is more thermodynamically favoured than the SE reaction, even though both SL and SE reactions are exergonic. Here, there is a possibility of etching if the collective barrier (at least Y − X) could be overcome under the reactor conditions. If the energy profile in Figure 3.13a is shifted along the vertical axis such that the SL reaction is exoergic and the SE reaction is endergonic, we obtain the energy profile in Figure 3.13b termed as "purely self-limiting". This is the ideal energy profile for the surface modification pulse in an ALE process since continuous etching is energetically unfavourable. The energy profile in Figure 3.13c is the reverse of that in Figure 3.13a since the SE reaction is energetically more favourable than the SL reaction (Y − X < 0). The collective barrier, if any, for etching would be comparatively lower than in the preferred self-limiting state, and it may be easily breached under the reactor conditions. Therefore, the energy profile in Figure 3.13c is termed as "preferred etching". Figure 3.13d is obtained by shifting the energy profile in Figure 3.13c such that the SL reaction is endergonic and the SE reaction is exergonic. This profile is termed "purely etching" since the precursor molecules should readily volatilize the surface atoms and proceed to the subsurface region to cause bulk etching without significant barriers. This is the ideal energy profile for a SE pulse. Thus, the shape of the energy profile at any given temperature and pressure will allow us to predict the net effect of the precursor–substrate interaction. To summarize, by comparing the energetics and thermodynamics of the SE (bulk → gas) and SL

(surface → surface) reactions, along with the minimum energetic barrier separating them, we can predict whether the gas of a particular precursor pulse will spontaneously etch the substrate material at the temperatures and pressures of interest.

Chapter References

(1) Jain, A.; Shin, Y.; Persson, K. A. Computational Predictions of Energy Materials Using Density Functional Theory. *Nat. Rev. Mater. 1* **2016**, *1* (1), 1–13. https://doi.org/10.1038/natrevmats.2015.4.

(2) Sholl, D. S.; Steckel, J. A. What Is Density Functional Theory? In *Density Functional Theory: A Practical Introduction*; John Wiley and Sons, 2009; pp 1–34. https://doi.org/10.1002/9780470447710.

(3) Koch, W.; Holthausen, M. C. Elementary Quantum Chemistry. In *A Chemist's Guide to Density Functional Theory*; Wiley, 2001; pp 3–18. https://doi.org/10.1002/3527600043.

(4) Born, M.; Oppenheimer, R. Zur Quantentheorie Der Molekeln. *Ann Phys* **1927**, *389* (20), 457–484. https://doi.org/10.1002/ANDP.19273892002.

(5) Bransden, B. H.; Joachain, C. J. Several- and Many-Particle Systems. In *Quantum Mechanics*; Pearson Prentice-Hall: Harlow, England, 2000; pp 496–497.

(6) Szabo, A.; Ostlund, N. L. *Modern Quantum Chemistry: Introduction to Advanced Electronic Structure Theory*; New York, 1996.

(7) Hohenberg, P.; Kohn, W. Inhomogeneous Electron Gas. *Phys. Rev.* **1964**, *136* (3B), 864–871.

(8) Rindt, C. C. M.; Gaastra-Nedea, S. V. Modeling Thermochemical Reactions in Thermal Energy Storage Systems. In *Advances in Thermal Energy Storage Systems: Methods and Applications*; Woodhead Publishing, 2015; pp 375–415. https://doi.org/10.1533/9781782420965.3.375.

(9) Orio, M.; Pantazis, D. A.; Neese, F. Density Functional Theory. *Photosynth Res* **2009**, *102* (2), 443–453. https://doi.org/10.1007/S11120-009-9404-8/FIGURES/2.

(10) Bloch, F. Über Die Quantenmechanik Der Elektronen in Kristallgittern. *Zeitschrift für Physik* **1929**, *52* (7–8), 555–600. https://doi.org/10.1007/BF01339455.

(11) Vanderbilt, D. Soft Self-Consistent Pseudopotentials in a Generalized Eigenvalue Formalism. *Phys Rev B* **1990**, *41* (11), 7892–7895. https://doi.org/10.1103/PhysRevB.41.7892.

(12) Hamann, D. R.; Schlüter, M.; Chiang, C. Norm-Conserving Pseudopotentials. *Phys Rev Lett* **1979**, *43* (20), 1494–1497. https://doi.org/10.1103/PhysRevLett.43.1494.

(13) Blöchl, P. E. Projector Augmented-Wave Method. *Phys Rev B* **1994**, *50* (24), 17953–17979. https://doi.org/10.1103/PhysRevB.50.17953.

(14) Sholl, D. S.; Steckel, J. A. Accuracy and Methods Beyond "Standard" Calculations. In *Density Functional Theory: A Practical Introduction*; John Wiley and Sons, 2009; pp 209–233. https://doi.org/10.1002/9780470447710.

(15) Perdew, J. P.; Wang, Y. Accurate and Simple Analytic Representation of the Electron-Gas Correlation Energy. *Phys. Rev.* **1992**, *45* (23), 13244. https://doi.org/10.1103/PhysRevB.45.13244.

(16) Perdew, J. P.; Burke, K.; Ernzerhof, M. Generalized Gradient Approximation Made Simple. *Phys. Rev. Lett.* **1996**, *77* (18), 3865–3868. https://doi.org/10.1103/PhysRevLett.77.3865.

(17) Perdew, J. P.; Ernzerhof, M.; Burke, K. Rationale for Mixing Exact Exchange with Density Functional Approximations. *J. Chem. Phys.* **1996**, *105* (22), 9982–9985. https://doi.org/10.1063/1.472933.

(18) Kresse, G.; Furthmüller, J. Efficient Iterative Schemes for Ab Initio Total-Energy Calculations Using a Plane-Wave Basis Set. *Phys. Rev. B* **1996**, *54* (16), 11169–11186. https://doi.org/10.1103/PhysRevB.54.11169.

(19) Kresse, G.; Joubert, D. From Ultrasoft Pseudopotentials to the Projector Augmented-Wave Method. *Phys. Rev. B* **1999**, *59* (3), 1758–1775. https://doi.org/10.1103/PhysRevB.59.1758.

(20) Togo, A.; Tanaka, I. First Principles Phonon Calculations in Materials Science. *Scripta Mater.* **2015**, *108*, 1–5. https://doi.org/10.1016/j.scriptamat.2015.07.021.

(21) TURBOMOLE. *TURBOMOLE v6.2 2010, A Development of University of Karlsruhe and Forschungszentrum Karlsruhe GmbH, 1989-2007, TURBOMOLE GmbH, since 2007. Available from http://www. turbomole.com (last accessed 27 Nov, 2019).*

(22) Schäfer, A.; Horn, H.; Ahlrichs, R. Fully Optimized Contracted Gaussian Basis Sets for Atoms Li to Kr. *J. Chem. Phys.* **1992**, *97* (4), 2571–2577. https://doi.org/10.1063/1.463096.

(23) Schäfer, A.; Huber, C.; Ahlrichs, R. Fully Optimized Contracted Gaussian Basis Sets of Triple Zeta Valence Quality for Atoms Li to Kr. *J. Chem. Phys.* **1994**, *100* (8), 5829–5835. https://doi.org/10.1063/1.467146.

(24) Henkelman, G.; Arnaldsson, A.; Jónsson, H. A Fast and Robust Algorithm for Bader Decomposition of Charge Density. *Comput Mater Sci* **2006**, *36* (3), 354–360. https://doi.org/10.1016/j.commatsci.2005.04.010.

(25) Sanville, E.; Kenny, S. D.; Smith, R.; Henkelman, G. Improved Grid-Based Algorithm for Bader Charge Allocation. *J Comput Chem* **2007**, *28* (5), 899–908. https://doi.org/10.1002/jcc.20575.

(26) Tang, W.; Sanville, E.; Henkelman, G. A Grid-Based Bader Analysis Algorithm without Lattice Bias. *Journal of Physics Condensed Matter* **2009**, *21* (8). https://doi.org/10.1088/0953-8984/21/8/084204.

(27) Yu, M.; Trinkle, D. R. Accurate and Efficient Algorithm for Bader Charge Integration. *Journal of Chemical Physics* **2011**, *134* (6). https://doi.org/10.1063/1.3553716.

(28) Grimme, S.; Antony, J.; Ehrlich, S.; Krieg, H. A Consistent and Accurate Ab Initio Parametrization of Density Functional Dispersion Correction (DFT-D) for the 94 Elements H-Pu. *J. Chem. Phys.* **2010**, *132* (15), 154104–154119. https://doi.org/10.1063/1.3382344.

(29) Jain, A.; Ong, S. P.; Hautier, G.; Chen, W.; Richards, W. D.; Dacek, S.; Cholia, S.; Gunter, D.; Skinner, D.; Ceder, G.; Persson, K. A. Commentary: The Materials Project: A Materials Genome Approach to Accelerating Materials Innovation. *APL Mater* **2013**, *1* (1). https://doi.org/10.1063/1.4812323.

(30) Hjorth Larsen, A. et al. The Atomic Simulation Environment - A Python Library for Working with Atoms. *Journal of Physics Condensed Matter* **2017**, *29* (27). https://doi.org/10.1088/1361-648X/aa680e.

(31) Momma, K.; Izumi, F. VESTA 3 for Three-Dimensional Visualization of Crystal, Volumetric and Morphology Data. *J Appl Crystallogr* **2011**, *44* (6), 1272–1276. https://doi.org/10.1107/S0021889811038970.

(32) Persson, K. Materials Data on HfO2 (SG:14) by Materials Project. 2014. https://doi.org/10.17188/1206948.

(33) Lowther, J. E.; Dewhurst, J. K.; Leger, J. M.; Haines, J. Relative Stability of ZrO2 and HfO2 Structural Phases. *Phys Rev B Condens Matter Mater Phys* **1999**, *60* (21), 14485–14488. https://doi.org/10.1103/PhysRevB.60.14485.

(34) Zhao, X.; Vanderbilt, D. First-Principles Study of Structural, Vibrational, and Lattice Dielectric Properties of Hafnium Oxide. *Phys Rev B* **2002**, *65* (23), 233106. https://doi.org/10.1103/PhysRevB.65.233106.

(35) Materials Data on HfO2 by Materials Project. July 22, 2020. https://doi.org/10.17188/1284096.

(36) Kiguchi, T.; Nakamura, S.; Akama, A.; Shiraishi, T.; Konno, T. J. Solid State Epitaxy of (Hf,Zr)O2 Thin Films with Orthorhombic Phase. *Journal of the Ceramic Society of Japan* **2016**, *124* (6), 689–693. https://doi.org/10.2109/JCERSJ2.16073.

(37) Plimpton, S. Fast Parallel Algorithms for Short-Range Molecular Dynamics. *J. Comput. Phys.* **1995**, *117* (1), 1–19. https://doi.org/10.1006/jcph.1995.1039.

(38) Mullins, R.; Gutiérrez Moreno, J. J.; Nolan, M. Origin of Enhanced Thermal Atomic Layer Etching of Amorphous HfO2. *Journal of Vacuum Science & Technology A* **2022**, *40* (2), 022604. https://doi.org/10.1116/6.0001614.

(39) Broglia, G.; Ori, G.; Larcher, L.; Montorsi, M. Molecular Dynamics Simulation of Amorphous HfO 2 for Resistive RAM Applications. *Model. Simul. Mater. Sc.* **2014**, *22* (6), 065006. https://doi.org/10.1088/0965-0393/22/6/065006.

(40) Ceresoli, D.; Vanderbilt, D. Structural and Dielectric Properties of Amorphous ZrO2 and HfO2. *Phys. Rev. B* **2006**, *74* (12), 125108. https://doi.org/10.1103/PhysRevB.74.125108.

(41) Shen, W.; Kumari, N.; Gibson, G.; Jeon, Y.; Henze, D.; Silverthorn, S.; Bash, C.; Kumar, S. Effect of Annealing on Structural Changes and Oxygen Diffusion in Amorphous HfO2 Using Classical Molecular Dynamics. *J. Appl. Phys* **2018**, *123* (8), 085113. https://doi.org/10.1063/1.5009439.

(42) Strand, J.; Kaviani, M.; Afanas'Ev, V. V.; Lisoni, J. G.; Shluger, A. L. Intrinsic Electron Trapping in Amorphous Oxide. *Nanotechnology* **2018**, *29* (12), 125703. https://doi.org/10.1088/1361-6528/aaa77a.

(43) Perevalov, T. V.; Gritsenko, V. A.; Erenburg, S. B.; Badalyan, A. M.; Wong, H.; Kim, C. W. Atomic and Electronic Structure of Amorphous and Crystalline Hafnium Oxide: X-Ray Photoelectron Spectroscopy and Density Functional Calculations. *J. Appl. Phys.* **2007**, *101* (5), 053704. https://doi.org/10.1063/1.2464184.

(44) Chen, T. J.; Kuo, C. L. First Principles Study of the Structural, Electronic, and Dielectric Properties of Amorphous HfO2. *J. Appl. Phys.* **2011**, *110* (6), 064105. https://doi.org/10.1063/1.3636362.

(45) Wang, Y.; Zahid, F.; Wang, J.; Guo, H. Structure and Dielectric Properties of Amorphous High-κ Oxides: HfO2, ZrO2, and Their Alloys. *Phys. Rev. B* **2012**, *85* (22), 224110. https://doi.org/10.1103/PhysRevB.85.224110.

(46) Scopel, W. L.; Da Silva, A. J. R.; Fazzio, A. Amorphous HfO2 and Hf1-x Six O via a Melt-and-Quench Scheme Using Ab Initio Molecular Dynamics. *Phys. Rev. B* **2008**, *77* (17), 172101. https://doi.org/10.1103/PhysRevB.77.172101.

(47) Chen, G. H.; Hou, Z. F.; Gong, X. G. Density Functional Calculations on Atomic and Electronic Structures of Amorphous HfO2/Si (001) Interface. *Appl. Phys. Lett.* **2009**, *95* (10), 102905. https://doi.org/10.1063/1.3226636.

(48) Materials Data on ZnO by Materials Project. July 14, 2020. https://doi.org/10.17188/1196748.

(49) Karzel, H.; Potzel, W.; Köfferlein, M.; Schiessl, W.; Steiner, M.; Hiller, U.; Kalvius, G.; Mitchell, D.; Das, T. Lattice Dynamics and Hyperfine Interactions in ZnO and ZnSe at High External Pressures. *Phys. Rev. B* **1996**, *53* (17), 11425. https://doi.org/10.1103/PhysRevB.53.11425.

(50) Wöll, C. The Chemistry and Physics of Zinc Oxide Surfaces. *Prog Surf Sci* **2007**, *82* (2–3), 55–120. https://doi.org/10.1016/J.PROGSURF.2006.12.002.

(51) Luo, J.; Liu, J. X.; Li, W. X. H2 Activation on Pristine and Substitutional ZnO(10$\bar{1}$0) and Cr2O3(001) Surfaces by Density Functional Theory Calculations. *J. Phys. Chem. C* **2022**, *126* (21), 9059–9068. https://doi.org/10.1021/ACS.JPCC.2C02607/ASSET/IMAGES/LARGE/JP2C02607_0011.JPEG.

(52) Materials Data on Ru by Materials Project. July 15, 2020. https://doi.org/10.17188/1206459.

(53) Arblaster, J. W. Crystallographic Properties of Ruthenium. *Platinum Metals Rev.* **2013**, *57* (2), 127–136. https://doi.org/10.1595/147106713X665030.

(54) Kondati Natarajan, S.; Nies, C. L.; Nolan, M. Ru Passivated and Ru Doped ϵ-TaN Surfaces as a Combined Barrier and Liner Material for Copper Interconnects: A First Principles Study. *J. Mater. Chem. C* **2019**, *7* (26), 7959–7973. https://doi.org/10.1039/c8tc06118a.

(55) Materials Data on TaN by Materials Project. July 15, 2020. https://doi.org/10.17188/1189196.

(56) Christensen, A. N.; Lebech, B. A Reinvestigation of the Structure of ε-Tantalum Nitride. *Acta Crystallogr. B* **1978**, *34* (1), 261–263. https://doi.org/10.1107/S0567740878002733.

(57) Mullins, R.; Kondati Natarajan, S.; Elliott, S. D.; Nolan, M. Self-Limiting Temperature Window for Thermal Atomic Layer Etching of HfO2 and ZrO2 Based on the Atomic-Scale Mechanism. *Chem. Mater.* **2020**, *32* (8), 3414–3426. https://doi.org/10.1021/acs.chemmater.9b05021.





Mullins, R. H. 2023. Modelling of thin film oxide growth and etching. PhD Thesis, University College Cork.

Please note that Chapter 4 (pp. 89-117) is unavailable due to a request by the author.

CORA Cork Open Research Archive http://cora.ucc.ie

5 Modelling Atomic Layer Etching of Amorphous HfO_2

In Chapter 4 we examined the difference in thermal ALE for the fluorination step for crystalline HfO_2 and ZrO_2 using HF.[1] In this chapter the HF pulse in the first step in thermal ALE of amorphous HfO_2 ($aHfO_2$) is examined in detail with first-principles DFT calculations of the fluorination mechanism. Experimental studies have shown that crystalline films have lower etch rates than amorphous films for thermal ALE of metal oxides such as HfO_2, ZrO_2, and $HfZrO_4$ at 250 °C and Al_2O_3 at 300 °C.[2,3] Amorphous materials have a lower density than their crystalline form, which may facilitate the fluorination that leads to an expansion of the metal oxide.[2] HF molecules adsorb at the surfaces of metal oxides by forming metal–F bonds and may remain intact or dissociate.[4] If HF dissociates, it may form Hf–F and O–H bonds, and release water, similar to previous studies on etch modelling for crystalline HfO_2, ZrO_2, and Al_2O_3.[1,4] The amount etched (etch rate) is determined by how much of the oxide surface is fluorinated; a larger fluoride film thickness after fluorination can lead to more fluoride removed during the ligand-exchange step and high etch rates.[2] Similar to the previous chapter we use the N−E analysis to predict the conditions at which a self-limiting (SL) or continuous spontaneous etch (SE) reaction becomes thermodynamically favourable, subject to kinetic barriers. We also determine the maximum coverage of metal−F bonds on the surface and use this coverage to calculate a theoretical etch rate for $aHfO_2$. We study the spontaneous formation of water as well as hydrogen peroxide that resulted from some of our relaxed geometries. Combining the thermodynamic and mechanistic investigation using first-principles simulation demonstrates the origin of the large difference in etch rates for crystalline and amorphous HfO_2 allowing the design of novel ALE processes for other technologically relevant materials.

5.1 Self-limiting vs Spontaneous Etch

To predict if the HF pulse will promote spontaneous etch (SE) or a self-limiting (SL) reaction on $aHfO_2$, the energetics and thermodynamics under given conditions are compared. In a spontaneous etch process, the bulk material is fully converted to gaseous products HfF_4 or $HfOF_2$ and water. In the self-limiting etch process, the surface of $aHfO_2$ is converted to HfF_4 or $HfOF_2$ (while the bulk is preserved), releasing water; this replaces surface oxygen with fluorine from HF. Table 1 shows s two possible SE and two possible SL reactions for the HF pulse on $aHfO_2$ as well as the reaction (free) energies at 0 K and a typical thermal ALE temperature of 520 K and the computed minimum barrier to spontaneous etching. A negative

minimum barrier would indicate that spontaneous etching is thermodynamically favourable and is prevented only by potential kinetic barriers.

Table 1: Reaction energies at 0 K (ΔE) and free energies at 520 K (ΔG) from the model SE and SL reactions after the HF pulse on $aHfO_2$. For this table, the product state is 8O/16F, and the numbers in parenthesis are the minimum barriers to continuous etching.

	Reactions	ΔE (eV/M)	ΔG (eV/M)
SE1	$1HfO_{2(b)} + 4HF_{(g)} \rightarrow 1HfF_{4(g)} + 2H_2O_{(g)}$	−1.44	−1.15
SL1	$1HfO_{2(surface)} + 4HF_{(g)} \rightarrow 1HfF_{4(surface)} + 2H_2O_{(g)}$	−4.07 (2.63)	−1.87 (0.72)
SE2	$1HfO_{2(b)} + 2HF_{(g)} \rightarrow 1HfOF_{2(g)} + 1H_2O_{(g)}$	3.35	2.58
SL2	$1HfO_{2(surface)} + 2HF_{(g)} \rightarrow 1HfOF_{2(surface)} + 1\ H_2O_{(g)}$	−2.04 (5.39)	−0.94 (3.52)

The energies in Table 1 are computed as follows:

$$E(SE1) = E\left(HfF_{4(g)}\right) + 2E\left(H_2O_{(g)}\right) - \left[E\left(HfO_{2(b)}\right) + 4E\left(HF_{(g)}\right)\right],$$

$$E(SL1) = E\left(HfF_{4(surface)}\right) + 2E\left(H_2O_{(g)}\right) - \left[E\left(HfO_{2(surface)}\right) + 4E\left(HF_{(g)}\right)\right],$$

$$E(SE2) = E\left(HfOF_{2(g)}\right) + E\left(H_2O_{(g)}\right) - \left[E\left(HfO_{2(b)}\right) + 2E\left(HF_{(g)}\right)\right],$$

$$E(SL2) = E\left(HfOF_{2(surface)}\right) + E\left(H_2O_{(g)}\right) - \left[E\left(HfO_{2(surface)}\right) + 2E\left(HF_{(g)}\right)\right].$$

The models are bulk $aHfO_2$ and $aHfO_2$ surface, while the reactant is gaseous HF and water is formed from the oxygen removed from $aHfO_2$. The energies are computed at 0 K within the DFT setup described in Chapter 3, section 3.8. The free energies are computed from,

$$\Delta G = \Delta H - T\Delta S$$

where the 0 K DFT energy is corrected by the change entropy at the chosen temperature; computation of the entropy contribution is also described in Chapter 3, section 3.9.

The SE1 and SE2 reactions convert the bulk $aHfO_2$ into a volatile metal fluoride or metal oxyfluoride, respectively, and water. In reaction SE1, four HF molecules are required to etch one unit of bulk HfO_2 forming HfF_4 and water. In reaction SE2, two HF molecules are needed to etch one unit of HfO_2 to form $HfOF_2$ and H_2O. In both SE reactions, the surface of the material before and after each precursor pulse is identical and, therefore, their contributions are not required in this model. The SL1 and SL2 reactions involve the conversion of the outermost surface layer of $aHfO_2$ into the nonvolatile metal fluoride and nonvolatile metal oxyfluoride respectively with the release of water molecules. The SL product state of a HfO_2 has a

composition of 8O/16F where 8 oxygen atoms originally present on the surface are removed and replaced by 16 fluorine. For both SL reactions, the surfaces are not identical before and after the pulse and their contributions have to be included. Negative free energy means that the corresponding reaction is exergonic (favorable), while positive free energy means that the corresponding reaction is endergonic (unfavorable). At 0 and 520 K, the SE1 reaction is favorable whereas the SE2 reaction is unfavorable. Table 1 shows that the barrier to spontaneous etch is positive for all the SE and SL reactions at 0 K, indicating that the self-limiting reaction is most favorable energetically and at 520 K this barrier to spontaneous etching, although reduced, remains positive. Therefore, up to 520 K, the reactions with HF in the first step will be preferentially self-limiting on $aHfO_2$, similar to crystalline HfO_2.[1]

Only the SE1 reaction is considered for further analysis, as the SE2 reaction is unfavorable at 0 and 520 K, and the SL2 reaction is less favorable than the SL1 reaction at 0 and 520 K. In addition, the high barrier to etch for the SL2 and SE2 reactions suggests that the spontaneous formation of the metal oxyfluoride is not likely at ALE-relevant temperatures around 520 K. The reaction free energy profiles (FEPs) of the SE1 and SL1 reactions are shown in Figure 5.1, and at a given temperature and reactant pressure, these show whether spontaneous etching or self-limited conversion of $aHfO_2$ into a nonvolatile metal fluoride layer are preferred. A reactant pressure of 0.2 Torr and a product pressure of 0.01 Torr are used and the temperature range is 0 - 1000 K.

In Figure 5.1, the self-limiting reaction is preferred up to 717 K, at 718 K, the minimum barrier to etch is zero with SE1 and SL1 being isoenergetic, and at temperatures higher than 718 K, spontaneous etching becomes more favorable. At 973 K, the self-limiting reaction becomes unfavorable, while spontaneous etching remains favorable. Surface hafnium atoms are easier to remove in the ligand-exchange step when more oxygen atoms are removed due to the reduced hafnium–oxygen bond interaction.

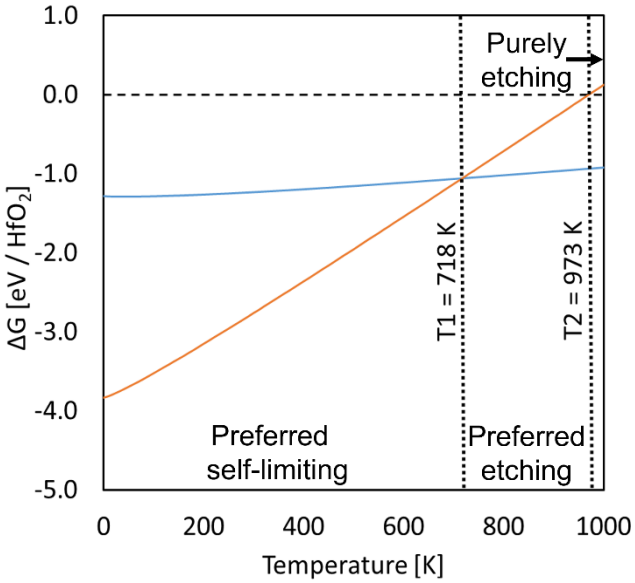


Figure 5.1: Free energy profile for the SE1 (blue) and SL1 (orange) reactions of $aHfO_2$ from 0 to 1000 K at the pressures given in the text. T1 is where the SL and SE reactions cross over for the 8O/16F model, and T2 is where spontaneous etching is preferred.

The surface of $aHfO_2$ has 19 oxygen atoms in the supercell that could react with the HF molecules; therefore, we study the FEPs for two other SL product models, 10O/20F (SL2) and 16O/32F (SL3) as shown in Table 2 and Figure 5.2 compares their thermodynamic stability with the 8O/16F model. For the 10O/20F model, 10 of the surface oxygen are removed and 20 fluorine are added to replace them. For 16O/32F, 16 oxygen are removed, and 32 fluorine are added to replace them. All three SL product states are more favorable than the SE reaction at 0 and 520 K with positive minimum barriers as shown in Table 2. Experimental work showed that the HF reaction is self-limiting on amorphous HfO_2 at 250 °C (523 K).[2] Figure 5.2 shows that the self-limiting product state models are more favorable than the spontaneous etch reaction at 523 K with the 16O/32F (SL3) being favorable up to 1302 K.

Table 2: Reaction (free) energies and minimum barriers at 0 and 520 K for the model self-limiting for 8O/16F, 10O/20F, and 16O/32F SL product states.

	SL product state	ΔE (0 K) (eV/M)	ΔG (520 K) (eV/M)
SE1	HfF_4	−1.44	−1.15
SL1	8O/16F	−4.07 (2.63)	−1.87 (0.72)
SL2	10O/20F	−4.02 (2.58)	−1.97 (0.82)
SL3	16O/32F	−5.51 (4.07)	−3.48 (2.33)

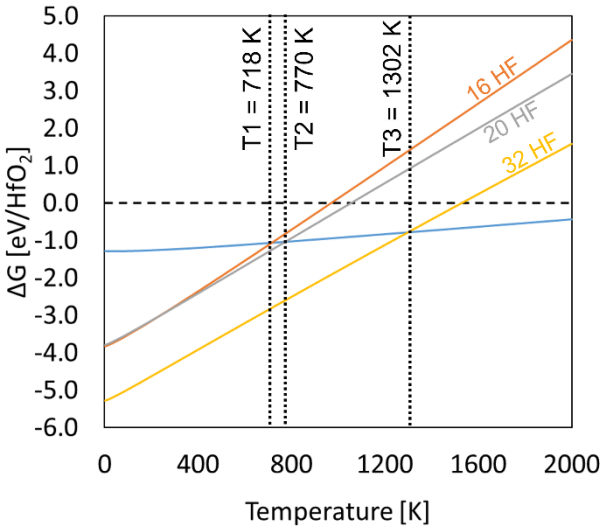


Figure 5.2: Free energy profiles of the spontaneous etching and self-limiting reac tions for $aHfO_2$. T1, T2, and T3 are the temperatures where the self-limiting and spontaneous etch reactions cross over for 8O/16F, 10O/20F, and 16O/32F models, respectively.

5.2 Adsorption of one HF to the bare amorphous HfO_2 surface

One HF molecule was adsorbed at the bare surface of $aHfO_2$ on different binding sites (labeled A, B, and C) that were chosen at random as typical examples of possible binding sites on the $aHfO_2$ surface. We computed the change in energy upon adsorption of the HF molecule at the $aHfO_2$ surface,

$$E(HF_{ads}) = E(HfO_2 - HF) - \left[E(HfO_2) + E\left(HF_{(g)}\right)\right],$$

where E(HfO_2–HF) is the total energy of the system with HF adsorbed and relaxed, E(HfO_2) is the total energy of the bare aHfO_2 surface, and E($HF_{(g)}$) is the gas-phase energy of a free HF molecule.

At each binding site, the HF molecule spontaneously dissociated to form Hf–F and O–H bonds as shown in Figure 5.3. Similar to the crystalline HfO_2 and ZrO_2,[1] HF dissociation proceeds after a stable metal–fluorine bond is formed. The Hf–F and O–H bond lengths are shown for each binding site in Figure 5.3. The computed adsorption energies for the dissociative adsorption of one HF molecule on the bare surface of aHfO_2 are −2.17, −2.92, and −2.00 eV at sites A, B, and C, respectively. These adsorption energies are more negative than on cHfO_2, most likely as a result of the surface disorder and range of coordination numbers of the surface atoms. This indicates that the fluorination steps in thermal self-limiting etch of aHfO_2 would proceed faster than on cHfO_2. The surface O atoms are l-fold, 2-fold, or 3-fold coordinated by surface Hf atoms with the 3-fold being dominant in the model used in this study. The surface Hf atoms are 5-fold, 6-fold, or 7-fold coordinated by surface O atoms with the 6-fold being dominant in the model used in this study. The lower coordination numbers in aHfO_2 promote the interaction with HF and metal fluorination.

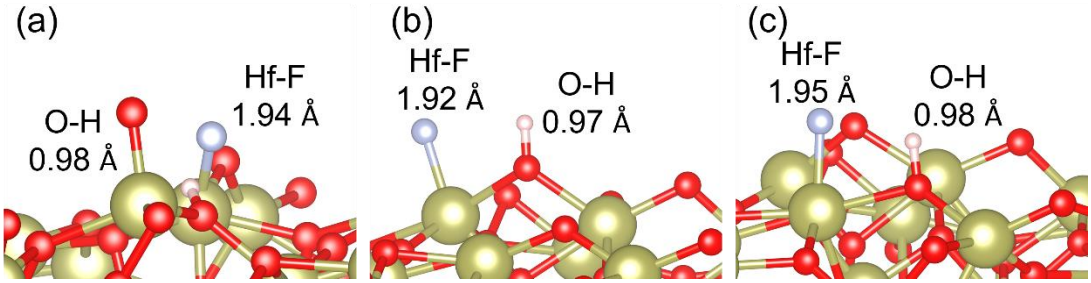


Figure 5.3: Relaxed adsorption structures for one HF molecule interacting with the bare surface of aHfO_2 for (a) 1HF A, (b) 1HF B, and (c) 1HF C. Colour scheme: Hf = gold, O = red H = white and F = light blue.

5.3 Stability of higher HF coverages

Similar to the previous chapter on crystalline HfO_2 and ZrO_2, higher HF coverages were examined by introducing up to 34 randomly oriented HF molecules per supercell approximately 3 Å from the bare surface of aHfO_2. This was studied to see if higher HF coverages would result in complete dissociation or a mixture of molecular and dissociative adsorption of the HF molecules. There are 18 topmost hafnium atoms on the surface of the supercell that may form Hf–F bonds and 19 surface oxygen atoms that can form O–H bonds or

as seen in some cases H_2O and H_2O_2. For HF coverages using 2, 3, 4, 5, and 8 molecules per supercell three different configurations (labeled A, B, and C) were used, for the 16 HF coverages two configurations (A and B) were used, and one configuration for HF coverages of 28, 30, 32, and 34 molecules per supercell. Some configurations from HF coverages of 2, 3, 4, and 5 HF resulted in spontaneous complete dissociation of the adsorbed HF molecules as shown in Figure 5.4. There was a mixture of molecular and dissociative adsorption of the HF molecules in all other HF adsorption configurations shown in Figure A 3 in the Appendix. The molecularly adsorbed HF molecules are likely to remain bonded to the surface in the next ALE step as they form strong bonds (Hf–F 6.7 eV)[5] and would likely dissociate when the kinetic barriers are reduced in the reactor during the ALE process. Similar to the previous chapter on crystalline HfO_2 and ZrO_2, the HF molecules that did not dissociate in the relaxed geometries form hydrogen bonds with the remaining HF molecules and dissociated F atoms, and at higher HF coverages, a more extensive hydrogen-bonded network is expected.

The binding energies per HF and per unit surface area of the material were computed as shown in Table 3. As the number of Hf–F bonds increases on the bare aHfO_2 surface with higher HF coverages, the binding energy per surface area becomes more favourable as shown in Table 3 and Figure 5.5(c) with Hf–F coverage from 1.1 ± 0.3 to 9.0 ± 0.3 HF/nm^2 with surface binding energies from −5.3 to −20.0 eV/nm^2.

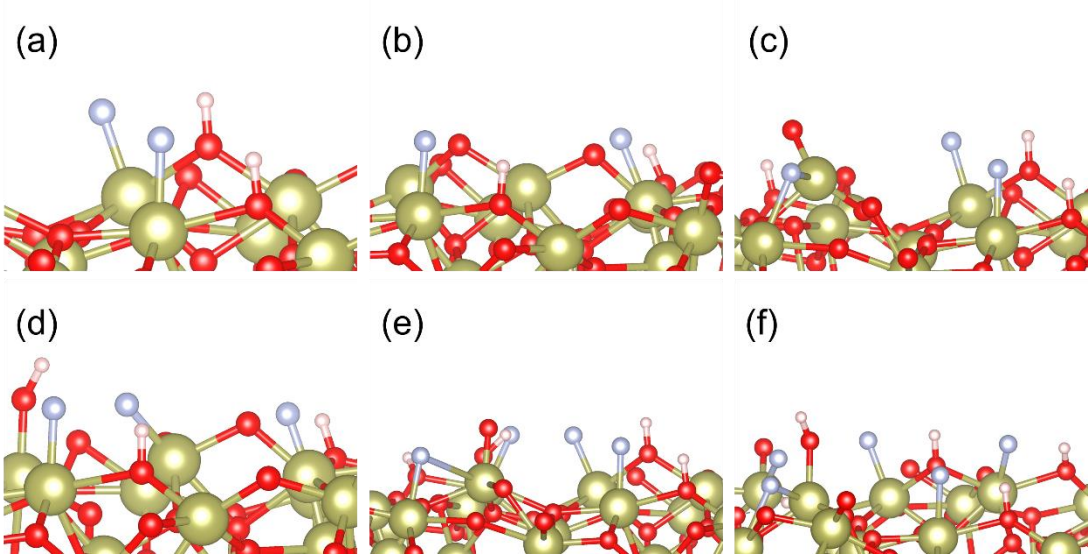


Figure 5.4: Relaxed geometries for HF coverages (a) 2HF B, (b) 2HF C, (c) 3HF B, (d) 3HF C, (e) 4HF B, and (f) 5HF A of amorphous HfO_2, were complete dissociation of HF occurred spontaneously. Colour coding is the same as in Figure 5.3.

Table 3: Adsorbate coverages and binding energies for the HF coverages on $aHfO_2$.

geometry	adsorbed HF (nm^{-2})	Hf-F (nm^{-2})	Dissociated HF (nm^{-2})	E_{bind} eV/HF	E_{bind} eV/nm^2
2HF A	1.1	0.5	0.5	−1.3	−1.4
2HF B	1.1	1.1	1.1	−2.2	−2.4
2HF C	1.1	1.1	1.1	−5.0	−5.3
3HF A	1.6	1.1	1.1	−1.7	−2.7
3HF B	1.6	1.6	1.6	−1.7	−2.8
3HF C	1.6	1.6	1.6	−2.3	−3.6
4HF A	2.1	1.6	1.6	−3.4	−7.2
4HF B	2.1	2.1	2.1	−1.8	−3.8
4HF C	2.1	1.6	1.6	−1.9	−3.9
5HF A	2.7	2.7	2.7	−1.8	−4.6
5HF B	2.7	2.7	2.7	−3.4	−8.9
5HF C	2.7	2.1	2.1	−1.7	−4.4
8HF A	4.2	3.7	3.2	−1.6	−6.6
8HF B	4.2	3.7	3.2	−1.6	−6.7
8HF C	4.2	3.2	2.7	−2.2	−9.4
16HF A	8.5	6.4	5.3	−1.7	−14.6
16HF B	8.5	3.7	3.7	−1.2	−9.9
28 HF	14.8	6.9	6.4	−1.2	−17.7
30HF	15.9	7.4	5.3	−1.1	−17.9
32HF	16.7	9.0	8.0	−1.2	−19.8
34HF	18.0	9.0	8.0	−1.1	−20.0

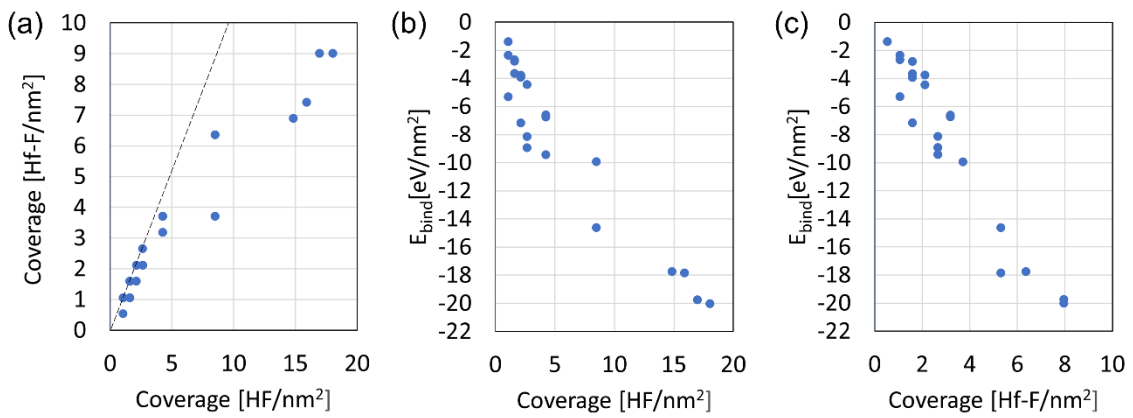


Figure 5.5: (a) Scatter plot for Hf–F cover age vs total HF coverage for the surface coverage values in Table 3. Plots (b) and (c) show the change in binding energy per square nanometer with an increase in HF and Hf–F coverage, respectively.

Hf–F coverage versus adsorbed HF coverage is shown in plot (a) in Figure 5.5 with the HF coverages that resulted in complete dissociation lying along the correlation line. This corresponds to coverages of 1.1, 1.6, 2.1, and 2.7 HF/nm^2. The remaining data points are HF coverages that correspond to geometries where partially dissociated HF and molecular adsorbed HF molecules are present and, therefore, lie below the correlation line. The Hf–F coverage starts to plateau at higher HF coverages suggesting a maximum coverage of 9.0 ± 0.3 Hf–F/nm^2. Also, note that the number of Hf–F/nm$_2$ is the same for HF coverages 32 and 34 HF. It is also shown that saturation in the binding energy is not reached at high HF coverages and Hf–F coverages, respectively, as shown in plots (b) and (c) in Figure 5.5. We use the highest adsorbed HF coverage of 34 HF with Hf–F coverage of 9.0 ± 0.3 Hf–F/nm^2 as the maximum coverage for the aHfO_2 etch rate prediction.

5.4 Spontaneous formation of H_2O and H_2O_2

H_2O spontaneously formed in some of the relaxed geometries such as 5HF C, 8HF C, and 16 HF A as shown in Figure 5.6. The dissociation of at least two HF molecules provides the hydrogen atoms required to form H_2O as a reaction product, which removes oxygen from aHfO_2 during ALE. The H–O–H bond angles were 103.5°, 105.1°, and 108.0° for 5HF C, 8HF C, and 16 HF A as shown in Figure 5.6. The energy to remove H_2O (energy of desorption) from the fluorinated surfaces of 5HF C, 8HF C, and 16 HF A, as typical examples where water was formed, was calculated using equation 4.1 from chapter 4. The desorption energies of H_2O on geometries 5HF C, 8HF C, and 16 HF A are 1.97, 1.47, and 1.67 eV, respectively. With the

high energy gain from HF adsorption at aHfO$_2$, we expect facile water desorption once it is formed.

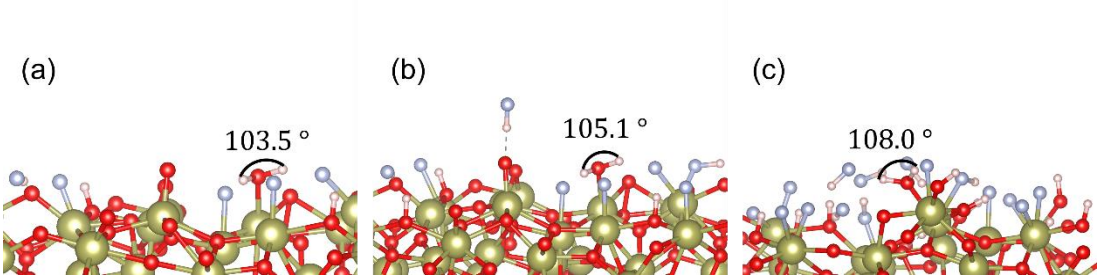


Figure 5.6: Relaxed geometries for HF coverages (a) 5HF C, (b) 8HF C, and (c) 16HF A were H2O formed spontaneously. Colour scheme same as in Figure 5.3.

The spontaneous formation of H_2O_2 was also observed at higher HF coverages such as 28HF as shown in Figure 5.7. Similar to H_2O, the dissociation of at least two HF molecules provides the hydrogen atoms required to form H_2O_2 as a reaction product which removes oxygen from aHfO$_2$. H_2O_2 formed in Figure 5.7 had an O–O bond length of 1.47 Å, O–H bond lengths of 1.05 Å and 1.02 Å, and H–O–O bond angles of 100.3° and 104.5°. The energy to remove H_2O_2 (energy of desorption) from the fluorinated surface of 28HF was calculated using equation 1 from chapter 4, where the "H_2O" terms were replaced with "H_2O_2." The desorption energy was calculated to be 0.47 eV which is low and can be achievable under process conditions to remove H_2O_2. Only the spontaneous formation of H_2O was observed in the previous chapter of HF coverages on crystalline HfO$_2$ and ZrO$_2$.

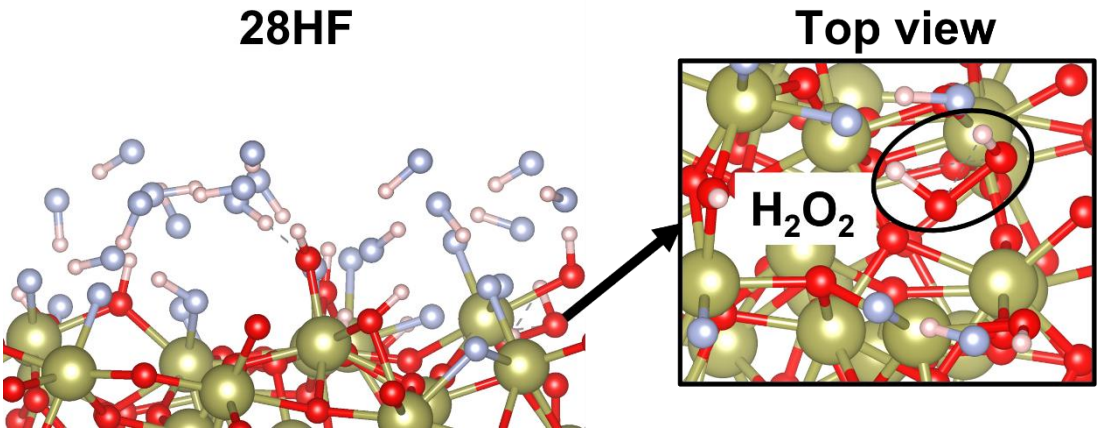


Figure 5.7: Relaxed geometry for 28HF, where H_2O_2 formed spontaneously. Colour scheme same as in Figure 5.3.

5.5 Discussion

Comparing the spontaneous etch reaction to the self-limiting reaction for the 8O/16F SL product state model, at all temperatures less than 520 K using reactant and product pressures of 0.2 and 0.01 Torr, respectively, the HF pulse on $aHfO_2$ is self-limiting in nature as the reaction energies for the self-limiting reaction were more favorable than the spontaneous etch reaction. From this, it is suggested that the first precursor pulse using HF will produce a stable and non-volatile layer of metal fluorides and H_2O or H_2O_2 as byproducts.

The reaction energies for the SL product state models 8O/16F and 10O/20F were similar up to 400 K due to the small difference in the degree of fluorination between the models. The 16O/32F SL product state model reaction energies were more favorable than the 8O/16F and 10O/20F reactions up to 1302 K. Compared to chapter 4 examining the fluorination step of crystalline HfO_2, the reaction energies for the 16O/32F product state model were less favorable than the partially fluorinated SL product state models. The greater the degree of fluorination on $aHfO_2$, the more favorable the reaction energies are, showing $aHfO_2$ favors higher fluorine content SL product states than less fluorinated SL product states, which will promote the self-limiting surface modification step. The replacement of oxygen with fluorine during fluorination may be easier due to the lower density of amorphous materials compared to crystalline materials.[2]

The spontaneous etch reaction and the self-limiting reactions mentioned above were considered at a constant reactant (HF) pressure of 0.2 Torr and a by-product pressure of 0.01 Torr. The reactant gas pressure is adjustable in the reactor whereas the product pressure is not an experimentally adjustable parameter.[6] Examining the spontaneous etch reaction and the self-limiting reactions at different reactant pressures at a constant product pressure was beyond the scope of this work. A previous study of the thermal ALE of TiO_2 using HF by Natarajan et al. examined the influence of reactant and product pressures on the FEPs of the spontaneous etch and self-limiting reactions that are similar to this work.[6] It was found that the temperature at which the FEPs of the spontaneous etch and self-limiting reactions cross over is constant at 360 K with respect to an increase in the reactant pressure with a constant product pressure.[6]

HF coverages on $aHfO_2$ ranging from 1.1 ± 0.3 to 18.0 ± 0.3 HF/nm^2 resulted in complete dissociation or mixed dissociated and molecular HF adsorption. Water and hydrogen peroxide form spontaneously after relaxation and their computed desorption energies are low enough to be overcome under process conditions. Maximum coverage of 9.0 ± 0.3 Hf–F/nm^2 was found at higher HF coverages to be used to calculate a theoretical etch rate. The surface area of the

$aHfO_2$ supercell is 1.88 nm^2 with 18 Hf atoms that can form Hf–F bonds that correspond to a coverage of 9.5 ± 0.3 Hf/nm^2. Using the maximum coverage of Hf–F 9.0 ± 0.3 Hf–F/nm^2, there will be about 0.95 F atoms per surface Hf. Similar to the analysis done in previous theoretical etch rate calculations for crystalline Al_2O_3,[4] HfO_2 and ZrO_2,[1] the amount of Hf that can be etched is one-quarter of the Hf–F coverage which is 2.3 ± 0.1 Hf/(nm^2 cycle) for $aHfO_2$. As the surface concentration of Hf atoms is 9.5 ± 0.3 Hf/nm^2, this etch rate corresponds to 0.2 monolayer/cycle. This corresponds to −78.8 ± 0.8 ng/(cm^2 cycle) and using our DFT density of bulk $aHfO_2$ (9.62 g/cm^3), our theoretical etch rate for $aHfO_2$ is −0.82 ± 0.02 Å/cycle. Our theoretical etch rate for $cHfO_2$ is −0.61 ± 0.02 Å/cycle.[1] The theoretical etch rate for $aHfO_2$ is greater than the theoretical etch rate for $cHfO_2$ by 0.21 Å/cycle.

Etch rates calculated from the experiment can differ with temperature and the reactant used in the second pulse. It was found experimentally using HF as the fluorinating reagent and DMAC as the ligand-exchange reagent at 250 °C the etch rate was 0.68 Å/cycle for $aHfO_2$ and 0.08 Å/cycle for $cHfO_2$.[2] Using HF as the fluorinating reagent and $TiCl_4$ as the ligand-exchange reagent at 250 °C the etch rate was 0.36 Å/cycle for $aHfO_2$ and 0.02 Å/cycle for $cHfO_2$.[2] We, therefore, qualitatively show the enhanced etch rate for $aHfO_2$ compared to $cHfO_2$ and provide origins of this enhanced etching on $aHfO_2$.

Unlike experimental etch rates, theoretical etch rates do not take kinetic effects into account. Hence, the maximum etch rate to remove a monolayer (ML) of material from $aHfO_2$ is also calculated. For one ML removal, 18 Hf atoms are used which requires a Hf–F coverage of 38.2 ± 0.3 F/nm^2. An etch rate of −3.47 Å/cycle was computed for one ML removal using the same method for calculating the theoretical etch rate. If an experimental etch rate greater than −3.47 Å/cycle it would suggest that subsurface Hf atoms are being etched and the reaction is no longer self-limiting. The published etch rates for metal oxides[2] are much lower than this maximum etch rate further confirming that self-limiting etching is observed.

The difference seen in thermal ALE etch rates of amorphous and crystalline HfO_2 may be due to higher density crystalline materials having bond lengths and configurations that are more uniform than for amorphous materials.[2] Amorphous materials may have void regions and undercoordinated atoms that allows for more binding sites during fluorination. HF adsorption studies for crystalline HfO_2 showed that every surface-bound F atom had a coordination number of one with surface Hf for Hf–F coverage of 7.0 ± 0.3 F/nm^2.[1] For amorphous HfO_2, the coordination number for surface-bound F atoms range from one to three, for a Hf–F coverage of 9.0 ± 0.3 F/nm^2. The greater the surface is fluorinated; the more material can be removed and a greater etch rate is obtained.

5.6 Conclusions

In this chapter, we present DFT calculations to understand the nature of the HF pulse on amorphous HfO_2 for thermal ALE. A thermodynamic analysis of the self-limiting and spontaneous etch reactions representing the fluorination on amorphous HfO_2 allowed us to predict whether the SE or SL reaction is favorable at a given temperature and a given pressure. At temperatures less than 520 K, the HF reaction is found to be in the preferred self-limiting state. This is a relatively inexpensive way to screen the reactant molecules for ALE of any given substrate. The adsorption of HF molecules on amorphous HfO_2 for HF coverages ranging from 1.1 ± 0.3 to 18.0 ± 0.3 HF/nm^2 along with analysis of H_2O and H_2O_2 formation was studied. From this analysis, we predict a theoretical etch rate based on the maximum possible coverage of surface-bound HF for amorphous HfO_2 which was calculated to be −0.82 ± 0.02 Å/cycle. This computed etch rate for amorphous HfO_2 is greater than the etch rate computed for crystalline HfO_2 from the previous chapter. We can use the presented methodology for the first pulse on crystalline and amorphous metal oxides to examine other reagents such as HCl with a similar analysis as well as examine the interaction of HF on ZnO, hydroxyl terminated crystalline HfO_2 and other oxide phase and surface facets of crystalline HfO_2.

Chapter References

(1) Mullins, R.; Kondati Natarajan, S.; Elliott, S. D.; Nolan, M. Self-Limiting Temperature Window for Thermal Atomic Layer Etching of HfO2 and ZrO2 Based on the Atomic-Scale Mechanism. *Chem. Mater.* **2020**, *32* (8), 3414–3426. https://doi.org/10.1021/acs.chemmater.9b05021.

(2) Murdzek, J. A.; George, S. M. Effect of Crystallinity on Thermal Atomic Layer Etching of Hafnium Oxide, Zirconium Oxide, and Hafnium Zirconium Oxide. *J. Vac. Sci. Technol. A* **2020**, *38* (2), 022608. https://doi.org/10.1116/1.5135317.

(3) Murdzek, J. A.; Rajashekhar, A.; Makala, R. S.; George, S. M. Thermal Atomic Layer Etching of Amorphous and Crystalline Al2O3 Films. *J. Vac. Sci. Technol. A* **2021**, *39* (4), 042602. https://doi.org/10.1116/6.0000995.

(4) Kondati Natarajan, S.; Elliott, S. D. Modeling the Chemical Mechanism of the Thermal Atomic Layer Etch of Aluminum Oxide: A Density Functional Theory Study of Reactions during HF Exposure. *Chem. Mater.* **2018**, *30* (17), 5912–5922. https://doi.org/10.1021/acs.chemmater.8b01930.

(5) Luo, Y. R. *Comprehensive Handbook of Chemical Bond Energies*; CRC Press, Boca Raton, 2007. https://doi.org/10.1201/9781420007282.

(6) Kondati Natarajan, S.; Cano, A. M.; Partridge, J. L.; George, S. M.; Elliott, S. D. Prediction and Validation of the Process Window for Atomic Layer Etching: HF Exposure on TiO2. *J. Phys. Chem. C* **2021**, *125* (46), 25589–25599. https://doi.org/10.1021/ACS.JPCC.1C08110/SUPPL_FILE/JP1C08110_SI_001.PDF.

University College Cork, Ireland
Coláiste na hOllscoile Corcaigh

CORA
Cork Open Research Archive
Cartlann Taighde Oscailte Chorcaí

Mullins, R. H. 2023. Modelling of thin film oxide growth and etching. PhD Thesis, University College Cork.

Please note that Chapter 6 (pp. 131-147) is unavailable due to a request by the author.

CORA Cork Open Research Archive http://cora.ucc.ie

7 Stability of NH_x-Surface Terminations of TaN Diffusion Barrier

In this chapter DFT calculations are used to explore the nature of the N_2/H_2 terminated TaN surfaces that are produced post plasma pulse in PEALD for the incorporation of Ru or Co into TaN. TaN is used as a diffusion barrier layer to prevent migration of copper, the currently used interconnect, into the dielectric layer in CMOS transistors.[1] Currently, the semiconductor industry uses a tri-layer stack of TaN/Ta/Cu with TaN as the barrier and Ta as the liner. However advanced interconnect technology will require high aspect ratio trench structures, therefore the copper, liner and barrier stack should only take up a small volume of the trench to preserve the low copper resistivity at the 14 nm node and smaller.[2] A proposed solution is a combined barrier and liner stack that was discussed in chapter 2 section 2.2.2. The Ru and Co PEALD processes discussed in chapter 2 section 2.2.3 saw that using NH_3 or N_2/H_2 plasmas yield films with high purity and low resistivity.

The mechanism of this plasma ALD involves the interaction of Ru and Co precursors with Cp and EtCp ligands, that are eliminated via hydrogen transfer from the NH_x-terminated TaN surface, leaving Ru or Co bonded to surface nitrogen. Therefore, deposition of Ru or Co requires both nitrogen and hydrogen. With this mechanism in mind, DFT simulation of ALD chemistries of Co and Ru requires a post N_2/H_2 or NH_3 plasma surface. Similar to earlier work on Ru, Co surfaces we consider a series of NH_x (x = 1, 2) terminations. We begin with single terminations of possible N_2/H_2 post plasma terminations on the ε-TaN (110) surface. This is then followed by higher coverages to find stable NH_x-terminations on TaN. Their reactivity towards different ruthenium and cobalt precursors will be discussed in chapter 8.

7.1 Charge analysis of bare ε-TaN (110) surface

The lowest energy surface[3] ε-TaN (110) surface is used with the full details of the surface model described in Chapter 3 section 3.9.6. The valence charges (Q) from the Bader charge partitioning scheme[4,5] of the various surface Ta atoms are $Ta^A = 3.0\ e^-$, $Ta^B = 3.6\ e^-$, $Ta^C = 3.7\ e^-$ and $Ta^D = 3.5\ e^-$. For the N atoms, the computed Bader charges are $N^a = 6.3\ e^-$ and $N^b = 6.4\ e^-$ as shown in Figure 7.1. Surface Ta atoms marked "A" are 6-fold and "B/C/D" are 3-fold coordinated by surrounding N atoms. Surface N^a atoms are 3-fold and N^b are 4-fold coordinated by surface Ta atoms. Surface N^b atoms have the same Ta-N bond length of 2.17 Å and N^a atoms have a Ta-N bond length of 2.09 Å with 6-fold Ta atoms and 1.97 Å with the 3-fold Ta atoms. The valence charges were computed by using the total charge density of the system which

includes the core charges. Considering possible NH_x terminations, there are 24 N atoms and 24 Ta atoms available to form N – H_x and Ta – NH_x bonds (x = 1 or 2) on the TaN (110) surface and these terminations are proposed possible surface terminations after the plasma half cycle in TaN ALD with NH_3 or N_2/H_2 plasma. Therefore, if all N sites form N – H_x bonds or all Ta sites form Ta – NH_x bonds, these are referred to as one monolayer (ML) of N – H_x or 1 ML of Ta – NH_x respectively.

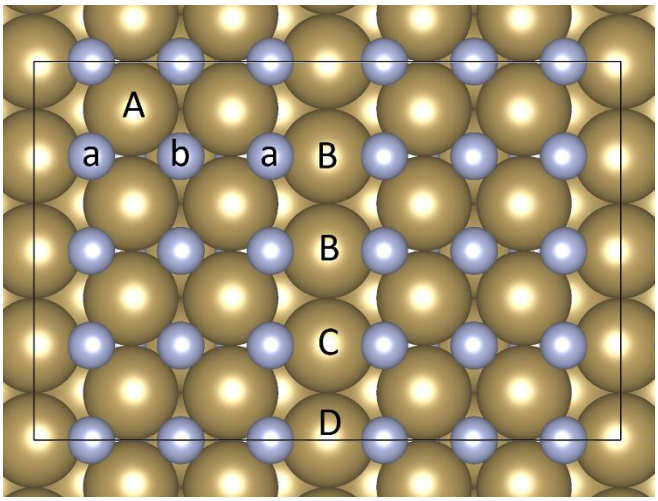


Figure 7.1. Top view of the ε-TaN (110) surface. Colour scheme is: Ta = brown and N = blue.

7.2 Surface Terminations of ε-TaN (110) to be studied

In this chapter, we examine the N_2/H_2 terminations of the bare ε-TaN (110) surface. Since there are nitrogen atoms terminating the ε-TaN (110) surface, we first consider terminations of N-H_x for the following coverages:

- 1 ML N-H
- 1 ML N-H_2
- 0.5 ML N-H/0.5 ML N-H_2

Considering surface Ta sites, other surface terminations and their coverages include:

- 1 ML Ta – NH
- 0.04 ML Ta – NH_2/0.42 ML Ta – NH/0.04 ML Ta-N
- 1 ML Ta – NH_2
- 0.67 ML Ta – NH_2
- 0.38 ML Ta – NH_2
- 0.67 ML N-H/0.67 ML Ta – NH_2

The chemisorption energy of the N_2/H_2 terminations is used to assess stability and is calculated using the formula in equation (7.1).

$$E_{ad} = E_{tot} - E_{TaN} - E_A \quad (7.1)$$

Where E_{tot}, E_{TaN} and E_A are the energy of the ε-TaN slab with termination (A = H_x, NH_x), the isolated ε-TaN slab model for the bare metal nitride surface and isolated adsorbate A respectively. The energy for the H_x and NH_x adsorbates is computed using the total energy of gas phase N_2 and H_2.

$$E_H = \frac{1}{2}(H_2) \quad (7.2)$$

$$E_{H_2} = H_2 \quad (7.3)$$

$$E_{NH} = \frac{1}{2}(E_{N_2} + E_{H_2}) \quad (7.4)$$

$$E_{NH_2} = \frac{1}{2}(E_{N_2}) + E_{H_2} \quad (7.5)$$

7.3 Single N-H_x and Ta-NH_x adsorbates

Single adsorbates of N-H_x and Ta-NH_x are first examined at different surface N and Ta sites to examine their preferred binding sites. The energy change for H adsorbed at N^a and N^b from equation (7.1) are -3.52 eV and -3.30 eV respectively and the Ta-N bonds are slightly increased by 0.10 Å as shown in panels (a) and (b) in Figure 7.2. The energy gain for NH_2 formation at N^a and N^b 4 is -4.80 eV and -4.37 eV respectively. The Ta-N distances are also increased by 0.20-0.35 Å for N^a and 0.26-0.28 Å for N^b where the N atom moves slightly outwards from the surface by 0.33-0.48 Å along the z-axis as shown in panels (c) and (d) in Figure 7.2. A Bader charge analysis also showed the adsorbed H_x species have little effect on the surface N atoms they bind to compared to the bare surface. the computed Bader charges on nitrogen are shown in Table 1.

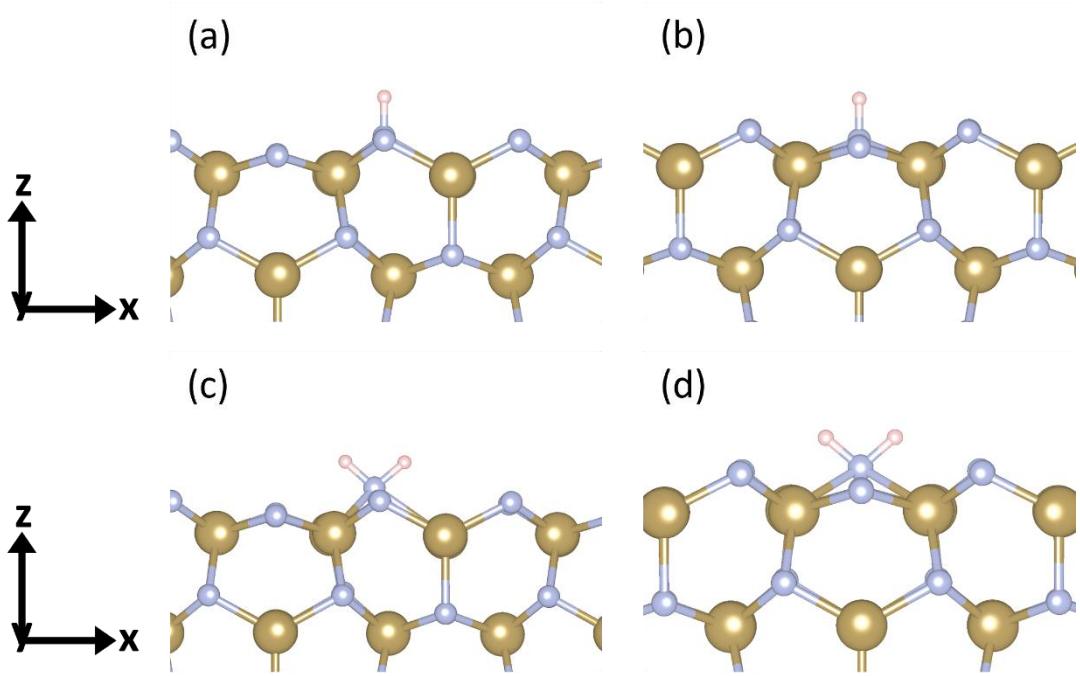


Figure 7.2: Single N-H_x adsorbed at different N sites on ε-TaN(110) surface. (a) N-H at N^a, (b) N-H at N^b, (c) N-H_2 at N^a and (d) N-H_2 at N^b. Colour scheme is: Ta = brown, N = blue and H = pink.

Table 1: Computed Bader charges for surface N atoms in bare ε-TaN in for the N-H_x structures shown in Figure 7.2.

	Bare TaN(110)	**N-H**	**N-H_2**
N^a	6.3 e^-	6.4 e^-	6.5 e^-
N^b	6.4 e^-	6.4 e^-	6.5 e^-

Next, we examine the Ta-NH_x species where NH (imine) and NH_2 (amine) are adsorbed at Ta^A, Ta^B and bridging between two Ta atoms Ta^{BC}. The energy change for NH at Ta^B, Ta^A and Ta^{BC} are -2.20 eV, -1.70 eV and -1.37 eV and the resulting geometries are shown in Figure 7.3 (a) – (c). The Ta-NH bond lengths are 1.96 Å, 1.78 Å and 2.03 Å (x2) for sites Ta^B, Ta^A and bridging Ta^{BC}. When NH is added to Ta^A the Ta atom becomes 4-fold coordinated to surface N atoms (excluding the added NH) and migrates outwards from the surface by 1.30 Å. A summary of the charges for the surface Ta atoms that form Ta-NH bonds is shown in Table 2 where Ta^A and Ta^{BC} atoms all experience small, if any change in atomic charge when NH is added. The energy change when adding NH_2 at Ta^B, Ta^A and Ta^{BC} is -4.07 eV, -5.52 eV and -4.32 eV respectively.

The added NH_2 remains in an upright position as shown in Figure 7.3 (d) – (f). Similar to adding NH, the addition of NH_2 to Ta^A results in the Ta atom becoming 4-fold coordinated by surrounding surface N atoms, and is further oxidised with a charge loss of 0.3 e^- as shown in Table 2.

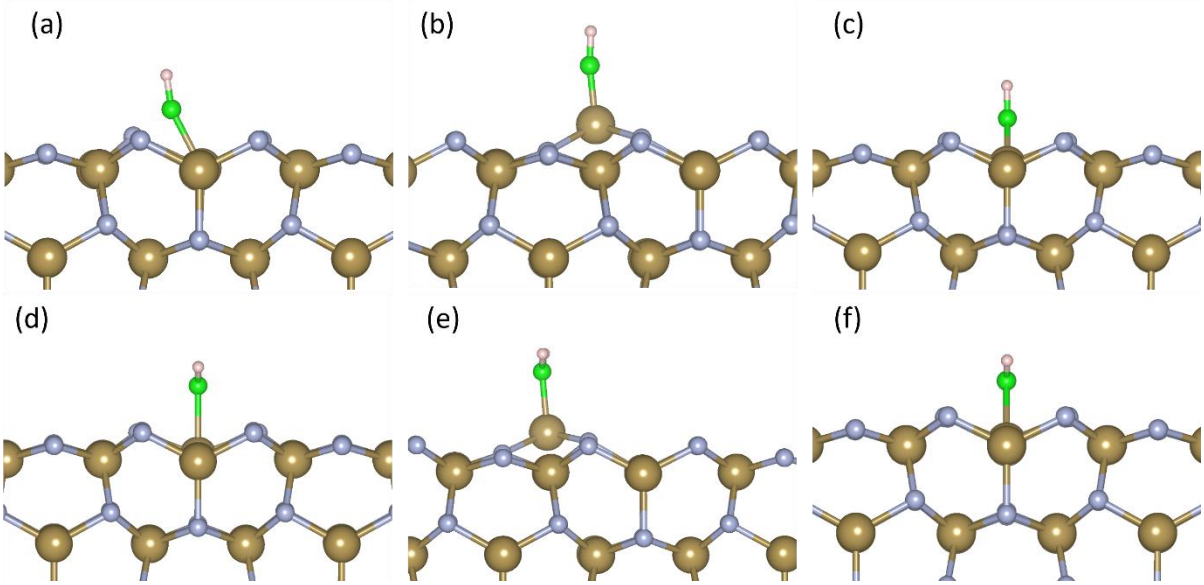


Figure 7.3: Single Ta-NH_x adsorbed at different Ta sites on ε-TaN(110) surface with N atoms from NH_x species highlighted in green for clarity. (a) Ta-NH at Ta c.n. 3, (b) Ta-NH at Ta c.n. 6, (c) Ta-NH bridging between two surface Ta c.n. 3 atoms, (d) Ta-NH_2 at Ta c.n. 3, (e) Ta-NH_2 at Ta c.n. 6 and (f) Ta-NH_2 bridging between two surface Ta c.n. 3 atoms. Colour scheme is: Ta = brown, N = blue & green and H = pink.

Table 2: Charges for Ta-NH_x adsorptions as shown in Figure 7.3.

	Bare ε-TaN (110)	**Ta with NH_x**	**Adsorbate**
Ta^B	3.6 e^-	3.6 e^-	NH
Ta^A	3.0 e^-	2.8 e^-	NH
Ta^{BC}	3.6 e^- 3.7 e^-	3.3 e^- 3.4 e^-	NH
Ta^B	3.6 e^-	3.5 e^-	NH_2
Ta^A	3.0 e^-	2.7 e^-	NH_2
Ta^{BC}	3.6 e^- 3.7 e^-	3.4 e^- 3.5 e^-	NH_2

7.4 Mixed NH/NH_2 terminations of ε-TaN (110)

Since the various N-H_x and Ta-NH_x terminations are all shown to be favourable we now investigate mixed N-H_x and Ta-NH_x terminations to explore if both terminations can be present. First, we consider one Ta and one N site each terminated with Ta-NH and N-H species, Figure 7.4 and one Ta and one N site terminated with Ta-NH and N-H_2, Figure 7.5. In most cases the structures relax with the starting terminations. The exception is the spontaneous transfer of hydrogen from N-H_2 to Ta-NH to form Ta-NH_2 observed where the initial Ta-NH is at Ta^A Figure 7.5 (b). The energy change for all structures is given in Table 3, indicate favourable surface termination of mixed N-H_x and Ta-NH on the bare ε-TaN(110) surface.

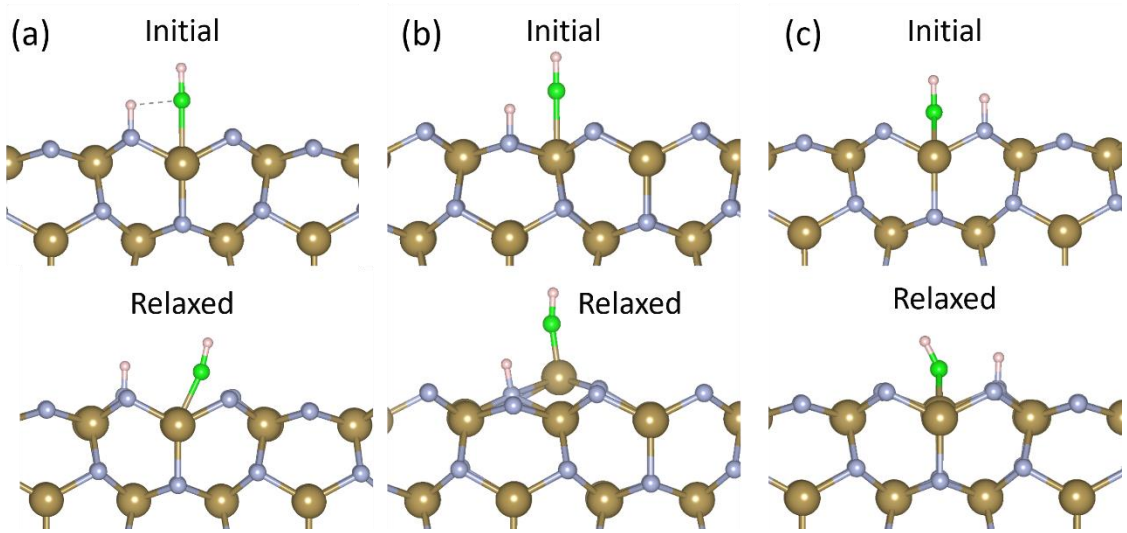


Figure 7.4: N-H and Ta-NH terminations on ε-TaN(110). (a) Ta-NH at Ta^B, (b) Ta-NH at Ta^A and (c) Ta-NH at Ta^{BC}. Colour scheme is the same as in Figure 7.3

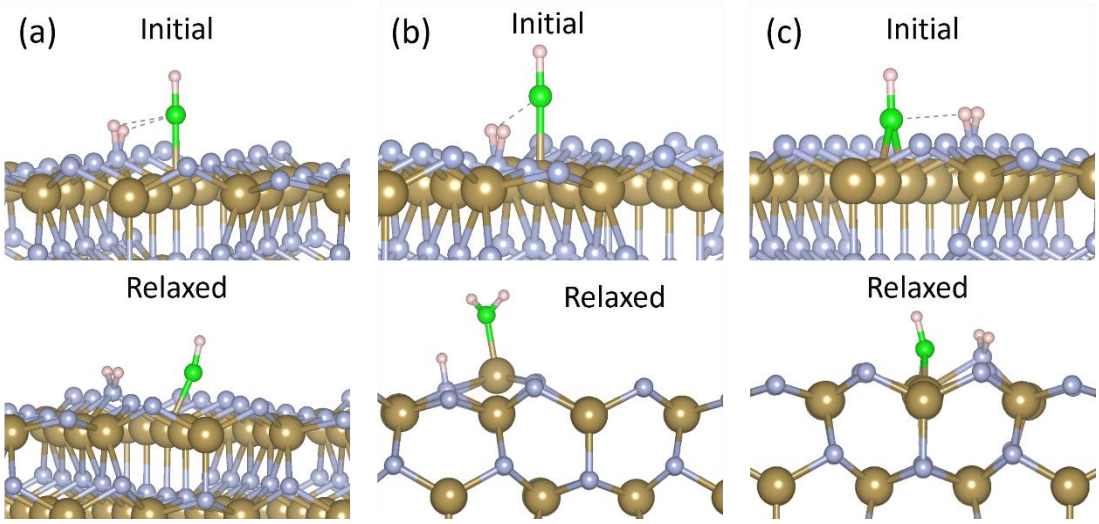


Figure 7.5: Rotated view from Figure 7.4 N-H_2 and Ta-NH terminations on ε-TaN(110). (a) Ta-NH at Ta^B, (b) Ta-NH at Ta^A and (c) Ta-NH at Ta^{BC}. Colour scheme is the same as in Figure 7.3.

Table 3: Energy change for NH_x and Ta-NH relaxed geometries in Figure 7.4 and Figure 7.5.

Surface termination	Eads (eV)
N-H, Ta-NH at Ta^B	-5.61
N-H, Ta-NH at Ta^A	-4.81
N-H, Ta-NH at Ta^{BC}	-4.93
$N-H_2$, Ta-NH at Ta^B	-7.48
$N-H_2$, Ta-NH at Ta^A	-9.37
$N-H_2$, Ta-NH at Ta^{BC}	-7.14

Next we examine NH_x with Ta-NH_2 whose structures are shown in Figure 7.6 and Figure 7.7. The spontaneous formation of NH_3 is observed with N-H when Ta-NH_2 is at Ta^B, see Figure 7.6 (a), after hydrogen is transferred from the surface nitrogen atom to the nearby NH_2. At the other Ta-NH_2 sites, no hydrogen transfer is observed and Ta^A becomes 4-fold coordinated by surface nitrogen atoms excluding the added NH_2 shown in panel (b) Figure 7.6. The spontaneous formation of NH_3 is observed for all Ta sites for mixed $N-H_2$ and Ta-NH_2 where hydrogen transfers from $N-H_2$ and bonds to the nearby NH_2 shown in Figure 7.7 leaving an N-H bond on the surface. The interaction energies are favourable for all $N-H_x$ and Ta-NH_2 relaxed geometries summarised in Table 4. This suggests that NH_2 terminations will not be stable at neighbouring N and Ta sites, with a preference for NH terminations.

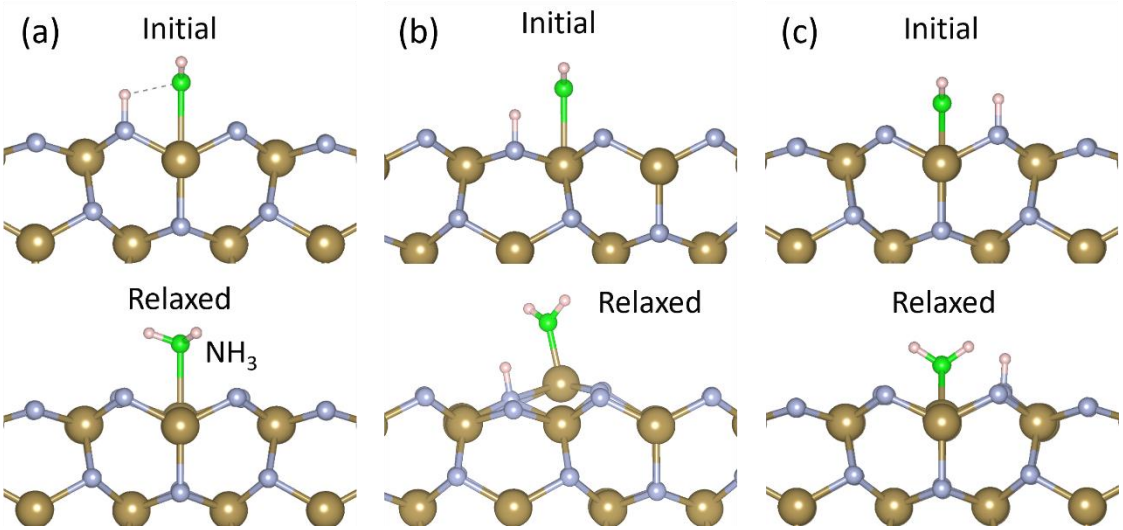


Figure 7.6: N-H and Ta-NH_2 terminations on ε-TaN (110). (a) Ta-NH_2 at Ta^B, (b) Ta-NH_2 at Ta^A and (c) Ta-NH_2 at Ta^{BC}. Colour scheme is the same as in Figure 7.3

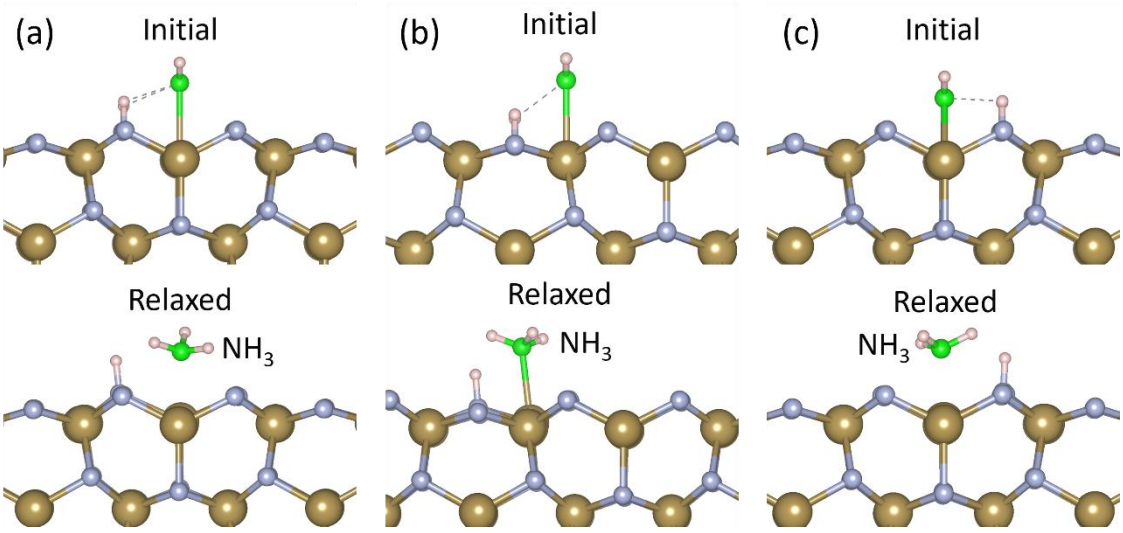


Figure 7.7: N-H_2 and Ta-NH_2 terminations on ε-TaN (110). (a) Ta-NH_2 at Ta^B, (b) Ta-NH_2 at Ta^A and (c) Ta-NH_2 at Ta^{BC}. Colour scheme is the same as in Figure 7.3.

Table 4: Adsorption energies for N-H_x and Ta-NH_2 relaxed geometries in Figure 7.6 and Figure 7.7.

Surface termination	**Eads (eV)**
N-H, Ta-NH_2 at Ta^B	-8.72
N-H, Ta-NH_2 at Ta^A	-9.36
N-H, Ta-NH_2 at Ta^{BC}	-9.44
N-H_2, Ta-NH_2 at Ta^B	-13.14
N-H_2, Ta-NH_2 at Ta^A	-12.97
N-H_2, Ta-NH_2 at Ta^{BC}	-12.15

7.5 One Monolayer Coverage of NH/NH_2 terminations of ε-TaN (110)

Studying single $N\text{-}H_x/Ta\text{-}NH_x$ adsorptions alone indicates stability of these terminations. For modelling ALD chemistry, we now consider coverages of NH_x species at TaN. The following termination at a coverage of 1 monolayer (1 ML) are examined:

- 1ML N-H/1ML Ta-NH
- 1ML $N\text{-}H_2$/1ML Ta-NH
- 1ML N-H/1ML $Ta\text{-}NH_2$
- 1ML $N\text{-}H_2$/1ML $Ta\text{-}NH_2$

The relaxed geometries shown in panels (a) – (d) in Figure 7.8.

Upon relaxation, spontaneous formation of N_2H_4, N_2H_3, N_2H_2 and N_2 occurred for 1ML N-H/1ML Ta-NH as shown in panel (a) in Figure 7.8. NH species from Ta-NH combined to form N_2H_2 which was followed by the transfer of hydrogen from a neighboring N_2H_2 to another N_2H_2 releasing N_2H_4 and N_2 during relaxation. N_2H_4 can also form from neighbouring NH_2 species bonding to each other. Hydrogen transfer from surface N-H to Ta-NH forms $Ta\text{-}NH_2$ and neighboring NH_2 and NH species combine to form N_2H_3 during relaxation. The spontaneous formation of NH_3 takes place by hydrogen transfer to NH/NH_2 species. In the next section the sub-ML coverages of 1ML of $N\text{-}H_x$ and 1ML $Ta\text{-}NH_2$ obtained will be studied.

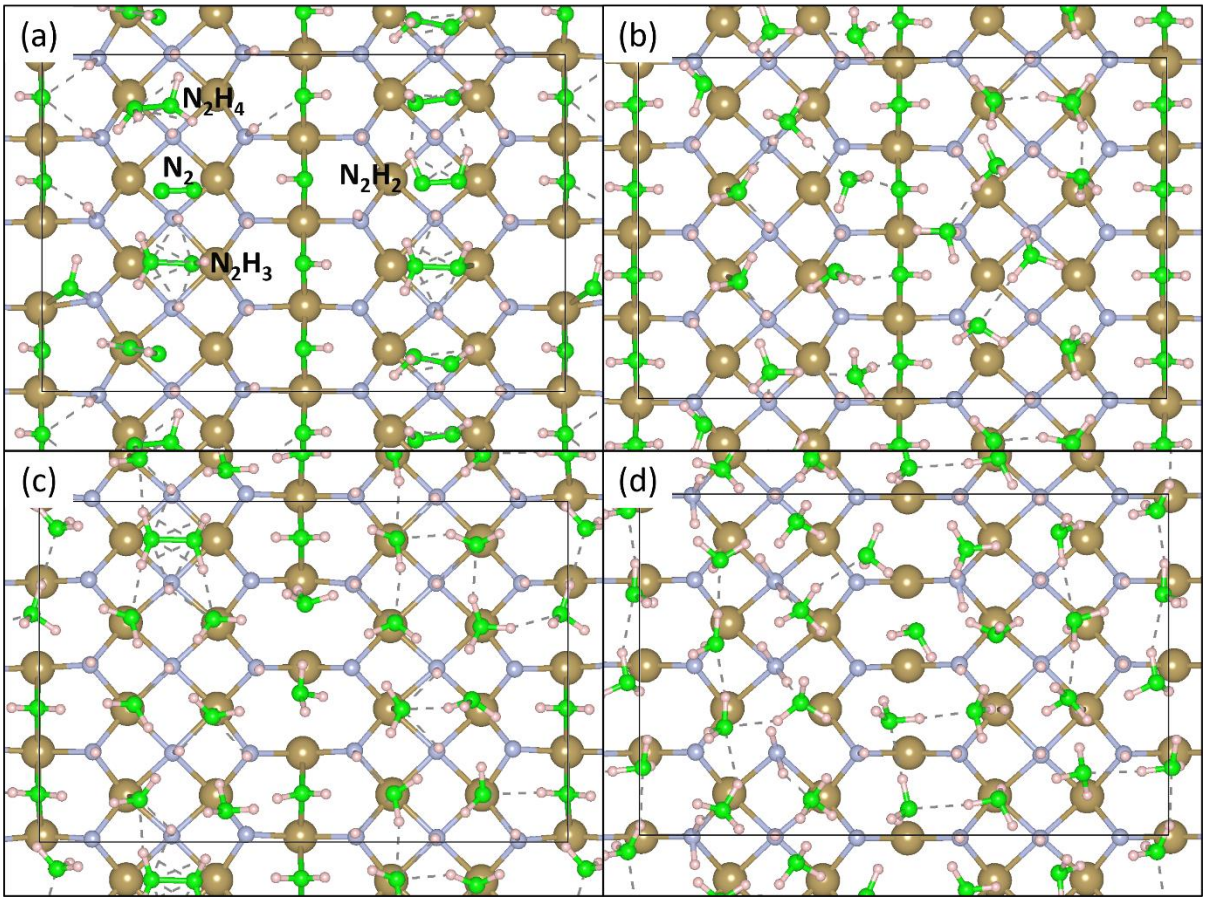


Figure 7.8: Top view of the relaxed structures starting from a coverage of 1Ml N-H_x/1ML Ta-NH_x on ε-TaN(110). (a) 1ML N-H/1ML Ta-NH, (b) 1ML N-H_2/1ML Ta-NH, (c) 1ML N-H/1ML Ta-NH_2 and (d) 1ML N-H_2/1ML Ta-NH_2. Bottom TaN layers have been removed for clarity. Colour scheme is the same as in Figure 7.3.

7.6 Coverage of N-H_x terminated ε-TaN (110)

In this section, N-H_x coverages are studied starting with 1ML N-H and 1 ML N-H_2, with the relaxed atomic structures shown in Figure 7.9 (a) and (b). The coverage of 1 ML N-H is stable upon relaxation with an energy gain of -2.63 eV per H, whereas relaxation of the initial 1 ML N-H_2 results in the formation of H_2 and new Ta-H bonds, with Ta-H distances of 1.88 – 1.91 Å and the energy change is -2.26 eV per H. Figure 7.9 (c) shows the relaxed structure for an initial coverage of 0.5 ML N-H/0.5 ML N-H_2 on ε-TaN with and energy change of -2.20 eV per H. Nitrogen atoms originally with c.n. 4 (N^b) that form N-H_2 bonds migrate upwards from the surface and have a coordination number of 2 highlighted in the purple boxes in Figure 7.9 (c).

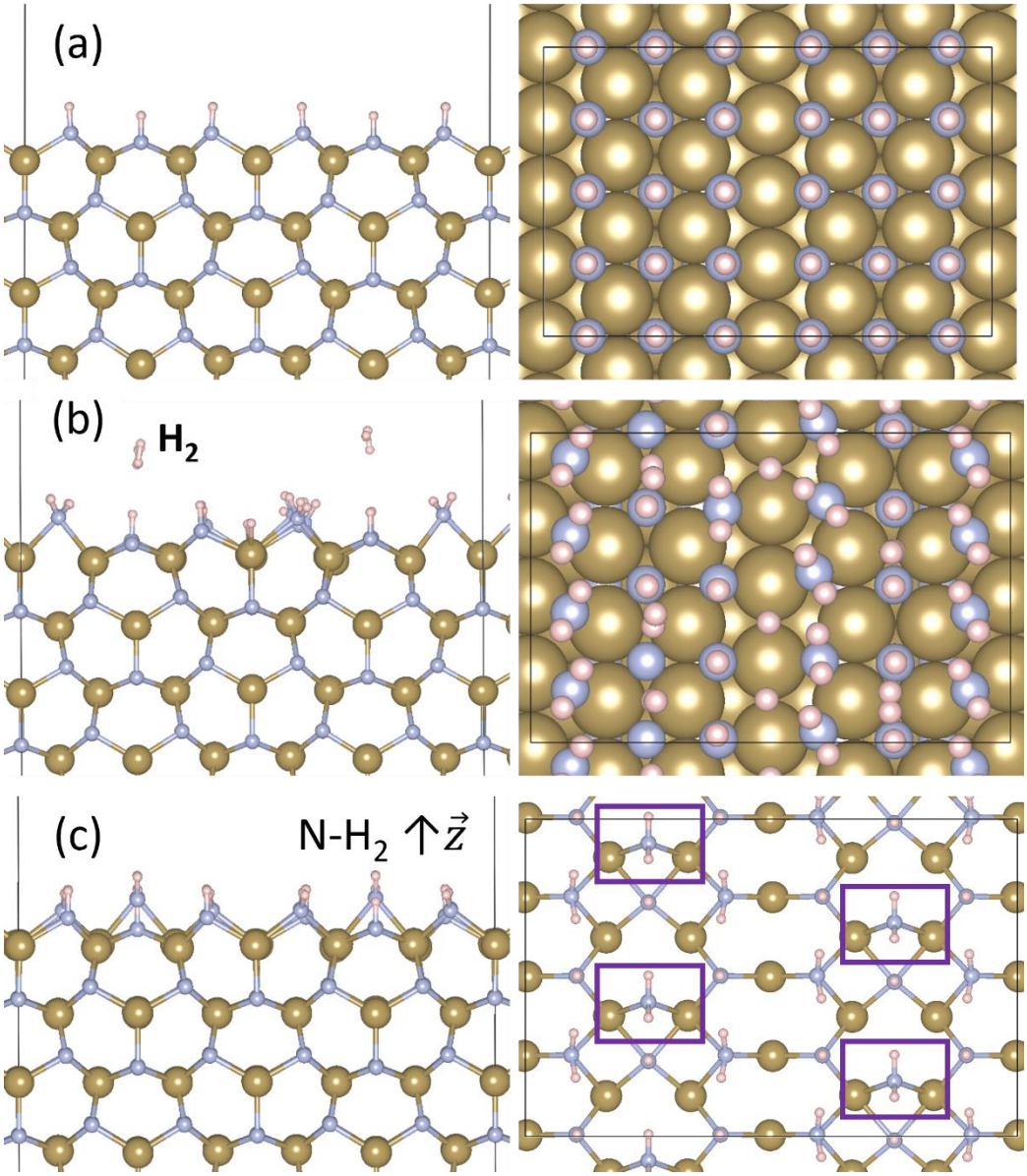


Figure 7.9: Side and top views of N-H_x terminated ε-TaN. (a) 1 ML N-H, (b) 1 ML N-H_2 and (c) 0.5 ML N-H/0.5 ML N-H_2. Colour scheme is the same as in Figure 7.2.

7.7 Coverage of Ta-NH_x terminated ε-TaN (110)

Figure 7.10 shows that the relaxed structures for initial coverage of 1 ML Ta-NH_x on ε-TaN results in N_xH_x byproducts. For 1 ML Ta-NH the formation of N_2H_2 as a result of the recombination of neighbouring NH species at Ta^A sites occurs. On the 1 ML Ta-NH_2 terminated ε-TaN surface the spontaneous formation of N_2H_4, N_2H_3 and NH_3 occurs as shown in Figure 7.10 (b). The energy change per NH_x for 1 ML Ta-NH and 1 ML Ta-NH_2 are -2.04 eV and -5.35 eV respectively. Coverages of 1 ML Ta-NH_x are not stable due to the formation of N_xH_x species and therefore coverages of less than one monolayer are explored next.

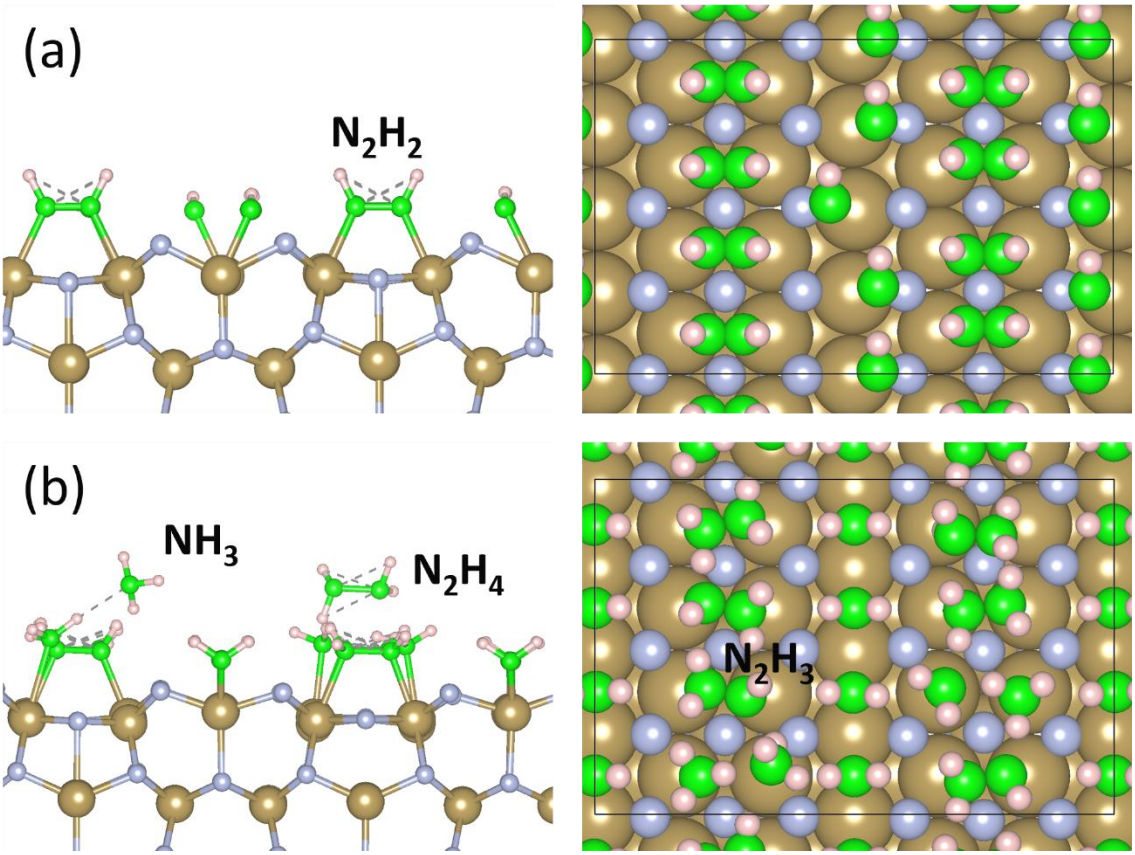


Figure 7.10: Side and top views of Ta-NH_x terminated ε-TaN. (a) 1 ML Ta-NH and (b) 1 ML Ta-NH_2. Colour scheme is the same as in Figure 7.3.

We find stable coverages of 0.04 ML Ta-NH_2/0.42 ML Ta-NH/0.04 ML Ta-N, Figure 7.11 (a), 0.67 ML Ta-NH_2 Figure 7.11 (b) and 0.38 ML Ta-NH_2 Figure 7.11 (c) and for these coverages, there was no formation of the byproducts discussed above for the initial 1ML Ta-NH_x coverages.

At a coverage of 0.5 ML of NH termination on the TaN surface, one NH_2 forms from spontaneous transfer of a hydrogen from one NH to a neighbouring NH, leaving a nitrogen atom that bonds to three Ta atoms shown in the red box of panel (a) in Figure 7.11. Therefore, the resulting coverage after relaxing the initial 0.5 ML NH structure is 0.04 ML Ta-NH_2/0.42 ML Ta-NH/0.04 ML Ta-N. The relaxed structures of 0.67 ML Ta-NH_2 and 0.38 ML Ta-NH_2 do not undergo any spontaneous hydrogen transfer or formation of any gas phase $(NH)_y$ species. A stable coverage of 0.67 ML N-H/0.67 ML Ta-NH_2 shown in Figure 7.12. Only Ta^C and Ta^D atoms were oxidized as indicated in the top view of 0.67 ML N-H/0.67 ML Ta-NH_2 with the value in black being the Ta charge for bare ε-TaN (110) and the value in red is the Ta charge after NH_2 adsorption.

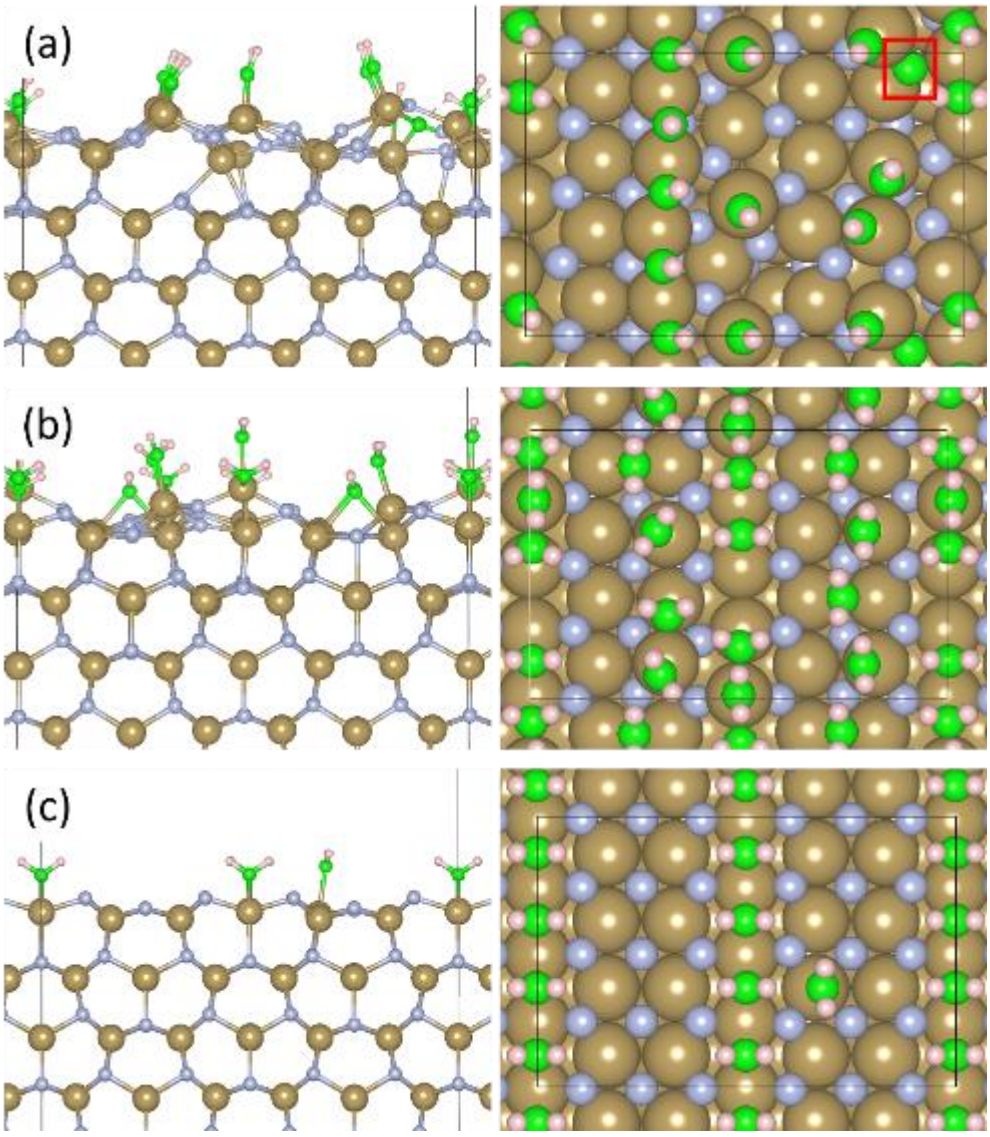


Figure 7.11: Side and top views of Ta-NH_x terminated ε-TaN. (a) 0.04 ML Ta-NH_2/0.42 ML Ta-NH/0.04 ML Ta-N, (b) 0.67 ML Ta-NH_2 and (c) 0.38 ML Ta-NH_2. Colour scheme is the same as in Figure 7.3.

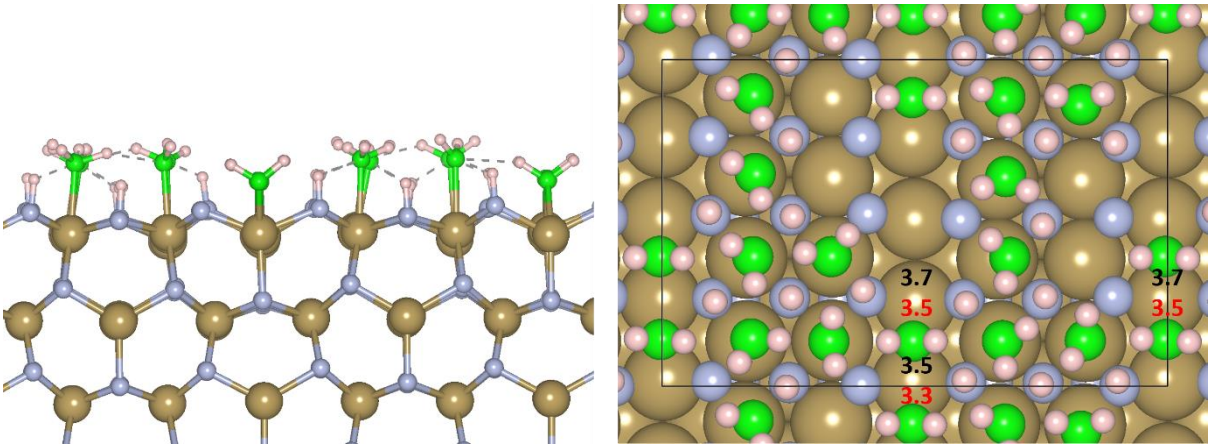


Figure 7.12: Side and top view of 0.67 ML N-H/0.67 ML Ta-NH_2 with computed Bader charge for Ta^C included. (red = Ta charge after NH_2 adsorption and black = Ta charge for bare ε-TaN (110)). Colour scheme is the same as in Figure 7.3.

Some surface Ta atoms are oxidised upon the adsorption of the NH_x species as shown in Figure 7.13 (a) – (c). The change in the computed Bader charge is 0.2-0.9 e^- for 0.04 ML Ta-NH_2/0.42 ML Ta-NH/0.04 ML Ta-N, 0.2-0.8 e^- for 0.67 ML Ta-NH_2 and 0.2-0.5 e^- for 0.38 ML Ta-NH_2. Surface Ta atoms for the coverage of 0.38 ML Ta-NH_2 remain Ta c.n. 3 and Ta c.n. 6 excluding the added NH_2 species. Note that the valence charge of Ta is 5 e^-, the computed charges show that some Ta atoms have been further oxidised.

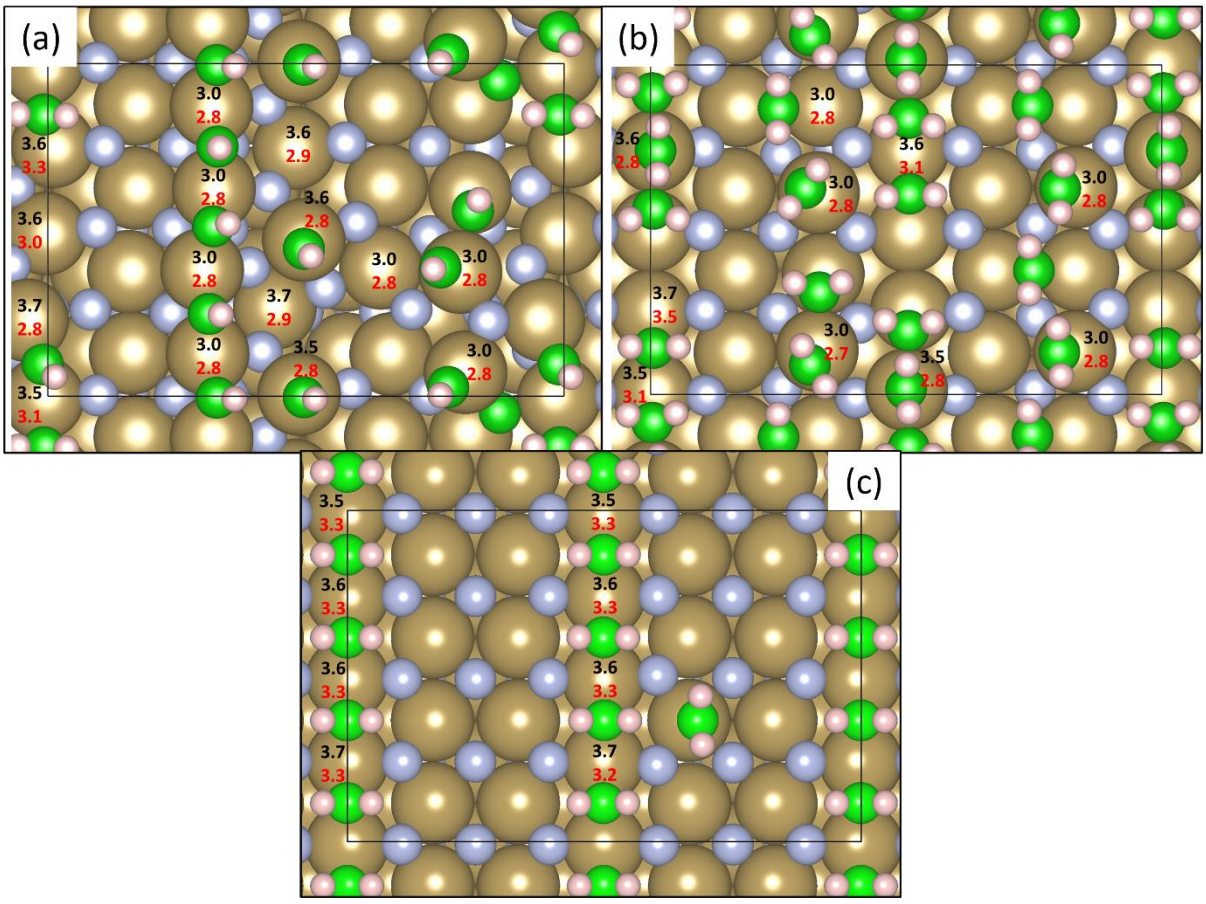


Figure 7.13: Oxidation of Ta atoms upon the adsorption of NH_x. Black is Ta charge for bare ε-TaN (110) surface and red is Ta charge after NH_x adsorption for (a) 0.04 ML Ta-NH_2/0.42 ML Ta-NH/0.04 ML Ta-N, (b) 0.67 ML Ta-NH_2 and (c) 0.38 ML Ta-NH_2. Colour scheme is the same as in Figure 7.3.

7.8 Conclusions

When modelling possible ALD chemistries on a target substrate it is important to explore the stability and coverage of different surface terminations. The ALD chemistry of TaN using nitrogen/hydrogen containing plasma species should yield a surface terminated with NH or NH_2 species which is then ready for the introduction of the metal precursor in the next full ALD cycle. For ε-TaN we have to consider surface terminations involving both surface Ta and N sites, which is more complex. We have explored models in which H species have adsorbed at surface nitrogen sites, yielding NH and NH_2 and adsorption of NH or NH_2 at Ta sites to find stable coverages of these terminations. Initially single N-H_x and Ta-NH_x species allowed us to examine their stability as isolated species on the otherwise bare ε-TaN (110) surface. For N-H_x, H adsorbs favourably at both types of N binding sites and NH_x is stable at all Ta surface sites. Some surface distortion can be seen, for both surface N and surface Ta, which can migrate

outwards by 0.38 – 0.44 Å and 1.30 Å respectively. Charge analysis showed that NH and NH_2 species oxidised the surface Ta atoms and surface N atoms that bond to added H_x species have little to no effect. There was no spontaneous transfer of hydrogen from the added NH/NH_2 species to surface N atoms. Adsorbing NH and NH_2 to neighbouring sites can promote H transfer to give NH_3 and N_2H_4. The spontaneous formation of NH_3 was observed for when N-H_x and Ta-NH_2 are direct neighbours. Starting from full surface coverages 1 ML N-H_x/1 ML Ta-NH_x spontaneous formation of N_2H_4, N_2H_3, N_2H_2, NH_3 and N_2 can occur showing the instability of these surface terminating species at highest coverages and showing that sub-ML coverage will be preferred. Stable coverages of 1 ML N-H, 0.5 ML N-H/0.5 ML N-H_2, 0.04 ML Ta-NH_2/0.42 ML Ta-NH/0.04 ML Ta-N, 0.67 ML Ta-NH_2, 0.38 ML Ta-NH_2 and 0.67 ML N-H/0.67 ML Ta-NH_2 will be used to examine the reactivity towards different ruthenium and cobalt precursors in the next chapter.

References

(1) Lane, M.; Dauskardt, R. H.; Krishna, N.; Hashim, I. Adhesion and Reliability of Copper Interconnects with Ta and TaN Barrier Layers. *J Mater Res* **2000**, *15* (1), 203–211. https://doi.org/10.1557/JMR.2000.0033.

(2) Kondati Natarajan, S.; Nies, C. L.; Nolan, M. The Role of Ru Passivation and Doping on the Barrier and Seed Layer Properties of Ru-Modified TaN for Copper Interconnects. *J. Chem. Phys.* **2020**, *152* (14), 144701. https://doi.org/10.1063/5.0003852.

(3) Kondati Natarajan, S.; Nies, C. L.; Nolan, M. Ru Passivated and Ru Doped ϵ-TaN Surfaces as a Combined Barrier and Liner Material for Copper Interconnects: A First Principles Study. *J. Mater. Chem. C* **2019**, *7* (26), 7959–7973. https://doi.org/10.1039/c8tc06118a.

(4) Sanville, E.; Kenny, S. D.; Smith, R.; Henkelman, G. Improved Grid-Based Algorithm for Bader Charge Allocation. *J Comput Chem* **2007**, *28* (5), 899–908. https://doi.org/10.1002/jcc.20575.

(5) Henkelman, G.; Arnaldsson, A.; Jónsson, H. A Fast and Robust Algorithm for Bader Decomposition of Charge Density. *Comput Mater Sci* **2006**, *36* (3), 354–360. https://doi.org/10.1016/j.commatsci.2005.04.010.

8 Incorporation of ruthenium or cobalt into TaN for a combined barrier and liner material

In this chapter the incorporation of ruthenium or cobalt into TaN is investigated for NH_x-terminated ε-TaN (110) surfaces that were discussed in chapter 7. This work is carried out for the design of a combined barrier and liner material that was developed in refs [1–4] discussed in chapter 2 section 2.2.2. Experimental PEALD processes for Ru and Co reported that NH_3 plasma or N_2/H_2 plasma are required to obtain metallic films with high purity and low resistivity.[5–12] In chapter 7 the post plasma pulse surfaces of ε-TaN (110) were studied, and stable NH_x-terminations were obtained:

- 1 ML N-H
- 0.5 ML N-H/0.5 ML N-H_2
- 0.04 ML Ta-NH_2/0.42 ML Ta-NH/0.04 ML Ta-N
- 0.67 ML Ta-NH_2
- 0.38 ML Ta-NH_2
- 0.67 ML N-H/0.67 ML Ta – NH_2

The reactivity of ruthenium and cobalt precursors $RuCp_2$, $Ru(EtCp)_2$, RuO_4, $CoCp_2$ and $Co(EtCp)_2$ are studied on the NH_x-terminated ε-TaN (110) surfaces listed above in this chapter using first-principles DFT. This allows us to understand the mechanism of Ru or Co PEALD on TaN using N_2/H_2 plasma as the coreactant.

We begin by studying the interaction of a single Cp-containing Ru/Co precursor on each NH_x-terminated ε-TaN (110) surface. This is followed by calculating the reaction energy after the first ligand is removed via hydrogen transfer from the NH_x-terminated ε-TaN (110) surface. Surfaces that favorably promote ligand elimination are further investigated by examining the reaction pathway which also includes activation barriers. The reactions for higher precursor coverages are also studied to determine the nature of the surface after the metal precursor pulse. Finally, the interaction of hydrogen plasma with the -Cp, -EtCp or oxygen ligands bound to the metal fragments on the surface is examined to determine if a subsequent hydrogen-including plasma pulse can remove these ligands to deposition Ru or Co on the surface. The results from this work can guide PEALD experiments for the incorporation of ruthenium and cobalt into TaN as a combined barrier and liner material.

8.1 Chemistry of Bis(cyclopentadienyl)ruthenium(II), $RuCp_2$, precursor at TaN surfaces

8.1.1 $RuCp_2$ interaction at 1 ML N-H-terminated ε-TaN surface

The ruthenium precursor $RuCp_2$ was adsorbed at the 1 ML N-H-terminated ε-TaN (110) surface in a perpendicular or upright interaction mode at the substrate with one Cp ring interacting with the surface or parallel to the surface, horizontal, with both Cp rings interacting with the surface.

The adsorption energy is defined by the formula:

$$E_{ads} = E_{tot} - E_{NH_x/metal} - E_{precursor} \quad (8.1)$$

where E_{tot}, $E_{NH_x/metal}$, and $E_{precursor}$ are the energy of the NH_x-terminated ε-TaN (110) slab with precursor $RuCp_2$, the slab model for the NH_x-terminated ε-TaN (110) surface, and isolated precursor $RuCp_2$ respectively. Negative interaction energy corresponds to exothermic interaction and all the energies were computed with the van der Waals correction[13] included. The interaction of $RuCp_2$ was favourable on the 1 ML N-H surface with strong interaction energies of -2.01 eV and -2.06 eV for the upright and horizontal interaction modes respectively with their geometries shown in panels (a) and (b) in Figure 8.1.

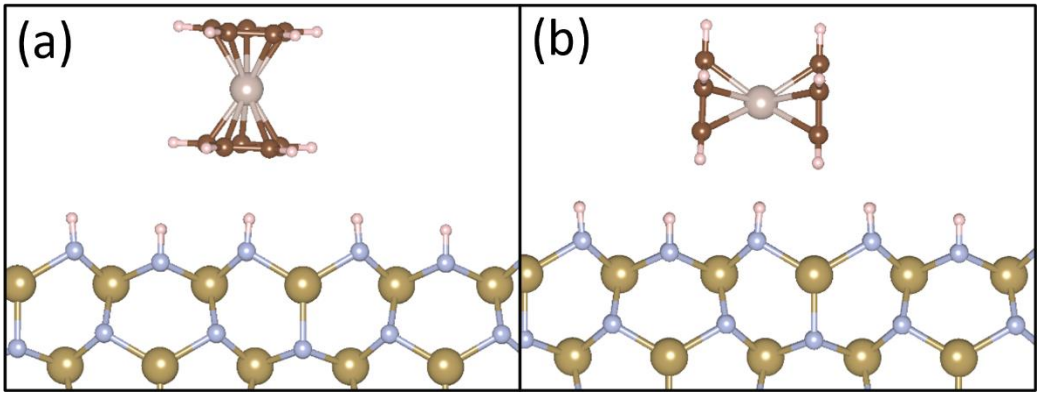


Figure 8.1. $RuCp_2$ interaction on 1 ML N-H terminated ε-TaN (110) surface. (a) Upright interaction mode and (b) horizontal interaction mode.
Colour scheme is Ta = brown, N = blue, H = pink, C = dark brown and Ru = grey.

The Cp ligand elimination is facilitated by hydrogen transfer from the N-H-terminated ε-TaN (110) surface to the Cp ring which forms CpH that may desorb. In Table 1, ΔE CpH 1 and ΔE CpH 2 are the reaction energies after the first and second CpH eliminations respectively. If the reaction energy after the first CpH elimination is favourable (exothermic) then the second CpH elimination is calculated. If ΔE CpH 1 is positive (endothermic), hydrogen transfer from the 1

ML N-H ε-TaN (110) surface to remove the first Cp ligand is unfavourable. There was no spontaneous hydrogen transfer observed therefore CpH elimination is modelled by removing one Cp ligand along with a surface H atom, section 8.1.3.

The reaction energies for the first CpH elimination are favourable whereas for the second CpH elimination they are unfavourable showing that hydrogen transfer from the surface can remove up to one Cp ligand from the $RuCp_2$ precursor at this coverage on the 1 ML N-H surface.

Table 1: Calculated interaction energies for $RuCp_2$ on NH_x-terminated ε-TaN (110) surfaces including the reaction energies after the first and second CpH elimination. (U) = upright interaction mode and (H) = horizontal interaction mode. The geometries for $RuCp_2$ interaction on the NH_x-terminated ε-TaN surfaces are shown in Figure 8.1 and Figure A 4 in the Appendix.

NH_x-terminated ε-TaN (110)	**E_{ads} (eV)**	**ΔE CpH 1 (eV)**	**ΔE CpH 2 (eV)**
N-H_x			
1 ML N-H (U)	-2.01	**-0.53**	1.54
1 ML N-H (H)	-2.06	**-1.12**	1.29
0.5 ML N-H/0.5 ML N-H_2 (U)	-0.81	0.29	
0.5 ML N-H/0.5 ML N-H_2 (H)	-0.51		
Ta-NH_x			
0.04 ML Ta-NH_2/0.42 ML Ta-NH/0.04 ML Ta-N (U)	-1.45	0.45	
0.04 ML Ta-NH_2/0.42 ML Ta-NH/0.04 ML Ta-N (H)	-0.64		
0.67 ML Ta-NH_2 (U)	-0.89	2.52	
0.67 ML Ta-NH_2 (H)	-0.63		
0.38 ML Ta-NH_2 (U)	-0.60		
0.38 ML Ta-NH_2 (H)	-0.85	1.80	
Mixed N-H, Ta-NH_2			
0.67 ML N-H/0.67 ML Ta – NH_2 (U)	-0.86	1.13	
0.67 ML N-H/0.67 ML Ta – NH_2 (H)	-0.62		

8.1.2 $RuCp_2$ interaction at other ε-TaN (110) surface terminations

The interaction energy for $RuCp_2$ on the 0.5 ML N-H/0.5 ML N-H_2 surface is -0.81 eV for the upright interaction mode and -0.51 eV for the horizontal interaction mode. For the horizontal interaction mode, CpH elimination was not calculated for that surface. The reaction energy for the first CpH elimination was also calculated for favourable $RuCp_2$ interactions on the other NH_x-terminated ε-TaN (110) surfaces which are all unfavourable as shown in Table 1. This indicates that CpH elimination through hydrogen transfer occurs exclusively on the 1 ML N-H ε-TaN (110) surface when using the $RuCp_2$ precursor.

8.1.3 Single $RuCp_2$ Reaction Pathway on 1 ML N-H ε-TaN

There was no spontaneous hydrogen transfer observed upon the interaction of $RuCp_2$ to the NH_x-terminated ε-TaN (110) surfaces therefore the hydrogen transfer step must overcome an activation barrier. Similar to our earlier work on Cp-containing precursors[14–16], the elimination of Cp ligands can proceed through hydrogen transfer, CpH formation and CpH desorption from the surface. Since the first Cp ligand elimination is overall favourable for $RuCp_2$ on the 1 ML N-H ε-TaN (110) surface for both interaction modes, the reaction pathway is studied by including the hydrogen transfer barriers for both the upright and horizontal interaction modes. Hydrogen transfer is modelled by moving a surface H atom to a Cp ligand of the precursor. The reaction energies of precursor interaction, hydrogen transfer, CpH formation and CpH desorption are calculated with reference to the 1 ML N-H ε-TaN (110) surface and free $RuCp_2$ as the starting reactants and free CpH as a product. CpH formation is the energy required for CpH to desorb from the precursor.

The reaction pathways for the upright and horizontal interaction modes of $RuCp_2$ on 1 ML N-H-terminated ε-TaN (110) are plotted in Figure 8.2 with the geometries for each step shown in Figure 8.3 and Figure 8.4. The individual reaction energies of each step are listed in Table A 1 in the Appendix.

The first hydrogen transfer to the Cp ligand is exothermic but has a high barrier of 1.17 eV for the upright interaction mode and a more moderate barrier of 0.58 eV for the horizontal precursor interaction mode. The formation and desorption of the first CpH is exothermic for both interaction modes with reaction energies -0.53 eV and -1.52 eV for the upright and horizontal interaction modes respectively.

The second hydrogen transfer to the remaining Cp ligand is exothermic with a moderate barrier of 0.48 eV but the CpH formation is endothermic as shown in plot (a) in Figure 8.2 for the upright interaction mode. The overall reaction energy becomes exothermic after the second

CpH desorption which may be due to the spontaneous formation of an Ru-H bond shown in panel (f) in Figure 8.3, with an Ru-H bond length of 1.59 Å. For the horizontal interaction mode, the overall reaction energy is endothermic at 1.27 eV after the second CpH formation and desorption with a moderate energy barrier of 0.76 eV for the second H transfer. Based on these results the elimination of the first Cp ligand from the horizontal interaction mode is favourable via H transfer from the 1 ML N-H ε-TaN (110) surface. Since the second CpH formation is ultimately endothermic for both interaction modes, the ε-TaN (110) surface will be terminated with RuCp fragments.

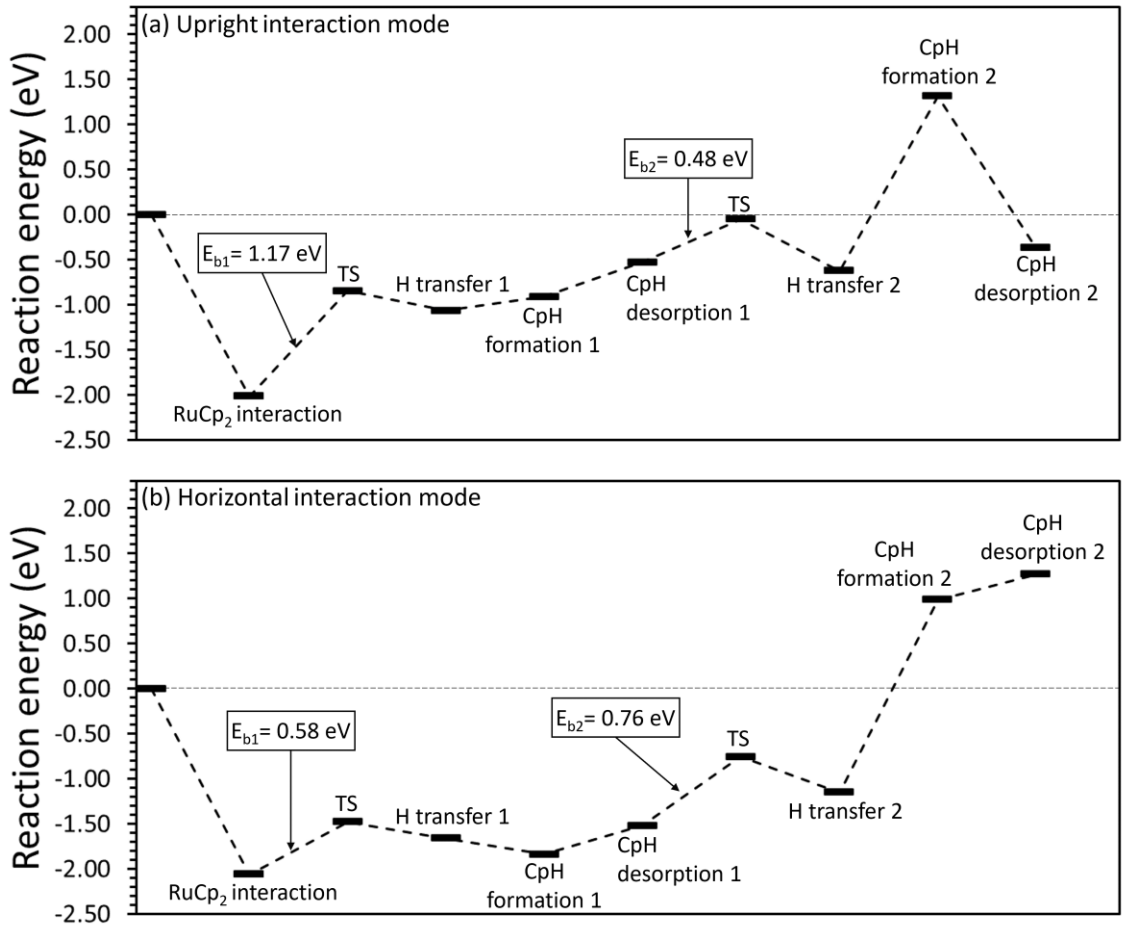


Figure 8.2. $RuCp_2$ reaction pathway on 1 ML N-H ε-TaN (110) for (a) upright interaction mode and (b) horizontal interaction mode with activation barriers (E_b) highlighted in boxes. TS corresponds to the transition state energy for hydrogen transfer. H in H transfer stands for hydrogen.

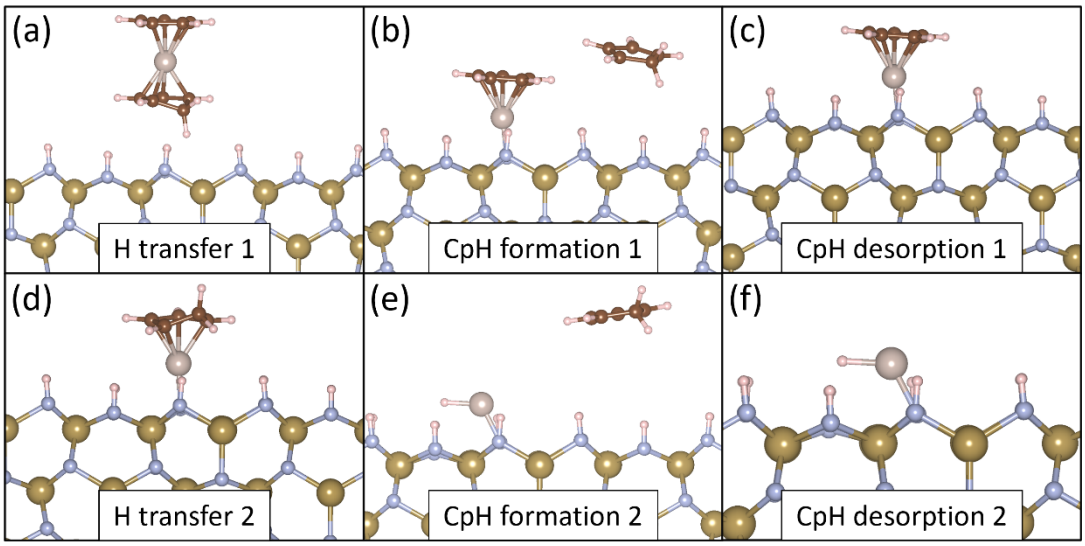


Figure 8.3. Geometries of the individual reaction pathway steps for the upright interaction mode of $RuCp_2$ on 1 ML N-H ε-TaN (110). Colour scheme is the same as in Figure 8.1.

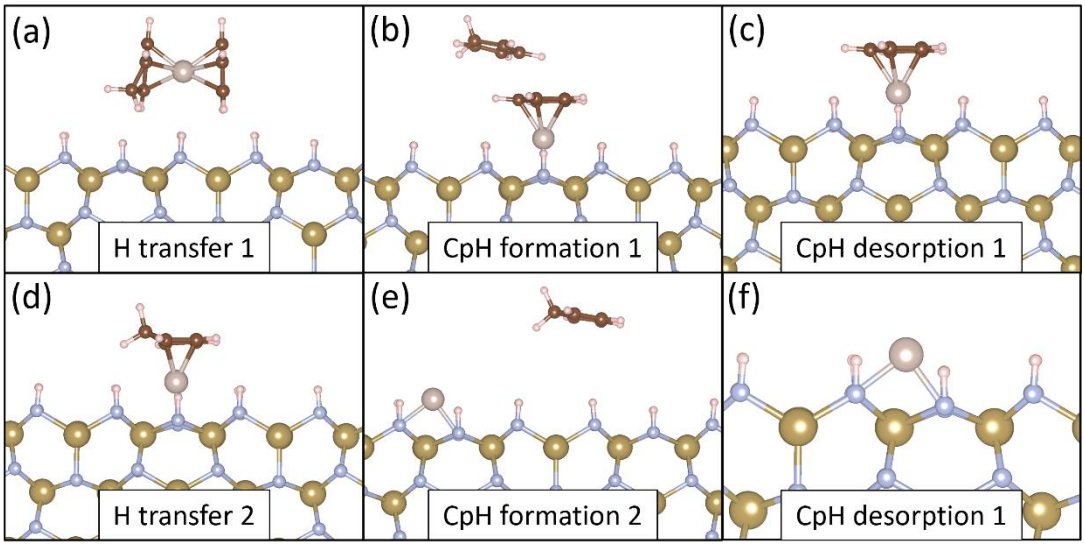


Figure 8.4. Geometries of the individual reaction pathway steps for the horizontal interaction mode of $RuCp_2$ on 1 ML N-H ε-TaN (110). Colour scheme is the same as in Figure 8.1.

8.1.4 Effect of $RuCp_2$ coverage on 1 ML N-H ε-TaN (110)

In this section the coverage of $RuCp_2$ on the 1 ML N-H ε-TaN (110) surface is studied. The interaction energies for two $RuCp_2$ precursors along with the reaction pathway for upright and horizontal interaction modes are plotted in Figure 8.5 with their respective geometries shown in Figure 8.6 and Figure 8.7. The interaction energy of two $RuCp_2$ precursors is calculated using equation (8.2):

$$E_{ads} = E_{tot} - E_{NH_x/metal} - 2 \times E_{precursor} \quad (8.2)$$

where E_{tot}, $E_{NH_x/metal}$, and $E_{precursor}$ are the energy of the NH_x-terminated TaN slab with two $RuCp_2$ precursors, the slab model for the NH_x-terminated TaN surface, and isolated precursor $RuCp_2$ respectively. The interaction energy for two $RuCp_2$ precursors on the 1 ML N-H ε-TaN (110) surface is favourable for both interaction modes; the upright interaction mode is more favourable by -0.27 eV.

After the first CpH elimination, the surface is terminated with one intact adsorbed $RuCp_2$ and a RuCp fragment bound to the surface through an Ru-N bond with overall favourable reaction energies of -1.54 eV and -1.44 eV for the upright and horizontal interaction modes respectively. There are two different pathways for subsequent CpH elimination which can result in a surface terminated with:

1) Two RuCp fragments bonded to the surface through Ru-N bonds.

or

2) An intact adsorbed $RuCp_2$ and Ru atom bound to the surface through Ru-N bonds.

For the upright interaction mode, route 1 mentioned above is favourable, with an overall energy change of -0.93 eV, while route 2 is unfavourable, being endothermic. This leaves two RuCp fragments bound to the surface. The elimination of a third CpH resulting in RuCp and Ru on the surface is unfavourable with an overall endothermic reaction energy of 1.85 eV. Therefore, for the upright adsorbed mode the surface will be terminated with two RuCp fragments. For the horizontal interaction mode, both routes 1 and 2 are unfavourable therefore the surface is terminated with an intact adsorbed $RuCp_2$ and RuCp fragment with overall reaction energy -1.44 eV. These results show that more Cp ligands can be removed via hydrogen transfer for the upright interaction mode for two $RuCp_2$ precursors on the 1 ML N-H ε-TaN (110) surface.

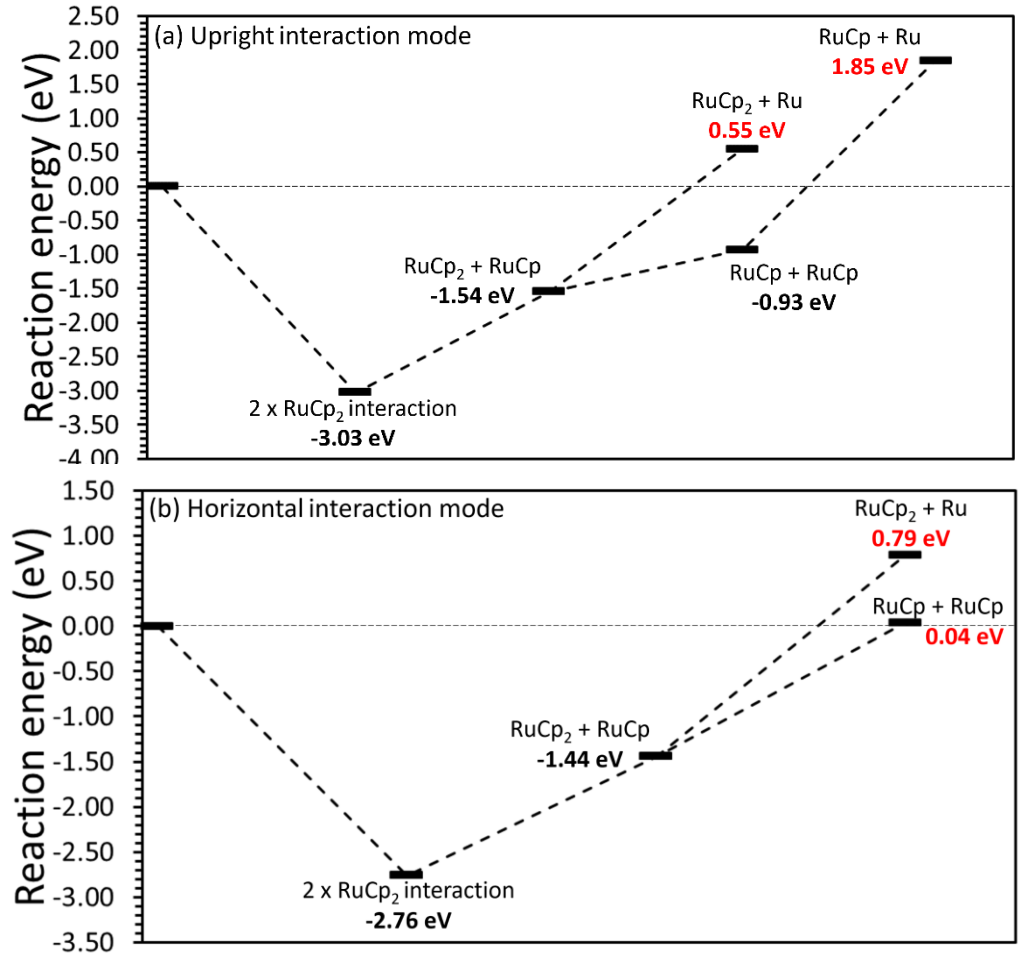


Figure 8.5. Reaction pathway for two $RuCp_2$ precursors on 1 ML N-H ε-TaN (110) surface for (a) upright interaction mode and (b) horizontal interaction mode.

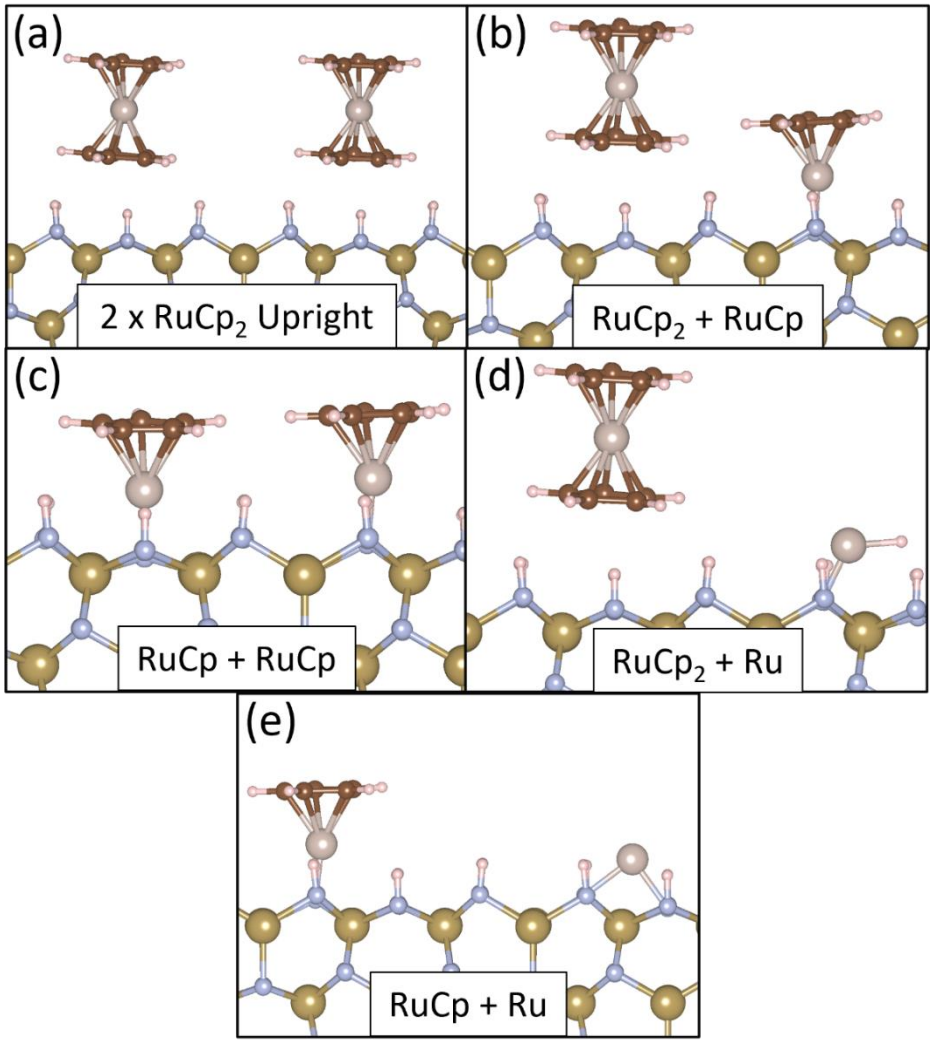


Figure 8.6. Geometries of the reaction pathway of two $RuCp_2$ precursors on 1 ML N-H ε-TaN (110) surface for the upright interaction mode reaction pathway shown in panel (a) in Figure 8.5. Colour scheme is the same as in Figure 8.1.

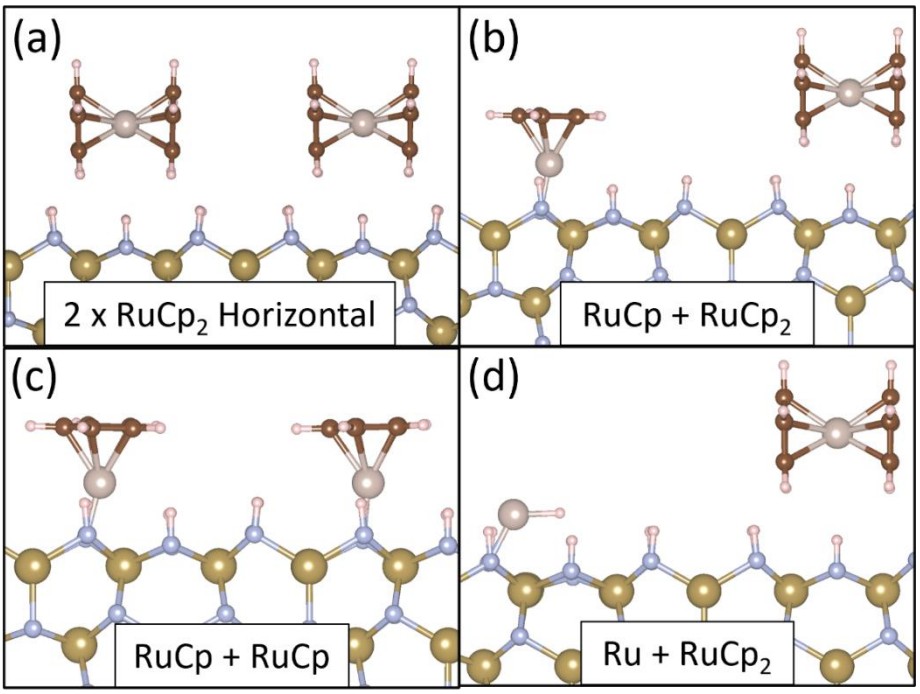


Figure 8.7. Geometries of the reaction pathway of two $RuCp_2$ precursors on 1 ML N-H ε-TaN (110) surface for the horizontal interaction mode reaction pathway shown in panel (b) in Figure 8.5. Colour scheme is the same as in Figure 8.1.

A higher coverage of four $RuCp_2$ (2.77 $RuCp_2/nm^2$) on the 1 ML N-H ε-TaN (110) surface in the upright interaction mode was calculated using equation (8.2) for 4 precursors. The interaction energy is favourable with an overall energy gain of -2.19 eV as shown in Figure 8.8. The further elimination of the remaining Cp ligands through hydrogen transfer from the surface is endothermic at 8.77 eV showing that post the $RuCp_2$ metal precursor pulse the surface is terminated with four RuCp fragments. Also the N-H TaN coverage changes from 1 ML N-H TaN to 0.83 ML N-H ε-TaN (110) as four hydrogen were used for the first CpH desorption from the four surface bound $RuCp_2$ precursors.

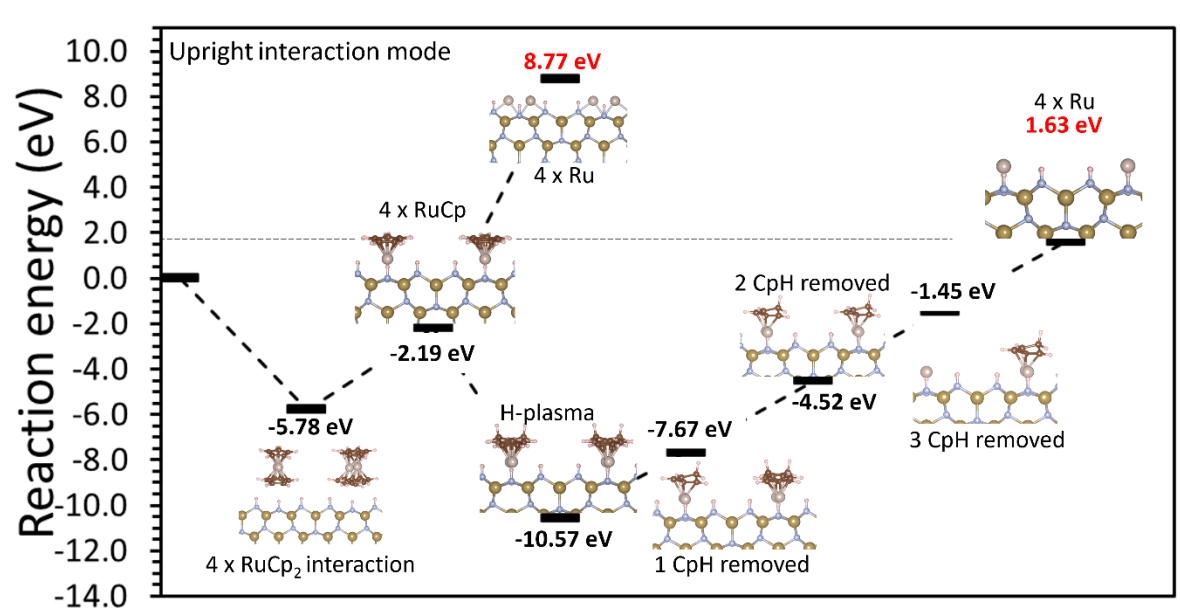


Figure 8.8. Reaction pathway for H plasma chemistry at four $RuCp_2$ precursors on the 1 ML N-H ε-TaN (110) surface. Colour scheme is the same as in Figure 8.1.

8.1.5 H_2 plasma radical chemistry on $RuCp_2$ treated 1 ML N-H ε-TaN (110) surface

In this section we examine the reactions of plasma generated •H radicals at the post metal precursor one $RuCp_2$ treated 1 ML N-H ε-TaN (110) surface. The surface H coverage has changed to 0.96 ML N-H ε-TaN (110) since a hydrogen was used for the first CpH desorption. We position one hydrogen radical 1.90 Å away from the Cp ring and relax. The energy of the •H radical is referred to half of gas phase H_2. The interaction energy of the •H radical is calculated using (8.3):

$$E_{ads} = E_{tot} - E_{sub} - E_{H\ radical} \qquad (8.3)$$

where E_{tot} is the energy of the surface treated with the •H radical, E_{sub} is the RuCp terminated 0.96 ML N-H TaN surface and $E_{H\ radical}$ is the energy of the plasma generated •H radical.

The interaction energy of the •H radical on the RuCp terminated 0.96 ML N-H ε-TaN (110) surface is -2.81 eV and -3.39 eV for both interaction modes showing it is favourable for H to bind to the Cp rings. The reaction pathways for the •H radical treated RuCp terminated 0.96 ML N-H ε-TaN (110) surface for both interaction modes are shown in Figure 8.9. The reaction energy after the first CpH desorption is favourable for both interaction modes with energies -0.53 eV and -1.52 eV for the upright and horizontal interaction modes respectively as seen previously in Figure 8.2. The •H radical bonds favourably with the Cp ring for both interaction

modes with exothermic reaction energies as shown in Figure 8.9. The overall reaction energy after CpH desorption is also exothermic for both interaction modes leaving a Ru terminated 0.96 ML N-H ε-TaN (110) surface. The spontaneous formation of a Ru-H bond occurred for the horizontal interaction mode with bond length 1.59 Å, shown in Figure 8.9 (b), which may help keep Ru stable on the surface.

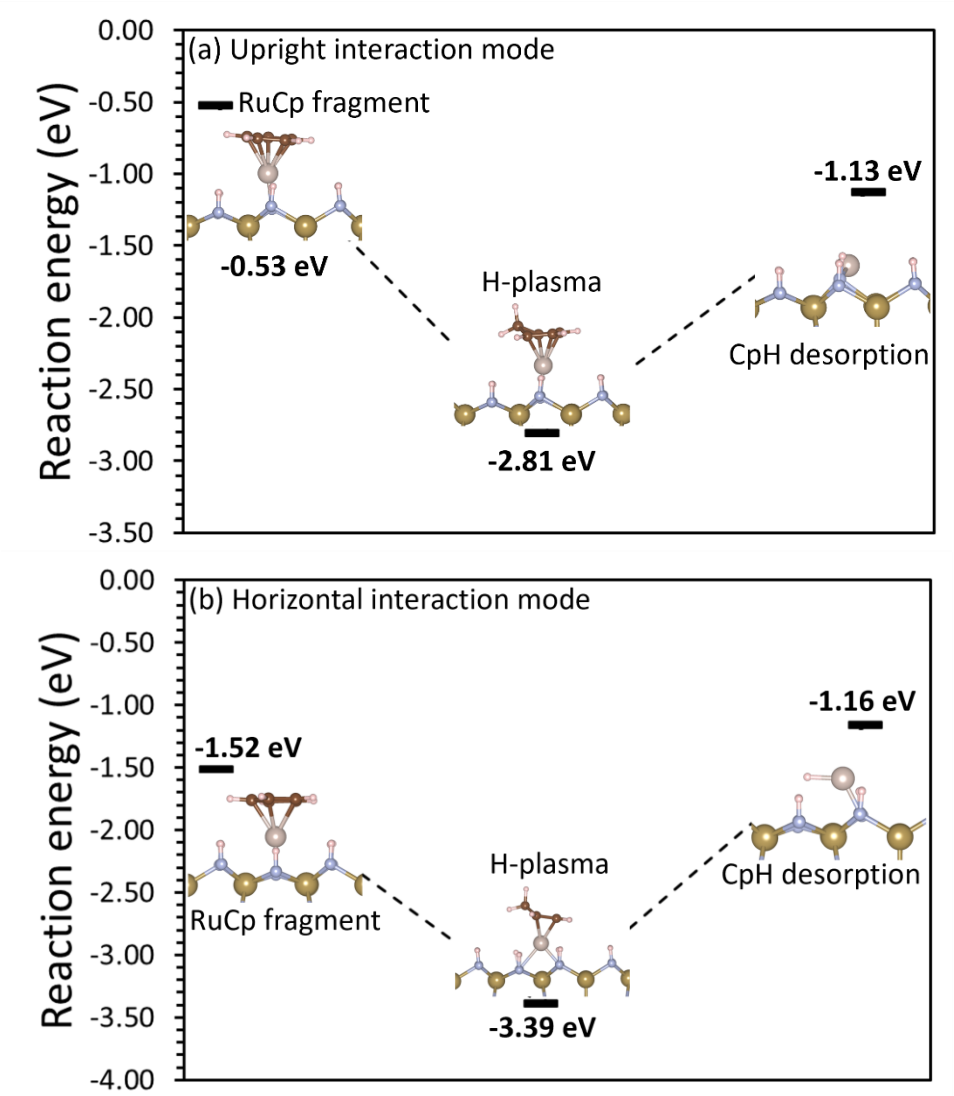


Figure 8.9. Reaction pathway of ˙H radical treated RuCp terminated 0.96 ML N-H ε-TaN (110) surface for (a) upright interaction mode and (b) horizontal interaction mode. Energies are relative to the energy of the RuCp adsorbed on the TaN surface. Colour scheme is the same as in Figure 8.1.

The reaction of plasma generated ˙H radicals at the $(RuCp)_4$ 0.83 ML N-H ε-TaN (110) surface is studied with a coverage of ˙H radicals of one radical per RuCp fragment.

The reaction energy for binding of 4 ˙H to the RuCp fragments is exothermic at -10.57 eV, that is -2.65 eV/H radical. Figure 8.8 shows the overall reaction pathway. The removal of the first

CpH is favourable with an overall reaction energy of -7.67 eV and is also favourable for the second and third removal of CpH with overall reaction energy of -1.45 eV after the third CpH was removed. The overall reaction energy goes endothermic at 1.63 eV after the last CpH was removed showing that up to three CpH can be removed favourably leaving one CpH on the surface. At a smaller coverage of one RuCp fragment on the surface the formation and desorption of CpH with plasma generated hydrogen is favourable whereas at a higher RuCp coverage not all CpH are removed favourably indicating that minimal carbon contamination is possible when using $RuCp_2$. Carbon contamination from $RuCp_2$ was found to be minimal[17] or undetected[18] from experimental Ru PEALD using $RuCp_2$.

8.2 ALD Chemistry with Bis(ethylcyclopentadienyl)ruthenium(II), $Ru(EtCp)_2$ Precursor

8.2.1 $Ru(EtCp)_2$ interaction at NH_x-terminated ε-TaN (110) surfaces

$Ru(EtCp)_2$ is another organometallic ruthenium precursor used in Ru ALD processes[5,19–21]; in our model each Cp ring carries one Et ligand giving composition $C_2H_5C_5H_4$. The interaction of $Ru(EtCp)_2$ was studied for the upright interaction mode (one EtCp ligand interacting with the surface) and the horizontal interaction mode (both EtCp ligands interacting with the surface) on the NH_x-terminated ε-TaN (110) surfaces. The interaction energies of $Ru(EtCp)_2$ are calculated using (8.1) along with the reaction energies for the first and second EtCpH elimination are listed in Table 2.

The interaction energy of $Ru(EtCp)_2$ is favourable on all NH_x-terminated TaN surfaces, ranging from -1.07 to -1.74 eV for upright and -0.95 to -2.36 eV for horizontal interaction modes. Comparing the interaction energies of $Ru(EtCp)_2$ to the previous $RuCp_2$ (section 8.1.1) shows that $Ru(EtCp)_2$ interacts more strongly with the NH_x-terminated ε-TaN (110) surfaces than $RuCp_2$ except for 1 ML N-H (U) where $RuCp_2$ interaction is stronger by 0.64 eV. The interaction of $Ru(EtCp)_2$ is 0.41 eV stronger than $RuCp_2$ for the horizontal interaction mode on the 0.5 ML N-H/0.5 ML N-H_2 ε-TaN (110) surface.

The reaction energy is calculated for the first EtCpH elimination for all surfaces. The first EtCpH elimination is favourable on the 1 ML N-H ε-TaN (110) (from the horizontal interaction mode) and the 0.67 ML N-H/0.67 ML Ta-NH_2 ε-TaN (110) (upright interaction mode), with reaction energies -0.69 eV and -0.42 eV respectively. Both the first and second EtCpH eliminations are favourable on the 0.5 ML N-H/0.5 ML N-H_2 ε-TaN (110) surface (horizontal

interaction mode) with an overall reaction energy -0.42 eV. Ligand elimination from $RuCp_2$ was only achieved on the 1 ML N-H ε-TaN (110) whereas with $Ru(EtCp)_2$ EtCp ligands can be eliminated on other NH_x-terminated ε-TaN (110) surfaces including 1 ML N-H. The geometries for $Ru(EtCp)_2$ interaction on the NH_x-terminated TaN surfaces that facilitate EtCpH elimination are shown in Figure 8.10.

Table 2. Calculated interaction energies for $Ru(EtCp)_2$ on NH_x-terminated ε-TaN (110) surfaces including the reaction energies after the first and second EtCpH elimination. (U) = upright interaction mode and (H) = horizontal interaction mode. The geometries for $Ru(EtCp)_2$ interaction on the NH_x-terminated ε-TaN (110) surfaces are shown in Figure 8.10 and Figure A 5 in the Appendix.

NH_x-terminated ε-TaN (110)	**E_{ads} (eV)**	**ΔE EtCpH 1 (eV)**	**ΔE EtCpH 2 (eV)**
N-H_x			
1 ML N-H (U)	-1.37	0.49	
1 ML N-H (H)	-2.36	**-0.69**	0.46
0.5 ML N-H/0.5 ML N-H_2 (U)	-1.20	1.90	
0.5 ML N-H/0.5 ML N-H_2 (H)	-0.92	**-0.38**	**-0.42**
Ta-NH_x			
0.04 ML Ta-NH_2/0.42 ML Ta-NH/0.04 ML Ta-N (U)	-1.74	1.87	
0.04 ML Ta-NH_2/0.42 ML Ta-NH/0.04 ML Ta-N (H)	-1.30	0.89	
0.67 ML Ta-NH_2 (U)	-1.07	1.41	
0.67 ML Ta-NH_2 (H)	-1.14	2.47	
0.38 ML Ta-NH_2 (U)	-1.19	1.30	
0.38 ML Ta-NH_2 (H)	-1.13	1.15	
Mixed N-H, Ta-NH_2			
0.67 ML N-H/0.67 ML Ta – NH_2 (U)	-1.35	**-0.42**	1.14
0.67 ML N-H/0.67 ML Ta – NH_2 (H)	-0.95	1.29	

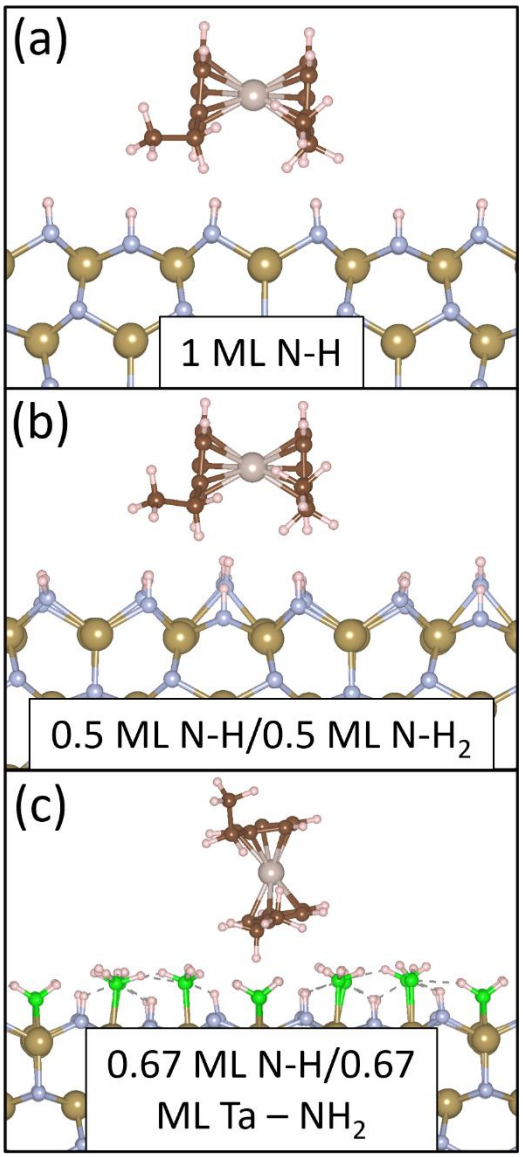


Figure 8.10. $Ru(EtCp)_2$ interaction on (a) 1 ML N-H horizontal interaction mode, (b) 0.5 ML N-H/0.5 ML N-H_2 horizontal interaction mode and (c) 0.67 ML N-H/0.67 ML Ta-NH_2 upright interaction mode ε-TaN (110) surfaces.
Colour scheme is Ta = brown, N = light blue & green, H = pink, C = dark brown and Ru = grey.

8.2.2 Single $Ru(EtCp)_2$ Reaction Pathway on NH_x-terminated ε-TaN

The reaction pathways of $Ru(EtCp)_2$ on the 1 ML N-H, 0.5 ML N-H/0.5 ML N-H_2 and 0.67 ML N-H/0.67 ML N-H_2 ε-TaN (110) surfaces are shown in Figure 8.11. The geometries of each step of the reaction pathways in plots (a) and (b) are shown in Figure 8.12 and Figure 8.13 respectively with the reaction energies of each step listed in Table A 2 in the Appendix. The formation and desorption of the first EtCpH is favourable on the 1 ML N-H ε-TaN (110) surface with a hydrogen transfer barrier of 1.19 eV. The overall reaction energy after the second EtCpH desorption is exothermic at -0.34 eV due to the spontaneous Ru-H bond that formed with Ru-H bond length of 1.59 Å shown in panel (f) in Figure 8.12 for the 1 ML N-H ε-TaN (110) surface. This was also observed previously for $RuCp_2$, showing again surface H migration may stabilise Ru. What's interesting is that the first hydrogen transfer barrier is larger for $Ru(EtCp)_2$ compared to $RuCp_2$ on the 1 ML N-H ε-TaN (110) surface for the horizontal interaction mode by 0.61 eV. The second hydrogen transfer barriers are comparable between both Ru precursors. For a single $Ru(EtCp)_2$ precursor interacting with the 1 ML N-H TaN ε-TaN (110) surface, the surface will be terminated with a RuEtCp fragment due to the reaction energy of the second EtCpH formation being endothermic at 1.14 eV.

The formation and desorption of the first EtCpH is also favourable on the 0.5 ML N-H/0.5 ML N-H_2 ε-TaN (110) surface and has a hydrogen transfer barrier of 0.99 eV. The barrier of the second hydrogen transfer is low at 0.22 eV and the overall reaction energy is exothermic after the second EtCpH desorption at -0.58 eV leaving the surface terminated with a Ru atom. The Ru atom is bound to the surface through Ru-N bonds of 2.07 Å and 2.16 Å as well as interacting with Ta atoms with distances of 2.40 Å and 2.61 Å.

Despite the reaction energy for the first EtCpH elimination being favourable for the 0.67 ML N-H/0.67 ML N-H_2 ε-TaN (110) surface in section 8.2.1, the reaction energy for the first hydrogen transfer is unfavourable at 1.66 eV as shown in plot (c) in Figure 8.11. Therefore, the formation and desorption of the first EtCpH on the 0.67 ML N-H/0.67 ML N-H_2 TaN surface is difficult to achieve due to the very high barrier of 3.02 eV for hydrogen transfer and endothermic reaction energy.

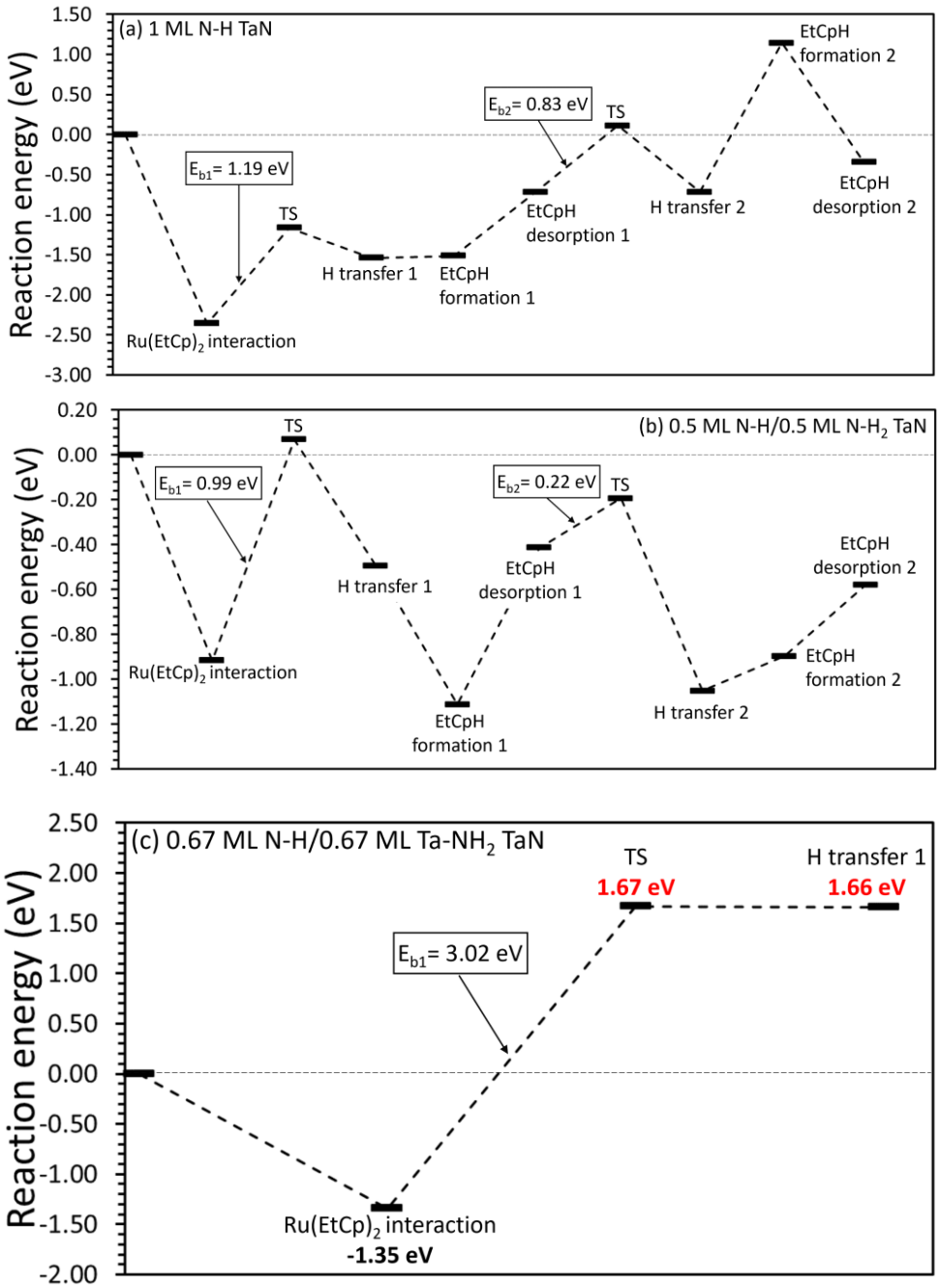


Figure 8.11. $Ru(EtCp)_2$ reaction pathway on (a) 1 ML N-H (horizontal interaction mode), (b) 0.5 ML N-H/0.5 ML N-H_2 (horizontal interaction mode) and (c) 0.67 ML N-H/0.67 ML Ta-NH_2 (upright interaction mode) ε-TaN (110) surfaces.

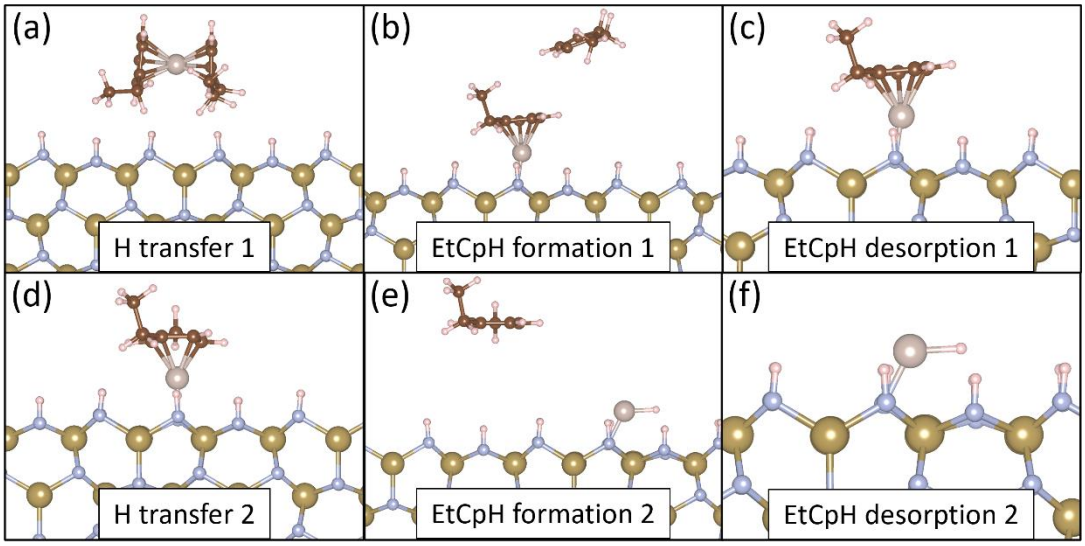


Figure 8.12. Geometries of the individual reaction pathway steps for the horizontal interaction mode of $Ru(EtCp)_2$ on 1 ML N-H ε-TaN (110). Colour scheme is the same as in Figure 8.1.

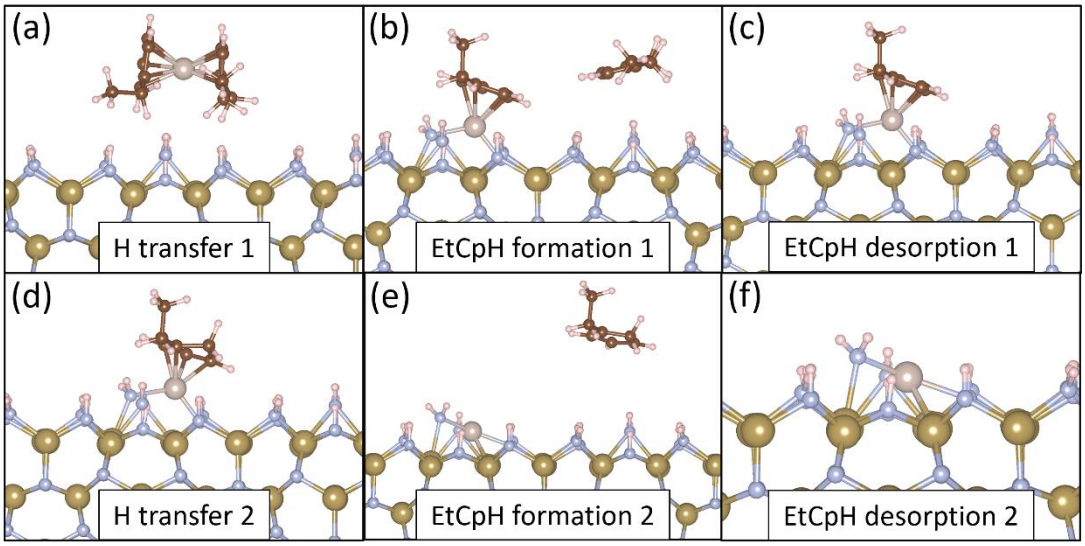


Figure 8.13. Geometries of the individual reaction pathway steps for the horizontal interaction mode of $Ru(EtCp)_2$ on 0.5 ML N-H/0.5 ML N-H_2 ε-TaN (110). Colour scheme is the same as in Figure 8.1.

8.2.3 Effect of $Ru(EtCp)_2$ coverage on 1 ML N-H ε-TaN and 0.5 ML N-H/0.5 ML N-H_2 ε-TaN

In this section we examine the effect of $Ru(EtCp)_2$ coverage on the NH_x-terminated ε-TaN (110) surfaces that facilitated EtCpH elimination for the single $Ru(EtCp)_2$ precursor interaction. The reaction pathways for two $Ru(EtCp)_2$ precursors adsorbed on the 1 ML N-H and 0.5 ML

N-H/0.5 ML N-H_2 ε-TaN (110) surfaces are shown in plots (a) and (b) respectively in Figure 8.14. The geometries of the reaction pathway steps are shown in Figure 8.15 and Figure 8.16 for the 1 ML N-H and 0.5 ML N-H/0.5 ML N-H_2 ε-TaN (110) surfaces respectively.

The interaction energy is favourable on both surfaces with values of -3.79 eV and -2.42 eV respectively calculated using equation (8.2). The first EtCpH elimination is overall exothermic with reaction energies of -2.25 eV and -1.78 eV for the 1 ML N-H and 0.5 ML N-H/0.5 ML N-H_2 ε-TaN (110) surfaces respectively. Note that the energy cost for the first EtCpH elimination is greater on 1 ML N-H ε-TaN (110) at 1.54 eV whereas on 0.5 ML N-H/0.5 ML N-H_2 ε-TaN (110) is it smaller being 0.64 eV.

The second EtCpH elimination follows the same strategy for the $RuCp_2$ precursors as described in section 8.1.4. For the 1 ML N-H ε-TaN (110) surface, the surface terminated with two RuEtCp fragments is favourable with an overall reaction energy of -0.47 eV and the surface terminated with an intact adsorbed $Ru(EtCp)_2$ and Ru metal is unfavourable with an overall endothermic reaction energy of 0.21 eV. The third EtCpH elimination from the surface terminated with two RuEtCp fragments is unfavourable with an overall endothermic reaction energy of 1.90 eV.

For the 0.5 ML N-H/0.5 ML N-H_2 ε-TaN (110) surface, both routes for the second EtCpH elimination are favourable with overall reaction energies of -1.01 eV and -1.63 eV respectively as shown in Figure 8.14 (b). The third EtCpH elimination is only favourable from the surface terminated with adsorbed $Ru(EtCp)_2$ and Ru metal at -0.87 eV. The elimination of the last EtCpH leaving two Ru atoms on the surface is unfavourable with an endothermic reaction energy of 1.71 eV.

Therefore after the interaction of two $Ru(EtCp)_2$ precursors on the 1 ML N-H ε-TaN (110) surface, the surface is terminated with two RuEtCp fragments which bond to the surface through Ru-N bonds with Ru-N distances of 1.91 Å and 1.89 Å. After the interaction of two $Ru(EtCp)_2$ precursors on the 0.5 ML N-H/0.5 ML N-H_2 ε-TaN (110) surface, the surface is terminated with an RuEtCp fragment and Ru metal with Ru-N bonds 2.01 – 2.18 Å. There was no spontaneous formation of Ru-H bonds in the resulting atomic structures for the favourable reaction pathways.

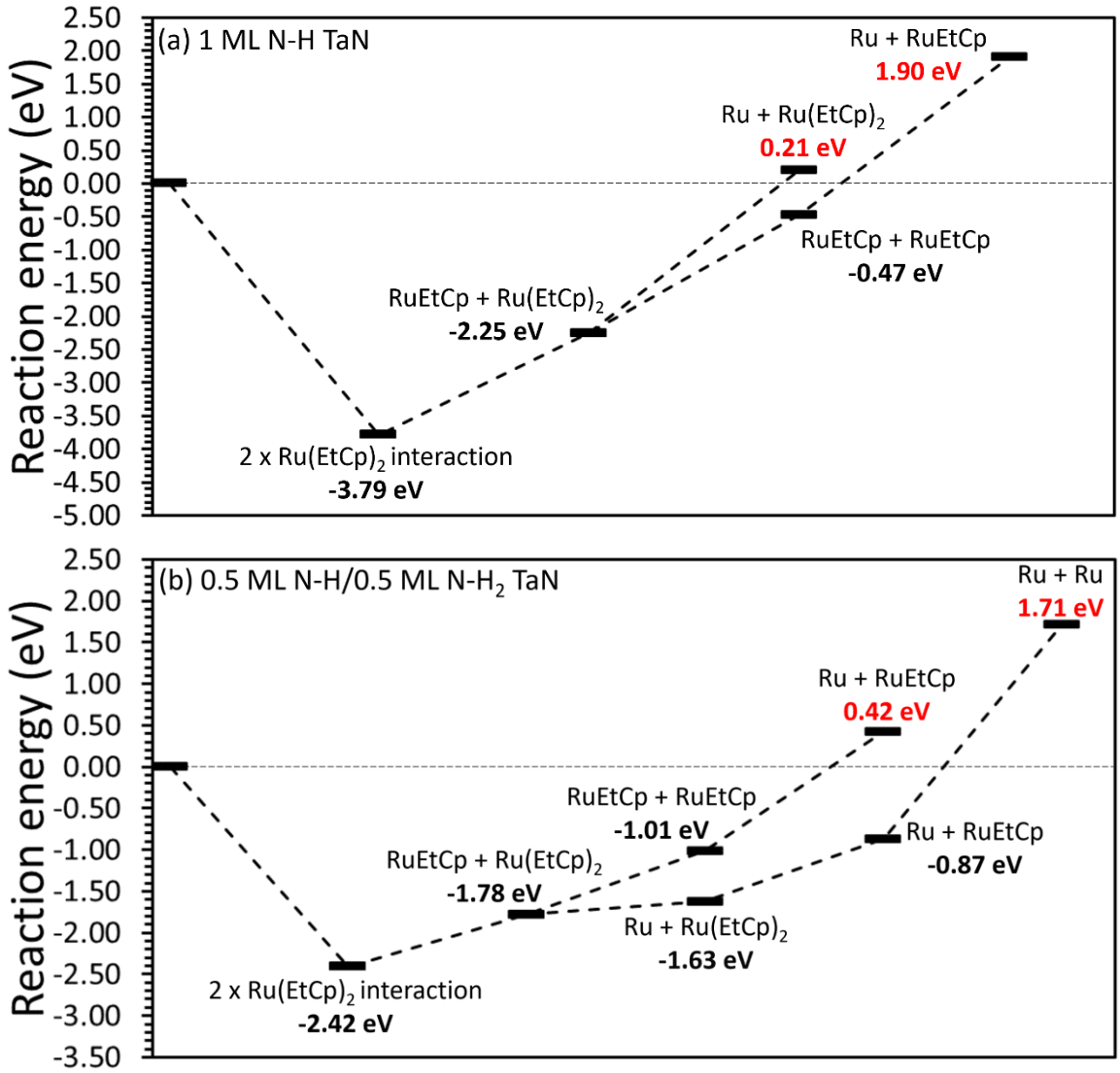


Figure 8.14 Reaction pathway for two $Ru(EtCp)_2$ precursors on (a) 1 ML N-H ε-TaN (110) surface and (b) 0.5 ML N-H/0.5 ML N-H_2 ε-TaN (110) surface.

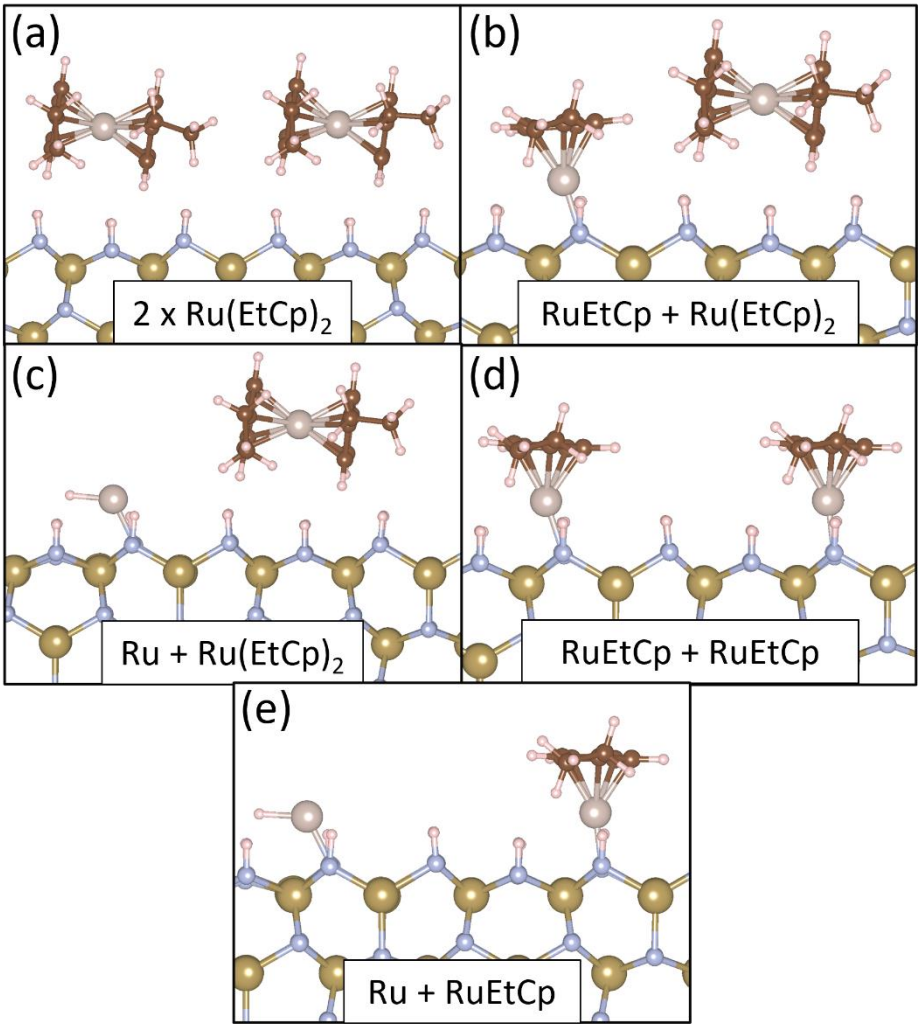


Figure 8.15 Geometries of two $Ru(EtCp)_2$ on the 1 ML N-H ε-TaN (110) surface. Colour scheme is the same as in Figure 8.1.

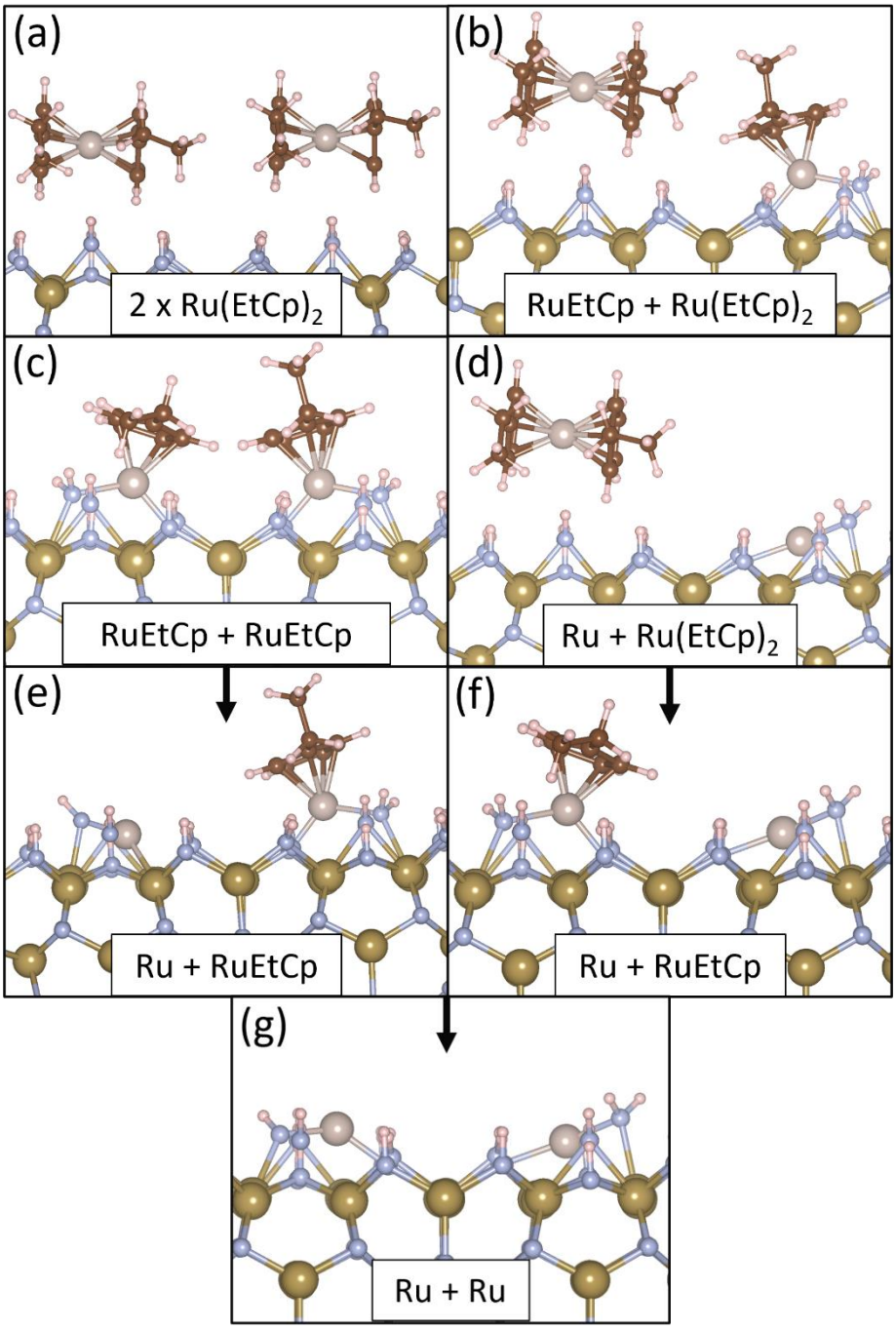


Figure 8.16 Geometries of two $Ru(EtCp)_2$ on the 0.5 ML N-H/0.5 ML N-H_2 ε-TaN (110) surface. Colour scheme is the same as in Figure 8.1.

8.2.4 H_2 plasma radical chemistry on $Ru(EtCp)_2$ treated 1 ML N-H and 0.5 ML N-H/0.5 ML N-H_2 ε-TaN surfaces

In this section the reactions of plasma generated $^{\bullet}H$ radical at the post metal precursor $Ru(EtCp)_2$ treated 1 ML N-H and 0.5 ML N-H/0.5 ML N-H_2 ε-TaN (110) surfaces are studied. On the 1 ML N-H ε-TaN (110) surface, the preferred termination is an RuEtCp fragment with an N-H coverage of 0.96 ML N-H TaN. Both EtCp ligands are removed as EtCpH via hydrogen transfer from the surface for the single interaction of $Ru(EtCp)_2$ on the 0.5 ML N-H/0.5 ML N-H_2 ε-TaN (110) surface. Therefore, we focus on the reaction of the $^{\bullet}H$ radical at the RuEtCp terminated 0.96 ML N-H ε-TaN (110) surface.

One hydrogen radical was placed 1.90 Å away from the EtCp ligand and the structure was allowed to relax. The $^{\bullet}H$ radical interaction energy calculated using equation (8.3) shows that the hydrogen radical bonds spontaneously to the EtCp ligand with an energy gain of -3.02 eV, while the overall reaction energy after EtCpH desorption is favourable at -1.16 eV as shown in Figure 8.17.

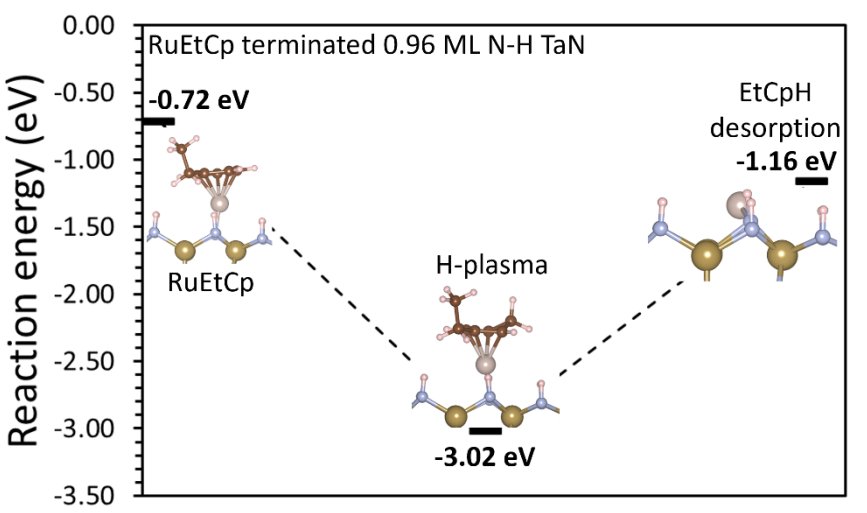


Figure 8.17 Reaction pathway of $^{\bullet}H$ radical treated RuEtCp terminated 0.96 ML N-H ε-TaN (110) surface. Colour scheme is the same as in Figure 8.1.

Next we explore the reactions of plasma generated $^{\bullet}H$ radicals for higher coverages of $Ru(EtCp)_2$ that were discussed in section 8.2.3. The 1 ML N-H ε-TaN (110) surface is terminated with two RuEtCp fragments after the interaction of the $Ru(EtCp)_2$ precursors and a surface N-H coverage of 0.92 ML N-H ε-TaN (110). The 0.5 ML N-H TaN/0.5 ML N-H_2 ε-TaN (110) surface is terminated with one RuEtCp fragment and one Ru atom after the interaction of the $Ru(EtCp)_2$ precursors with an N-H_x coverage of 0.42 ML N-H/0.46 ML N-H_2 ε-TaN (110).

The interaction energy for the formation of EtCpH is -5.17 eV and the overall reaction energy after hydrogen plasma adsorption and EtCpH desorption is favourable at -3.31 eV for $(RuEtCp)_2$ 0.92 ML N-H ε-TaN (110). The reaction pathways for both surfaces are plotted in Figure 8.18. Both Ru atoms form Ru-N bonds in the range of 1.97 – 2.15 Å and there is a spontaneous transfer of hydrogen from the surface to the Ru atoms with an Ru-H bond length of 1.67 Å. On the RuEtCp and Ru terminated 0.42 ML N-H/0.46 ML N-H_2 ε-TaN (110) surface the formation of CpH is favourable with an energy gain of -3.07 eV and an overall reaction energy is favourable after EtCpH desorption at -1.98 eV. Both Ru atoms bond to the surface through Ru-N bonds which lie in the range of 2.06 – 2.15 Å.

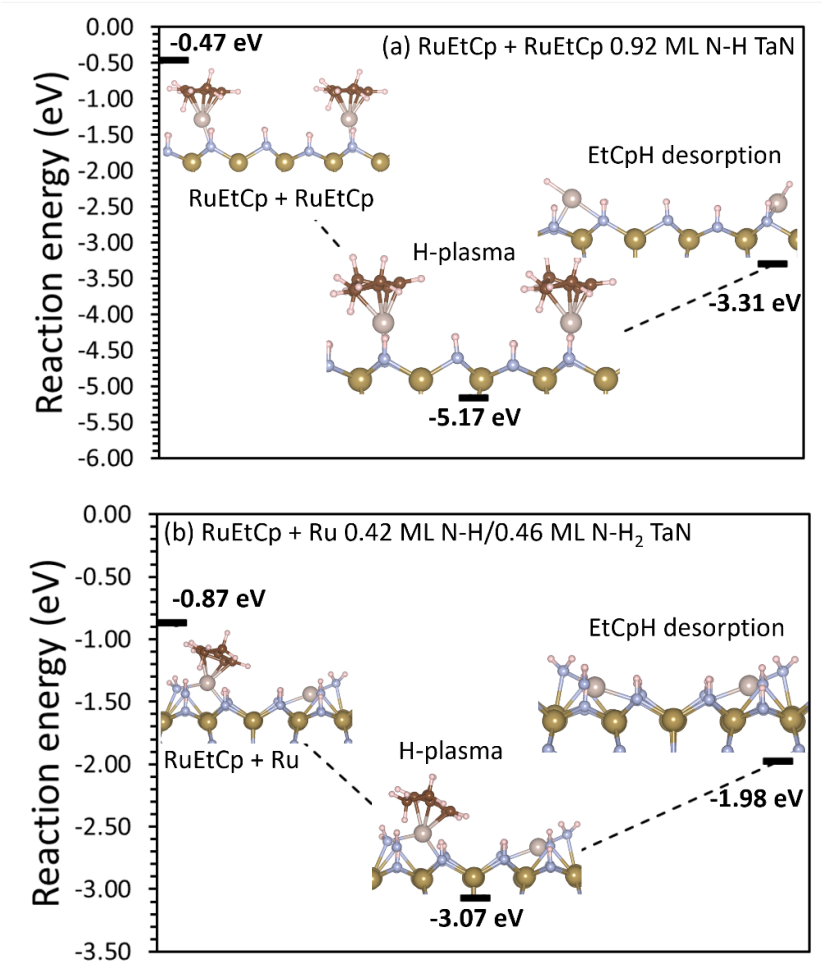


Figure 8.18 Reaction pathway of ˙H radical treated (a) $(RuEtCp)_2$ 0.92 ML N-H ε-TaN (110) and (b) RuEtCp & Ru 0.42 ML N-H/0.46 ML N-H_2 ε-TaN (110). Colour scheme is the same as in Figure 8.1.

8.3 Chemistry of ToRuS, RuO_4, precursor on ε-TaN surfaces

8.3.1 RuO_4 adsorption at NH_x-terminated ε-TaN surfaces

RuO_4 is another ruthenium precursor used in Ru ALD processes.[22–26] We explore how a molecule of RuO_4 interacts at the TaN surfaces and given that H_2 or H_2 plasma are used in Ru ALD with this precursor[23–25] removing oxygen as water, we also compute the reaction energies for water elimination that are shown in Table 3 together with the RuO_4 interaction energies on the NH_x-terminated ε-TaN (110) surfaces. The interaction energies were calculated using equation (8.1).

The interaction of RuO_4 is favourable on all NH_x-terminated ε-TaN (110) surfaces, with an energy gain of -3.72 eV at 1 ML N-H ε-TaN (110) surface and -4.71 eV at 0.5 ML N-H/0.5 ML N-H_2 ε-TaN (110) surface. The geometries of RuO_4 adsorption on the 1 ML N-H and the 0.5 ML N-H/0.5 ML N-H_2 ε-TaN (110) surfaces are shown in Figure 8.19. There is spontaneous hydrogen transfer from the 1 ML N-H ε-TaN (110) surface to oxygen as shown in panel (a) in Figure 8.19 with O-H bond length of 1.01 Å. RuO_4 also forms Ta-O bonds with oxygen of the precursor of 2.22 Å on 1 ML N-H TaN and 2.17 Å/ 2.21 Å on 0.5 ML N-H/0.5 ML N-H_2 ε-TaN (110) as shown in Figure 8.19. H_2O elimination is not favourable on surfaces with added NH_x terminations with the RuO_4 adsorption geometries shown in Figure A 6 in the Appendix.

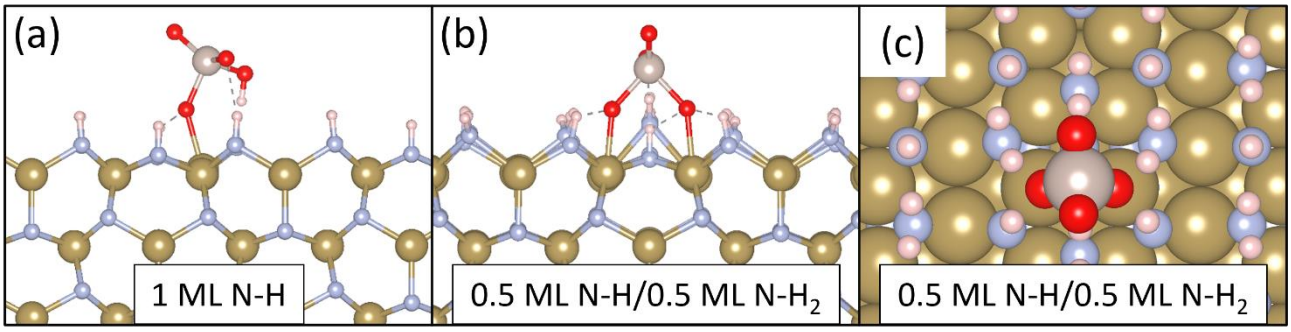


Figure 8.19. RuO_4 adsorption on (a) 1 ML N-H and (b) 0.5 ML N-H/0.5 ML N-H_2 ε-TaN (110) surfaces. (c) Top view of RuO_4 on 0.5 ML N-H/0.5 ML N-H_2 ε-TaN (110). Colour scheme is Ta = brown, N = light blue, H = pink, O = red and Ru = grey.

Table 3. Calculated adsorption energies for RuO_4 on NH_x-terminated ε-TaN (110) surfaces including the reaction energies after each H_2O elimination. The geometries for RuO_4 adsorption on the NH_x-terminated ε-TaN (110) surfaces are shown in Figure 8.19 and Figure A 6 in the Appendix.

NH_x-terminated TaN	**E_{ads} (eV)**	**ΔE H_2O 1 (eV)**	**ΔE H_2O 2 (eV)**	**ΔE H_2O 3 (eV)**	**ΔE H_2O 4 (eV)**
N-H_x					
1 ML N-H	-3.72	**-3.71**	**-6.57**	**-5.41**	**-5.41**
0.5 ML N-H/0.5 ML N-H_2	-4.71	**-5.51**	**-8.45**	**-9.20**	**-8.13**
Ta-NH_x					
0.04 ML Ta-NH_2/0.42 ML Ta-NH/0.04 ML Ta-N	-0.82	0.79			
0.67 ML Ta-NH_2	-1.20	2.03			
0.38 ML Ta-NH_2	-0.92	2.81			
Mixed N-H, Ta-NH_2					
0.67 ML N-H/0.67 ML Ta – NH_2	-0.93	1.51			

8.3.2 Single RuO_4 Reaction Pathways

8.3.2.1 1 ML N-H ε-TaN (110) surface

The reaction pathway to remove oxygen from RuO_4 adsorbed on the 1 ML N-H ε-TaN (110) surface is studied. Here we examine possible hydrogen transfer from the surface N-H terminations to oxygen of RuO_4 to form H_2O, thus eliminating oxygen. In Figure 8.20 (a) the reaction pathway for oxygen elimination from RuO_4 adsorbed on the 1 ML N-H ε-TaN (110) surface is shown with the geometries of each step shown in Figure 8.21.

As discussed previously in section 8.3.1, a hydrogen spontaneously transfers from the 1 ML N-H ε-TaN (110) surface to an oxygen when RuO_4 adsorbs on the surface. The reaction energies of hydrogen transfer to this Ru-OH and subsequent H_2O loss are exothermic (overall energy gain of -3.73 eV), with a moderate activation barrier of 0.67 eV.

Subsequent hydrogen transfer from the surface to oxygen is favourable with low barriers of 0.49, 0.43, 0.09 and 0.32 eV and including barrierless hydrogen transfer in steps 2 and 4. After the second favourable H_2O elimination, the RuO_2 fragment binds to the surface through an Ru-N bond with an Ru-N distance of 2.02 Å as shown in Figure 8.21 (e).

The overall reaction energy after all the oxygen are removed is exothermic at -5.09 eV and ruthenium bonds to the surface through Ru-N bonds with Ru-N distances of 2.02 Å and 1.94 Å. In all cases, the H migration barriers are low suggesting this chemistry can take place under mild conditions, which is consistent with the relatively low temperature for Ru ALD with ToRuS[23–25].

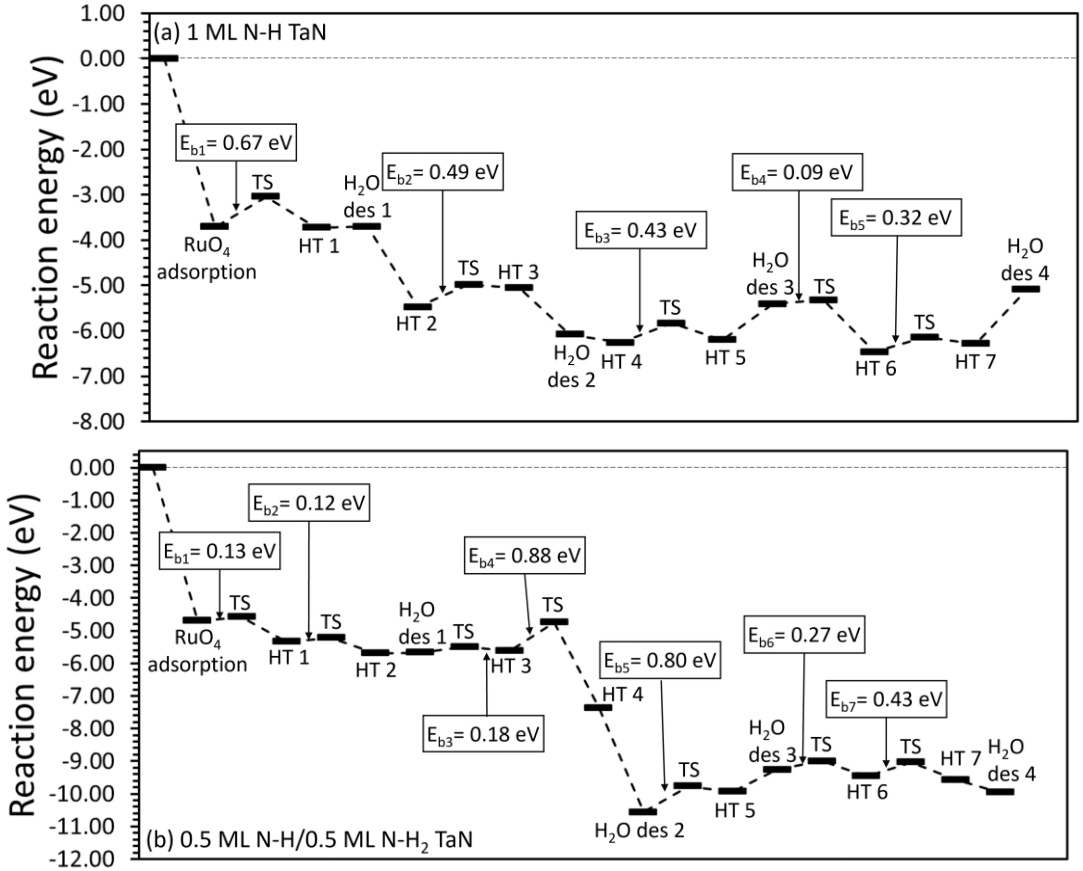


Figure 8.20. RuO_4 reaction pathway on (a) 1 ML N-H and (b) 0.5 ML N-H/0.5 ML N-H_2 ε-TaN (110) surfaces. Note the abbreviations HT = hydrogen transfer and des = desorption.

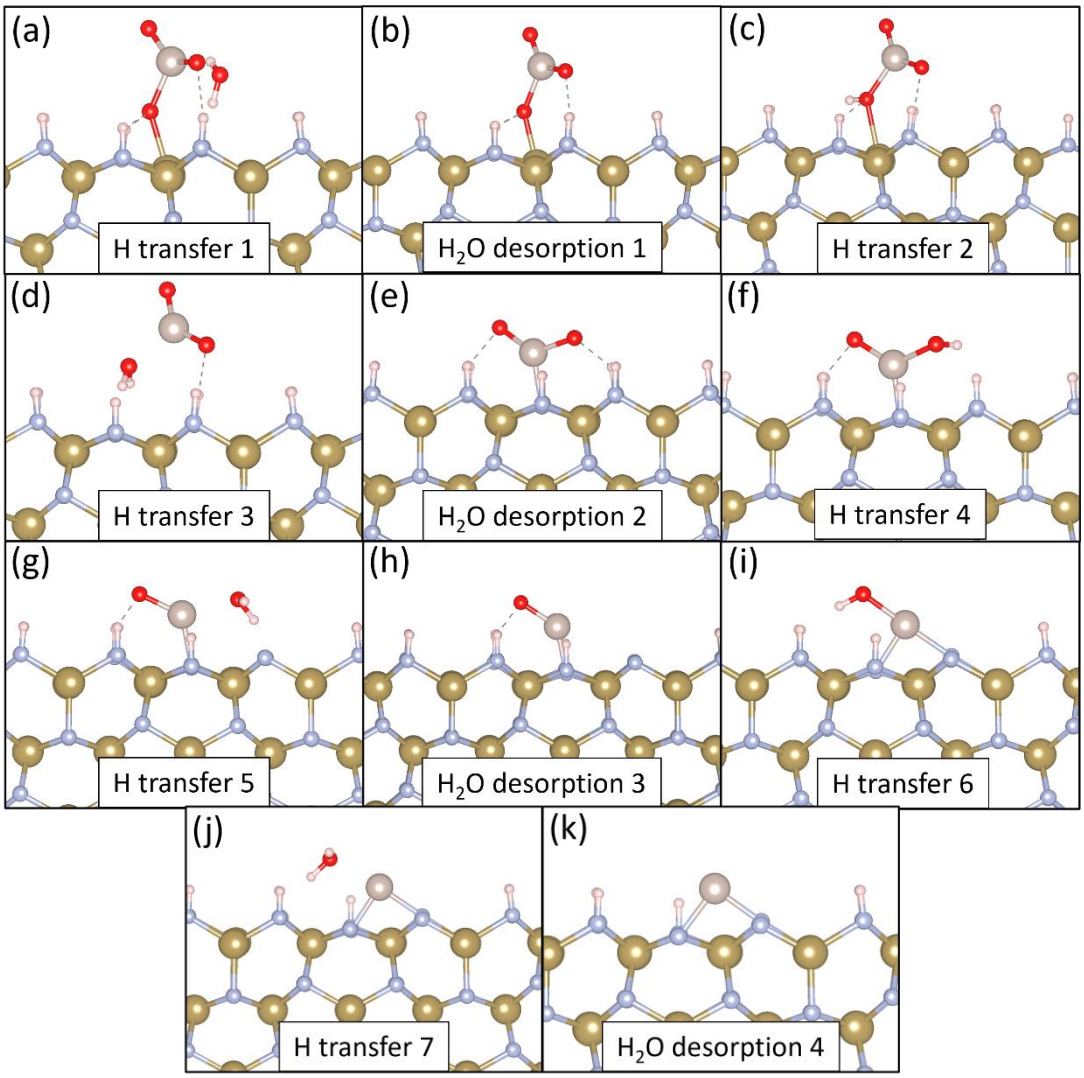


Figure 8.21. Geometries of the individual reaction pathway steps for RuO_4 on 1 ML N-H ε-TaN (110). Colour scheme is the same as in Figure 8.19.

8.3.2.2 RuO_4 chemistry on 0.5 ML N-H/0.5 ML N-H_2 ε-TaN (110) surface

The reaction pathway for oxygen elimination from RuO_4 adsorbed on 0.5 ML N-H/0.5 ML N-H_2 ε-TaN (110) surface is shown in Figure 8.20 (b) with the geometries of each step shown in Figure 8.22. The reaction energies of the first and second hydrogen transfers to form H_2O are exothermic with low barriers for hydrogen migration of 0.13 eV and 0.12 eV respectively and the first H_2O elimination reaction is favourable. Further hydrogen transfer reaction energies are exothermic with low to moderate barriers.

After the second H_2O desorption there was a spontaneous transfer of oxygen from RuO_2 to the surface forming Ta-O bonds with Ta-O distances of 2.17 Å and 2.16 Å and an O-H bond length of 0.97 Å, shown in Figure 8.22 (f). There was also a spontaneous transfer of hydrogen from

the surface to ruthenium forming a Ru-H bond with an Ru-H distance of 1.64 Å where ruthenium interacts with the surface through a Ta-Ru bond with a Ta-Ru distance of 2.62 Å. The overall reaction energy after all the oxygen are removed is exothermic at -9.95 eV. Ruthenium now bonds to the surface through Ru-N bonds of 1.96 Å and 2.03 Å as shown in Figure 8.22 (k). The reaction pathways for both surfaces demonstrate that oxygen can be easily removed as H_2O leaving Ru deposited on the surface due to the overall exothermic reaction energies and low to moderate hydrogen transfer barriers. The values of the reaction energies of each step along the reaction pathways in Figure 8.20 are listed in Table A 3 in the Appendix.

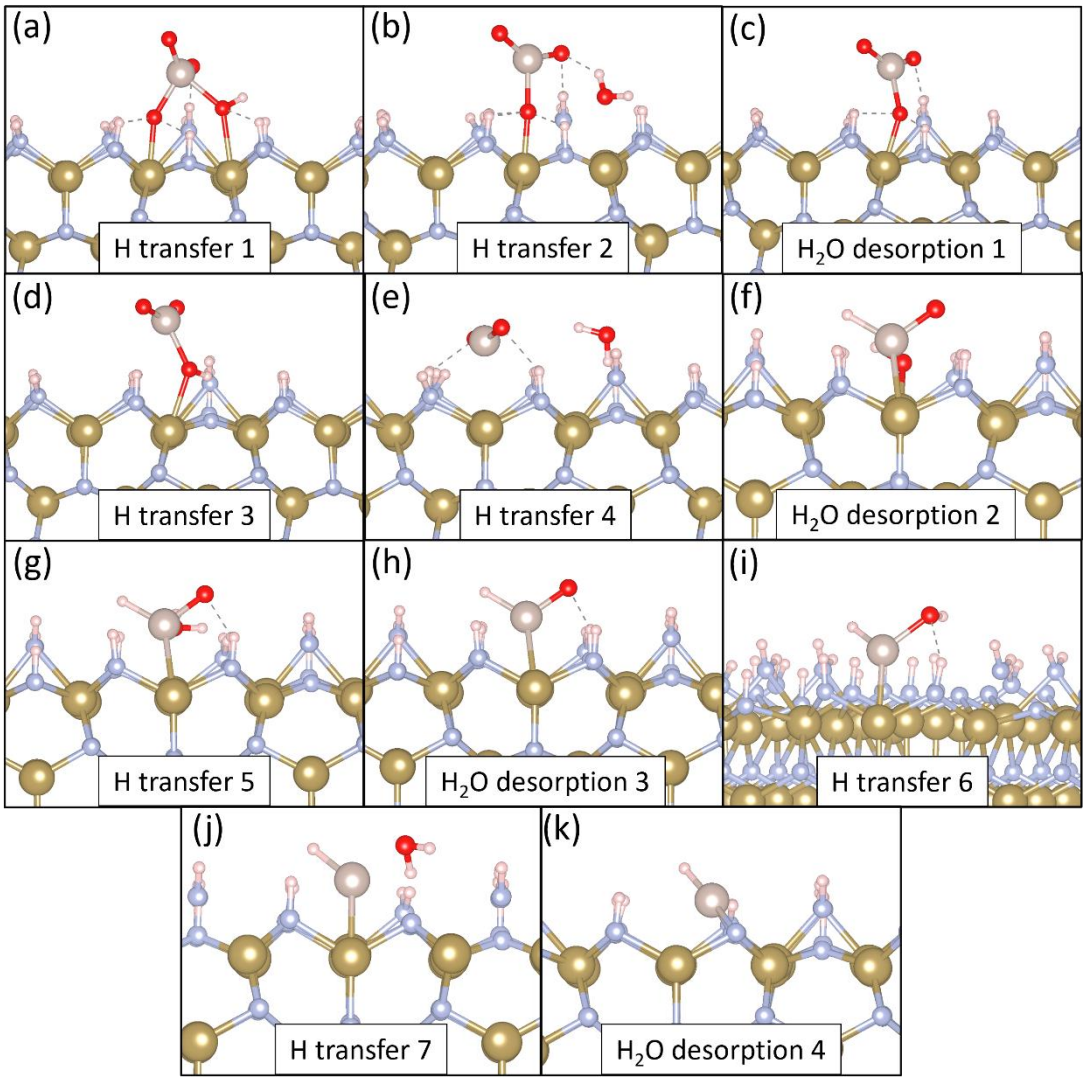


Figure 8.22. Geometries of the individual reaction pathway steps for RuO_4 on 0.5 ML N-H/0.5 ML N-H_2 ε-TaN (110). Colour scheme is the same as in Figure 8.19.

8.3.3 H_2 plasma radical chemistry on RuO_4 treated 0.5 ML N-H/0.5 ML N-H_2 ε-TaN surface

With a single RuO_4 precursor on the 1 ML N-H and 0.5 ML N-H/0.5 ML N-H_2 ε-TaN (110) surfaces all oxygen can be favourably removed as H_2O via hydrogen transfer from the surface. In this section higher coverages of RuO_4 on the 0.5 ML N-H/0.5 ML N-H_2 ε-TaN (110) surface are studied along with the reactions of plasma generated $^{\bullet}H$ radical at the post metal precursor RuO_4 treated 0.5 ML N-H/0.5 ML N-H_2 ε-TaN (110) surface.

The 0.5 ML N-H/0.5 ML N-H_2 ε-TaN (110) surface was chosen due to the higher hydrogen content that can accommodate more H_2O formation at increased RuO_4 coverages. Coverages of up to 6 RuO_4 were adsorbed on the 0.5 ML N-H/0.5 ML N-H_2 ε-TaN (110) surface. The geometries and exothermic adsorption energies of coverages of 2 to 5 RuO_4 adsorbed on the 0.5 ML N-H/0.5 ML N-H_2 ε-TaN (110) surface are shown in Figure A 7 in the Appendix. The coverage of 6 x RuO_4 is shown in Figure 8.23 (a) where the spontaneous formation of one H_2O and six O-H bonds occurs with an overall exothermic adsorption energy of -28.94 eV (-4.82 eV / RuO_4).

The first H_2O elimination involves the loss of an oxygen atom as H_2O from each RuO_4 and therefore six H_2O are removed as shown in Figure 8.23 (b) with an exothermic reaction energy -28.81 eV (-4.80 eV / H_2O elimination). The same strategy also applies for the second and third rounds of H_2O desorption with clearly overall exothermic reaction energies as shown in Figure 8.24 for a total of 18 H_2O removed.

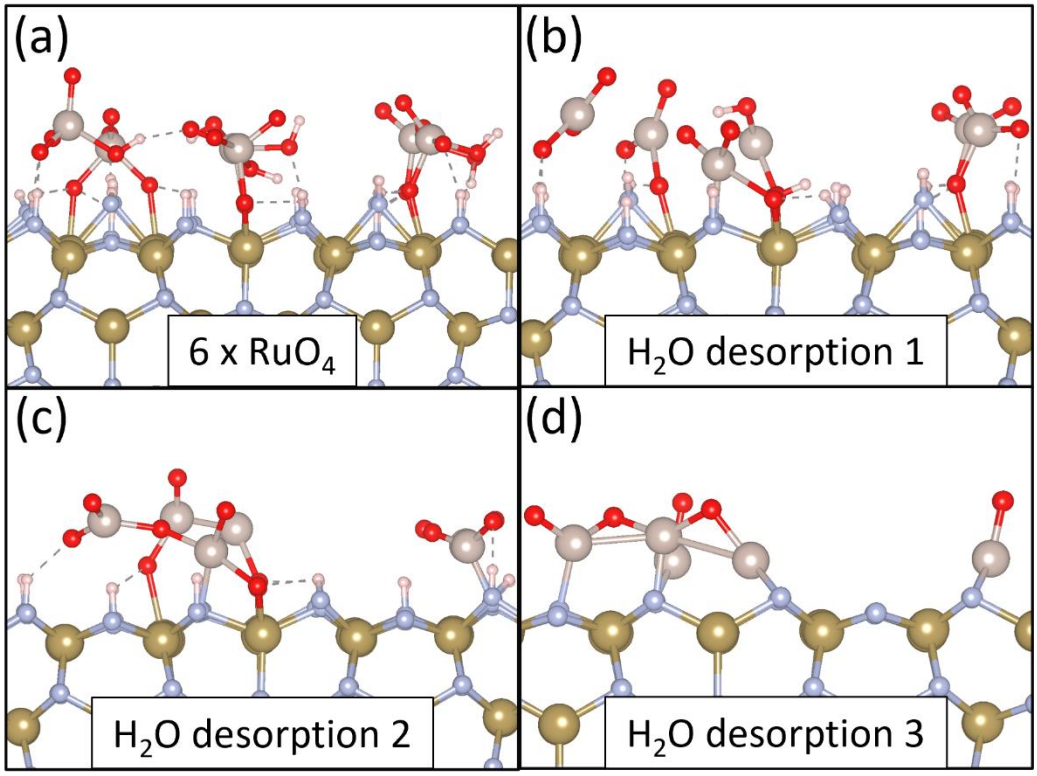


Figure 8.23. Higher coverage of 6 × RuO_4 on 0.5 ML N-H/0.5 ML N-H_2 ε-TaN (110) surface. (a) Adsorption of 6 × RuO_4, (b) First 6 × H_2O desorption, (c) Second 6 × H_2O desorption and (d) Fourth 6 × H_2O desorption. Colour scheme is the same as in Figure 8.19.

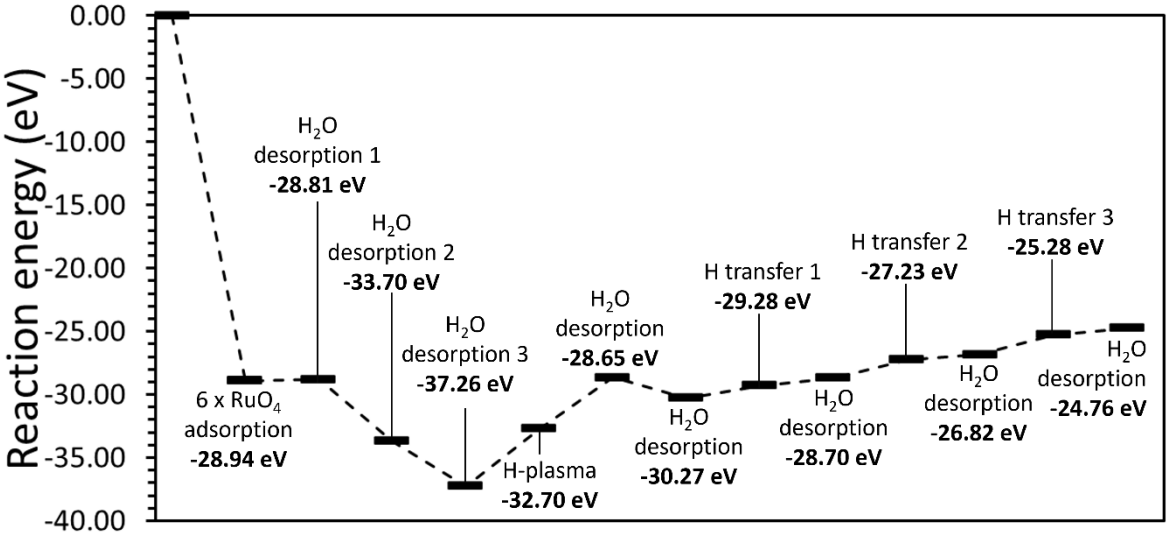


Figure 8.24 Reaction pathway of 6 × RuO_4 on 0.5 ML N-H/0.5 ML N-H_2 ε-TaN (110) surface.

The ε-TaN surface is now terminated with 6 x RuO shown in Figure 8.25 (a) and all surface hydrogen have been removed to eliminate H_2O desorption. We now introduce the plasma generated •H radicals to react at the RuO terminated ε-TaN surface. Two hydrogen radicals are placed near each oxygen atom and therefore a total on twelve hydrogen radicals are placed on the surface. The interaction energies for the hydrogen plasma radicals at oxygen are favourable and upon relaxation two H_2O and two H_2 molecules are spontaneously formed, together with new O-H and N-H bonds as shown in Figure 8.25 (b).

The two H_2O were removed, and upon further relaxation, another H_2O spontaneously formed between oxygen and H_2 shown in Figure 8.25 (c). The remaining H_2 dissociated into Ru-H and O-H with Ru-H and O-H distances of 1.62 Å and 0.97 Å respectively after H_2O was removed; Figure 8.25 (d). Figure 8.25 (e) – (g) show H_2O formation and removal until all oxygen is eliminated leaving a TaN surface terminated with 6 x Ru atoms with an overall exothermic reaction energy of -24.76 eV.

Each Ru atom bonds to the surface through Ru-N bonds in the range 1.90 Å – 2.07 Å. Four Ru atoms form Ru-Ru bonds of 2.45 Å, 2.59 Å and 2.89 Å as shown in Figure 8.26 (a). Nitrogen atoms marked "x" in Figure 8.26 (a) are available to form new N-H_x bonds in the hydrogen plasma pulse which are needed for the next ALD cycle.

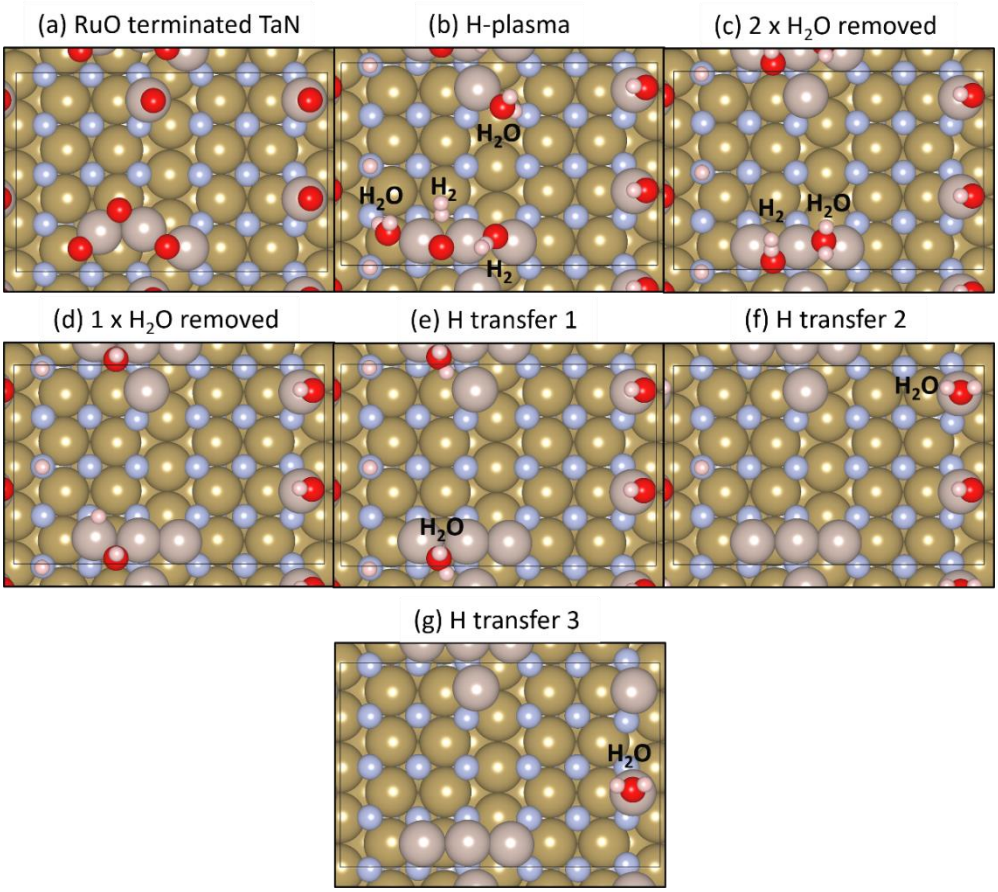


Figure 8.25. H-plasma on post metal precursor RuO_4 treated 0.5 ML N-H/0.5 ML N-H_2 ε-TaN (110) surface. Colour scheme is the same as in Figure 8.19.

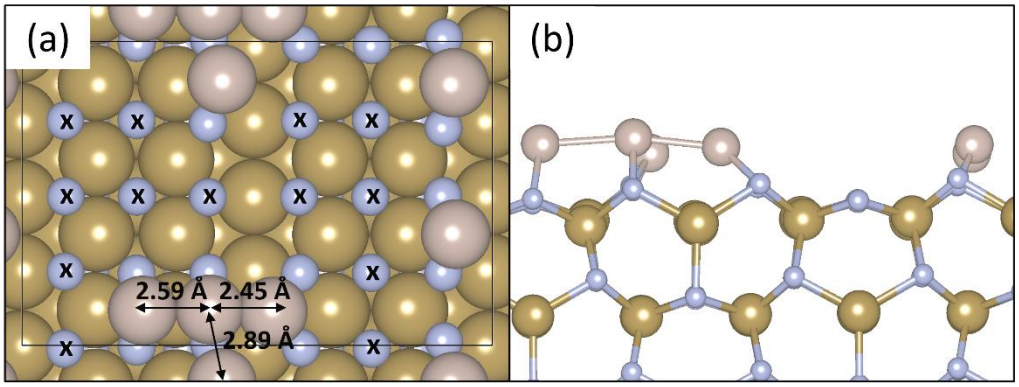


Figure 8.26. 6 x Ru on ε-TaN (110) surface. (a) Top view and (b) side view. Colour scheme is Ta = brown, N = light blue and Ru = grey.

8.4 ALD chemistry of Bis(cyclopentadienyl)cobalt(II), $CoCp_2$, at ε-TaN surfaces

8.4.1 $CoCp_2$ interaction at NH_x-terminated ε-TaN surfaces

The $CoCp_2$ precursors interacted at the different NH_x-terminated ε-TaN (110) surfaces in the upright and a horizontal interaction modes. The interaction energy was calculated using equation (8.1). The energies of $CoCp_2$ at each NH_x-terminated ε-TaN (110) surface are shown in Table 4.

The interaction of $CoCp_2$ is favourable on all NH_x-terminated ε-TaN (110) surfaces. Given the relatively weak interaction with the 0.5 ML N-H/0.5 ML N-H_2 and the 0.67 ML Ta-NH_2 ε-TaN (110) surfaces we do not further explore these surface terminations.

Table 4: Calculated interaction energies for $CoCp_2$ on NH_x-terminated ε-TaN (110) surfaces including the reaction energies after the first and second CpH elimination. (U) = upright interaction mode and (H) = horizontal interaction mode. The geometries for $CoCp_2$ interaction on the NH_x-terminated ε-TaN (110) surfaces are shown in Figure 8.27 and Figure A 8 in the Appendix.

NH_x-terminated TaN	**E_{ads} (eV)**	**ΔE CpH 1 (eV)**	**ΔE CpH 2 (eV)**
N-H_x			
1 ML N-H (U)	-0.72	**-2.07**	0.20
1 ML N-H (H)	-0.86	**-1.63**	0.90
0.5 ML N-H/0.5 ML N-H_2 (U)	-0.66		
0.5 ML N-H/0.5 ML N-H_2 (H)	-0.47		
Ta-NH_x			
0.04 ML Ta-NH_2/0.42 ML Ta-NH/0.04 ML Ta-N (U)	-1.53	0.42	
0.04 ML Ta-NH_2/0.42 ML Ta-NH/0.04 ML Ta-N (H)	-1.67	0.40	
0.67 ML Ta-NH_2 (U)	-0.88	1.99	
0.67 ML Ta-NH_2 (H)	-0.58		
0.38 ML Ta-NH_2 (U)	-1.42	1.88	
0.38 ML Ta-NH_2 (H)	-1.56	0.25	
Mixed N-H, Ta-NH_2			
0.67 ML N-H/0.67 ML Ta – NH_2 (U)	-1.22	**-0.72**	2.91
0.67 ML N-H/0.67 ML Ta – NH_2 (H)	-1.12	**-0.76**	2.91

The reaction energy for the first CpH elimination is favourable for both interaction modes on the 1 ML N-H and 0.67 ML Ta-NH_2/0.67 ML N-H ε-TaN (110) surfaces (for which the reaction energies are highlighted in Table 4) and the geometries for the $CoCp_2$ interaction modes on these surfaces shown in Figure 8.27. We found for the other NH_x-terminated ε-TaN (110) surfaces that have favourable $CoCp_2$ interaction energies, the reaction energy for the first CpH elimination is unfavourable so we neglect these TaN surface terminations. Comparing to $RuCp_2$ on the 1 ML N-H ε-TaN (110) surface in section 8.1.1, the interaction energy of $CoCp_2$ is weaker on this surface. However, after the first CpH elimination from $CoCp_2$ there is an energy gain of 1.35 eV, whereas $RuCp_2$ experiences an energy loss of 1.48 eV for the upright interaction mode, for example.

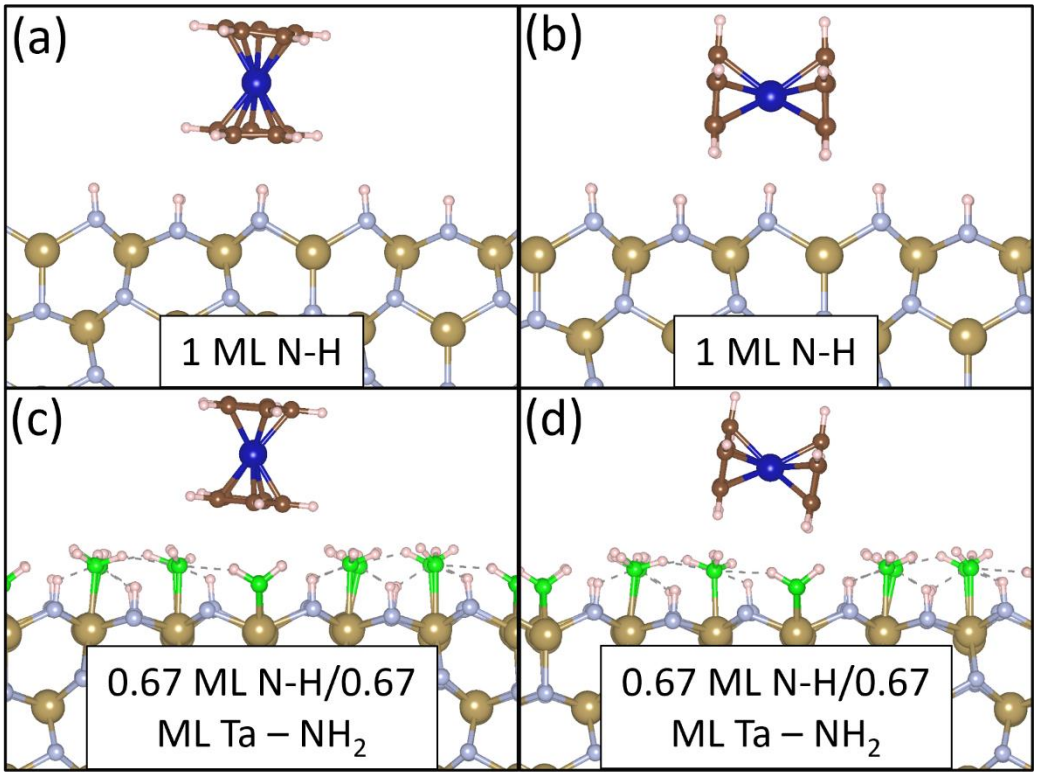


Figure 8.27. Atomic structure of $CoCp_2$ interaction modes on (a) Upright interaction mode on 1 ML N-H, (b) Horizontal interaction mode on 1 ML N-H, (c) Upright interaction mode on 0.67 ML Ta-NH_2/0.67 ML N-H and (d) Horizontal interaction mode on 0.67 ML Ta-NH_2/0.67 ML N-H ε-TaN (110) surfaces.
Colour scheme is Ta = brown, N = light blue & green, H = pink, C = dark brown and Co = dark blue.

8.4.2 Single $CoCp_2$ Reaction Pathway on NH_x-terminated ε-TaN

The reaction pathway of a single $CoCp_2$ precursor on the 1 ML N-H and 0.67 ML N-H/0.67 ML Ta-NH_2 (upright interaction mode) ε-TaN (110) surfaces are examined. The reaction energies of the $CoCp_2$ precursor interaction, hydrogen transfer, CpH formation and CpH desorption are computed with reference to the 1 ML N-H and 0.67 ML N-H/0.67 ML Ta-NH_2 ε-TaN (110) surfaces and free $CoCp_2$ as the reactants and free CpH as the product.

Hydrogen transfer from the 1 ML N-H ε-TaN (110) surface to the Cp ligand of the intact adsorbed $CoCp_2$ precursor is barrierless with comparable reaction energies of -2.50 and -2.66 eV for the upright and horizontal interaction modes respectively as shown in Figure 8.28. There is a moderate energy cost of 0.60 eV for the formation of CpH, and CoCp binds to the surface through a Co-N bond of 1.81 Å for both interaction modes as shown in panel (b) in Figure 8.29 and Figure 8.30. The reaction energy after the first CpH desorption is favourable at -1.63 and -1.64 eV for both interaction modes and are comparable.

The second hydrogen transfer has a low barrier of 0.31 eV for the upright interaction mode and a favourable reaction energy of -2.52 eV after the second hydrogen transfer as shown in Figure 8.28 (a). There is a high energy cost of 2.27 eV for CpH to break from the surface bound Co atom, therefore for a single $CoCp_2$ precursor in the upright interaction mode up to one Cp ligand can be removed via hydrogen transfer. For the horizontal interaction mode, the second hydrogen to the remaining Cp ring has a high activation barrier of 1.79 eV and the reaction energy of the second CpH desorption is thermoneutral, therefore showing up to one Cp ligand can be removed through hydrogen transfer.

In Figure 8.31 the reaction pathway for $CoCp_2$ on the 0.67 ML N-H/0.67 ML Ta-NH_2 ε-TaN (110) surface is shown. The reaction energy for the first hydrogen transfer is exothermic and the barrier to hydrogen transfer is higher, at 1.33 eV, although this does not prevent hydrogen transfer at typical ALD temperatures. Interesting, we find spontaneous formation of N_2H_3 at the surface after the first hydrogen transfer. which is shown in Figure 8.31 (a). The N-N bond is 1.47 Å and the desorption of this species N_2H_3 is favourable, being exothermic by -0.41 eV. The formation and desorption of the first CpH is overall endothermic showing that Cp ligand elimination is challenging due to the high barrier and overall unfavourable reaction energy for the first CpH formation and desorption. The spontaneous formation of N_2H_3 also indicates that the NH_x (x = 1 & 2) terminations are unstable on the surface after a hydrogen transfer from one of the Ta-NH_2 surface terminations to the Cp ligand.

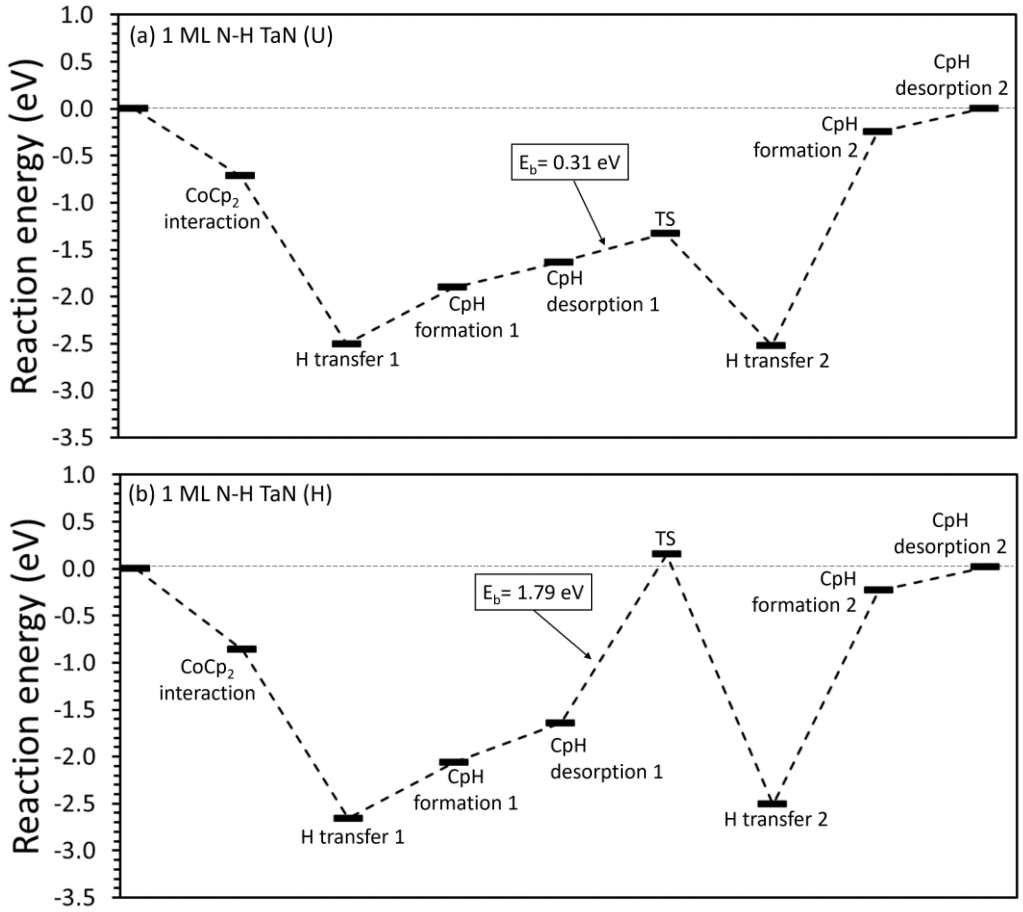


Figure 8.28: $CoCp_2$ reaction pathway on (a) 1 ML N-H (upright interaction mode) and (b) 1 ML N-H (horizontal interaction mode) ε-TaN (110) surfaces.

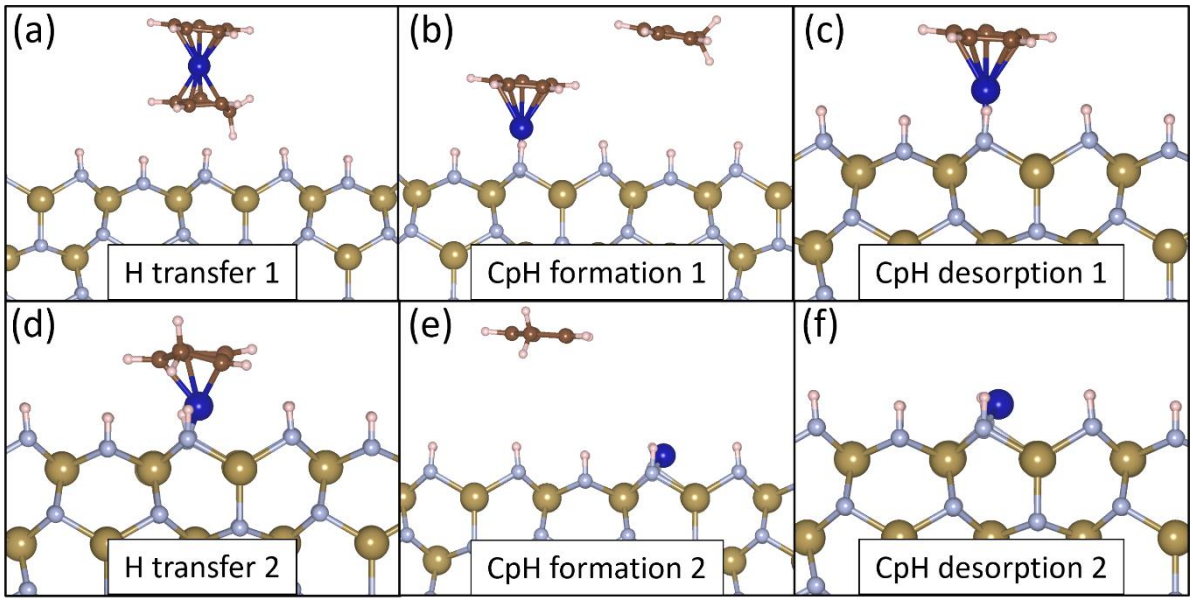


Figure 8.29: Geometries of the individual reaction pathway steps for the upright interaction mode of $CoCp_2$ on 1 ML N-H ε-TaN (110). Colour scheme is the same as in Figure 8.27.

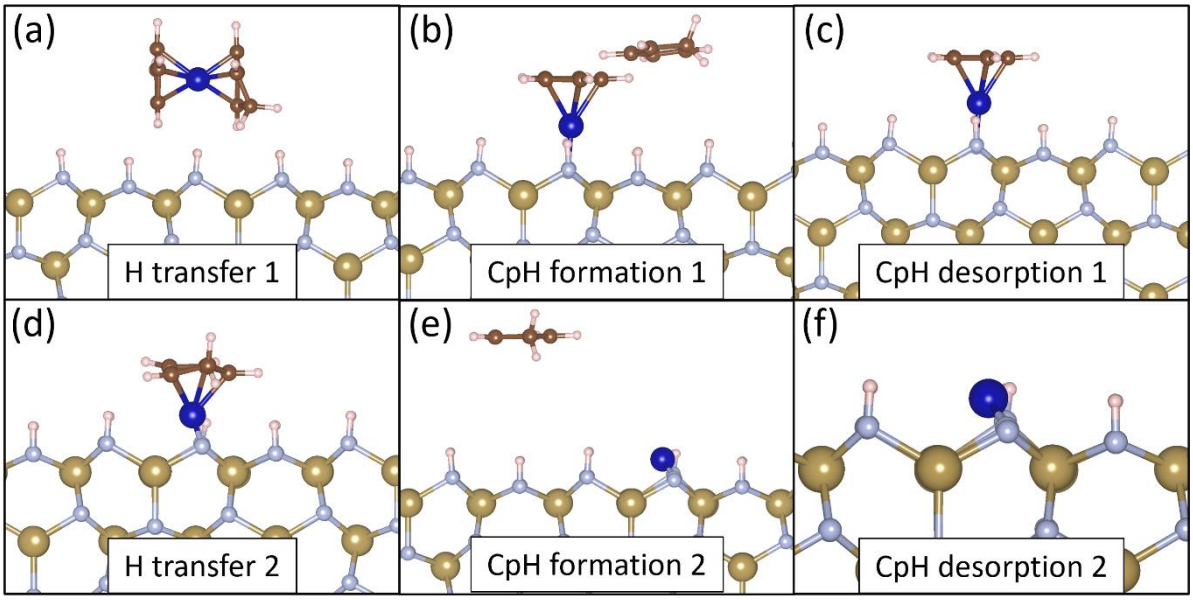


Figure 8.30: Geometries of the individual reaction pathway steps for the horizontal interaction mode of $CoCp_2$ on 1 ML N-H ε-TaN (110). Colour scheme is the same as in Figure 8.27.

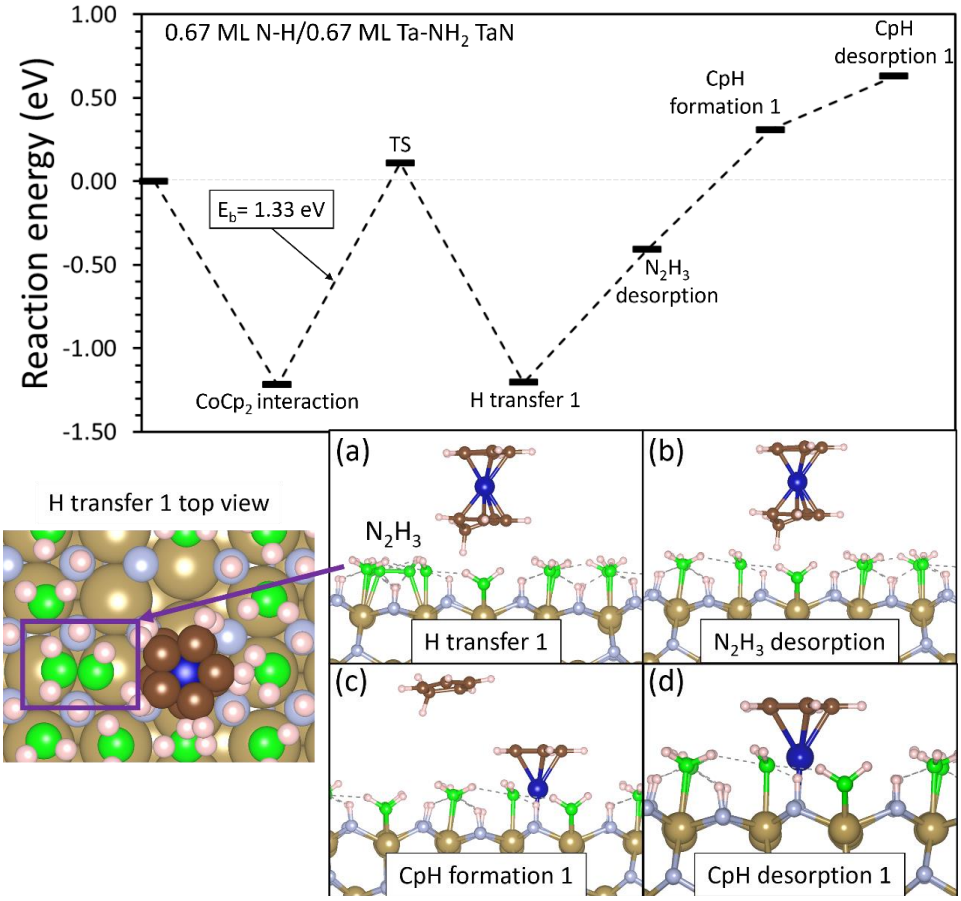


Figure 8.31: $CoCp_2$ reaction pathway on 0.67 ML N-H/0.67 ML Ta-NH_2 ε-TaN (110) surface with the geometries shown. Colour scheme is the same as in Figure 8.27

8.4.3 Chemistry of $CoCp_2$ 1 ML N-H ε-TaN at higher $CoCp_2$ coverage

The effect of $CoCp_2$ coverage on the 1 ML N-H ε-TaN (110) surface is investigated for the upright and horizontal interaction modes of two $CoCp_2$ precursors. The interaction energy of two $CoCp_2$ precursors, which have a surface coverage of 1.38 $CoCp_2/nm^2$, is calculated using equation (8.2) where E_{tot}, $E_{NH_x/metal}$, and $E_{precursor}$ are the energy of the NH_x-terminated TaN slab with two $CoCp_2$ precursors, the slab model for the NH_x-terminated TaN surface, and isolated precursor $CoCp_2$ respectively.

The interaction of two $CoCp_2$ on the 1 ML N-H ε-TaN (110) surface has a favourable energy gain of -3.03 eV (-1.52 eV/precursor) and -1.54 eV (-0.77 eV/precursor) for the upright and horizontal interaction modes as shown in Figure 8.32. Comparing to single $CoCp_2$ interaction on the 1 ML N-H ε-TaN (110) surface, a second $CoCp_2$ increase the interaction energy by 0.80 eV for the upright interaction mode whereas there is minimal change for the horizontal interaction mode. The loss of one CpH from one of the precursors gives $CoCp_2$ and CoCp on the surface, with the latter bound to the surface through a new Co-N bond. For the upright interaction mode there is a small energy cost of 0.32 eV with an exothermic reaction energy of -2.71 eV. The horizontal interaction mode has an energy gain of 1.39 eV, giving an overall exothermic reaction energy of -2.93 eV.

There are two different pathways for subsequent CpH elimination starting from $CoCp_2$ and CoCp fragments to produce a surface terminated with two CoCp fragments or an intact $CoCp_2$ and a bare Co atom. A surface terminated with two CoCp fragments shown in Figure 8.33 (c) is favourable for the upright interaction mode at -3.36 eV and there is no further favourable loss of Cp ligands through hydrogen transfer.

For the horizontal interaction mode the reaction pathway in Figure 8.32 (b) shows that both routes are overall exothermic, but the surface terminated with two CoCp fragments shown in Figure 8.34 (c) is clearly more favourable by 2.02 eV. Although $CoCp_2$ and Co is exothermic, the activation barrier for H transfer to release CpH would be at least 2.32 eV which is not favourable at typical ALD processing temperatures, so we can assume this pathway is not probable. Considering the elimination of a third CpH the surface is terminated with a CoCp fragment and Co atom (shown in Figure 8.34 (e) and (f)) and although this is overall exothermic with a total reaction energy -0.48 eV through the CoCp + CoCp route, the activation barrier will be too high to be overcome. For completeness, the elimination of the remaining Cp ligand leaving two Co surface bound atoms is endothermic. Therefore, at a higher coverage of two

$CoCp_2$ precursors, the surface will be terminated with two CoCp fragments, which can then interact with hydrogen plasma from the second half reaction.

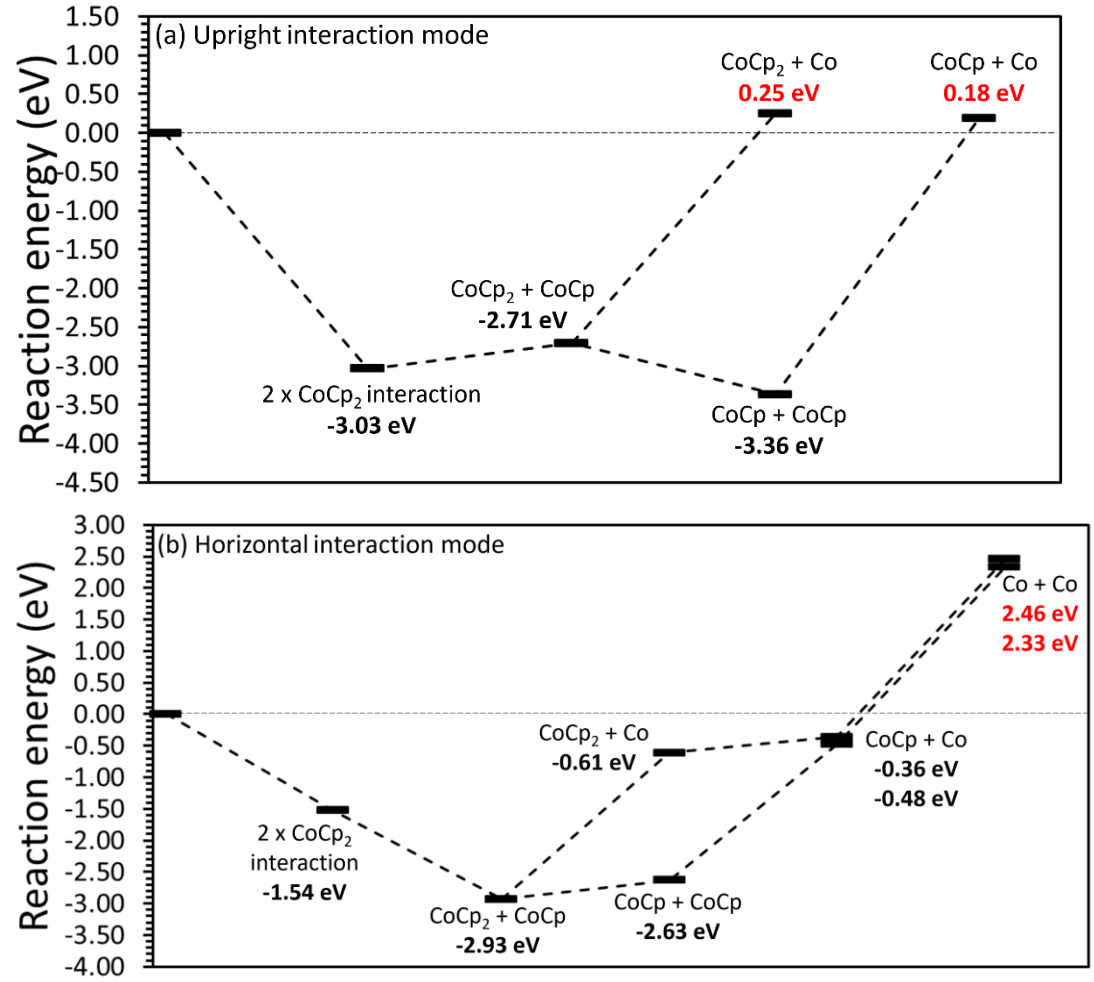


Figure 8.32: Reaction pathway for two $CoCp_2$ precursors on 1 ML N-H ε-TaN (110) surface for (a) upright interaction mode and (b) horizontal interaction mode.

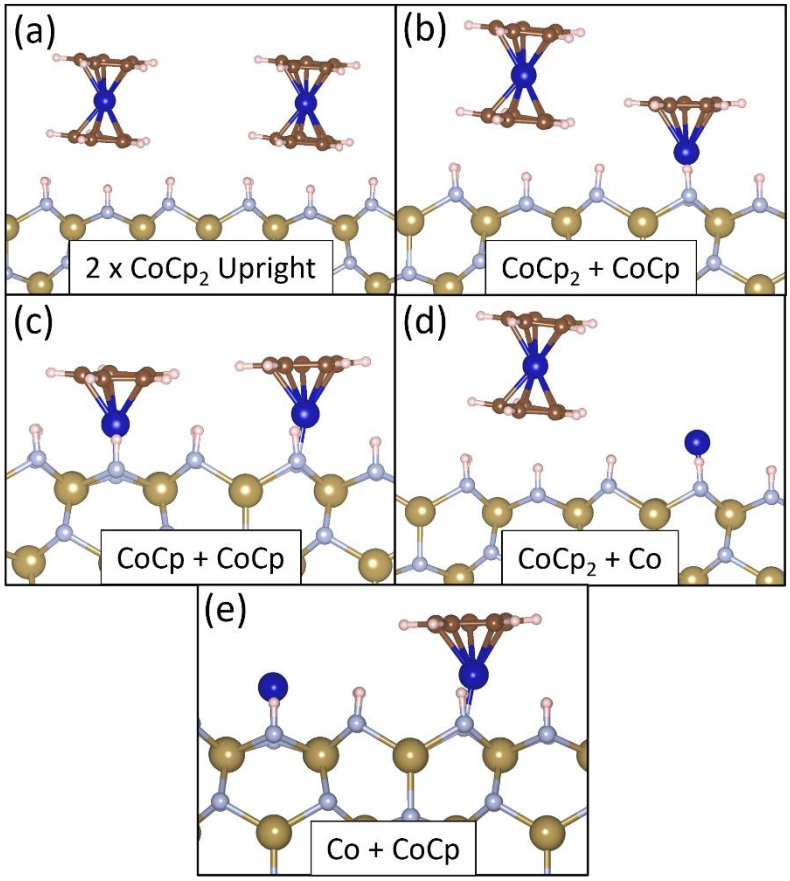


Figure 8.33: Geometries of the reaction pathway of two $CoCp_2$ precursors on 1 ML N-H ε-TaN (110) surface for the reaction pathway shown in Figure 8.32 (a). Colour scheme is the same as in Figure 8.27

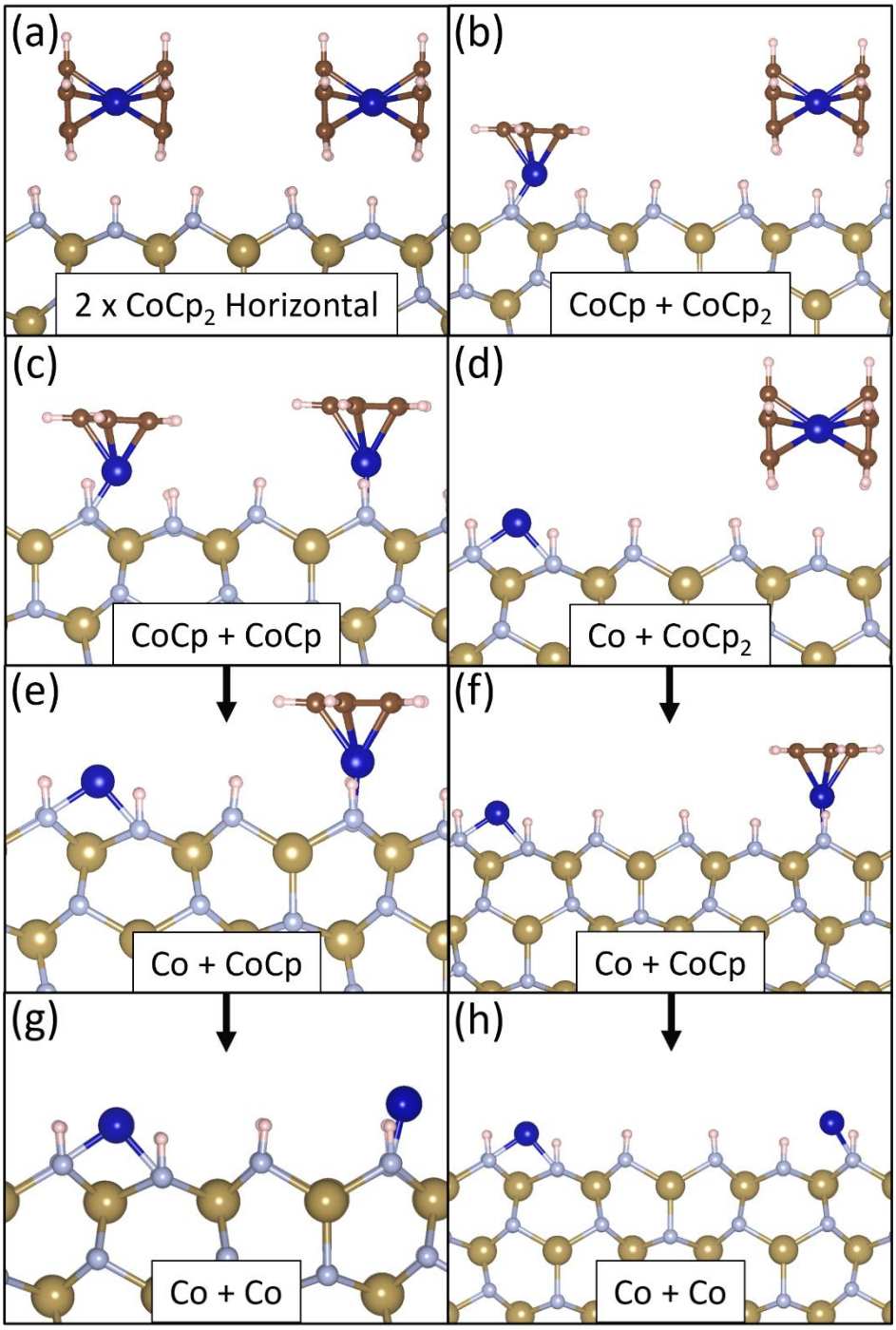


Figure 8.34: Geometries of the reaction pathway of two $CoCp_2$ precursors on 1 ML N-H ε-TaN (110) surface for the reaction pathway shown in Figure 8.32 (b). Colour scheme is the same as in Figure 8.32.

A higher coverage of four $CoCp_2$ precursors, giving a surface coverage of 2.77 $CoCp_2/nm^2$, is examined on the 1 ML N-H ε-TaN (110) surface with the interaction energy calculated using equation (8.2) where the number of precursors is 4. The interaction of four $CoCp_2$ on the 1 ML N-H TaN surface is favourable with a total interaction energy of -5.09 eV (-1.26 eV / $CoCp_2$), shown in Figure 8.35. A higher coverage of $CoCp_2$ has increased the interaction energy per $CoCp_2$ precursor by 0.40 eV compared to a single $CoCp_2$. The elimination of the first Cp ligand from each $CoCp_2$ precursor as CpH via hydrogen transfer from the surface is favourable with a total energy gain (relative to the bare surface and gas phase $CoCp_2$ precursors) of -4.85 eV leaving a surface terminated with four CoCp fragments. The further elimination of up to two more Cp ligands as CpH via hydrogen transfer from the surface is exothermic, but we would expect a very high activation barrier for this process, Figure 8.35. The reaction energy becomes endothermic and unfavourable for a surface terminated with one CoCp fragment and three Co atoms. Therefore after the interaction of four $CoCp_2$ precursors, the surface can be terminated with four CoCp fragments. The N-H coverage also changes from 1 ML N-H TaN to 0.83 ML N-H ε-TaN (110) due to four surface hydrogen being removed as CpH. We also note there was no spontaneous formation of Co-H bonds.

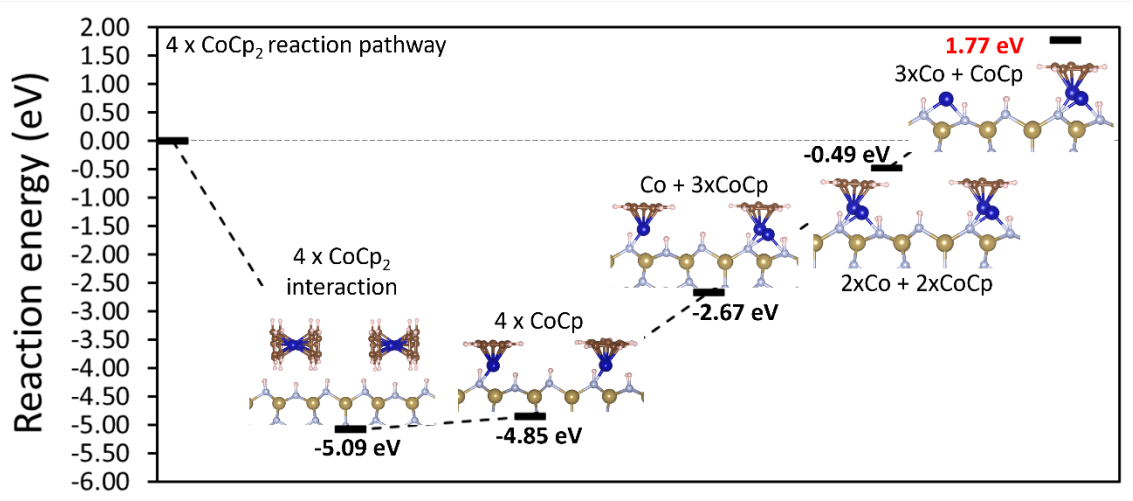


Figure 8.35 Reaction pathway for four $CoCp_2$ precursors adsorbed on the 1 ML N-H ε-TaN (110) surface. Colour scheme is the same as in Figure 8.27.

8.4.4 H_2 plasma radical chemistry $CoCp_2$ precursor fragments on the 1 ML N-H ε-TaN surface

The reactions of plasma generated ˙H radicals at the post $CoCp_2$ precursor 1 ML N-H ε-TaN (110) surface are studied in this section. After interaction with a single $CoCp_2$ precursor surface coverage of H is reduced to 0.96 ML N-H ε-TaN (110). One hydrogen radical 1.90 Å away from the Cp ring allow the structure to relax, from which the ˙H radical interaction energy was calculated using equation (8.3). After relaxing the ˙H radical binds to the Cp ligand with a favourable reaction energy of -4.46 eV. The overall reaction energy after desorption of this CpH is exothermic at -2.42 eV and the reaction pathway and structures are shown in Figure 8.36. The Co bonds to the surface through two new Co-N bonds with Co-N distances of 1.83 Å and 1.87 Å.

Looking at the $(CoCp)_2$ 0.92 ML N-H ε-TaN (110) surface, section 8.4.3, two ˙H radical binds favourably to both Cp ligands at -6.95 eV as shown in Figure 8.39 (b). Co atoms bond to the surface through Co-N bonds of 1.82 Å and 1.83 Å with an overall reaction energy of -1.26 eV.

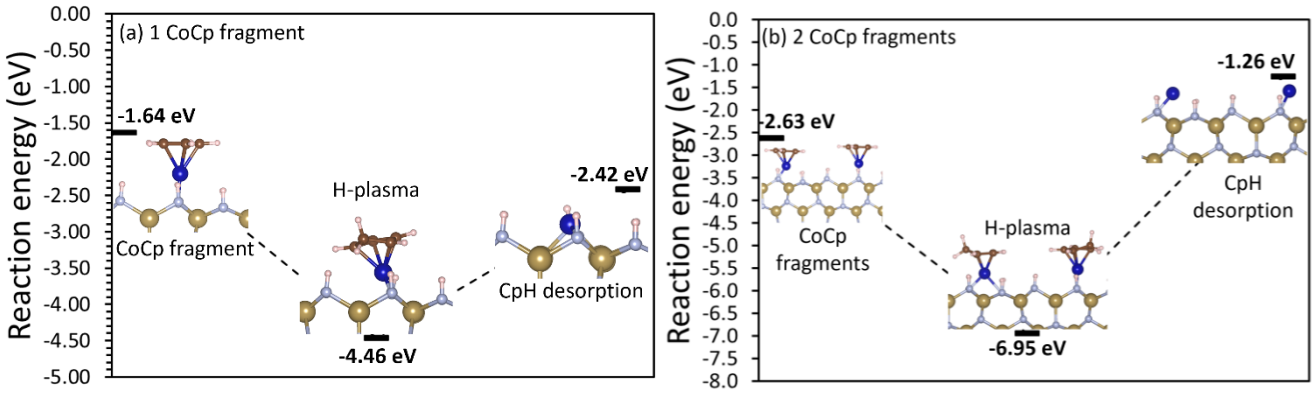


Figure 8.36 Reaction pathways of ˙H radical treated $(CoCp)_x$ terminated (a) 0.96 ML N-H and (b) 0.92 ML N-H ε-TaN (110) surfaces. Colour scheme is the same as in Figure 8.27.

We also saw in section 8.4.3 that the 0.83 ML N-H ε-TaN (110) surface terminated with 4 CoCp with a coverage of 2.77 $CoCp_2/nm^2$, is stable and therefore the interaction of hydrogen radicals at this CoCp-terminated surface is also examined. The same strategy is used where a ˙H radical is placed 1.90 Å away from each Cp ring and the structure is allowed to relax. The overall reaction energy after CpH formation and desorption is favourable for the $(CoCp)_4$ 0.83 ML N-H ε-TaN (110) surface at -1.30 eV as shown in Figure 8.37 (a) where Co bonds to the surface through Co-N bonds of 1.75 – 1.83 Å. There was no spontaneous formation of Co-H bonds. Comparing to a coverage of 4 RuCp on the same surface in section 8.1.5, not all RuCp

fragments were removed favourably, leading to possible carbon contamination. For completeness the reaction of plasma generated $^{\bullet}H$ radicals is tested at the $(CoCp)_3$ + Co 0.79 ML N-H and the $(CoCp)_2$ + $(Co)_2$ 0.75 ML N-H ε-TaN (110) surfaces. However the overall reaction energy after the CpH desorption is endothermic at 0.09 eV and 1.38 eV respectively shown in (b) and (c) in Figure 8.37. As these coverages would require high barriers we would expect that for 2.77 $CoCp_2/nm^2$ the pathway shown in Figure 8.37 (a) removes the remaining Cp ligands.

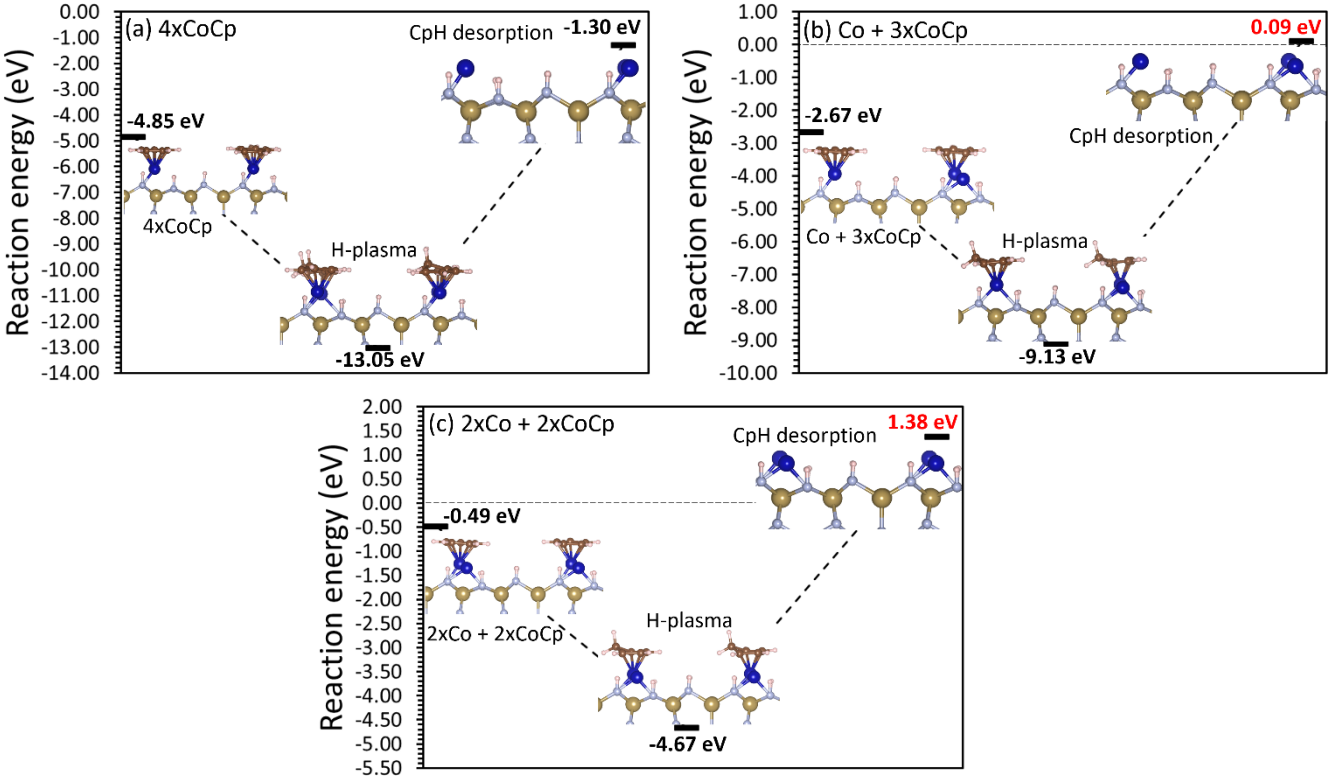


Figure 8.37: Reaction pathway of plasma generated hydrogen radicals at (a) $(CoCp)_4$ 0.83 ML N-H, (b)) $(CoCp)_3$ + Co 0.79 ML N-H and (c) $(CoCp)_2$ + $(Co)_2$ 0.75 ML N-H ε-TaN (110).

8.5 ALD Chemistry with the Bis(ethylcyclopentadienyl)cobalt(II), $Co(EtCp)_2$ precursor

8.5.1 7.4.1 $Co(EtCp)_2$ interaction at NH_x-terminated ε-TaN surfaces

The interaction of $Co(EtCp)_2$ is favourable on all the NH_x-terminated ε-TaN (110) surfaces for both interaction modes, from the computed energy changes shown in Table 5. The reaction energy for the elimination of the first EtCp ligand through hydrogen transfer is favourable on the 1 ML N-H, 0.5 ML N-H/0.5 ML N-H_2, and 0.67 ML Ta-NH_2 ε-TaN (110) surfaces for the upright precursor interaction mode. It is also favourable on the 0.67 ML N-H/0.67 ML Ta-NH_2 ε-TaN (110) surface in the upright interaction mode and the corresponding structures are shown in Figure 8.38. The reaction energies for the first EtCpH elimination on the 0.38 ML Ta-NH_2 ε-TaN (110) surface are only weakly favourable therefore this surface is not considered for further investigation. The reaction energies also suggest that elimination of the Second EtCpH is favourable on the 0.5 ML N-H/0.5 ML N-H_2 ε-TaN (110) surface for upright interaction mode with an exothermic reaction energy of -0.77 eV.

Table 5: Calculated interaction energies for $Co(EtCp)_2$ on NH_x-terminated ε-TaN (110) surfaces including the reaction energies after the first and second EtCpH elimination. (U) = upright interaction mode and (H) = horizontal interaction mode. The geometries for $Co(EtCp)_2$ interaction on the NH_x-terminated ε-TaN (110) surfaces are shown in Figure 8.38 and Figure A 9 in the Appendix.

NH_x-terminated TaN	**E_{ads} (eV)**	**ΔE EtCpH 1 (eV)**	**ΔE EtCpH 2 (eV)**
N-H_x			
1 ML N-H (U)	-1.31	**-2.23**	0.14
1 ML N-H (H)	-1.18	**-0.66**	0.96
0.5 ML N-H/0.5 ML N-H_2 (U)	-1.28	**-1.46**	**-0.77**
0.5 ML N-H/0.5 ML N-H_2 (H)	-0.90	**-0.73**	1.31
Ta-NH_x			
0.04 ML Ta-NH_2/0.42 ML Ta-NH/0.04 ML Ta-N (U)	-2.13	0.61	
0.04 ML Ta-NH_2/0.42 ML Ta-NH/0.04 ML Ta-N (H)	-2.06	0.04	
0.67 ML Ta-NH_2 (U)	-1.41	**-0.27**	3.56
0.67 ML Ta-NH_2 (H)	-1.08	1.38	
0.38 ML Ta-NH_2 (U)	-2.20	-0.06	5.40
0.38 ML Ta-NH_2 (H)	-1.91	-0.13	5.25
Mixed N-H, Ta-NH_2			
0.67 ML N-H/0.67 ML Ta – NH_2 (U)	-1.86	**-2.73**	0.97
0.67 ML N-H/0.67 ML Ta – NH_2 (H)	-1.58	3.10	

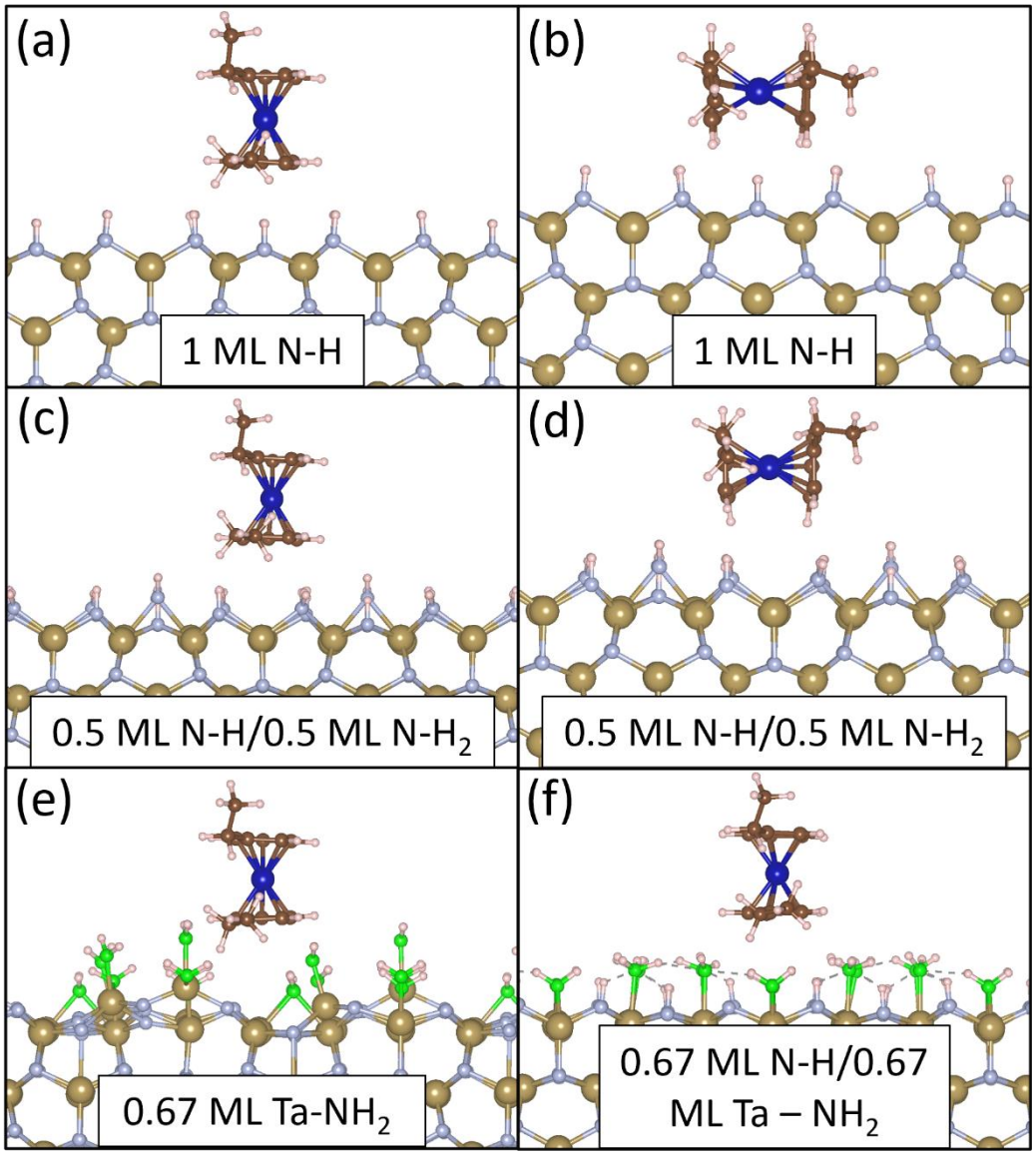


Figure 8.38. $Co(EtCp)_2$ interaction on (a) 1 ML N-H upright interaction mode, (b) 1 ML N-H horizontal interaction mode, (c) 0.5 ML N-H/0.5 ML $N-H_2$ upright interaction mode, (d) 0.5 ML N-H/0.5 ML $N-H_2$ horizontal interaction mode, (e) 0.67 ML $Ta-NH_2$ and (f) 0.67 ML N-H/0.67 $Ta-NH_2$ ML upright interaction mode on the ε-TaN (110) surfaces. Colour scheme is the same as in Figure 8.27.

8.5.2 Single $Co(EtCp)_2$ Reaction Pathway on NH_x-terminated ε-TaN

The reaction pathway for EtCp ligand elimination is explored for a single $Co(EtCp)_2$ precursor interacting on the 1ML N-H, 0.5 ML N-H/0.5 ML N-H_2, 0.67 ML Ta-NH_2 and 0.67 ML N-H/0.67 ML Ta-NH_2 ε-TaN (110) surfaces in the upright precursor interaction mode. In Figure 8.39 the reaction pathways for EtCp ligand loss on (a) 1 ML N-H and (b) 0.5 ML N-H/0.5 ML N-H_2 ε-TaN (110) surfaces are plotted. The formation and desorption of the first EtCpH is favourable, with a moderate activation barrier of 0.79 eV on the 1 ML N-H ε-TaN (110) surface. The reaction energy of the second EtCpH desorption is unfavourable with a high barrier of 1.45 eV, meaning that Co-EtCp fragments should persist on the surface.

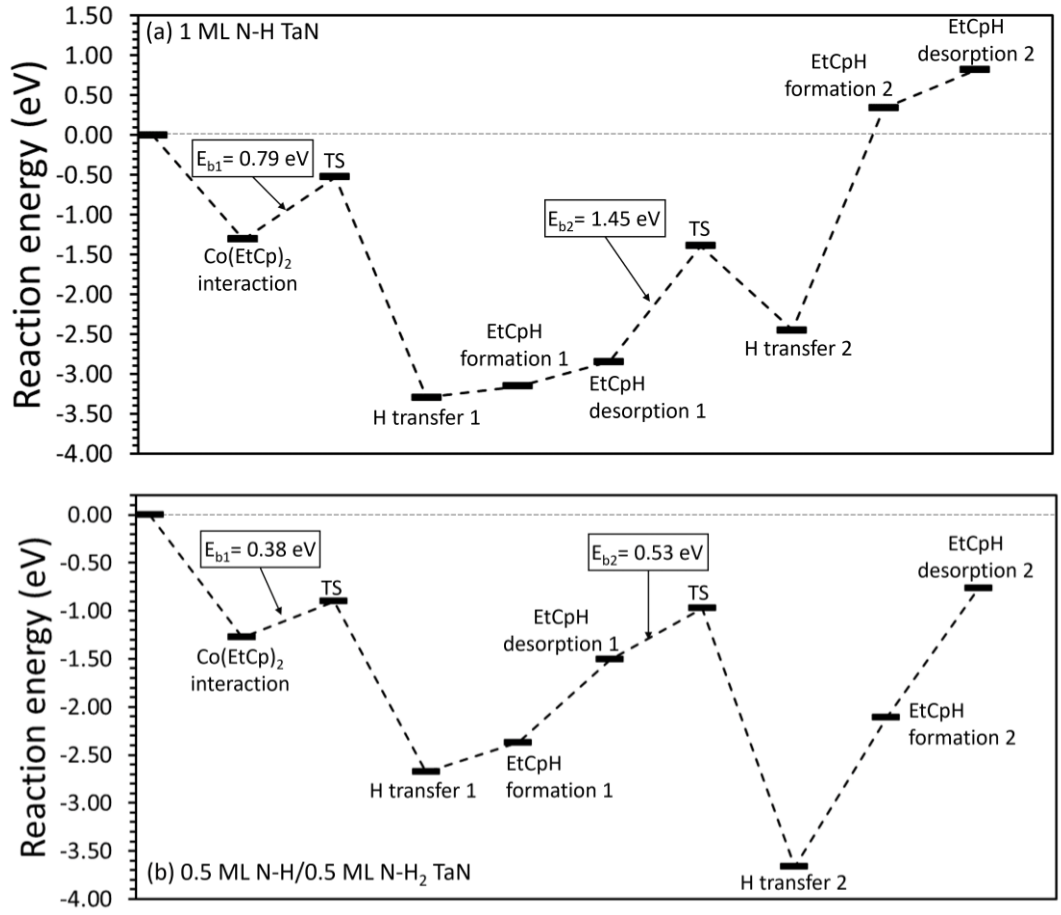


Figure 8.39. $Co(EtCp)_2$ reaction pathway on (a) 1 ML N-H and (b) 0.5 ML N-H/0.5 ML N-H_2 ε-TaN (110) for the upright interaction mode.

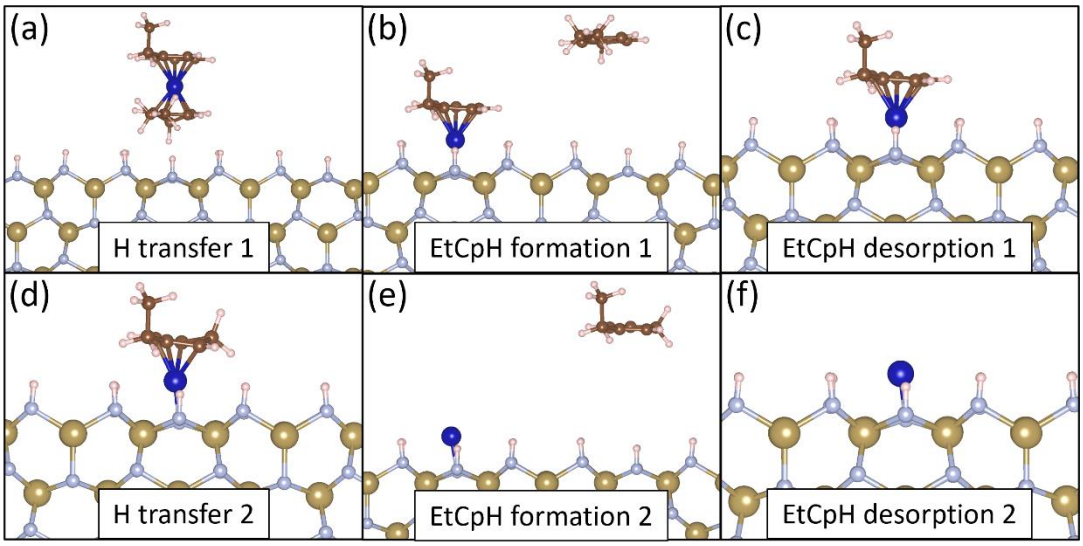


Figure 8.40. Geometries of the individual reaction pathway steps for the upright interaction mode of $Co(EtCp)_2$ on 1 ML N-H ε-TaN (110). Colour scheme is the same as in Figure 8.27.

On the 0.5 ML N-H/0.5 ML N-H_2 ε-TaN (110), surface the overall reaction energy after the second EtCpH desorption is exothermic at -0.77 eV with low computed activation barriers of 0.38 eV and 0.53 eV for the first and second hydrogen transfer steps, respectively. There is also a spontaneous transfer of hydrogen from the surface to cobalt forming a Co-H bond with a Co-H distance of 1.62 Å shown in panel (f) in Figure 8.41. This Co-H bond may help stabilise Co after the second ligand loss. This is also the first spontaneous Co-H bond to occur from our calculations with Co precursors. Figure 8.40 and Figure 8.41 show the geometries for the steps in the reaction pathways for $Co(EtCp)_2$ on the 1 ML N-H and 0.5 ML N-H/0.5 ML N-H_2 ε-TaN (110) surfaces respectively. These results show that for $Co(EtCp)_2$, up to one EtCp ligand can be eliminated on the 1 ML N-H ε-TaN (110) surface whereas both EtCp ligands can be removed via hydrogen transfer on the 0.5 ML N-H/0.5 ML N-H_2 ε-TaN (110) surface. The reaction energies for each step along the reaction pathways shown in Figure 8.39 are listed in Table A 2 in the Appendix.

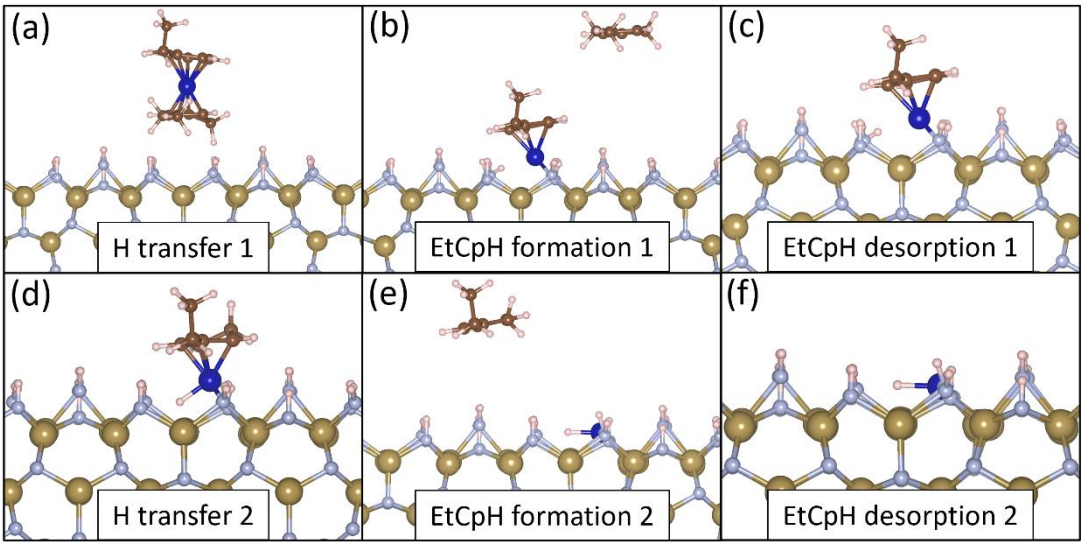


Figure 8.41. Geometries of the individual reaction pathway steps for the upright interaction mode of $Co(EtCp)_2$ on 0.5 ML N-H/0.5 ML N-H_2 ε-TaN (110). Colour scheme is the same as in Figure 8.27.

On the 0.67 ML Ta-NH_2 and 0.67 ML N-H/0.67 ML Ta-NH_2 ε-TaN (110) surfaces, the reaction energies for the first hydrogen transfer to the EtCp ligand of $Co(EtCp)_2$ are endothermic and have very high barriers of 2.15 eV and 2.42 eV, respectively as shown in Figure 8.42. On these surfaces the endothermic reaction energy and high barriers would make it difficult for the first EtCpH elimination from $Co(EtCp)_2$. This was also found for $CoCp_2$ on the 0.67 ML N-H/0.67 ML Ta-NH_2 ε-TaN (110) surface in section 8.4.2, showing that both Co precursors do not interact favourably with surfaces that include Ta-NH_2 surface terminations. $Co(EtCp)_2$ reacts favourably on the 0.5 ML N-H/0.5 ML N-H_2 ε-TaN (110) surface and can lose both EtCp ligands whereas Cp ligand loss is unfavourable for $CoCp_2$. Similar to $RuCp_2$ and $Ru(EtCp)_2$ the addition of Et functional group to the Cp ring provides enhanced precursor reactivity.

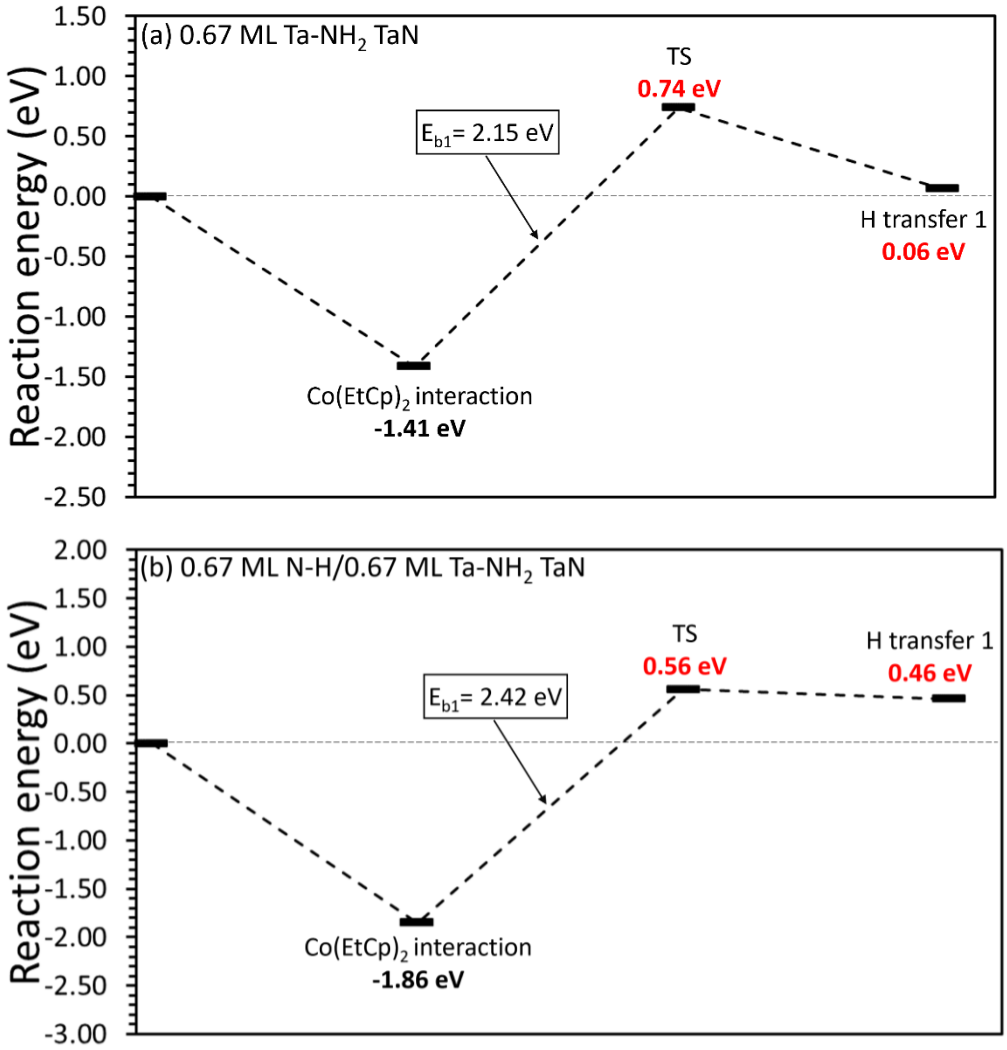


Figure 8.42. $Co(EtCp)_2$ reaction pathway on (a) 0.67 ML Ta-NH_2 and (b) 0.67 ML N-H/0.67 ML Ta-NH_2 ε-TaN (110) surfaces for the upright interaction mode.

8.5.3 Effect of $Co(EtCp)_2$ coverage on the 1 ML N-H and 0.5 ML N-H/0.5 ML N-H_2 ε-TaN Surfaces

A higher coverage of two $Co(EtCp)_2$ precursors on the 1 ML N-H and 0.5 ML N-H/0.5 ML N-H_2 ε-TaN (110) surfaces is now examined. The interaction energy of two $Co(EtCp)_2$ precursors is -4.08 eV (-2.04 eV/precursor) on 1 ML N-H and -2.78 eV (-1.39 eV/precursor) on 0.5 ML N -H/0.5 ML N-H2 ε-TaN (110) surfaces. These interaction energies per precursor show that increasing the coverage of $Co(EtCp)_2$ enhances $Co(EtCp)_2$ interaction with the surface by 0.73 eV on 1 ML N-H and 0.11 eV on 0.5 ML N -H/0.5 ML N-H2 ε-TaN (110) surfaces. The interaction of two $Co(EtCp)_2$ precursors on the 1 ML N-H ε-TaN (110) surface is more favourable by 2.54 eV compared to two $CoCp_2$.

In Figure 8.43 the reaction pathways for two $Co(EtCp)_2$ precursors interacting on the (a) 1 ML N-H and (b) 0.5 ML N-H/0.5 N-H_2 ε-TaN (110) surfaces are plotted with the geometries shown in Figure 8.44 and Figure 8.45. On both TaN surfaces, we find that surfaces terminated with two Co(EtCp) fragments or one $Co(EtCp)_2$ and a Co atom are both thermodynamically favourable. After the third EtCpH elimination the preference is for both surfaces to be terminated with a Co(EtCp) fragment and a Co atom. For the 1 ML N-H ε-TaN (110) surface, this is favourable, being exothermic by -0.71 eV when proceeding from the surface terminated with an intact adsorbed $Co(EtCp)_2$ and Co atom. It is thermoneutral when proceeding from the surface terminated with two CoEtCp fragments. Considering the first route, there is an energy cost of 2.85 eV to go to the surface terminated with one $Co(EtCp)_2$ and a Co atom. However there is an energy gain of 0.36 eV when going to the surface terminated with two CoEtCp fragments and it is reasonable to say that this is the most probable surface termination given the thermoneutral reaction energy for the third EtCp ligand elimination.

On the 0.5 ML N-H/0.5 ML N-H_2 ε-TaN (110) surface, the elimination of the first EtCp ligand via hydrogen transfer is exothermic at -2.18 eV leaving one $Co(EtCp)_2$ and a CoEtCp fragment and has a moderate energy cost of 0.60 eV. Similar to the previous surface, after the second EtCp ligand elimination the surface can be terminated by either a (a) $Co(EtCp)_2$ and Co atom or (b) two CoEtCp fragments. The reaction pathway in Figure 8.43 (b) show that both routes are possible with energy costs of 0.72 eV and 0.71 eV respectively. The same applies after the third ligand elimination where the surface is terminated with a CoEtCp fragment and Co atom, but it is the route that originated from (a) that results in complete ligand elimination with two Co atoms on the surface that is overall favourable with a small energy gain of -0.20 eV. The final EtCp elimination has an energy cost of 0.49 eV.

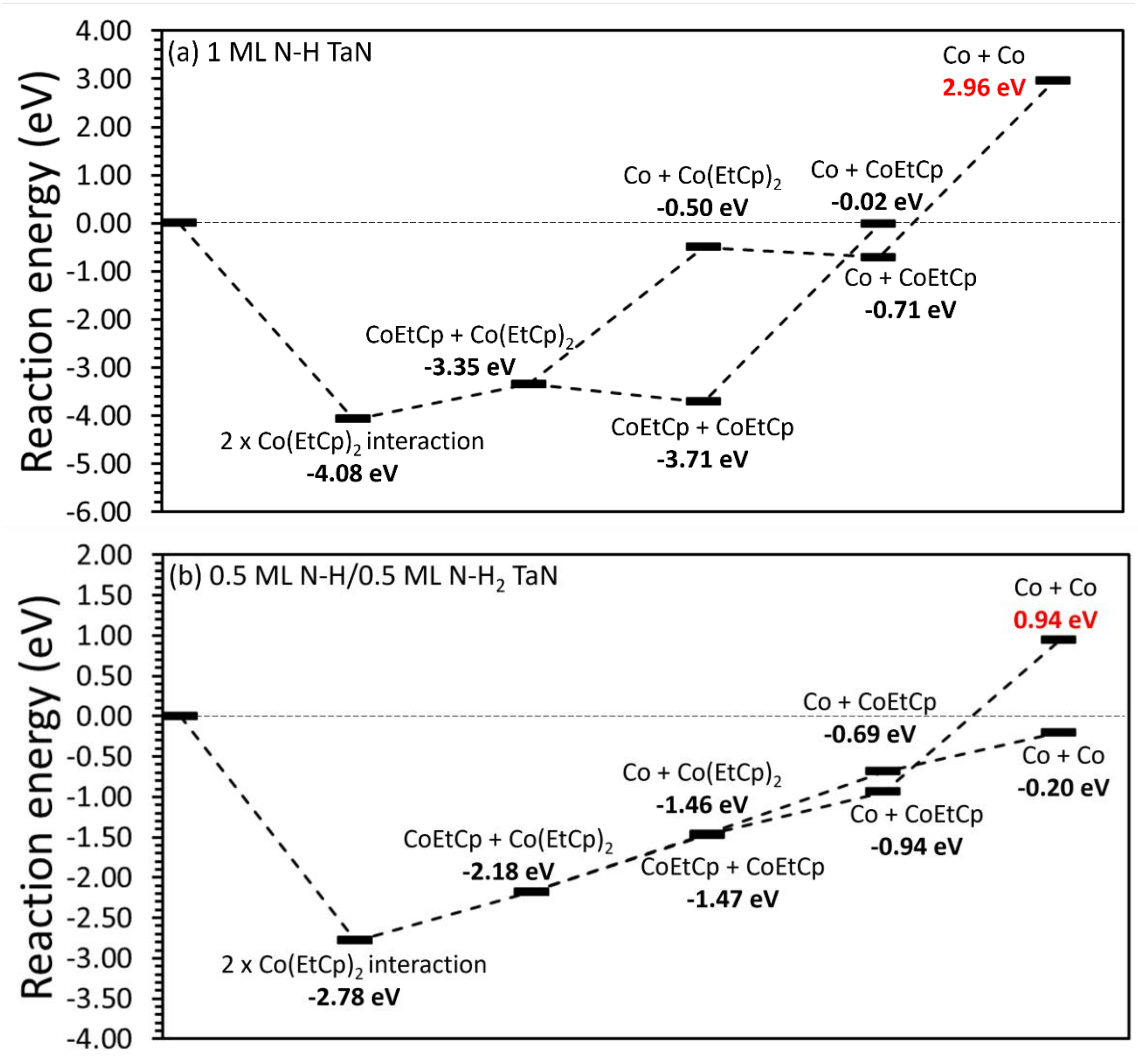


Figure 8.43 Reaction pathway for two $Co(EtCp)_2$ precursors on (a) 1 ML N-H surface and (b) 0.5 ML N-H/0.5 ML N-H_2 ε-TaN (110) surfaces.

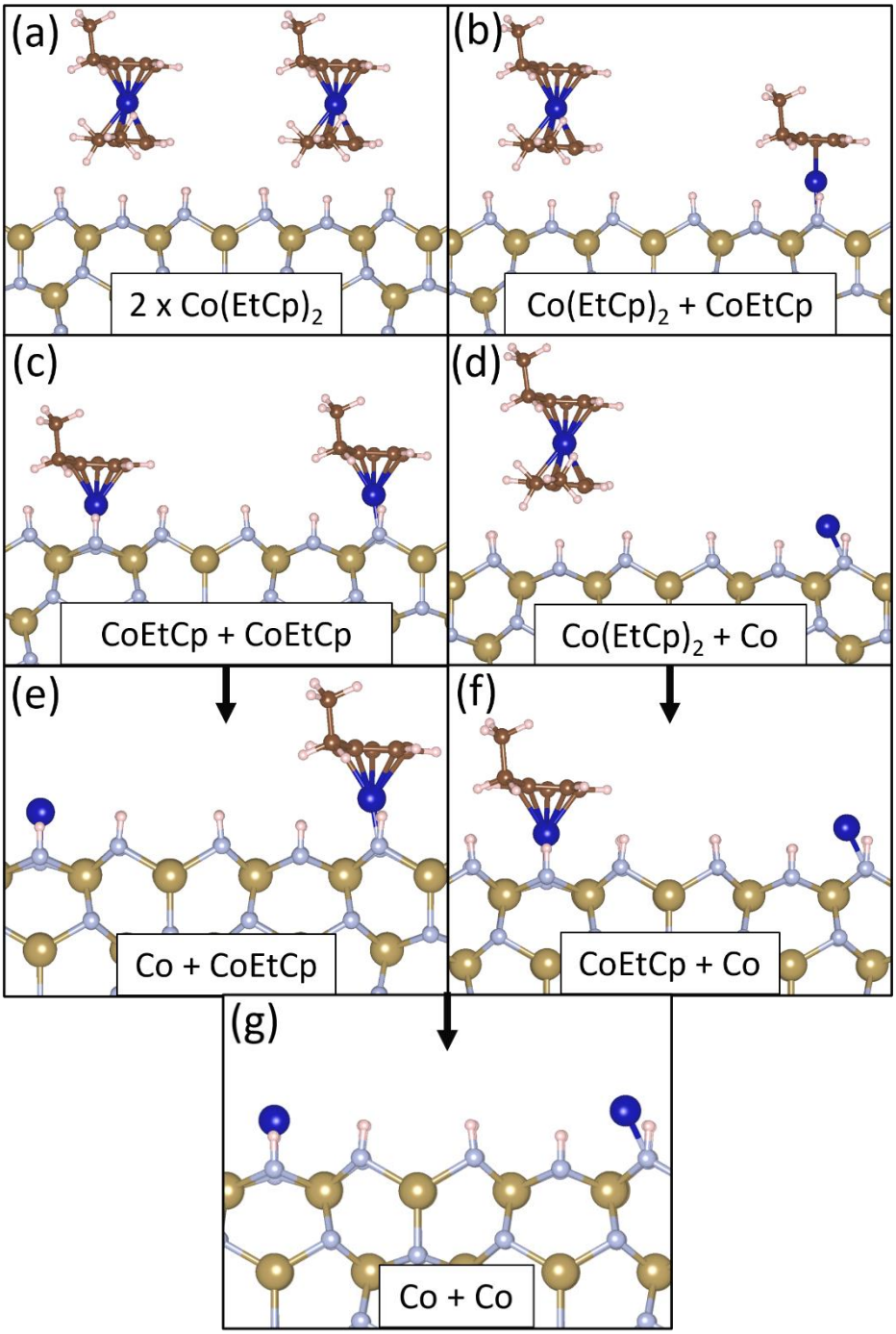


Figure 8.44. Geometries of two $Co(EtCp)_2$ adsorbed on the 1 ML N-H ε-TaN (110) surface. Colour scheme is the same as in Figure 8.27.

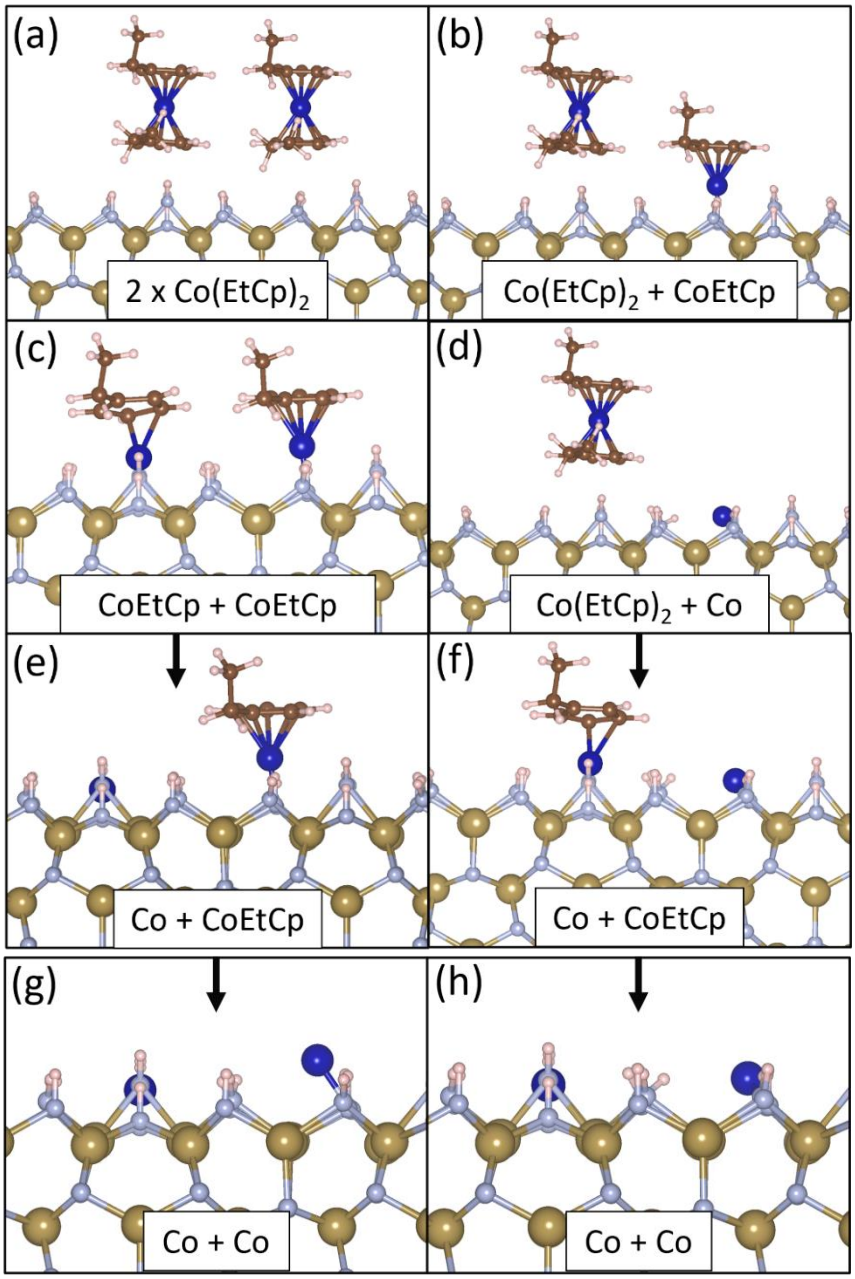


Figure 8.45 Geometries of two $Co(EtCp)_2$ adsorbed on the 0.5 ML N-H/0.5 ML N-H_2 ε-TaN (110) surface. Colour scheme is the same as in Figure 8.27.

8.5.4 H_2 plasma radical chemistry on $Co(EtCp)_2$ treated 1 ML N-H ε-TaN surface

The reactions of plasma generated •H radical at the post $Co(EtCp)_2$ precursor 1 ML N-H ε-TaN (110) surface is studied for one and two $Co(EtCp)_2$ precursors. The 0.5 ML N-H/0.5 ML N-H_2 ε-TaN (110) surface is not studied in this section since all EtCp ligands can be favourably eliminated via hydrogen transfer from the surface, and H plasma radicals would bind to these Co sites to yield Co-H terminated surfaces. From our earlier work[14,27,28] using ammonia or N_2/H_2 plasma would yield a Co-NH terminated surface. The N-H coverage for single precursor changes to 0.96 ML N-H ε-TaN (110) since one surface hydrogen was used for the first EtCpH elimination. The hydrogen radical is placed 1.90 Å away from the EtCp ligand and the interaction energy is calculated using equation (8.3). The overall reaction energy after •H radical adsorption followed by EtCpH formation and elimination is favourable at -1.25 eV leaving a Co atom bonding to the surface through Co – N bonds of 1.84 Å and 2.32 Å as shown in Figure 8.46 (a).

We showed in section 8.5.3 that the 1 ML N-H ε-TaN (110) surface would be terminated with two CoEtCp fragments. For completeness similar to $CoCp_2$, we study the interaction of the •H radical at the CoEtCp-Co 0.88 ML N-H and $(CoEtCp)_2$ 0.92 ML N-H ε-TaN (110) surfaces. For the CoEtCp-Co 0.88 ML N-H ε-TaN (110) surface, a hydrogen radical is placed 1.90 Å away from the EtCp ligand. The interaction energy shows that overall reaction energy after EtCpH formation and desorption is endothermic, being 0.66 eV as shown in Figure 8.46 (b). On the $(CoEtCp)_2$ 0.92 ML N-H ε-TaN (110) surface two hydrogen radicals is placed 1.90 Å away from the EtCp ligands. Figure 8.46 (c) shows that the overall reaction energy is exothermic at -1.65 eV after EtCpH formation and desorption. Like $CoCp_2$, the overall reaction energy is endothermic after EtCpH desorption for hydrogen plasma adsorption on a surface that contains Co atoms. The presence of CoEtCp fragments appears to promote the reaction of hydrogen plasma to remove the remaining EtCp ligands favourably and this apparent enhancement of reactivity upon replacing Cp with EtCp is a general finding.

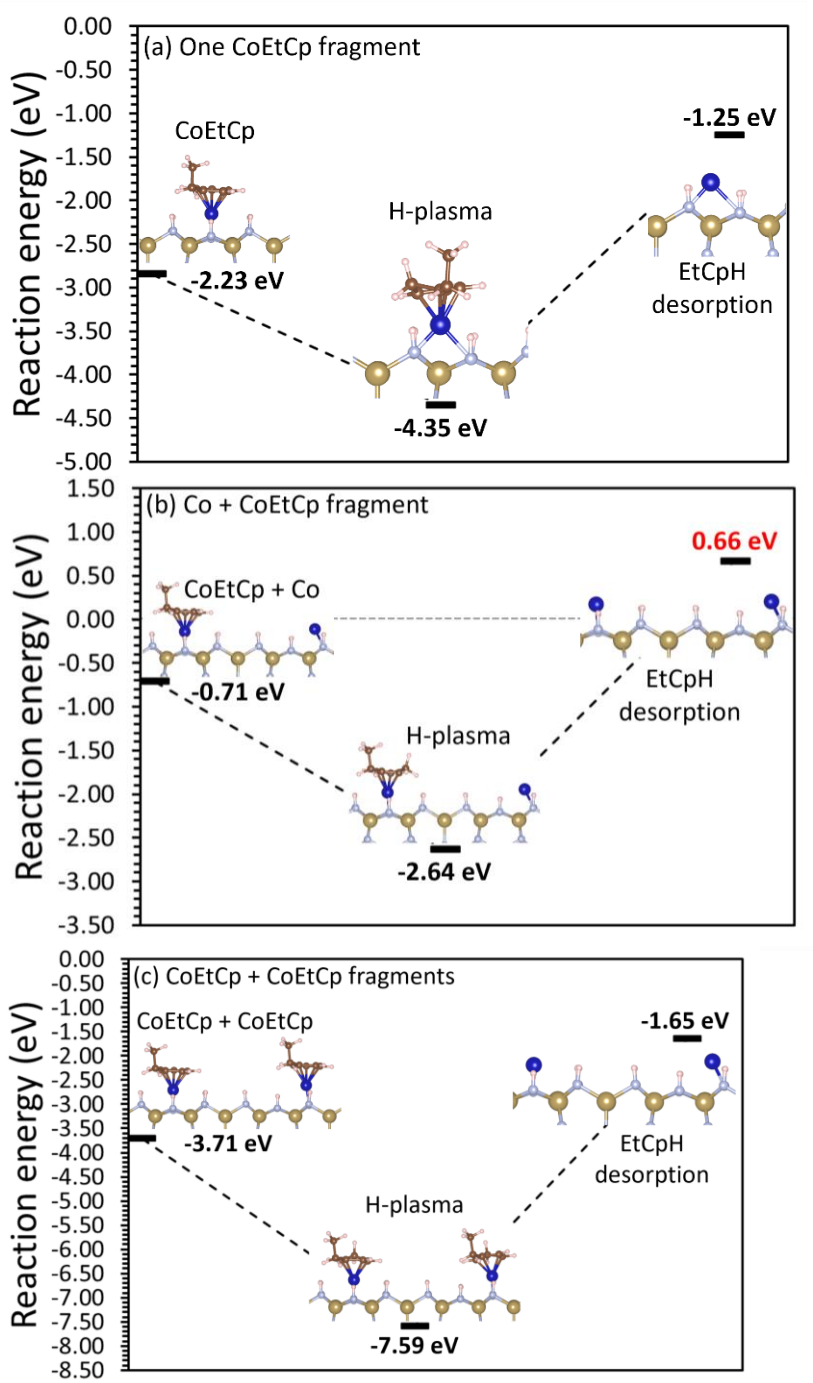


Figure 8.46 Reaction pathway of •H radical treated (a) CoEtCp 0.96 ML N-H, (b) Co & CoEtCp 0.88 ML N-H and (c) $(CoEtCp)_2$ 0.92 ML N-H ε-TaN (110) surfaces. Colour scheme is the same as in Figure 8.27.

8.6 Discussion

In this chapter, the reactivity of ruthenium and cobalt precursors $RuCp_2$, $Ru(EtCp)_2$, RuO_4, $CoCp_2$ and $Co(EtCp)_2$ were studied the NH_x-terminated ε-TaN (110) surfaces from Chapter 7. Hydrogen transfer from the surfaces containing Ta-NH_x surface terminations to promote ligand elimination from the Ru/Co precursors was unfavourable. This suggests that *ε*-TaN (110) surfaces with added NH_x (higher content of nitrogen on the surface) inhibit deposition of ruthenium and cobalt. Whereas *ε*-TaN (110) surfaces containing N-H_x terminations show to be promising for ruthenium and cobalt deposition.

The first Cp ligand loss via hydrogen transfer was only favourable on the 1 ML N-H *ε*-TaN (110) surface for $RuCp_2$ leaving $(RuCp)_y$ (y = 1 or 4) fragments on the surface. Hydrogen plasma removed the Cp ligand favourably for one RuCp fragment, but not all Cp species were removed favorably at the higher $(RuCp)_4$ coverage possibly inducing carbon contamination. The same was also found for $CoCp_2$ where the first Cp ligand is removed favourably via hydrogen transfer from the 1 ML N-H *ε*-TaN (110) surface. The reaction pathways for the upright and horizontal interaction modes of $CoCp_2$ showed that the energetics were very similar despite the interaction mode. Hydrogen plasma interacted favourable with the $(CoCp)_y$ surface fragments leaving Co atoms on the surface.

Ligand loss from $Ru(EtCp)_2$ and $Co(EtCp)_2$ precursors was favourable on the 1 ML N-H and the 0.5 ML N-H/0.5 ML N-H_2 *ε*-TaN (110) surfaces. The first EtCp ligand elimination via hydrogen transfer was favourable for the interaction of one or two $Ru(EtCp)_2$ or $Co(EtCp)_2$ on the 1 ML N-H *ε*-TaN (110) surface. Hydrogen plasma removed the remaining EtCp ligands favourably from the RuEtCp/CoEtCp surface fragments. Both ligands are removed favourably for a single $Ru(EtCp)_2$ on the 0.5 ML N-H/0.5 ML N-H_2 *ε*-TaN (110) surface leaving an Ru atom on the surface bound to surface nitrogen. Whereas for two $Ru(EtCp)_2$, up to three EtCp ligands can be removed favourably in the first half-cycle with hydrogen plasma being required to remove the final EtCp ligand. $Co(EtCp)_2$ showed to have a higher reactivity with the 0.5 ML N-H/0.5 ML N-H_2 *ε*-TaN (110) surface as all EtCp ligands were eliminated favourably via hydrogen transfer from the surface. Only the horizontal interaction modes promoted ligand loss for $Ru(EtCp)_2$ whereas both interaction modes were favourable for $Co(EtCp)_2$ with the upright being more favourable.

Hydrogen transfer barriers of 0.58 eV (horizontal interaction mode) and 1.17 eV (upright interaction mode) were found to promote the first Cp ligand loss from $RuCp_2$ whereas the first hydrogen transfer barriers for $CoCp_2$ was barrierless on the 1 ML N-H *ε*-TaN (110) surface.

The first hydrogen transfer barrier was also higher for $Ru(EtCp)_2$ on the 1 ML N-H ε-TaN (110) surface at 1.19 eV (horizontal interaction mode) compared to $Co(EtCp)_2$ at 0.79 eV (upright interaction mode). On the 0.5 ML N-H/0.5 ML N-H_2 ε-TaN (110) surface, hydrogen transfer barriers were 0.99 eV and 0.22 eV for $Ru(EtCp)_2$ and 0.38 eV and 0.53 eV for $Co(EtCp)_2$ to promote the elimination of all EtCp ligands with the first barrier being smaller for $Co(EtCp)_2$. By comparing the HOMO-LUMO energy gap between the ruthenium and cobalt Cp-containing precursors in Table 6, it is clear the cobalt precursors have a higher reactivity compared to the ruthenium precursor due to smaller HOMO-LUMO gaps for Co-containing precursors. Note that when comparing between -Cp and -EtCp precursors of ruthenium or cobalt, the differences between the respective HOMO-LUMO energy gaps are minimal. Figure A 10 in the Appendix shows the ruthenium and cobalt precursors studied in this chapter. The Ru-Cp distances are all 2.18 Å in $RuCp_2$ and in $Ru(EtCp)_2$ the distances are within the range of 2.18 – 2.20 Å. In $CoCp_2$ the Co-Cp distances are 2.07 – 2.14 Å and for $Co(EtCp)_2$ there is minimum difference with distances of 2.07 – 2.15 Å.

Table 6: HOMO-LUMO energy gap for ruthenium and cobalt precursors.

Precursor	HOMO-LUMO Energy Gap (eV)
$RuCp_2$	3.89
$Ru(EtCp)_2$	3.88
$CoCp_2$	0.44
$Co(EtCp)_2$	0.49
RuO_4	3.11

RuO_4 is more reactive compared to $RuCp_2$ and $Ru(EtCp)_2$ with a smaller HOMO-LUMO energy gap. All Ru-O distances are 1.70 Å. The interaction energies of RuO_4 on the 1 ML N-H and 0.5 ML N-H/0.5 ML N-H_2 ε-TaN (110) surfaces are highly exothermic. Oxygen can be eliminated through hydrogen transfer from the surface removing it as water, even at higher RuO_4 coverages (4.15 RuO_4/nm^2) with moderate energy barriers. When all surface hydrogen is depleted, hydrogen plasma can remove the remaining oxygen atoms leaving Ru atoms on the ε-TaN (110) surface.

Experimental PEALD processes reported that when using just N_2 or H_2 plasma alone, the lack of NH_x species in the plasma led to higher O, C and N impurities in the bulk of the film.[12] In PEALD process that incorporates NH_3 or N_2/H_2 plasma, Ru films were deposited using

$Ru(EtCp)_2$ with impurity levels of O, C and N below the detection limit showing that there was no nitrogen incorporation into the Ru film.[6] Metallic Ru can be deposited on a RuN_x layer using $Ru(EtCp)_2$ and H_2 plasma, however RuN_x is unstable above 275 °C where it decomposes into metallic Ru and nitrogen.[29] NH_3 plasma with $CoCp_2$ on Si and SiO_2 substrates produced metallic Co films with minimal N incorporation.[10]

Substrates that lack NH_x sites can reduce the reactivity of $RuCp_2$ and $CoCp_2$ precursors at that surface.[16] The elimination of the first Cp ligand from both precursors via H transfer is thermoneutral on the hydrogen terminated Si substrate and the second Cp ligand removal is highly endothermic with 2.09 eV for $RuCp_2$ and 2.83 eV for $CoCp_2$.[16] H-terminated ruthenium surfaces Ru(001), Ru(101) and Ru(100) hinders $RuCp_2$ adsorption with endothermic adsorption energies of 1.73 and 1.13 eV with it being thermoneutral in Ru(100).[30] On the hydrogen terminated Si surface with nitrogen incorporation, Cp ligand elimination for both precursors is endothermic.[16] In contrast, the ε-TaN (110) surface contains nitrogen surface atoms which can form $N\text{-}H_x$ sites with just hydrogen plasma to promote ligand loss from the precursors examined in this chapter. The elimination of both Cp ligands of $RuCp_2$ is endothermic on the NH_x-terminated Si surface (x = 1,2) whereas for $CoCp_2$ the first Cp ligand removal is exothermic at -0.21 eV with the first H transfer having an activation barrier of 0.73 eV and is endothermic for the second Cp ligand removal.[16] We saw for *ε*-TaN (110) surfaces that contained $Ta\text{-}NH_x$ sites, ligand elimination is endothermic for all Ru and Co precursors.

8.7 Conclusions

In this chapter, the reactivity of ruthenium and cobalt precursors on NH_x-terminated *ε*-TaN (110) surfaces was examined. Reaction energies were overall endothermic after CpH, EtCpH or H_2O elimination for surfaces terminated with additional $Ta\text{-}NH_x$ terminations. This shows that the TaN surface can be treated with just hydrogen plasma and surfaces such as 1 ML N-H and 0.5 ML N-H/0.5 ML $N\text{-}H_2$ *ε*-TaN (110) can promote ligand elimination. Ligand elimination was only favourable on the 1 ML N-H *ε*-TaN (110) surface for $RuCp_2$ and $CoCp_2$. $Ru(EtCp)_2$ and $Co(EtCp)_2$ had higher reactivity on the 0.5 ML N-H/0.5 ML $N\text{-}H_2$ *ε*-TaN (110) surface with enhanced removal of EtCp ligands especially for $Co(EtCp)_2$. Hydrogen plasma can help eliminated -Cp and -EtCp ligands from surface fragments of CoCp, CoEtCp and RuEtCp. Not all -Cp ligands can be removed favourably from higher coverages of RuCp fragments. RuO_4 interaction along with H_2O formation via hydrogen transfer from the surface was highly exothermic and the risk of oxygen contamination is minimized by the favourable interaction of hydrogen plasma to remove remaining oxygen from the surface. This work will help guide

experimental PEALD for the incorporation of ruthenium or cobalt into TaN as a combined barrier and liner material.

References

(1) Kondati Natarajan, S.; Nies, C. L.; Nolan, M. Ru Passivated and Ru Doped ϵ-TaN Surfaces as a Combined Barrier and Liner Material for Copper Interconnects: A First Principles Study. *J. Mater. Chem. C* **2019**, *7* (26), 7959–7973. https://doi.org/10.1039/c8tc06118a.

(2) Kondati Natarajan, S.; Nies, C. L.; Nolan, M. The Role of Ru Passivation and Doping on the Barrier and Seed Layer Properties of Ru-Modified TaN for Copper Interconnects. *J. Chem. Phys.* **2020**, *152* (14), 144701. https://doi.org/10.1063/5.0003852.

(3) Nies, C. L.; Natarajan, S. K.; Nolan, M. Control of the Cu Morphology on Ru-Passivated and Ru-Doped TaN Surfaces – Promoting Growth of 2D Conducting Copper for CMOS Interconnects. *Chem. Sci.* **2022**, *13* (3), 713–725. https://doi.org/10.1039/D1SC04708F.

(4) Nies, C. L.; Nolan, M. Incorporation of Tungsten or Cobalt into TaN Barrier Layers Controls Morphology of Deposited Copper. *J. Phys. Mater.* **2023**, *6* (3), 035008. https://doi.org/10.1088/2515-7639/acdeaa.

(5) Kwon, O.-K.; Kwon, S.-H.; Park, H.-S.; Kang, S.-W. PEALD of a Ruthenium Adhesion Layer for Copper Interconnects. *J. Electrochem. Soc.* **2004**, *151* (12), C753. https://doi.org/10.1149/1.1809576/XML.

(6) Kwon, O. K.; Kwon, S. H.; Park, H. S.; Kang, S. W. Plasma-Enhanced Atomic Layer Deposition of Ruthenium Thin Films. *Electrochemical and Solid-State Letters* **2004**, *7* (4), C46. https://doi.org/10.1149/1.1648612.

(7) Kwon, S.-H.; Kwon, O.-K.; Kim, J.-H.; Oh, H.-R.; Kim, K.-H.; Kang, S.-W. Initial Stages of Ruthenium Film Growth in Plasma-Enhanced Atomic Layer Deposition. *J Electrochem Soc* **2008**, *155* (5), H296. https://doi.org/10.1149/1.2868779/XML.

(8) Sari, W.; Eom, T.-K.; Kim, S.-H.; Kim, H. Plasma Enhanced Atomic Layer Deposition of Ruthenium Thin Films Using Isopropylmethylbenzene-Cyclohexadiene-Ruthenium and NH3 Plasma. *J Electrochem Soc* **2011**, *158* (1), D42. https://doi.org/10.1149/1.3515320/XML.

(9) Kim, S.-W.; Kwon, S.-H.; Jeong, S.-J.; Kang, S.-W. Improvement of Copper Diffusion Barrier Properties of Tantalum Nitride Films by Incorporating Ruthenium Using PEALD. *J. Electrochem. Soc.* **2008**, *155* (11), H885. https://doi.org/10.1149/1.2975341/XML.

(10) Lee, H. B. R.; Kim, H. High-Quality Cobalt Thin Films by Plasma-Enhanced Atomic Layer Deposition. *Electrochemical and Solid-State Letters* **2006**, *9* (11), G323. https://doi.org/10.1149/1.2338777.

(11) Yoon, J.; Lee, H.-B.-R.; Kim, D.; Cheon, T.; Kim, S.-H.; Kim, H. Atomic Layer Deposition of Co Using N2/H2 Plasma as a Reactant. *J Electrochem Soc* **2011**, *158* (11), H1179. https://doi.org/10.1149/2.077111JES/XML.

(12) Vos, M. F. J.; Van Straaten, G.; Kessels, W. M. M. E.; Mackus, A. J. M. Atomic Layer Deposition of Cobalt Using H2-, N2-, and NH3-Based Plasmas: On the Role of the Co-Reactant. *Journal of Physical Chemistry C* **2018**, *122* (39), 22519–22529. https://doi.org/10.1021/ACS.JPCC.8B06342/ASSET/IMAGES/LARGE/JP-2018-06342U_0007.JPEG.

(13) Grimme, S.; Antony, J.; Ehrlich, S.; Krieg, H. A Consistent and Accurate Ab Initio Parametrization of Density Functional Dispersion Correction (DFT-D) for the 94 Elements H-Pu. *J. Chem. Phys.* **2010**, *132* (15), 154104–154119. https://doi.org/10.1063/1.3382344.

(14) Liu, J.; Lu, H.; Zhang, D. W.; Nolan, M. Reaction Mechanism of the Metal Precursor Pulse in Plasma-Enhanced Atomic Layer Deposition of Cobalt and the Role of Surface Facets. *Journal of Physical Chemistry C* **2020**, *124* (22), 11990–12000. https://doi.org/10.1021/acs.jpcc.0c02976.

(15) Liu, J.; Lu, H.; Zhang, D. W.; Nolan, M. Reactions of Ruthenium Cyclopentadienyl Precursor in the Metal Precursor Pulse of Ru Atomic Layer Deposition. *J. Mater. Chem. C* **2021**, *9* (8), 2919–2932. https://doi.org/10.1039/d0tc03910a.

(16) Liu, J.; Mullins, R.; Lu, H.; Zhang, D. W.; Nolan, M. Nucleation of Co and Ru Precursors on Silicon with Different Surface Terminations: Impact on Nucleation Delay. *J. Phys. Chem. C* **2023**, *127* (28), 13651–13658. https://doi.org/10.1021/ACS.JPCC.3C02933.

(17) Park, S. J.; Kim, W. H.; Maeng, W. J.; Yang, Y. S.; Park, C. G.; Kim, H.; Lee, K. N.; Jung, S. W.; Seong, W. K. Effect Oxygen Exposure on the Quality of Atomic Layer Deposition of Ruthenium from Bis(Cyclopentadienyl)Ruthenium and Oxygen. *Thin Solid Films* **2008**, *516* (21), 7345–7349. https://doi.org/10.1016/J.TSF.2008.02.011.

(18) Park, S. J.; Kim, W. H.; Lee, H. B. R.; Maeng, W. J.; Kim, H. Thermal and Plasma Enhanced Atomic Layer Deposition Ruthenium and Electrical Characterization as a Metal Electrode. *Microelectron. Eng.* **2008**, *85* (1), 39–44. https://doi.org/10.1016/J.MEE.2007.01.239.

(19) Lee, D. J.; Yim, S. S.; Kim, K. S.; Kim, S. H.; Kim, K. B. Formation of Ru Nanotubes by Atomic Layer Deposition onto an Anodized Aluminum Oxide Template. *Electrochem. Solid-State Lett.* **2008**, *11* (6), K61. https://doi.org/10.1149/1.2901542/XML.

(20) Kwon, S.-H.; Kwon, O.-K.; Kim, J.-H.; Jeong, S.-J.; Kim, S.-W.; Kang, S.-W. Improvement of the Morphological Stability by Stacking RuO2 on Ru Thin Films with Atomic Layer Deposition. *J. Electrochem. Soc.* **2007**, *154* (9), H773. https://doi.org/10.1149/1.2750448/XML.

(21) Yim, S. S.; Lee, D. J.; Kim, K. S.; Kim, S. H.; Yoon, T. S.; Kim, K. B. Nucleation Kinetics of Ru on Silicon Oxide and Silicon Nitride Surfaces Deposited by Atomic Layer Deposition. *J. Appl. Phys.* **2008**, *103* (11), 113509. https://doi.org/10.1063/1.2938052.

(22) Gatineau, J.; Yanagita, K.; Dussarrat, C. A New RuO4 Solvent Solution for Pure Ruthenium Film Depositions. *Microelectron. Eng.* **2006**, *83* (11–12), 2248–2252. https://doi.org/10.1016/j.mee.2006.10.013.

(23) Minjauw, M. M.; Rijckaert, H.; Driessche, I. Van; Detavernier, C.; Dendooven, J. Nucleation Enhancement and Area-Selective Atomic Layer Deposition of Ruthenium Using RuO4 and H2 Gas. *Chem. Mater.* **2019**, *31* (5), 1491–1499. https://doi.org/10.1021/acs.chemmater.8b03852.

(24) Minjauw, M. M.; Dendooven, J.; Capon, B.; Schaekers, M.; Detavernier, C. Near Room Temperature Plasma Enhanced Atomic Layer Deposition of Ruthenium Using the RuO4-Precursor and H2-Plasma. *J. Mater. Chem. C* **2015**, *3* (19), 4848–4851. https://doi.org/10.1039/C5TC00751H.

(25) Minjauw, M. M.; Dendooven, J.; Capon, B.; Schaekers, M.; Detavernier, C. Atomic Layer Deposition of Ruthenium at 100 °C Using the RuO4-Precursor and H2. *J. Mater. Chem. C* **2015**, *3* (1), 132–137. https://doi.org/10.1039/C4TC01961J.

(26) An, C. H.; Jeon, W.; Kim, S. H.; Cho, C. J.; Kwon, D. S.; Kim, D. G.; Lee, W.; Hwang, C. S. Substrate Effects on the Growth Behavior of Atomic-Layer-Deposited Ru Thin Films Using RuO4 Precursor and N2/H2 Mixed Gas. *J. Phys. Chem. C* **2019**, *123* (36), 22539–22549. https://doi.org/10.1021/ACS.JPCC.9B03727/ASSET/IMAGES/LARGE/JP9B03727_0007.JPEG.

(27) Liu, J.; Nolan, M. Coverage and Stability of NH X-Terminated Cobalt and Ruthenium Surfaces: A First-Principles Investigation. *Journal of Physical Chemistry C* **2019**, *123* (41), 25166–25175. https://doi.org/10.1021/acs.jpcc.9b06287.

(28) Liu, J.; Lu, H.; Zhang, D. W.; Nolan, M. Self-Limiting Nitrogen/Hydrogen Plasma Radical Chemistry in Plasma-Enhanced Atomic Layer Deposition of Cobalt. *Nanoscale* **2022**, *14* (12), 4712–4725. https://doi.org/10.1039/D1NR05568B.

(29) Damayanti, M.; Sritharan, T.; Mhaisalkar, S. G.; Gan, Z. H. Effects of Dissolved Nitrogen in Improving Barrier Properties of Ruthenium. *Appl Phys Lett* **2006**, *88* (4), 1–3. https://doi.org/10.1063/1.2167610.

(30) Phung, Q. M.; Pourtois, G.; Swerts, J.; Pierloot, K.; Delabie, A. Atomic Layer Deposition of Ruthenium on Ruthenium Surfaces: A Theoretical Study. *J. Phys. Chem. C* **2015**, *119* (12), 6592–6603. https://doi.org/10.1021/JP5125958/SUPPL_FILE/JP5125958_SI_001.PDF.

9 Modelling Atomic Layer Deposition of Ru using RuO_4 and H_2

This chapter studies the reaction mechanism for ALD of Ru using RuO_4 and H_2. Ru is a metal with many potential uses due to its low bulk resistivity (7 μΩ), high work function (4.7 eV), high chemical and thermal stability and catalytic activity.[1] Given difficulties in depositing conducting copper at reduced length scales[2], Ru can be used as a seed layer for Cu electroplating because it is immiscible with Cu, has adhesive properties towards Cu and has a high melting point of 2334 °C, while Ru is also a leading candidate to replace Cu as low level interconnect.[3] A carbon free precursor ToRuS (RuO_4 in a solvent) was used to overcome the problems with impurities when depositing Ru thin films.[4] For growing Ru metal the co-reactant used with ToRuS is H_2, which is a reducing agent.[4] ToRuS is non-toxic, non-corrosive, non-flammable, a liquid over a wide range of temperatures and compatible with most materials. RuO_4 has a high oxidation state of +8 and can be used as a reactant for ALD; it can be an oxidizing agent and a Ru source.[5–7]

We first examine the coverages of RuO_4 on the Ru surface to determine the coverage at which the precursor saturates. We then compute the Bader charges of the Ru atoms in the surface and the subsurface layers for different RuO_4 coverages to determine the coverage at which all top surface Ru atoms are oxidized, producing a RuO_2 overlayer. We then examine the proposed reduction step that uses H_2 to reduce RuO_2 by introducing H_2 molecules individually to the surface with the highest RuO_4 coverage and allowing relaxation.

9.1 Coverage of RuO_4 Precursors

A sideview of the bare Ru (001) surface is shown in Figure 9.1 with the top surface layer labelled “S” and the layer underneath “S” labelled “S – 1”. Each layer contains 16 Ru atoms, with Ru-Ru distances of 2.72 in the layer and 2.59 Å between layers. We denote ruthenium atoms in the top surface layer Ru^S and ruthenium atoms from the RuO_4 precursor Ru^P when referencing to them in the text.

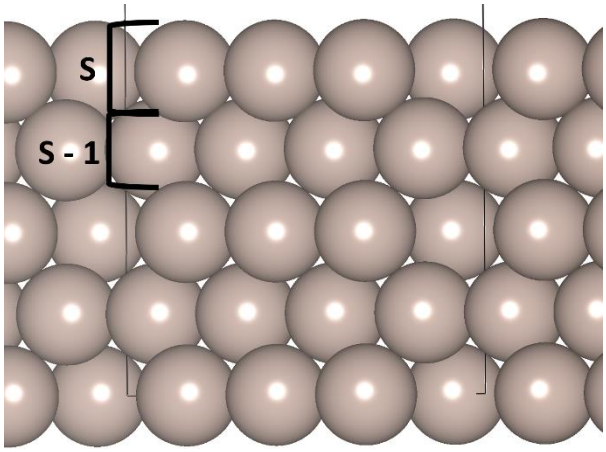


Figure 9.1 Side view of the bare Ru (001) surface. S denotes the top layer and S -1 denotes the layer below S. Colour scheme: Ru = grey.

An experimental study of Ru ALD using RuO_4 and H_2 found that the first half reaction was driven by the reaction of RuO_4 with the Ru surface as shown in ((9.1)[8]:

$$Ru + RuO_4 \rightarrow 2RuO_2 \qquad (9.1)$$

It was also shown experimentally that RuO_4 does not decompose on the RuO_2 surface.[9,10] Therefore when all the metal surface sites are covered with RuO_2, RuO_4 should no longer react showing self-saturated behaviour.[9] In this section the coverage of the RuO_4 precursor molecule is examined using a model of the bare Ru (001) surface to determine the preferred saturation coverage of RuO_4 on the Ru surface. RuO_4 molecules are adsorbed on the bare Ru surface in different configurations and the binding energy is computed from the formula:

$$E_{bind} = E_{tot} - E_{slab} - \left(M \times E_{RuO_4}\right) \qquad (9.2)$$

Where E_{tot} is the total energy of the system with M adsorbed RuO_4 species, E_{slab} is the total energy of the bare Ru metal surface and E_{RuO_4} is the isolated gas-phase energy of the precursor RuO_4. E_{bind} can also be written per adsorbed RuO_4, for example, dividing E_{bind} by 4 for a coverage of four RuO_4 precursors.

The binding energies are presented per unit surface area and are plotted as a function of the number of RuO_4 molecules and number of Ru^S–O bonds. Figure 9.2 (a) shows the change in binding energies versus RuO_4 coverage and Figure 9.2 (b) shows the change in binding energies

versus the number of new Ru^S–O bonds formed between Ru in the starting surface and O from the precursor. The number of Ru^S–O bonds is measured to compare against the RuO_4 coverages to test if increasing the precursor coverage will result in more Ru^S–O bonds, or if there is a limit to the number of Ru^S–O bonds formed at the maximum precursor coverage. If the number of Ru^S–O bonds plateaus as the RuO_4 coverage increases, this shows that the maximum number of Ru^S–O bonds have been reached on the Ru (001) surface which suggests saturating behaviour.

The value of E_{bind/nm^2} starts to plateau at a coverage of 3.39 RuO_4/nm^2 and coverages of 4.25 and 5.09 RuO_4/nm^2 are also possible shown in Figure 9.2 (a). The number of Ru^S–O bonds also starts to plateau at higher RuO_4 coverages and as the E_{bind/nm^2} increases, showing that the saturating coverage is at 5.09 RuO_4/nm^2 with an Ru^S–O bond coverage of 23.49/nm^2. The interaction of another RuO_4 precursor on the 5.09 RuO_4/nm^2 covered Ru surface had a very weak interaction energy of -0.17 eV and did not form any new bonds with the surface or surface adsorbed RuO_4, shown in Figure 9.3, and we therefore propose that this precursor will most likely be removed in a purge step. From this the maximum coverage is 5.09 RuO_4/nm^2 on the Ru (001) surface.

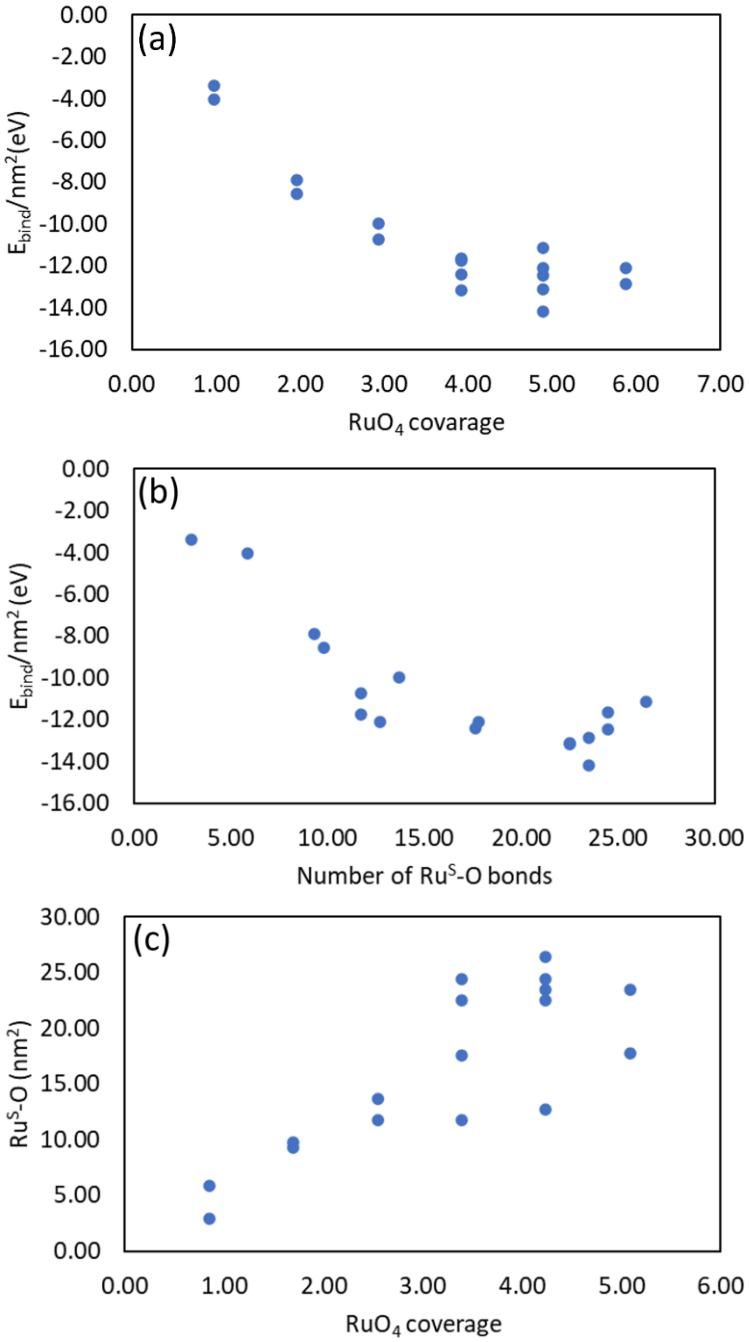


Figure 9.2 Scatter plots for (a) and (b) change in binding energy per square nanometre with change in RuO_4 coverage and coverage of Ru^S-O bonds respectively. (c) Coverage of Ru^S-O bonds versus RuO_4 coverage.

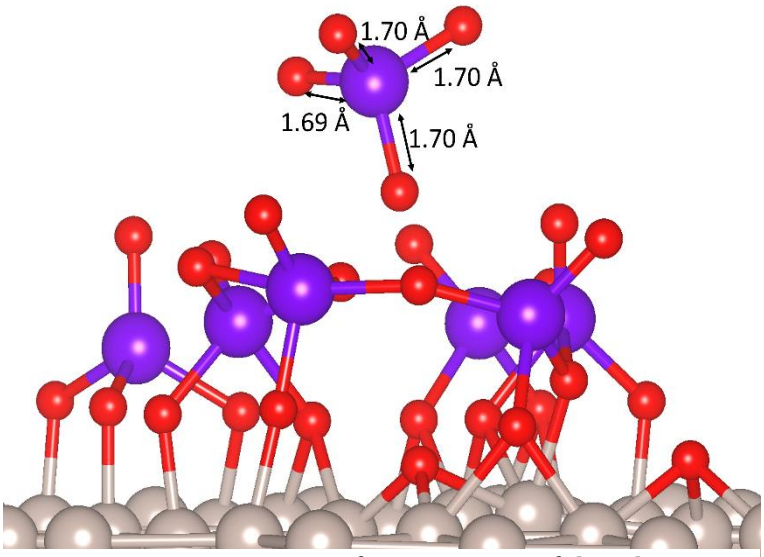


Figure 9.3 Atomic structure after interaction of the 7th RuO_4 on the 6 x RuO_4 terminated Ru surface. Colour scheme is: Ru = grey, O = red and Ru from RuO_4 = purple.

Figure 9.4 shows the atomic structures for different adsorption configurations for coverages of one (0.85 RuO_4/nm^2), two (1.70 RuO_4/nm^2) and three (2.54 RuO_4/nm^2) RuO_4 on the starting Ru surface. Generally in all configurations (except for one adsorbed RuO_4 Figure 9.4 (b)) one oxygen atom detaches from the RuO_4 precursor and bonds directly to the Ru surface and does not directly follow the reaction in equation (9.1) showing that kinetic barriers may need to be overcome for RuO_2 to form on the Ru surface. Other oxygen atoms remain bound to Ru^P and form a bridge to the Ru surface, while there are always terminal oxygen that remain in the precursor.

Similar behaviour for oxygen is observed for coverages of four (3.39 RuO_4/nm^2) and five (4.24 RuO_4/nm^2) adsorbed RuO_4, shown in Figure 9.5. Again there are exceptions where no oxygen detaches, e.g. four RuO_4 in Figure 9.5 (b) and five RuO_4 in Figure 9.5 (g). The E_{bind} per adsorbed RuO_4 for the RuO_4 coverages shown in Figure 9.4 and Figure 9.5 are given in Table A 4 in the Appendix. The coverage of six (5.09 RuO_4/nm^2) will be examined in more detail as this coverage is the saturation coverage of RuO_4 on the Ru surface. Recall that RuO_4 should no longer react after all the metal surface sites are covered with RuO_2, and this was shown by the weak interaction energy of the 7th RuO_4 precursor at the 5.09 RuO_4/nm^2 surface. Thermal ALD of Ru using RuO_4 and H_2 had a high growth per cycle of 1 Å/cycle[9], therefore the highest coverage of RuO_4/nm^2 on our surface is used for the H_2 reduction step and is discussed in more detail next. There was also no spontaneous formation of O_2 observed for any RuO_4 coverages at Ru (001).

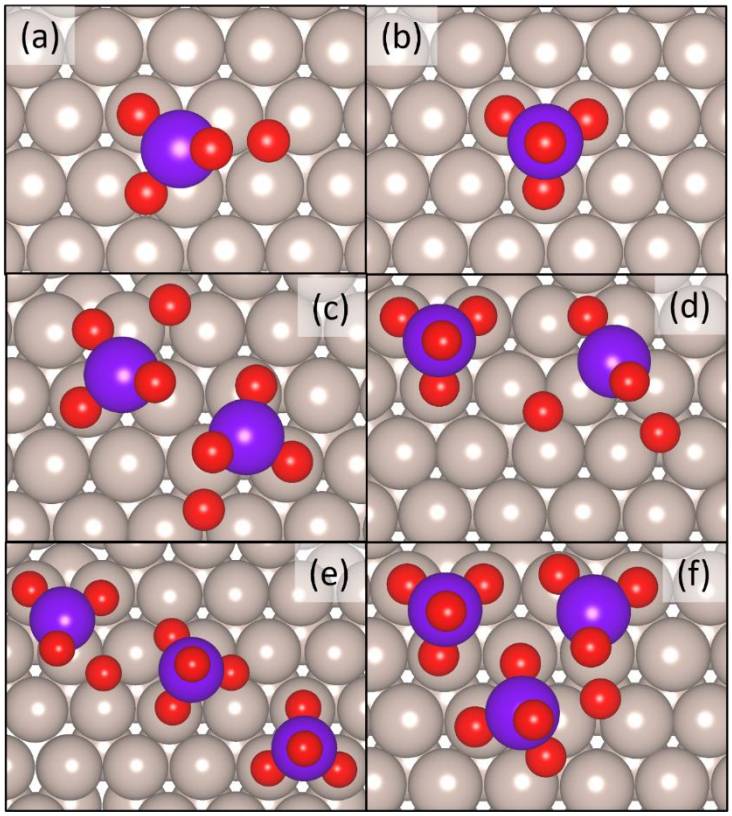


Figure 9.4 RuO_4 coverages for one RuO_4 (a) & (b), two RuO_4 (c) & (d) and three RuO_4 (e) & (f). Colour scheme is the same as in Figure 9.3.

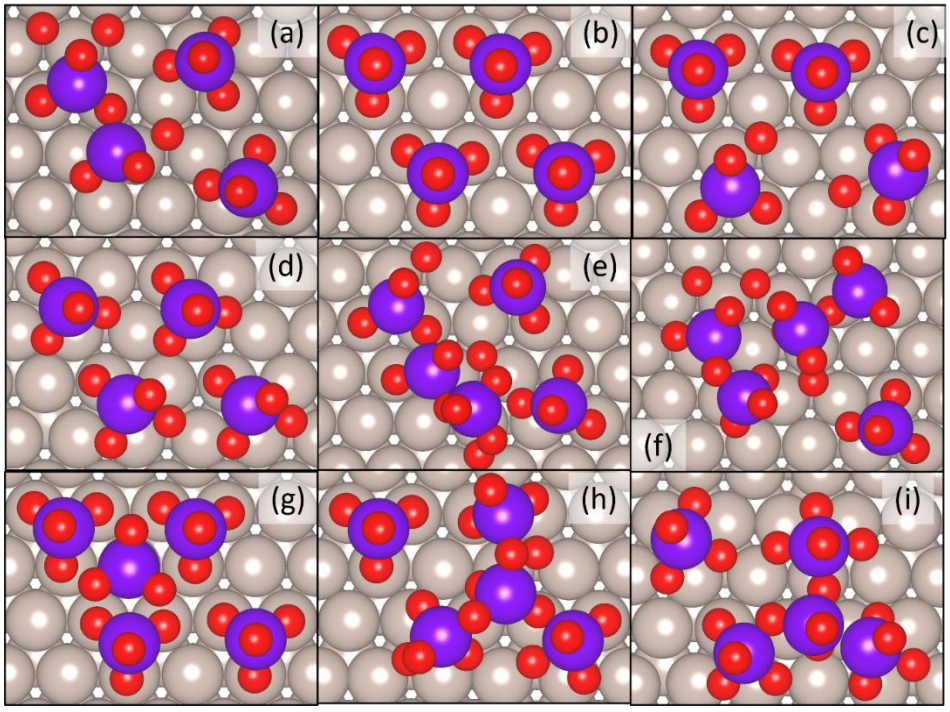


Figure 9.5 RuO_4 coverages for four RuO_4 (a) - (d) and five RuO_4 (e) - (i). Colour scheme is the same as in Figure 9.3.

Table 1: Summary of Ru-O bond lengths including RuO_4 in the gas phase, bulk RuO_2, Ru^S-O bonds from 5.09 RuO_4/nm^2 coverage and Ru^P-O bonds. (P = precursor).

	Bond length (Å)	
$RuO_{4\ (g)}$	1.70 (x2), 1.87, 1.94	
$RuO_{2\ (bulk)}$	1.94, 1.99	
Ru^S-O (O detached from RuO_4)	1.92 – 2.02	
Ru^S-O (O bridging to Ru surface)	O c.n. 2	O c.n.3
	1.93 – 2.02	1.97 – 2.19
Ru^P-O (O c.n. 1)	1.67 – 1.71	

The top view with a coverage of six RuO_4 (5.09 RuO_4/nm^2) is shown in Figure 9.6 (a). The two oxygen atoms labelled with "*" detached from the precursors and formed Ru^S-O of 1.92 – 2.02 Å and with coordination number of 3 with surrounding Ru^S atoms which are comparable in length to the Ru-O bond lengths in $RuO_{2(bulk)}$ listed in Table 1. The $RuO_{2\ (bulk)}$ bond lengths are reference to the tetragonal phase.[11] Oxygen atoms labelled "1 – 3" indicate their coordination number. Oxygen atoms labelled "2" and "3" form Ru^S-O bonds (see Table 1) and Ru^P-O bonds (1.82 – 2.16 Å) and bridge the two types of Ru species. The range of Ru^S-O bond lengths for oxygen with a coordination number of 2 are comparable with the $RuO_{2(bulk)}$ bond lengths. For oxygen with a coordination number of 3, some Ru^S-O bond lengths are longer compared to Ru-O in $RuO_{2(bulk)}$. Also note that one oxygen atom with a coordination number of 2 lies directly under a Ru atom from RuO_4 and is hidden in the top view.

The other Oxygen atoms labelled "1" have only one bond with Ru^P, i.e. these oxygen atoms do not interact with any Ru^S sites and have Ru^P-O distances of 1.67 – 1.71 Å. These Ru^P-O distances compare in length to the shorter Ru-O bonds in $RuO_{4\ (g)}$ of 1.70 Å. Oxygen atoms marked with "x" bridge between two Ru^P atoms from RuO_4 precursors, with Ru^P–O bond lengths of 1.82 – 2.00 Å. The Ru^S-Ru^S bond lengths also deviated from 2.72 Å as shown in Figure 9.6 (b) where the coverage of 5.09 RuO_4/nm^2 was removed for clarity. Ru^S sites that formed Ru^S-O bonds with oxygen that detached from RuO_4 saw an increase in the Ru^S-Ru^S bond length to 2.82 – 3.03 Å. The increase in Ru^S-Ru^S bond lengths also led to a decrease in some Ru^S-Ru^S bonds by up to 0.20 Å.

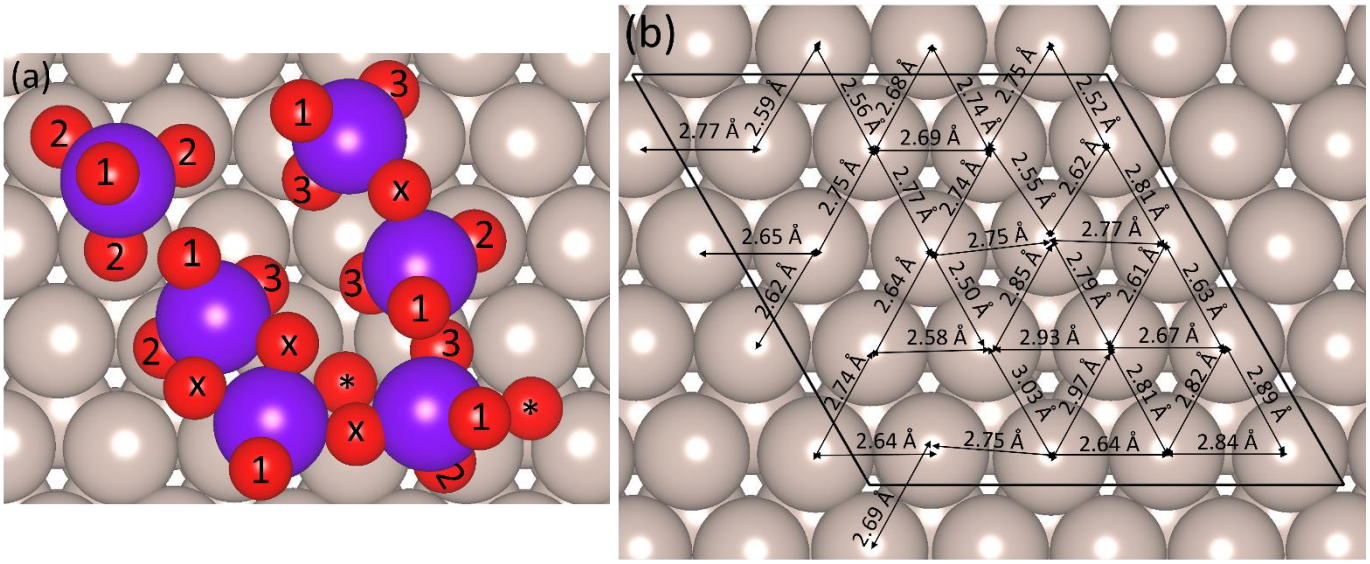


Figure 9.6 (a) Top view of 5.09 RuO_4/nm^2 coverage on Ru surface. (b) Ru^S-Ru^S bond lengths in top surface layer. (note added Ru and O atoms removed for clarity). Colour scheme is the same as in Figure 9.3.

The side view of 5.09 RuO_4/nm^2 is shown in Figure 9.7 showing that we can divide the oxygen atoms into two regions: those that interact with the initial Ru surface are in "Region 1" and oxygen atoms that do not bind to the surface are in "Region 2". Region 1 contains 58.3 % of oxygen atoms. Region 2 oxygen have a coordination number of 1 or have coordination number 2 which bridge between Ru^P atoms from neighbouring RuO_4 precursors.

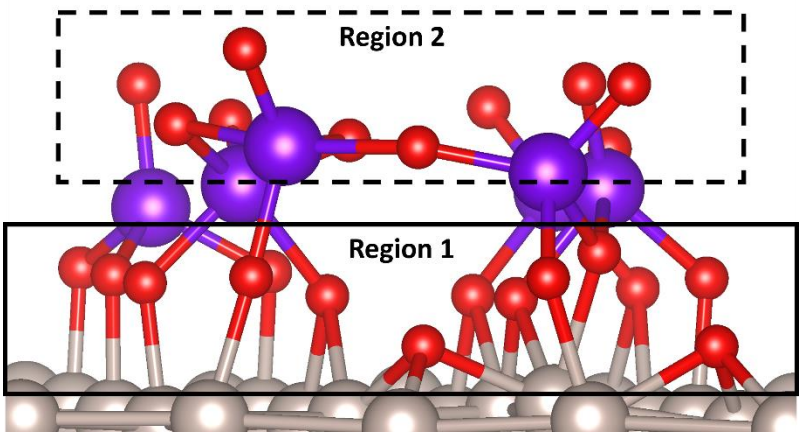


Figure 9.7 Side view of 6 x RuO_4 on Ru surface. Colour scheme is the same as in Figure 9.3.

To characterize the nature of Ru species after precursor adsorption, we use the Bader charge analysis. All ruthenium atoms in each layer of the bare surface have a net computed charge of 0.0 which is expected for a metal. The valence charge of Ru is 8.0, by subtracting the charge measured of Ru^S from the Bader analysis from the valence charge we calculate the net charge on the atom. The charge of ruthenium in gas phase RuO_4 is 5.9 e^-, which will be compared to the charge of Ru^P atoms for the various RuO_4 coverages. The net charge of Ru in gas phase RuO_4 is 2.1 e^-. Each oxygen atom in gas phase RuO_4 has a computed charge of 6.5 e^- showing oxygen has been reduced with a net charge of -0.5 e^-, using O valence charge of 6.0. Table 2 shows the charges on the Ru^P atoms at coverages of 0.85 – 5.09 RuO_4/nm^2. Every Ru^P atom has been reduced after it bonded to the Ru (001) surface due to the increase in charge compared to the gas phase RuO_4. Desorption of oxygen from Ru^P as well as oxygen bridging to Ru^S atoms facilitates the reduction of the Ru^P atoms.

Table 2: Computed charge on Ru^P atoms for different RuO_4 coverages on the Ru (001) surface.

Coverage RuO_4/nm^2	Ru^P charge (e^-)
0.85	6.2
1.70	6.7, 6.8
2.54	6.4, 6.7, 6.8
3.39	6.3, 6.5, 6.7 (x2)
4.24	6.0, 6.3, 6.4, 6.6, 6.7
5.09	6.2 (x4), 6.3 (x2)
Gas phase RuO_4	5.9

The Bader net atomic charge (BNAC) is plotted for each Ru^S atom in layer S with no precursor adsorption and for coverages of 0.85 – 5.09 RuO_4/nm^2 and the results are shown in Figure 9.8. For the bare Ru surface, the BNAC of the Ru atoms are 0.0. When one RuO_4 interacts with the surface, the BNAC for three Ru atoms in layer S that form Ru^S-O bonds are 0.3 e^-. This change in computed Bader charge is consistent with partial oxidation of these surface Ru atoms. The other BNAC for the Ru atoms in layer S for one RuO_4 are unchanged.

For a coverage of 1.70 RuO_4/nm^2 again we see Ru^S atoms oxidised, with BNAC ranging from 0.0 – 0.4 e^-. Ru^S atoms that did not form Ru^S-O bonds remained metallic with a BNAC of 0.0 e^-. Ru^S atoms that bond to one oxygen atom are less oxidised with a BNAC of 0.2 – 0.3 e^- compared to Ru^S atoms that form two bonds with oxygen, including oxygen that has detached

from RuO_4 with a BNAC of 0.4 e^-. The same also applies to the coverage of 2.54 RuO_4/nm^2 where the BNAC of Ru^S atoms range from 0.1 – 0.4 e^-.

At a coverage of 3.39 RuO_4/nm^2 every Ru^S atom has been oxidised, and the computed BNAC are in the range of 0.2 – 0.5 e^-. Ru^S atoms are increasingly oxidised with more Ru^S-O bonds as well as with bonding to detached oxygen with a BNAC of 0.4 e^- and 0.5 e^-. All Ru^S atoms are also oxidised for coverages of 4.24 and 5.09 RuO_4/nm^2 where the BNAC range from 0.2 – 0.6 e^- for the coverage of 5.09 RuO_4/nm^2. Again, Ru^S atoms with fewer Ru^S-O bonds are less oxidised than Ru^S atoms with a higher number of oxygen bonds showing a range of oxidation states is possible. The BNAC are also plotted for the Ru^P atoms for the different RuO^4 coverages in Figure 9.8. The BNAC for the Ru^P atoms is greater than the Ru^S due to the low charge of Ru^P in gas phase RuO_4. However, we already saw from Table 2 these Ru^P atoms are reduced after adsorbing to the Ru (001) surface.

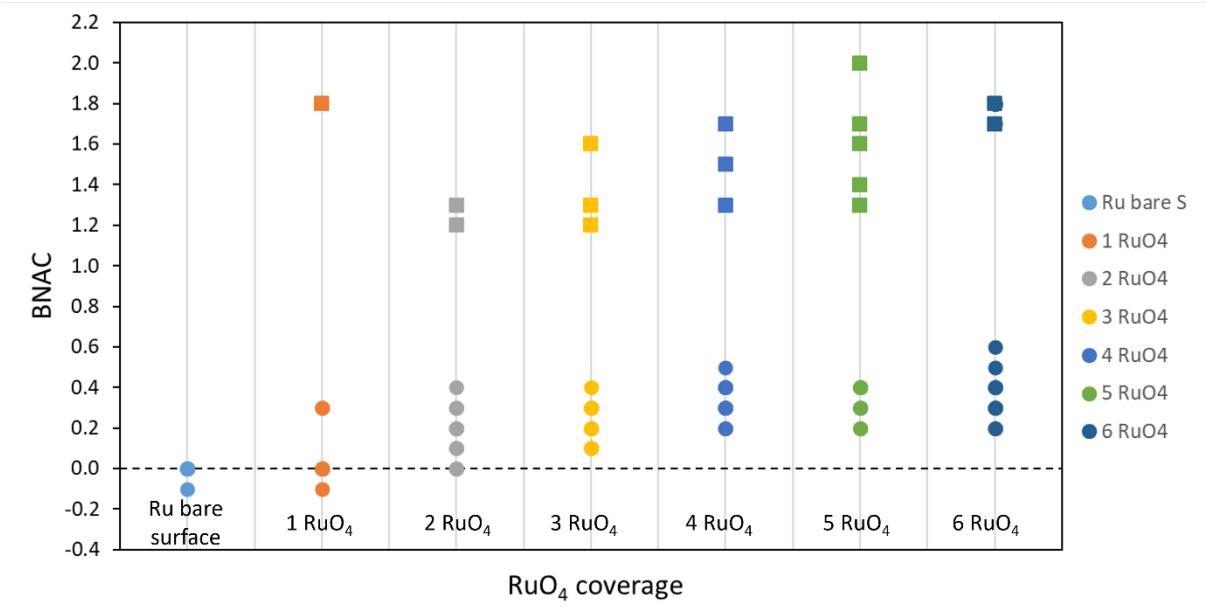


Figure 9.8 Calculated Bader net atomic charge plots for the bare Ru surface and coverages of 0.85 – 5.09 RuO_4/nm^2 for layer S of the Ru (001) surface. The circle data points refers to Ru^S atoms and square data points refers to Ru^P atoms. Note that some data points overlap for Ru^S and Ru^P atoms with the same BNAC value.

It is interesting to note that we previously saw that the binding energy plateaus at a coverage of 3.39 RuO_4/nm^2 in Figure 9.2 (a) while the number of Ru^S-O bonds also plateaus at this coverage in Figure 9.2 (c). From the charge analysis we know that all Ru^S atoms are oxidised at a coverage of 3.39 RuO_4/nm^2, showing that both interaction energy and the number of Ru^S-O bonds start to saturate when all Ru^S atoms are oxidised. For comparison and to assess if Ru

oxidation extends beyond the surface to Ru^{S-1}, the Bader charge analysis is carried out for the Ru^{S-1} atoms in layer S-1 that was shown in Figure 9.1. At all RuO_4 coverages, none of the Ru^{S-1} atoms were oxidised with BNAC being no more than 0.1 e^- showing that oxidation only occurs for Ru^S atoms.

9.2 Reaction of H_2 with Surface Bound RuO_4 Precursors

The co-reactant used in Ru ALD with RuO_4 in ref 1, is H_2 which reduces RuO_2 to Ru metal and the oxygen is removed as H_2O.[9] In this section the reduction of the RuO_4 terminated Ru (001) surface at saturation coverage with H_2 is studied. The interaction energy of H_2 is defined by the formula:

$$E_{ads} = E_{tot} - E_{RuO4-Ru} - E_{H_2} \quad (9.3)$$

Where E_{tot}, $E_{RuO4\text{-}Ru}$ and E_{H_2} are the energies of the 5.09 RuO_4/nm^2 terminated Ru surface with H_2, the 5.09 RuO_4/nm^2 terminated Ru surface and an isolated gas-phase H_2 molecule, respectively. The reduction of the 5.09 RuO_4/nm^2 terminated Ru surface was modelled by adding individual H_2 molecules, and computing the H_2 interaction energy and H_2O desorption energy. There are 24 oxygen atoms available on the 5.09 RuO_4/nm^2 terminated Ru surface, and therefore the interaction of up to 24 H_2 will be studied. The interaction energies for up to 20 H_2 are listed in Table 3 and in each case the interaction with H_2 spontaneously formed H_2O, as shown in Figure 9.9. The H_2O desorption energies listed in Table 3 are all relatively low and will be overcome at process conditions. Note that the desorption energy is negative for the 7^{th} and 11^{th} H_2O removal. This is due to a favourable surface rearrangement after H_2O was removed. For example, after the 7^{th} H2O was removed, a Ru^P atom formed Ru^P-Ru^S bonds of 2.61 - 2.68 Å with the Ru surface.

After 20 H_2 and corresponding water removal, the surface shows 6 Ru^P atoms and 4 oxygen atoms in Figure 9.10. All Ru^P have Ru^P-Ru^P and Ru^P-Ru^S distances in the range of 2.32 – 2.73 Å and 2.38 – 2.77 Å respectively. The remaining four oxygen have Ru^S-O bonds of 1.98 – 2.06 Å and all oxygen are coordinated by 3 Ru^S atoms.

Table 3: H_2 interaction energy and H_2O desorption energy for H_2 reduction of the 5.09 RuO_4/nm^2 terminated Ru surface. Energies are listed up until 20 oxygen have been removed.

	E_{ads} (eV)	**H_2O E_{des} (eV)**
1 H_2	-2.03	0.99
2 H_2	-1.56	0.91
3 H_2	-1.70	0.97
4 H_2	-5.87	0.67
5 H_2	-2.19	0.85
6 H_2	-1.28	0.53
7 H_2	-2.09	-0.47
8 H_2	-0.84	0.77
9 H_2	-1.18	0.19
10 H_2	-2.45	0.84
11 H_2	-1.70	-1.24
12 H_2	-1.99	0.94
13 H_2	-0.74	0.61
14 H_2	-0.94	1.08
15 H_2	-0.59	0.66
16 H_2	-0.62	0.98
17 H_2	-1.35	1.06
18 H_2	-0.98	0.87
19 H_2	-1.47	1.18
20 H_2	-0.92	0.65

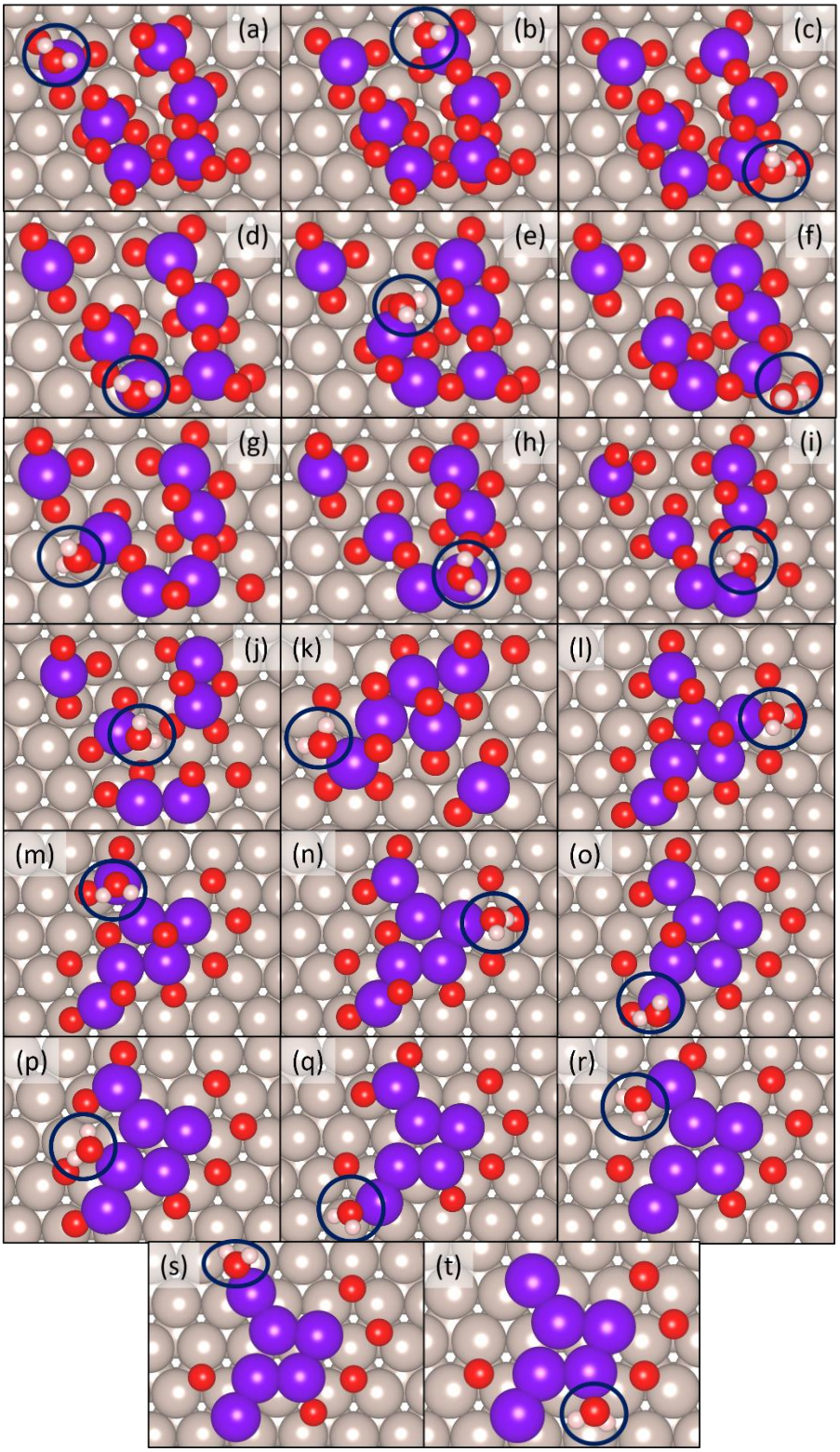


Figure 9.9 Interaction of up to 20 H_2 with the 5.09 RuO_4/nm^2 terminated Ru surface where H_2O spontaneously formed at each H_2 interaction. H_2O highlighted in a circle in each pane (a) - (t). Colour scheme is: Ru = grey, O = red, H = pink and Ru from RuO_4 = purple.

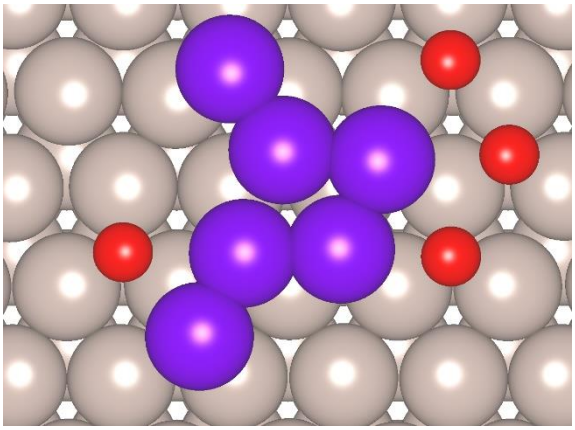


Figure 9.10: Ru (001) surface terminated with 6 Ru^P and four O atoms after the interaction of up to 20 H_2 molecules. Colour scheme is the same as in Figure 9.9.

For 21 H_2 to 24 H_2, H_2 did not form water with any of the remaining oxygen atoms in our zero K DFT calculations and instead formed O-H/Ru^P-H bonds as shown in Figure 9.11 with interaction energies of -0.54 eV, -0.30 eV, -0.91 eV and -0.84 eV for the 21st – 24th H_2 interactions respectively. After the 24th H_2 interaction the surface has 5 Ru^P-H bonds of 1.77 – 1.92 Å and 3 O-H bonds (all O-H distances are 0.98 Å) shown in Figure 9.11 (d). The Ru^P atoms have Ru^P-Ru^P distances of 2.34 – 2.69 Å between themselves which are smaller compared to the typical Ru^S-Ru^S bond of 2.72 Å. They also have Ru^P-Ru^S distances of 2.38 – 2.78 Å. The Ru atoms lie flat on the surface as shown in Figure 9.11 (e).

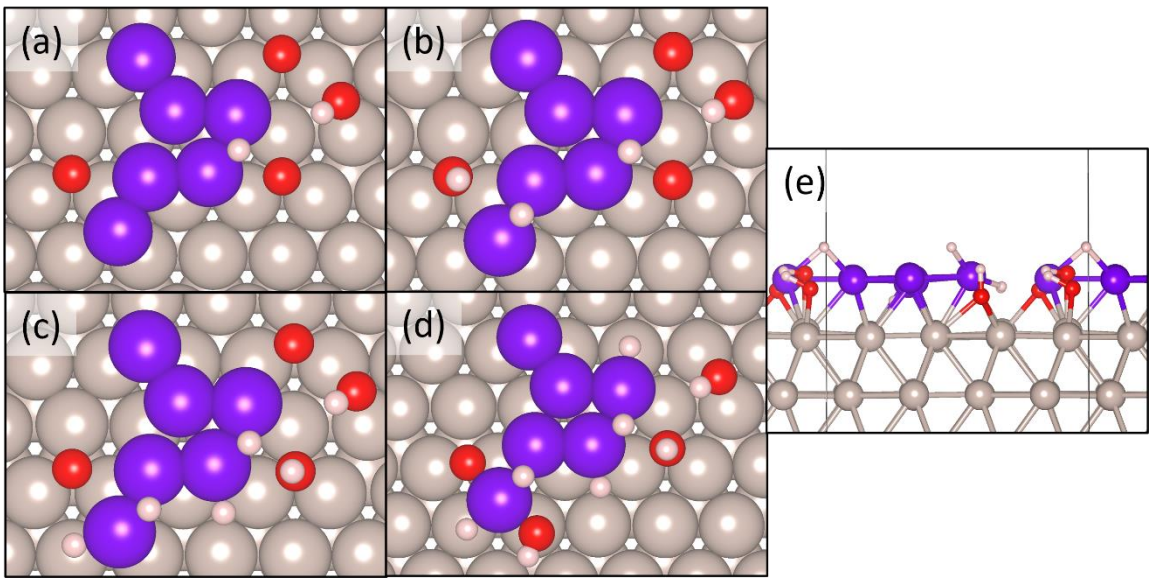


Figure 9.11 Interaction of the 21st - 24th added H_2 where H_2 dissociated into O-H and Ru-H bonds. Colour scheme is the same as in Figure 9.9

Starting from the structure in Figure 9.11 (d), the reaction pathway is studied with the energy barriers for hydrogen transfer included for reactions such as H transfer from Ru^P to O forming H_2O, as shown in Figure 9.12 and the geometries are shown in Figure 9.13. The reaction energy for the first hydrogen transfer from Ru^P to OH to form H_2O is favourable at -0.63 eV but has a high barrier of 1.45 eV. If the high barrier is overcome there is an energy gain after the H_2O desorption where the reaction energy is -1.17 eV. The second hydrogen transfer to form H_2O is barrierless with an energy gain of -0.32 eV and a small energy cost of 0.44 eV for H_2O desorption. The third hydrogen transfer to form another H_2O has a high barrier of 1.93 eV, however like the first hydrogen transfer, the reaction energy is favourable at -1.23 eV with a small energy cost of 0.39 eV for H_2O desorption. The fourth hydrogen transfer forms an O-H bond with a small barrier of 0.37 eV however the reaction energy is thermoneutral after the fifth hydrogen transfer, so a barrier is not calculated.

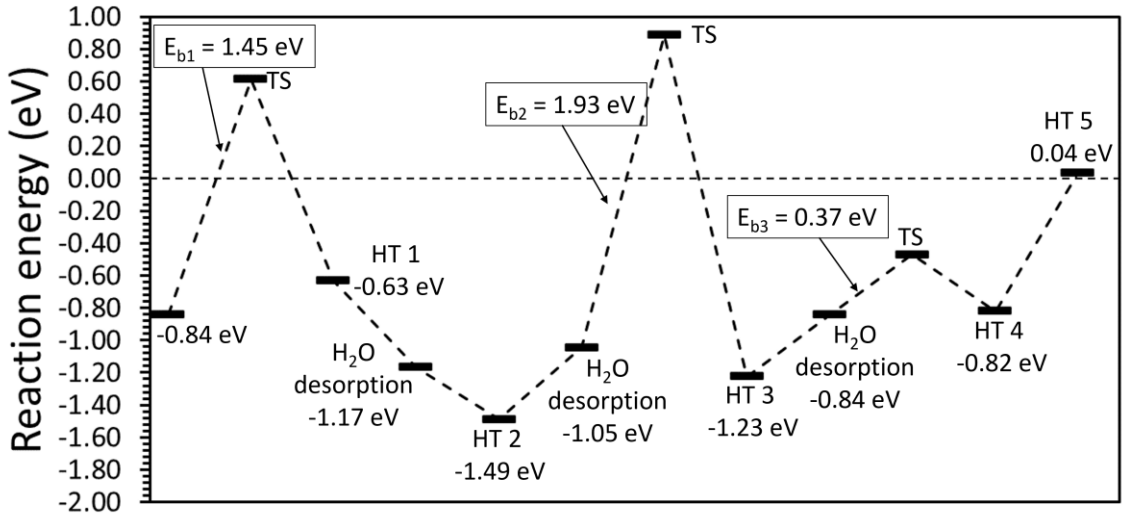


Figure 9.12 Reaction pathway for H_2O formation and desorption to remove oxygen from the Ru surface. HT = hydrogen transfer. TS = transition state.

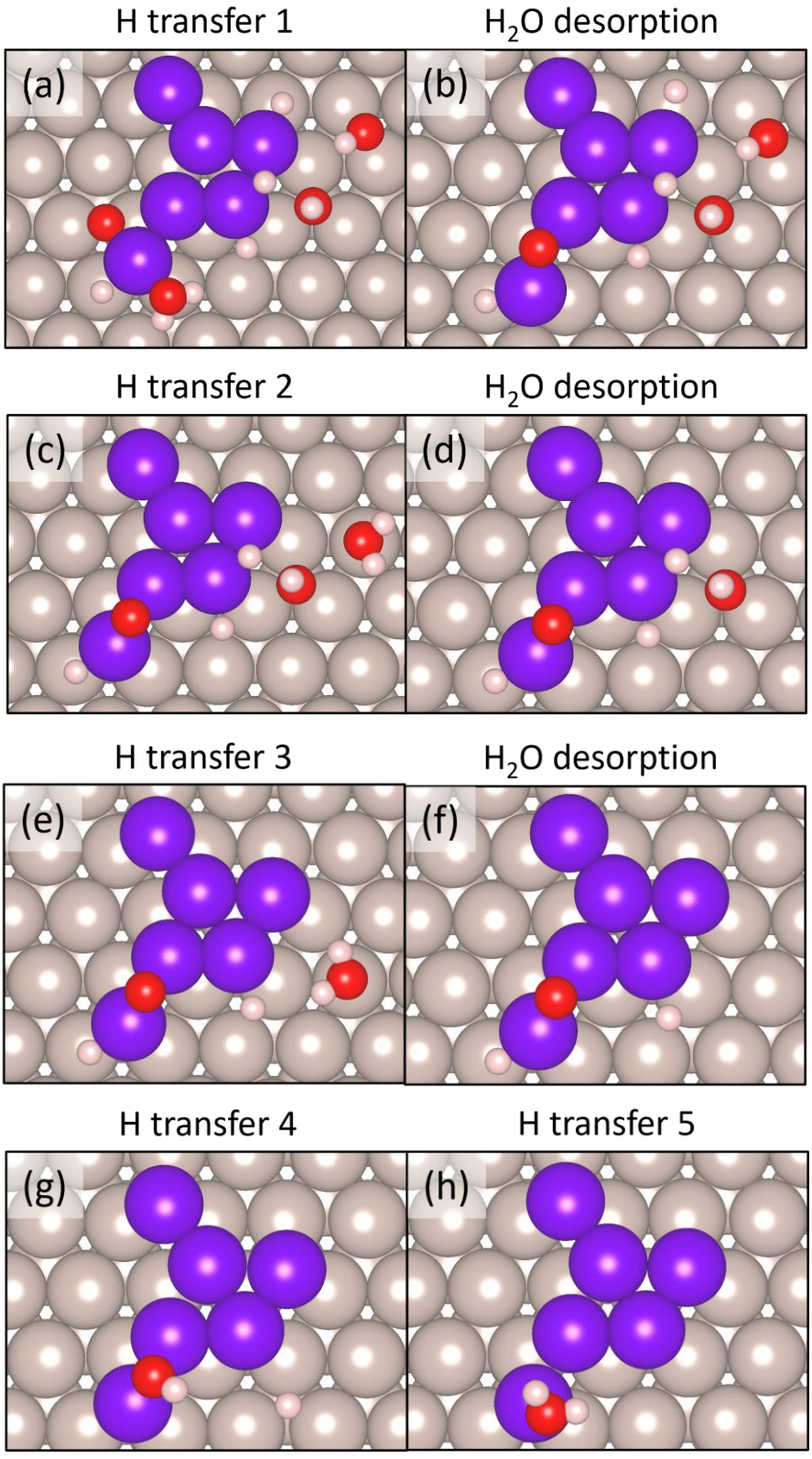


Figure 9.13 Geometries for the reaction pathway steps in Figure 9.12.

The favourable interaction energies of H_2 with the surface to form H_2O show that oxygen can be easily removed. After the 20th oxygen atom from our maximum RuO_4 coverage is removed (Figure 9.9 (t)), the Ru^P atoms are bonded to each other at 2.32 – 2.73 Å forming a clear structural motif of the Ru (001) surface and bind to Ru^S in the surface at 2.38 – 2.77 Å and do not have any bonds to oxygen. These added Ru^P atoms are also reduced with computed BNAC of 0.0 - 0.1 showing they are now metallic. Half of the Ru^S atoms remain oxidized with BNAC of 0.2 and 0.4 as shown in Table 4. The analysis above suggests that some surface Ru^S atoms are partially oxidized due to the persistence of oxygen on the Ru surface, where the high computed activation barriers suggest it is more difficult to remove.

Table 4: BNAC for Ru^S atoms after 20th O is removed.

BNAC (e^-)	Number of Ru^S atoms with this BNAC
0.0 – 0.1	8
0.2	4
0.4	4

It was observed experimentally that at 100 ºC the concentration of oxygen to ruthenium was measured to be 2 % whereas at 75 ºC it was high at 44 % since the thermal H_2-reduction is limited below 100 ºC.[9] Our results then suggest that surface bound oxygen with accompanying activation barriers for H migration to form and release oxygen as H_2O will be partly responsible for this oxygen incorporation. The experimental growth per cycle was high at 1 Å per cycle at 100 ºC due to the reactivity of RuO_4.[9] At a process temperature of 100 ºC the barrier for hydrogen transfer to oxygen may be reduced and thus promote H_2O formation. Temperatures above 100 ºC are not suitable as RuO_4 starts to thermally decompose.

9.3 Conclusions

It was found that at higher coverages of RuO_4 on the Ru surface the number of Ru^S-O bonds level off at a coverage of 23.49 nm^2 as well as the binding energy at -12.87 eV/nm^2 showing that saturation had been reached. The charge analysis also showed that oxygen starts to saturate when all Ru^S atoms are oxidized and further adsorption of another RuO_4 precursor was only weakly favourable and did not bind to the surface. H_2 is an effective reducing agent as it

removes oxygen as H_2O with favourable interaction energies and relatively low desorption energies. Given that some of the barriers for hydrogen transfer were very high, it is possible that H_2O would not form which could lead to a small level of oxygen contamination since most of the oxygen was removed favorably as H_2O as previously discussed.

Chapter References

(1) Kotsugi, Y.; Han, S. M.; Kim, Y. H.; Cheon, T.; Nandi, D. K.; Ramesh, R.; Yu, N. K.; Son, K.; Tsugawa, T.; Ohtake, S.; Harada, R.; Park, Y. B.; Shong, B.; Kim, S. H. Atomic Layer Deposition of Ru for Replacing Cu-Interconnects. *Chem. Mater.* **2021**, *33* (14), 5639–5651. https://doi.org/10.1021/acs.chemmater.1c01054.

(2) Li, B.; Sullivan, T. D.; Lee, T. C.; Badami, D. Reliability Challenges for Copper Interconnects. *Microelectronics Reliability* **2004**, *44* (3), 365–380. https://doi.org/10.1016/J.MICROREL.2003.11.004.

(3) Kwon, O. K.; Kim, J. H.; Park, H. S.; Kang, S. W. Atomic Layer Deposition of Ruthenium Thin Films for Copper Glue Layer. *J. Electrochem. Soc.* **2004**, *151* (2), G109. https://doi.org/10.1149/1.1640633/XML.

(4) Gatineau, J.; Yanagita, K.; Dussarrat, C. A New RuO4 Solvent Solution for Pure Ruthenium Film Depositions. *Microelectron. Eng.* **2006**, *83* (11–12), 2248–2252. https://doi.org/10.1016/j.mee.2006.10.013.

(5) Minjauw, M. M.; Feng, J.-Y.; Sajavaara, T.; Detavernier, C.; Dendooven, J. Atomic Layer Deposition of Ternary Ruthenates by Combining Metalorganic Precursors with RuO4 as the Co-Reactant. *Dalton Trans.* **2022**. https://doi.org/10.1039/d1dt03543f.

(6) Hämäläinen, J.; Ritala, M.; Leskelä, M. Atomic Layer Deposition of Noble Metals and Their Oxides. *Chem. Mater.* **2013**, *26* (1), 786–801. https://doi.org/10.1021/CM402221Y.

(7) Minjauw, M. M.; Rijckaert, H.; Driessche, I. Van; Detavernier, C.; Dendooven, J. Nucleation Enhancement and Area-Selective Atomic Layer Deposition of Ruthenium Using RuO4 and H2 Gas. *Chem. Mater.* **2019**, *31* (5), 1491–1499. https://doi.org/10.1021/acs.chemmater.8b03852.

(8) Yuan, Z.; Puddephatt, R. J.; Sayer, M. Low-Temperature Chemical Vapor Deposition of Ruthenium Dioxide from Ruthenium Tetroxide: A Simple Approach to High-Purity RuO2 Films. *Chemistry of Materials* **1993**, *5* (7), 908–910. https://doi.org/10.1021/CM00031A004/ASSET/CM00031A004.FP.PNG_V03.

(9) Minjauw, M. M.; Dendooven, J.; Capon, B.; Schaekers, M.; Detavernier, C. Atomic Layer Deposition of Ruthenium at 100 °C Using the RuO4-Precursor and H2. *J. Mater. Chem. C* **2015**, *3* (1), 132–137. https://doi.org/10.1039/C4TC01961J.

(10) Backman, U.; Lipponen, M.; Auvinen, A.; Tapper, U.; Zilliacus, R.; Jokiniemi, J. K. On the Transport and Speciation of Ruthenium in High Temperature Oxidising Conditions. *Radiochim. Acta* **2005**, *93* (5), 297–304. https://doi.org/10.1524/RACT.93.5.297.64280/MACHINEREADABLECITATION/RIS.

(11) Materials Data on RuO2 by Materials Project. May 2, 2020. https://doi.org/10.17188/1307989.

University College Cork, Ireland
Coláiste na hOllscoile Corcaigh

CORA
Cork Open Research Archive
Cartlann Taighde Oscailte Chorcaí

Mullins, R. H. 2023. Modelling of thin film oxide growth and etching. PhD Thesis, University College Cork.

Please note that Chapter 10 (pp. 247-259) is unavailable due to a request by the author.

CORA Cork Open Research Archive http://cora.ucc.ie

Appendix

A1: Supplementary Material for Chapter 4

Figure A 1 and Figure A 2 show for HfO_2 and ZrO_2 the geometries that did not result in complete dissociation of the HF molecules.

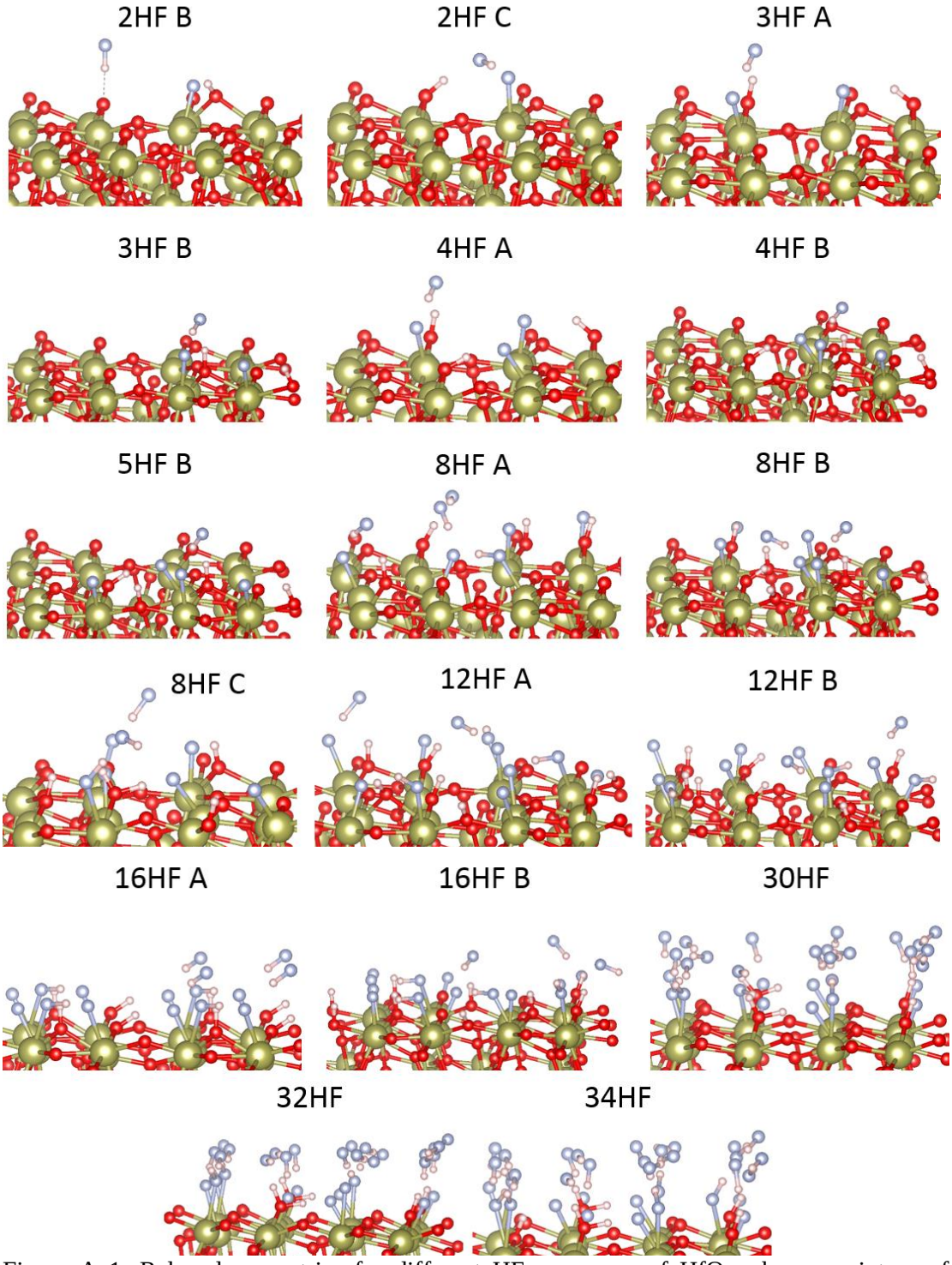


Figure A 1: Relaxed geometries for different HF coverages of HfO_2 where a mixture of molecular and dissociative adsorption of HF is observed. Colour scheme Colour scheme: Hf = gold, O = red and H = white.

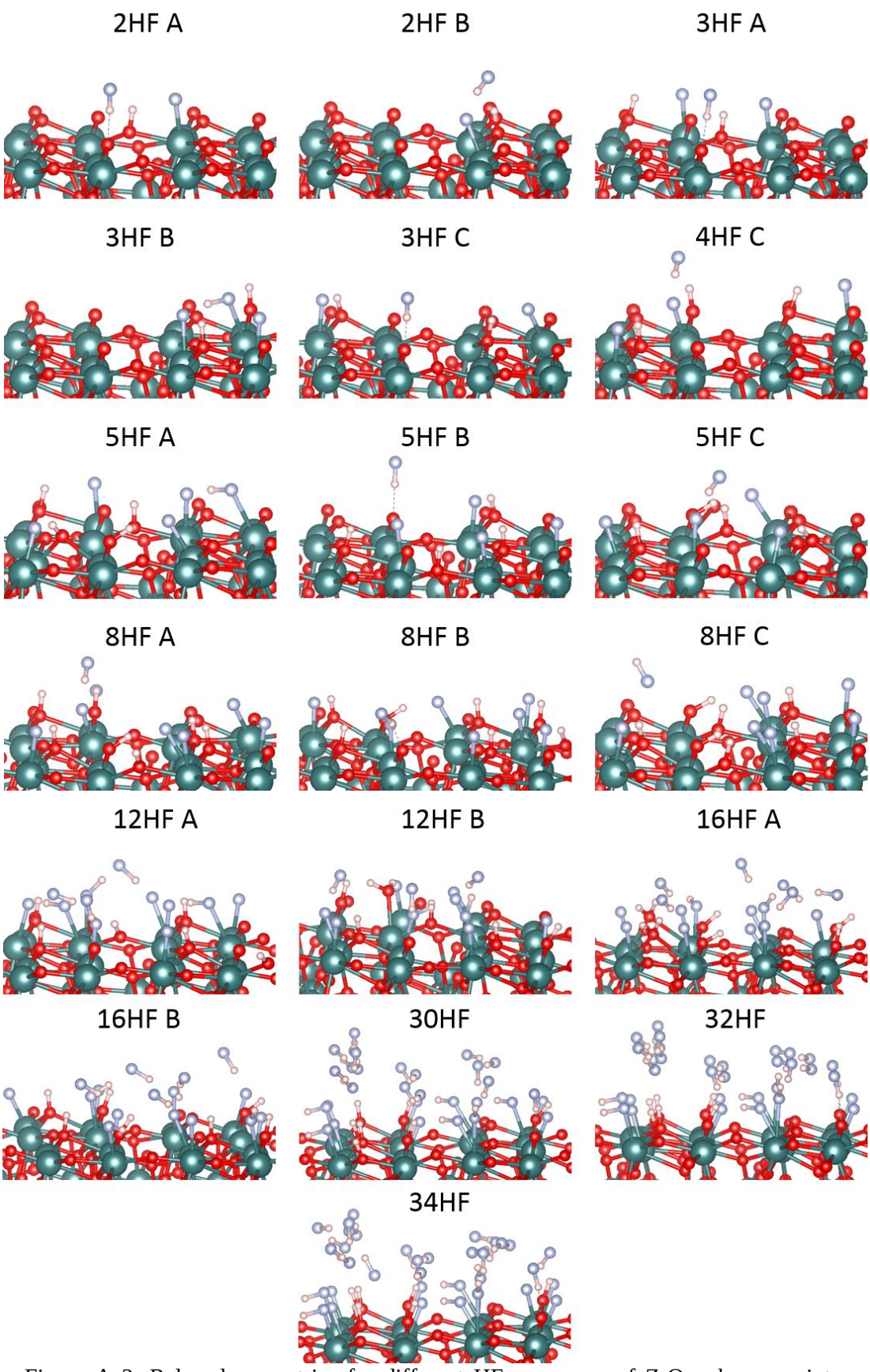


Figure A 2: Relaxed geometries for different HF coverages of ZrO_2 where a mixture of molecular and dissociative adsorption of HF is observed. Colour scheme: Zr = green, O = red and H = white.

A2: Supplementary Material for Chapter 5

Figure A 3 shows for amorphous HfO_2 the geometries that did not result in complete dissociation of the HF molecules.

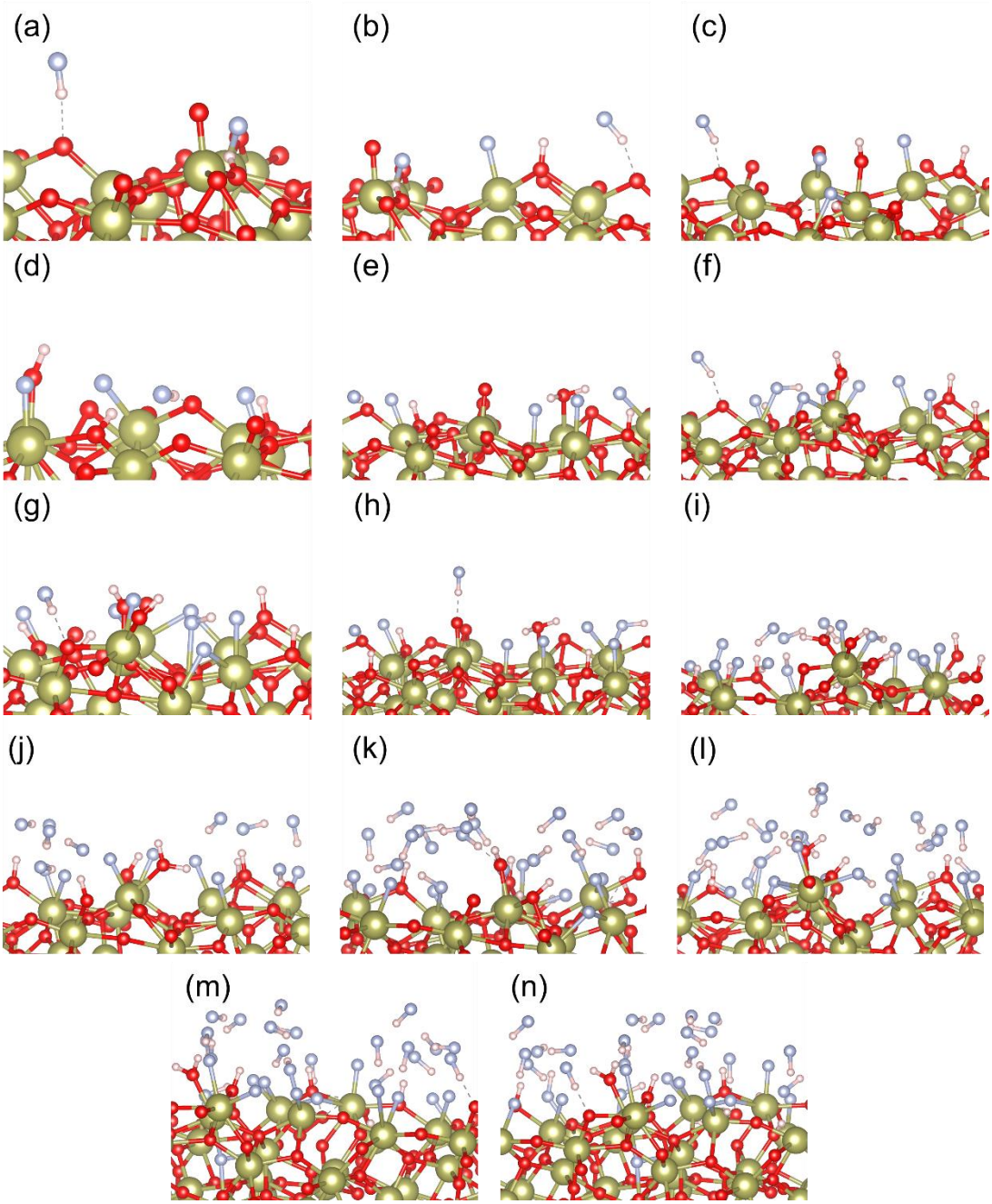


Figure A 3: Relaxed geometries for different HF coverages of amorphous HfO_2 where a mixture of molecular and dissociative adsorption of HF is observed. (a) 2HF A, (b) 3HF A, (c) 4HF A (d) 4HF C, (e) 5HF C, (f) 8HF A, (g) 8HF B, (h) 8HF C, (i) 16HF A, (j) 16HF B, (k) 28HF, (l) 30HF, (m) 32 HF and (n) 34 HF. Colour scheme same as in **Error! Reference source not found.**.

A3: Supplementary Material for Chapter 8

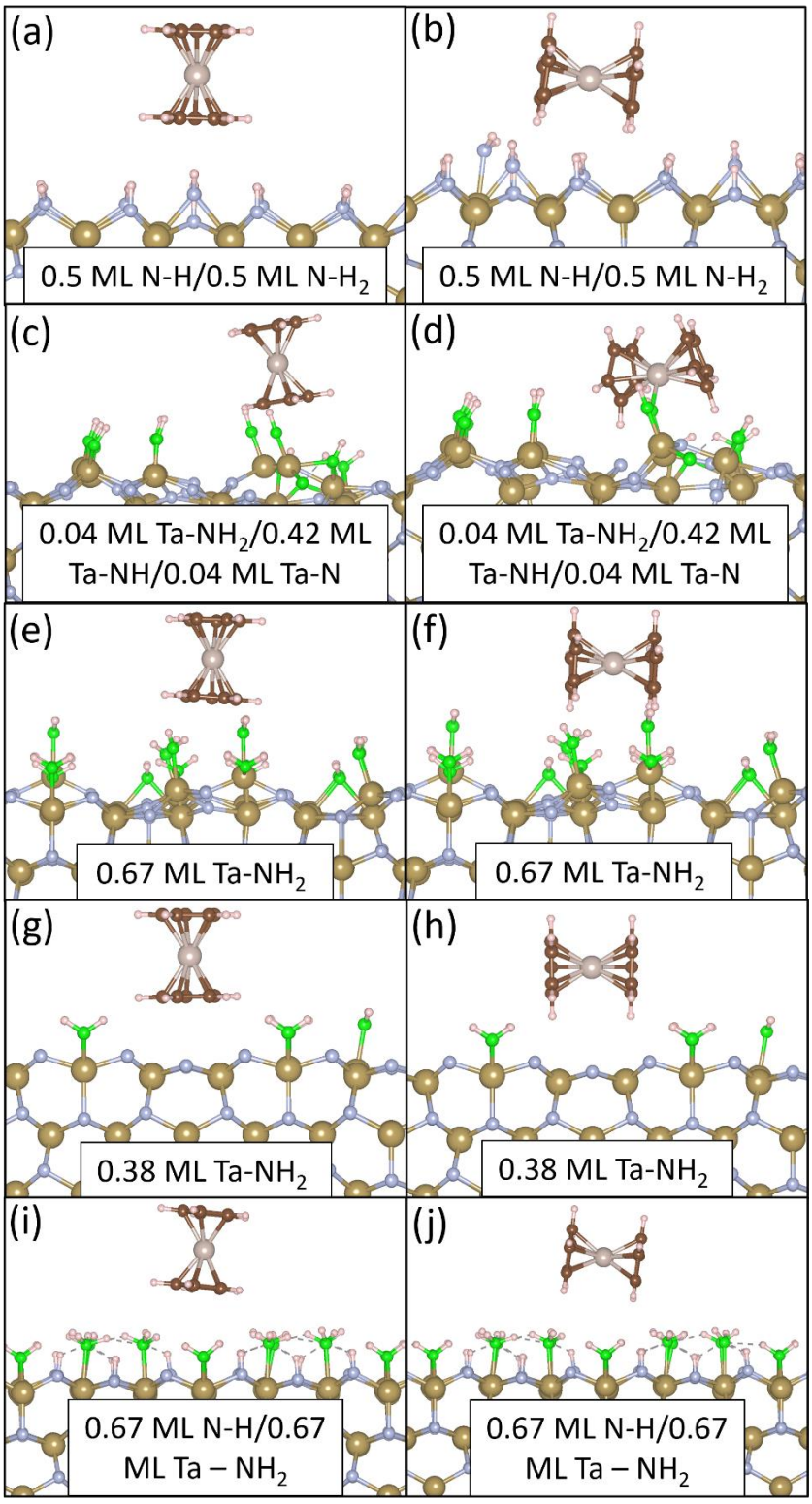


Figure A 4. $RuCp_2$ interaction at NH_x-terminated TaN surfaces. Colour scheme is Ta = brown, N = blue & green, H = pink, C = dark brown and Ru = grey.

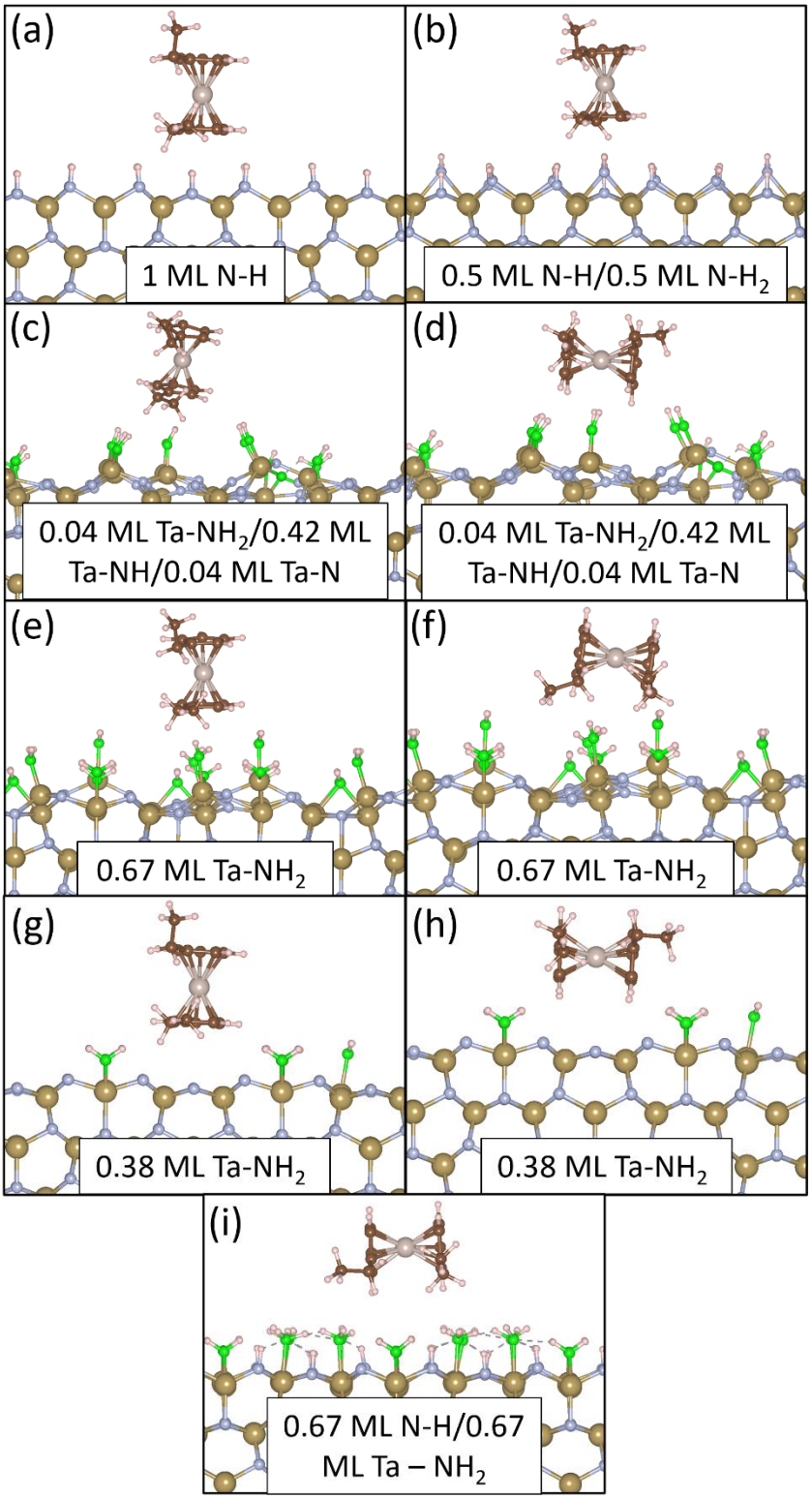


Figure A 5. $Ru(EtCp)_2$ adsorption at NH_x-terminated TaN surfaces. Colour scheme is the same as in Figure A 4.

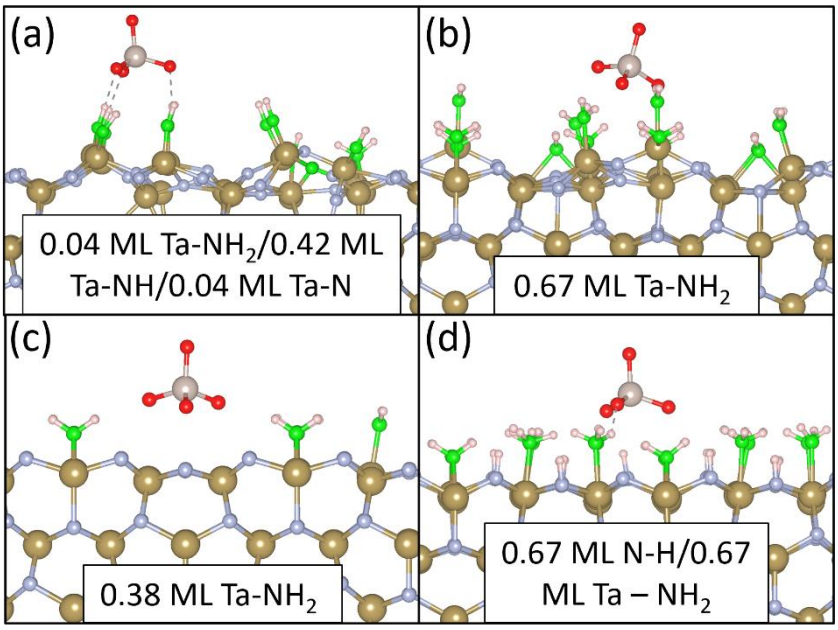


Figure A 6. RuO_4 adsorption at NH_x-terminated TaN surfaces. Colour scheme is Ta = brown, N = light blue & green, H = pink, O = red and Ru = grey.

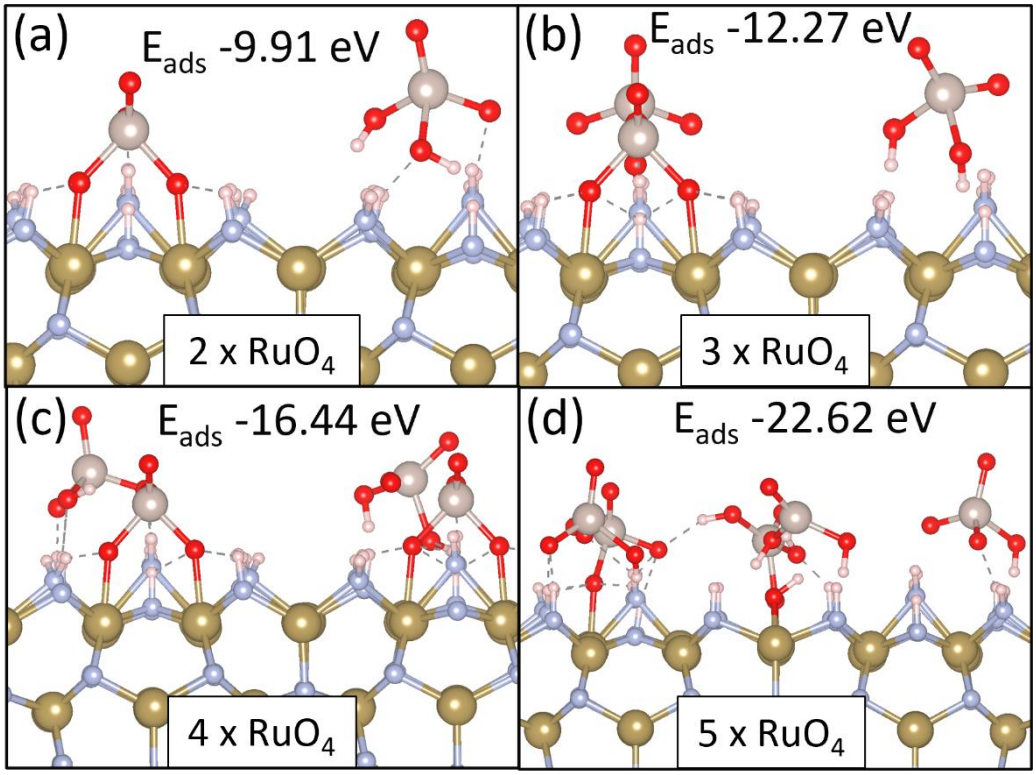


Figure A 7. RuO_4 coverages on 1 ML N-H TaN. Colour scheme is Ta = brown, N = light blue, H = pink, O = red and Ru = grey.

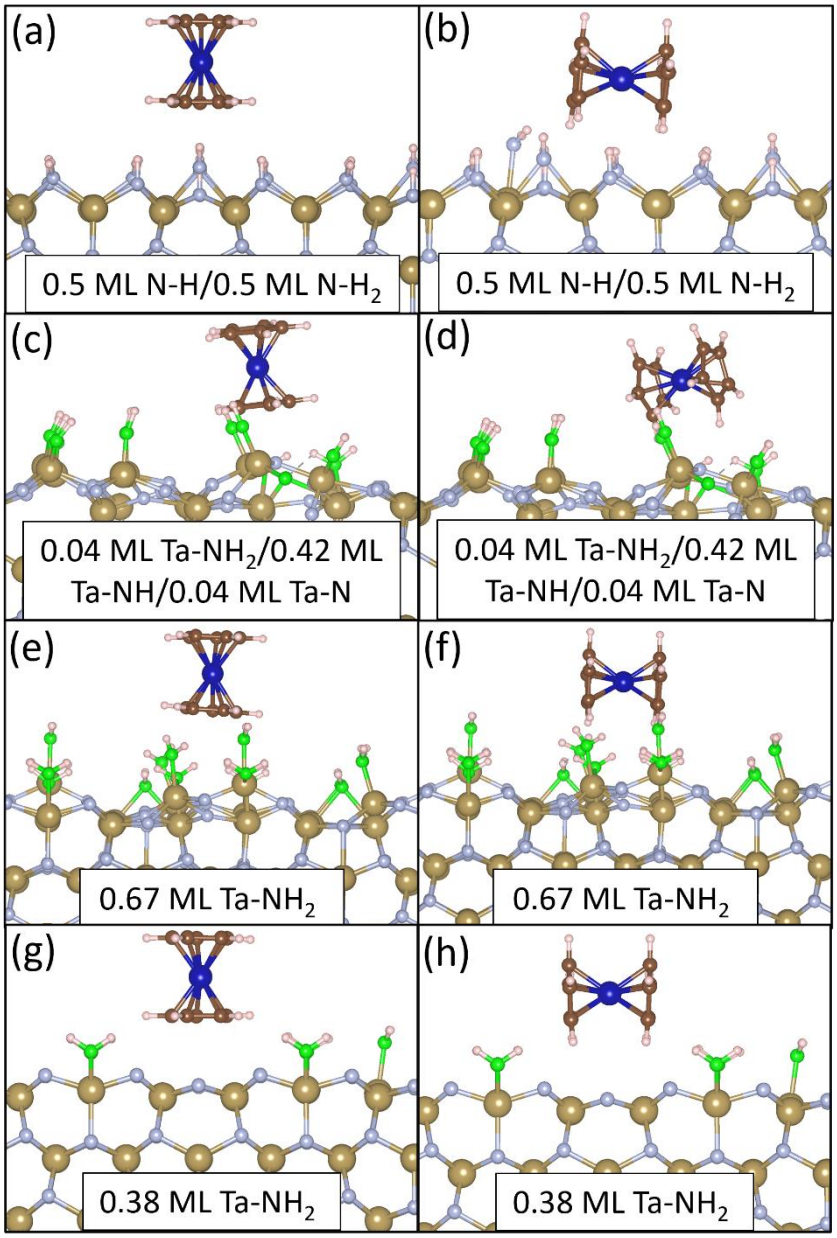


Figure A 8. $CoCp_2$ adsorption at NH_x-terminated TaN surfaces. Colour scheme is Ta = brown, N = blue & green, H = pink, C = dark brown and Co = dark blue.

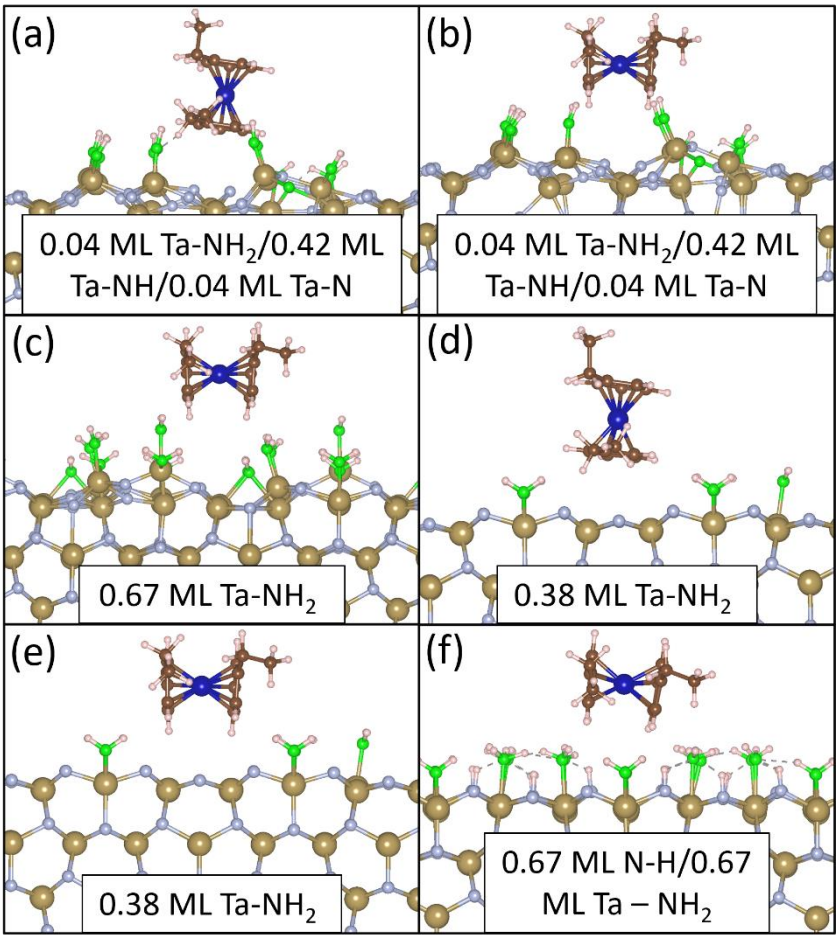


Figure A 9. $Co(EtCp)_2$ adsorption at NH_x-terminated TaN surfaces. Colour scheme is the same as in Figure A 8.

Table A 1. Reaction pathway energies for precursors $RuCp_2$ and $CoCp_2$ on 1 ML N-H TaN surface and for $CoCp_2$ on the 0.67 ML N-H/0.67 ML Ta-NH_2 TaN surface.

Reaction energy (eV)	$RuCp_2$ 1 ML N-H (H)	$RuCp_2$ 1 ML N-H (U)	$CoCp_2$ 1 ML N-H (H)	$CoCp_2$ 1 ML N-H (U)	$CoCp_2$ 0.67 ML N-H/0.67 ML Ta-NH_2 TaN
Precursor adsorption	-2.06	-2.01	-0.86	-0.72	-1.22
TS	-1.48	-0.85			0.11
H transfer	-1.66	-1.07	-2.66	-2.50	-1.21
CpH formation	-1.84	-0.91	-2.06	-1.90	0.31
CpH desorption	-1.52	-0.53	-1.64	-1.63	0.63
TS	-0.76	-0.05	0.15	-1.33	
H transfer	-1.15	-0.62	-2.51	-2.52	
CpH formation	0.99	1.31	-0.23	-0.25	
CpH desorption	1.27	-0.37	0.02	0.00	

Table A 2. Reaction pathway energies for $Ru(EtCp)_2$ and $Co(EtCp)_2$ on 1 ML N-H and 0.5 ML N-H/0.5 ML N-H_2 TaN surfaces.

Reaction energy (eV)	$Ru(EtCp)_2$ 1 ML N-H (H)	$Ru(EtCp)_2$ 0.5 ML N-H/0.5 ML N-H_2 (H)	$Co(EtCp)_2$ 1 ML N-H (U)	$Co(EtCp)_2$ 0.5 ML N-H/0.5 ML N-H_2 (U)
Precursor adsorption	-2.36	-0.92	-1.31	-1.28
TS	-1.17	0.07	-0.53	-0.90
H transfer	-1.54	-0.49	-3.29	-2.68
EtCpH formation	-1.52	-1.11	-3.16	-2.37
EtCpH desorption	-0.72	-0.41	-2.85	-1.51
TS	0.11	-0.19	-1.39	-0.97
H transfer	-0.72	-1.05	-2.45	-3.66
EtCpH formation	1.14	-0.90	0.34	-2.11
EtCpH desorption	-0.34	-0.58	0.82	-0.77

Table A 3. Reaction pathway energies for RuO_4 on 1 ML N-H TaN and 0.5 ML N-H/0.5 ML N-H_2 TaN surfaces.

Reaction energy (eV)	RuO_4 1 ML N-H	Reaction energy (eV)	RuO_4 0.5 ML N-H/0.5 ML N-H_2
Precursor adsorption	-3.72	Precursor adsorption	-4.71
Ts	-3.05	Ts	-4.58
H transfer 1	-3.73	H transfer 1	-5.34
H_2O desorption	-3.70	Ts	-5.21
TS	-3.70	H transfer 2	-5.70
H transfer 2	-5.47	H_2O desorption	-5.66
Ts	-4.98	Ts	-5.49
H transfer 3	-5.06	H transfer 3	-5.62
H_2O desorption	-6.08	Ts	-4.74
TS	-6.08	H transfer 4	-7.36
H transfer 4	-6.26	H_2O desorption	-10.56
TS	-5.83	Ts	-9.77
H transfer 5	-6.20	H transfer 5	-9.94
H_2O desorption	-5.41	H_2O desorption	-9.26
TS	-5.32	Ts	-8.99
H transfer 6	-6.46	H transfer 6	-9.46
TS	-6.14	Ts	-9.04
H transfer 7	-6.29	H transfer 7	-9.57
H_2O desorption	-5.09	H_2O desorption	-9.95

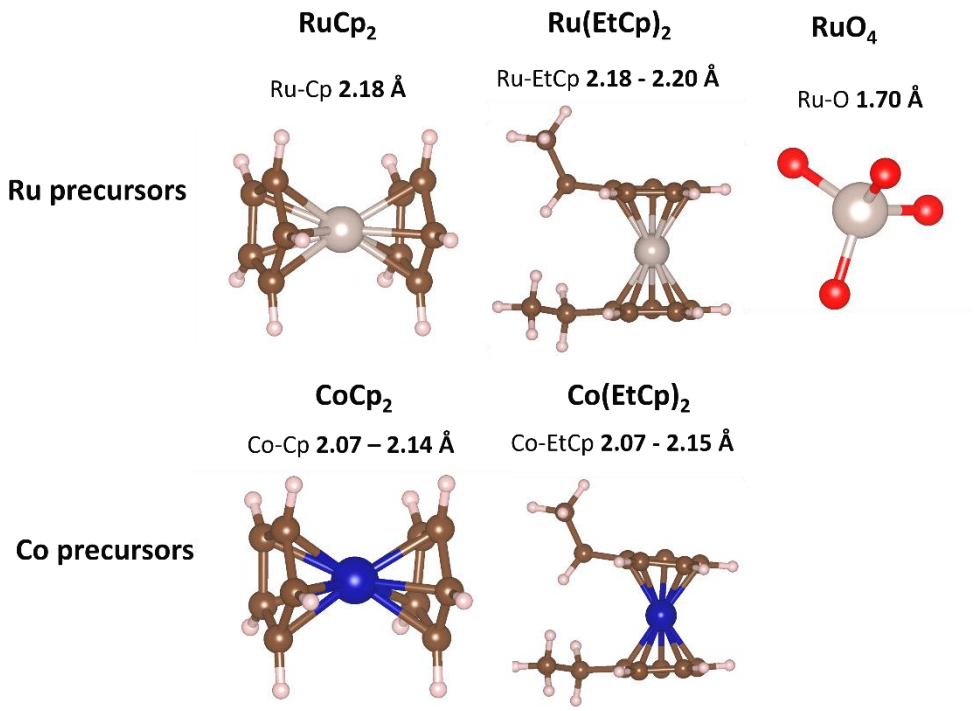


Figure A 10. Atomic structures of the ruthenium and cobalt precursors studied in chapter 8.

A4: Supplementary Material for Chapter 9

Table A 4: E_{bind} per adsorbed RuO_4 for RuO4 coverages of 1 to 5 at different configurations as shown in Figures 9.4 and 9.5 in chapter 9. M = number of RuO_4 precursors.

RuO_4 Coverage	E_{bind}/M (eV)
1 RuO_4 A	-4.14
1 RuO_4 B	-3.44
2 RuO_4 A	-4.38
2 RuO_4 B	-4.04
3 RuO_4 A	-3.40
3 RuO_4 B	-3.51
4 RuO_4 A	-3.37
4 RuO_4 B	-3.01
4 RuO_4 C	-3.18
4 RuO_4 D	-2.98
5 RuO_4 A	-2.68
5 RuO_4 B	-2.55
5 RuO_4 C	-2.37
5 RuO_4 D	-2.78
5 RuO_4 D	-2.18